

## Electroweak and Higgs Physics at Very High Energy

Présentée le 30 septembre 2022

Faculté des sciences de base  
Laboratoire de physique théorique des particules  
Programme doctoral en physique

pour l'obtention du grade de Docteur ès Sciences

par

**Lorenzo RICCI**

Acceptée sur proposition du jury

Prof. L. Villard, président du jury  
Dr A. Wulzer, directeur de thèse  
Prof. A. Pomarol, rapporteur  
Prof. P. Nason, rapporteur  
Prof. J. Penedones, rapporteur



Whatever the final laws of nature may be,  
there is no reason to suppose  
that they are designed to make physicists happy.  
— Steven Weinberg





# Acknowledgments

Four years of PhD are a lot of time and so much happened. Even if I am terrible in writing these sentimental things, I will try to do my best to thank the many people that accompanied me during this time.

The first acknowledgments go to my advisor Andrea Wulzer. Andrea welcomed me in the EPFL group when I was just a Master student in Padua. For me it was a very formative and important experience. It made me realize what kind of researcher I would like to become. Then, during my PhD, I understood how hard can be to do that kind of high quality research. Andrea taught me not only lots of physics but also how to be precise and how not to leave anything to chance. One of the great lesson I have learned from him is that a good researcher should not only be expert in one thing, but he should have a all-around knowledge (even if this implies doing heavy numerics). Research together has gone through a lot of ups and downs. I reckon that during the downs, it might have been hard working with me. Yet, Andrea has been really patient and in the end he made me realize that passing though lots of dead-ends is an essential part of the learning process and of our job. I really learn a lot from him and few lines will never be enough to give him credit for all what he taught me. I just want to say that if I ever became a good researcher, I somehow would owe it to Andrea and I thank him for that.

During my PhD I also had the privilege to have Riccardo Rattazzi as a second advisor. There are many reasons why I must thank him and why I was so extremely lucky to find him on my way. I have to say that Riccardo, apart from being a fantastic physicist, he is a very empathetic person who really guided me especially towards the end of my PhD. I should mention Riccardo's obsession for sharing the "know-how" to students and younger generations of physicists. Whoever is in the field knows how vast is his knowledge and how lucky I have been, if I only were capable to take a small part of this legacy with me. I also must thank Riccardo for supporting me in one of the hardest moment in my career, when I was just looking at the glass half-empty and he showed me the variety of opportunities I had.

I must add that both Andrea and Riccardo have been extremely patient with me. They

## Acknowledgments

---

not only gave me the opportunity to start research, but they also encouraged and pushed me in the negative moments, which are unavoidably part of this job. I owe them most of what I know and what I will try to learn in the next steps of my journey.

During these four years, I had the chance to meet and interact with lots of extraordinary physicists at EPFL and not only. From classes to seminars, all the EPFL theoretical physics laboratories represent a fantastic environment where to study physics, grow and do research. I also must mention the fruitful discussions at lunch in front of the tasty Antonio's pizzas ("Spettacolo" just to name one of his bests).

The number of people that I should thank for what I did and what I learned is huge. Here just a partial list of the people I collaborated with: Siyu Chen, Gabriel Cuomo, Majid Ekhterachian, Alfredo Glioti, Filippo Nardi, Giuliano Panico, Marc Riembau, Emmanuel Stamou, Riccardo Torre and Luca Vecchi.

Among them, I feel especially grateful to Luca and Giuliano. From them I learned lots of physics, from model building to collider phenomenology, and they supported and guided me in the difficult process of doing research.

Even during a worldwide pandemic, I also had the chance to enjoy Switzerland thanks to good friends and colleagues, with whom I shared bad and good time. It is impossible to give credit to all of them, but I will try.

Starting from Cubotron, I must thank Gabriel for all the football matches we saw together. Your spirited reactions to every goal conceded by Naples, made my sad Saturday nights at Cubotron a little bit funnier. Thanks to Alfredo for overselling me Andrea's skills on Mathematica and thanks to Andrea for all the help with Mathematica, your skills are actually impressive. Thanks Aditya for all the times I beat you in football and for teaching me a little bit of Hindi. Thanks Kamran for introducing me to the fantastic Persian food (excluded your pizza with ketchup) and for suggesting me a successful career as an Iranian baker. Thanks Miguel for the dinners and beers at CERN. Thanks Marc (even if I'm still waiting for the paella) for all our unborn PRLs. Thanks Siyu for the sky trips. Thanks Gil for the sad nights working at our theses in Cargèse, while the other students were having fun (thanks also to the Cargèse Physics Institute for the hospitality). I thank all the rest of the fantastic PhD group I found here at EPFL, Adrien, Joao, Kin, Eren, Filippo, Jan and I hope I didn't forget anyone.

Moving outside Cubotron, I must thank Giovanni for the unrepeatable celebrations for the European cup and for initiating me to climbing. Thanks Bernardo for all the time together outside our fantastic apartment in Rue de Chavannes. Thanks to Valerio, Davide, Gabriele, Giulia and all the people in Genève for all the dinner and party together. A special thank to Valerio ("il mozzo") for your birthday party that I do remember very well.

I want to thank my family and my friends all, from Teramo to Padua. You always supported me in my choices and pushed me to do my best.

## Acknowledgments

---

Finally I must thank Giulia for reading this thesis and all my published and unpublished manuscripts, I know that you were waiting for some awkward official acknowledgments. I thank you for all the time together and for always being there for me.

*Lausanne, 30<sup>th</sup> September, 2022*

Lorenzo Ricci





# Abstract

Effective Field Theories (EFTs) allow a description of low energy effects of heavy new physics Beyond the Standard Model (BSM) in terms of higher dimensional operators among the SM fields. EFTs are not only an elegant and consistent way to describe heavy new physics but they represent, at the same time, a valuable experimental tool for collider searches. The Standard Model Effective Field Theory naturally parametrizes the space of models BSM and measuring its interactions is, nowadays, substantial part of the theoretical and the experimental program at the (HL-)LHC and at future colliders. In this thesis we address the theoretical challenges of this Beyond the Standard Model precision program, following three different paths.

Firstly, we present some results towards the so-called high- $p_T$  program at the (HL-)LHC, targeting to measure energy growing effects of higher dimensional operators in the tail of kinematic distributions. Concretely, we focus on dilepton production and we study the sensitivity to flavor universal dimension-six operators interfering with the SM and enhanced by the energy. We produce theoretical predictions for the SM and the dim-6 EFT operators at NLO-QCD, including 1-loop EW logs. Our predictions are based on event reweighting of SM Montecarlo simulations and allow an easy scan of the multi-dimensional new physics parameter space on data. Furthermore we asses the impact of the various sources of theoretical uncertainties and we study the projected sensitivity of (HL-)LHC to the EFT interactions under consideration and to concrete BSM scenario. We then turn to future colliders and in particular to very high energy lepton colliders. In this context we study the potential of such machines with about 10 TeV center of mass energy to probe Higgs, ElectroWeak and Top physics at 100 TeV via precise measurements of EFT interactions. A peculiar aspect of so energetic ElectroWeak processes is the prominent phenomenon of the EW radiation. On one hand we find that consistent and sufficiently accurate predictions require resummations, that we perform at double logarithmic order. On the other hand we show how the study of the radiation pattern can enhance the sensitivity to new physics. We assess our results in Composite Higgs and Top scenarios and minimal  $Z'$  models.

Finally, we move to a top-down perspective and we perform a phenomenological study of composite Higgs models with partially composite Standard Models quarks. Starting from maximally symmetric scenarios that realize minimal flavor violation, we test various

## Abstract

---

assumptions for the flavor structure of the strong sector. Among the different models we consider, we find that there is an optimal amount of symmetries that protects from (chromo-)electric dipoles and reduces, at the same time, constraints from other flavor observables.

**Keywords:** Effective Field Theories, Precision physics, Beyond the Standard Model, Flavor physics, Future Colliders, Collider physics, Composite Higgs, Partial compositeness

# Riassunto

Le teorie efficaci di campo (EFT) consentono una descrizione a bassa energia di nuova fisica pesante dopo lo Standard Model (SM), in termini di operatori efficaci. Le EFTs non sono solo un modo elegante e consistente per descrivere nuova fisica pesante ma rappresentano, allo stesso tempo, un efficiente strumento sperimentale per la ricerca ai collider. Infatti, la teoria efficace dello Standard Model parametrizza naturalmente lo spazio dei modelli di nuova fisica. Misurare con precisione le interazioni che vi appartengono è una parte sostanziale del programma teorico e sperimentale di (HL-)LHC e dei collider futuri.

Questa tesi riassume alcune delle sfide teoriche di questo programma di fisica di precisione, che vengono discusse attraverso 3 diversi capitoli.

Prima di tutto, ci focalizziamo sul cosiddetto programma di high- $p_T$  di (HL-)LHC, mirato a misurare nuove interazioni efficaci nella coda delle distribuzioni cinematiche. In pratica studiamo l'impatto di operatori di dimensione 6, universali nel flavor e che crescono con l'energia, in processi di produzione di due leptoni. Le predizioni teoriche utilizzate sono ottenute tramite ripesamento di simulazioni MonteCarlo basate sullo SM. Queste predizioni sono estremamente precise (NLO-QCD + 1-loop EW Logs) e permettono di spaziare agevolmente su un ampio spazio di parametri di nuova fisica per un efficiente confronto con i dati.

Il secondo capitolo è dedicato ai "future collider" ed in particolare ai collider di leptoni ad alta energia. In questo contesto studiamo il potenziale di tali macchine, con circa 10 TeV di energia del centro di massa, per testare la fisica Elettrodebole, dell'Higgs e del Top fino a 100 TeV, tramite misure di precisione delle interazioni di EFT. Un aspetto peculiare dei processi Elettrodeboli ad energie così alte è l'importante fenomeno della radiazione Elettrodebole. Da un lato troviamo che predizioni consistenti e sufficientemente accurate richiedono risommazioni, che eseguiamo al doppio logaritmo. Dall'altro lato mostriamo come lo studio del pattern di radiazione può aumentare la sensibilità alla nuova fisica. Inoltre, quantifichiamo i nostri risultati in scenari di Higgs e Top composti e in modelli minimali di  $Z'$ .

Infine, cambiamo prospettiva e ci concentriamo su uno studio fenomenologico di modelli di Higgs composto che includono quark dello SM parzialmente composti. Partendo da scenari massimamente simmetrici, che realizzano l'ipotesi di "Minimal Flavor Violation",

## Riassunto

---

studiamo varie ipotesi riguardo la struttura del flavor del settore forte. Tra i diversi modelli che consideriamo, troviamo delle assunzioni ottimali che non generano dipoli (cromo-)elettrici e riducono, allo stesso tempo, l'impatto delle altre osservabili di flavor.

**Keywords:** Teorie di campo efficaci, Fisica di precisione, Fisica dopo il modello Standard, Fisica del Flavor, Future Colliders, Fisica del collider, Higgs composto, Partial compositeness

# Foreword

The thesis is schematically organized as follows:

- Chapter 1 is based on [1,2]
  1. L. Ricci, R. Torre, and A. Wulzer, *On the  $W\mathcal{E}Y$  interpretation of high-energy Drell-Yan measurements*, *JHEP* **02** (2021) 144 [[2008.12978](#)]
  2. G. Panico, L. Ricci and A. Wulzer, *High-energy EFT probes with fully differential Drell-Yan measurements*, *JHEP* **07** (2021) 086 [[2103.10532](#)]
- Chapter 2 is mostly based on [3]
  3. S. Chen, A. Glioti, R. Rattazzi, L. Ricci and A. Wulzer, *Learning from radiation at a very high energy lepton collider*, *JHEP* **05** (2022) 180 [[2202.10509](#)]and contains a short introduction on the resummation of IR effects in QFT.
- Chapter 3 is mostly based on a 4th paper to appear
  4. A. Glioti, R. Rattazzi, L. Ricci and L. Vecchi, *To appear*



# Contents

<b>Acknowledgments</b>	<b>i</b>
<b>Abstract</b>	<b>v</b>
<b>Riassunto</b>	<b>vii</b>
<b>Foreword</b>	<b>ix</b>
<b>Introduction</b>	<b>1</b>
The Standard Model Effective Field Theory . . . . .	4
Searching for New Physics far from the EW scale . . . . .	8
<b>1 Precision physics from the tail</b>	<b>11</b>
1.1 New Physics in High-Energy dilepton-Drell Yan . . . . .	12
1.2 Theoretical predictions via event reweighting . . . . .	15
1.2.1 Fixed-order QCD corrections . . . . .	16
1.2.2 Reweighting POWHEG . . . . .	21
1.2.3 Electroweak logarithms . . . . .	24
1.3 The Drell-Yan Likelihood . . . . .	31
1.3.1 Cross-section parametrization . . . . .	32
1.3.2 Parametric and theoretical uncertainties . . . . .	33
1.3.3 Statistical inference . . . . .	38
1.3.4 LHC projections . . . . .	39
1.4 Fully differential measurements . . . . .	44
1.4.1 Tree-level distributions . . . . .	44
1.4.2 Bounds on the Universal parameters $W$ and $Y$ . . . . .	47
1.4.3 General quark-lepton interactions . . . . .	50
1.4.4 Experimental uncertainties . . . . .	57
1.5 Sensitivity to Minimal $Z'$ models . . . . .	59
1.6 Conclusion and outlook . . . . .	63
<b>2 Precision physics from Very High Energy Leptons collisions</b>	<b>67</b>
2.1 Learning from radiation at VHEL . . . . .	68
2.2 All-orders IR Double Logs . . . . .	71

## Contents

---

2.2.1	The method of the asymptotic dynamics . . . . .	72
2.2.2	The Infrared Evolution Equation . . . . .	79
2.3	Di-fermion and di-boson production at VHEL . . . . .	91
2.3.1	Di-fermion production . . . . .	91
2.3.2	Di-boson production . . . . .	96
2.4	Sensitivity projections . . . . .	100
2.4.1	W&Y operators . . . . .	100
2.4.2	Diboson operators . . . . .	105
2.4.3	BSM sensitivity . . . . .	112
2.5	Conclusion and outlook . . . . .	117
<b>3</b>	<b>A light composite Higgs vs flavor observables</b>	<b>121</b>
3.1	Composite Higgs . . . . .	122
3.2	Partial Compositeness . . . . .	124
3.2.1	Symmetric strong sector . . . . .	127
3.3	Less symmetric strong sector . . . . .	134
3.3.1	Right-handed compositeness . . . . .	134
3.3.2	Left-handed compositeness . . . . .	143
3.3.3	Other possibilities . . . . .	146
3.4	Experimental constraints . . . . .	147
3.4.1	Universal constraints . . . . .	147
3.4.2	Anomalous couplings to SM gauge bosons . . . . .	149
3.4.3	Dipole operators . . . . .	152
3.4.4	Four-fermions operators . . . . .	154
3.5	Conclusion and outlook . . . . .	158
<b>A</b>	<b>Appendices for Chapter 1</b>	<b>161</b>
A.1	Explicit formulas . . . . .	161
A.2	Kinematical variables . . . . .	164
A.3	Correlation matrices . . . . .	165
A.4	LHC projections . . . . .	166
<b>B</b>	<b>Appendices for Chapter 2</b>	<b>169</b>
B.1	Radiation integrals . . . . .	169
B.2	High-energy EW multiplets . . . . .	173
B.3	<b>3<sup>rd</sup></b> family operators . . . . .	175
B.4	Summary plots . . . . .	176
<b>C</b>	<b>Appendices for Chapter 3</b>	<b>181</b>
C.1	Additional details on the models . . . . .	181
C.1.1	$U(2) \times U(3)_{\text{RC}}$ . . . . .	181
C.1.2	$U(2)_{\text{RC}}^2$ . . . . .	183
C.1.3	$U(2)_{\text{LC}}$ . . . . .	184



Bibliography	204
Curriculum Vitae	205



# Introduction

The Standard Model (SM) represents one of the greatest successes in the history of physics. In 2012 ATLAS [4] and CMS [5] announced the discovery of a spin-0 and mass 125 GeV resonance, compatible with the Higgs Boson. This was the last missing piece of the puzzle and after that the SM was finally experimentally confirmed.

In these ten years after the Higgs boson discovery, we started a new step toward the exploration of fundamental physics, the characterization of the Higgs sector. Moreover much effort from both the experimental and the theoretical physics communities converted the LHC from a discovery machine to a precision one and even if we are still at an early stage of the LHC data interpretation, there is already an evidence of a first remarkable result. The on-shell couplings of the Higgs boson are measured with 10% or more accuracy and this is suggesting the Higgs looks like an elementary particle up to a scale of roughly 1 TeV. So we are in a situation where we know that there is some new physics but we have no guaranteed of where to find it.

Despite of its experimental success, the SM gives just a partial description of nature and many questions are still open. Starting from energy scales far away from what we can actually test in our laboratories, we already know that the SM is limited and can describe processes below a maximum cut-off  $\Lambda_{SM}$ . In fact, the SM embeds a perturbative description of gravity, defined as a semiclassical expansion around general relativity. Yet, we know that processes at energies where quantum gravity becomes relevant ( $E \sim M_P \sim 10^{19}\text{GeV}$ ), would eventually violate perturbative unitarity. In more simple words, our calculations tell us that processes at the Plank scale  $M_P$  would not conserve probabilities, meaning that the SM is inconsistent at energies above  $\Lambda_{SM} \lesssim M_P$ . Gravity at the Plank scale  $M_P$  establishes an upper limit for where we are guaranteed to find something new. Apart from gravity, there are many more phenomena that are not accounted by the SM. Among them, neutrino oscillations, dark matter, matter anti-matter asymmetry, the CMB. At the same time there are still open questions behind what is actually described by the SM. What is the origin of the peculiar SM flavor structure? Why QCD seems to preserve CP? Why the proton lifetime is so long? And finally, what is the mechanism behind the EW symmetry breaking?

## Introduction

---

Many of the previous arguments point towards heavy new physics in the far UV. For instance neutrino oscillations suggest new physics at  $E \sim 10^{14}$  GeV or flavor observations seems compatible with  $E \sim 10^8$  GeV. These numbers are clearly large and incomparable with the energy we can actually touch in the foreseeable future. One of the previous question, however, can be addressed only proceeding in the exploration of the partially studied TeV energy range. In fact, establishing and quantifying the gap above the EW scale can unveil the mystery behind the generation of masses in the SM and why we observe this failure of dimensional analysis, as known as *fine-tuning*.

We illustrate this argument through a simple example [6].

### An invitation: the light electron mass

We learn in textbooks classical electromagnetism as the theory describing the interactions among the electric and magnetic fields and electrons. We also learn that a static electron generate a Coulomb potential  $V_{Coulomb} = \frac{e}{4\pi r}$ , where  $e$  is the electric charge and  $r$  is the distance from the electron. It is clear that electromagnetism fails to describe phenomena at very short distances, as fact of matters the Coulomb electric field would carry infinite energy in the proximity of the electron. In light of the previous discussion it is legitimate to wonder, what is the cut-off  $\mathcal{R}_{EM}$  of the electromagnetism, i.e. the minimal distance after which classical electromagnetism is not valid anymore and it must be replaced by a more fundamental theory?

The experimental radius of the electron is  $r_e < 10^{-17}cm$  and this set the maximum cut-off for the electromagnetism. Yet,  $10^{-17}cm$  seems an extremely small number, at least compared with the only length suggested by dimensional analysis  $\frac{e^2}{4\pi m_e} \sim 10^{-13}cm$ . It would be peculiar if  $\mathcal{R}_{EM} = r_e$  and dimensional analysis would fail of four order of magnitude in predicting  $\mathcal{R}_{EM}$ .

To better quantify this statement we can imagine to compute the measured electron mass  $m_e$  starting from the new fundamental theory and to split our calculation into two contributions

$$\begin{aligned} m_e &= \int_0^{+\infty} dr \frac{d\tilde{m}_e}{dr} = \int_{\mathcal{R}_{EM}}^{+\infty} dr \frac{d\tilde{m}_e}{dr} + \int_0^{\mathcal{R}_{EM}} dr \frac{d\tilde{m}_e}{dr} \\ &= \delta_{EM}m_e + \delta_{BEM}m_e, \end{aligned} \tag{1}$$

where  $\tilde{m}_e$  is the functional form of the electron mass in terms of the new physics parameters. The first term in eq. (1) includes the effects of the old classical electromagnetism, up to a distance  $\mathcal{R}_{EM}$ , and  $\delta_{BEM}m_e$  is the contribution from new physics Beyond the electromagnetism. Moreover, we know how to compute the first contribution  $\delta_{EM}m_e$ , it is just the electron self-energy from to the Coulomb potential  $\delta_{EM}m_e = \alpha/\mathcal{R}_{EM}$ , with  $\alpha = 1/137$  the electromagnetic structure constant. If no new physics occurs before hitting the electron radius  $\delta_{EM}|_{\mathcal{R}_{EM} \sim r_e} \simeq 70$  GeV, this is a huge number and an extremely precise cancellation must take place between  $\delta_{EM}m_e$  and  $\delta_{BEM}m_e$  in order to reproduce

$m_e$ . We can quantify this through the so-called fine-tuning parameter  $\Delta = \delta_{\text{EM}} m_e / m_e$ . Setting the EM cut-off at the electron radius means a fine tuning  $\Delta = 10^5$ , i.e. of 5 order of magnitude. This is evidently paradoxical and this can be appreciated doing the mental exercise of computing the electron mass from the hypothetical theory BEM. There, two completely distinct effects have to be computed with 5 digits precision just to get the first digit in  $m_e$ . Notice that if this, from a theoretical physicist perspective seems extremely peculiar, from a more technical point of view poses a concrete problem. If there is a large fine-tuning it means that the new short-distance theory cannot practically predict the electron mass, since it would technically require an extremely high precision.

In the case of the electron Nature has chosen a different path with respect to the fine-tuning. In fact, at a length well above  $10^{-17} \text{ cm}$ , electromagnetism is modified by the quantum production of electron-positron pairs. Moreover EM it is replaced at short distances by the more fundamental Quantum ElectroDynamics (QED), which includes also quantum mechanical effects. It is interesting that QED solves the electron naturalness problem even without a microscopic explanation for the electron mass. The solution is that the QED contribution to the electron mass is determined up to a multiplicative constant, fixed as a function of the Beyond QED contribution. More precisely

$$m_e = \delta_{\text{BQED}} \left( 1 + \frac{\delta_{\text{QED}}}{\delta_{\text{BQED}}} \right), \quad \frac{\delta_{\text{QED}}}{\delta_{\text{BQED}}} = \frac{3\alpha}{4\pi} \log \left( \frac{1}{\mathcal{R}_{\text{QED}} m_e} \right), \quad (2)$$

where crucially the second term grows logarithmically as a function of the cut-off. This growth is way milder than the powerlike growth in  $\delta_{\text{EM}} m_e$ . Furthermore we can notice that self-energy contribution to the electron mass is proportional to the mass itself and vanishes in the  $m_e \rightarrow 0$  limit. This remarkable property is peculiar of fermions and related to the approximate chiral symmetry re-obtained in the  $m_e = 0$  limit.

The situation of the SM, after ten years from the Higgs boson discovery is closely analogous to the one just described of classical electromagnetism. In practice, given  $\Lambda_{\text{SM}}$  we can play the same game and imagine to compute the Higgs mass  $m_h = 125 \text{ GeV}$ , starting from a more fundamental theory beyond the SM. Since now we have a purely quantum mechanical problem we can directly talk about energies, so  $\Lambda_{\text{SM}}$  is the energy cut-off of the SM and we have

$$\begin{aligned} m_h^2 &= \int_0^{\Lambda_{\text{SM}}} dE \frac{d\tilde{m}_h^2}{dE} + \int_{\Lambda_{\text{SM}}}^{+\infty} dE \frac{d\tilde{m}_h^2}{dE} . \\ &= \delta_{\text{SM}} m_h^2 + \delta_{\text{BSM}} m_h^2 \end{aligned} \quad (3)$$

Again we can define the fine-tuning as  $\Delta = \delta_{\text{SM}} m_h^2 / m_h^2$ , where  $\delta_{\text{SM}} m_h^2$  can be easily computed in perturbation theory. The leading contribution is the one related to top loops and it reads

$$\delta_{\text{SM}} m_h^2 = \frac{3y_t^2}{8\pi^2} \Lambda_{\text{SM}}^2, \quad (4)$$

and we can see that this contribution is quadratically enhanced by a large cut-off. In principle, we can imagine no new physics to occur before the Planck scale, setting  $\Lambda_{\text{SM}} = M_P$  we get a fine-tuning of 32 orders of magnitude. This seems extremely paradoxical: any theory BSM that can predict the Higgs mass would require extremely precise calculations (more than 30 digits), making this hypothetical calculation unfeasible. Moreover if nature respects naturalness we would expect new physics to show up at scales not too far from the TeV range. For instance  $\Lambda = 5 \text{ TeV}$  corresponds to a fine tuning of only two digits that seems still compatible with the naturalness principle. We remark that, if we don't consider the cosmological constant, the Higgs mass is the only parameter of the SM in this paradoxical situation.

To conclude, another crucial aspect, is that some solutions to the Higgs hierarchy problem have been proposed, among all the most remarkable are supersymmetry and compositeness (that will be discussed in ch 3). This is to say that there are examples of natural solutions to the hierarchy problem and this poses the paradox. Why nature should chose fine-tuning if there are natural choices?

Thanks to the huge experimental effort we can finally address this question. The large Hadron Collider (LHC) can perform precision measurements at the TeV range and exactly this year it is starting the third run of collisions. Feasible future collider proposals foresee processes with center of mass energy of tens of TeV. Exploring physics at the TeV it is a concrete plan to characterize the unknown and to establish what we know about fundamental physics.

## The Standard Model Effective Field Theory

The Standard Model is the most general Effective Field Theory (EFT) describing the interactions among all the particles we have observed so far. Phenomenological inputs together with a consistent description of spin-1 fields, requires the SM to be redundant under the  $SU(3)_c \times SU(2)_L \times U(1)_Y$  gauge group. Apart from that (and Lorentz invariance) no more constraints are required to the SM that is described only by its field content. The matter content features three generation of following Weyl fermions

$$q_L^i, \quad u_R^i, \quad d_R^i, \quad l_L^i, \quad e_R^i,$$

and a single scalar, the Higgs field  $H$ . All the quarks  $q_L, u_R, d_R$  transform in the fundamental of  $SU(3)_c$ , the left-handed fermions

$$q_L \equiv \begin{pmatrix} u_L \\ d_L \end{pmatrix}, \quad l_L \equiv \begin{pmatrix} \nu_L \\ e_L \end{pmatrix},$$

Field	$SU(3)_c$	$SU(2)_L$	$U(1)_Y$
$q_L$	3	2	$\frac{1}{6}$
$u_R$	3	1	$\frac{2}{3}$
$d_R$	3	1	$-\frac{1}{3}$
$l_L$	1	2	$-\frac{1}{2}$
$e_R$	1	1	-1
$H$	1	1	$\frac{1}{2}$

Table 1 – Gauge quantum numbers of the Standard Model matter fields.

and the Higgs  $H$  are doublets of  $SU(2)_L$ . The gauge quantum numbers of all the matter fields are summarized in table 1. The Lagrangian reads

$$\mathcal{L}_{SM} = \mathcal{L}_{SM}^{d \leq 4} + \mathcal{L}_{SM}^{d > 4}, \quad (5)$$

where the first term  $\mathcal{L}_{SM}^{d \leq 4}$  is the textbook-like “Standard Model” and it includes all the interactions that would survive in the limit where  $\Lambda_{SM} \rightarrow +\infty$ , i.e. in the limit where the SM is valid up to arbitrary high-scales (and we forget about gravity). Apart from neutrino oscillations,  $\mathcal{L}_{SM}^{d \leq 4}$  describes all the interactions observed so far. In order to fix the conventions and the notation, we briefly describe  $\mathcal{L}_{SM}^{d \leq 4}$

$$\mathcal{L}_{SM}^{d \leq 4} = \mathcal{L}_g + \mathcal{L}_H + \mathcal{L}_Y + \mathcal{L}_\theta, \quad (6)$$

The first addend  $\mathcal{L}_g$  includes the kinetic terms and the gauge interactions

$$\mathcal{L}_{gauge} = -\frac{1}{4}G^{\mu\nu a}G_{\mu\nu}^a - \frac{1}{4}W^{\mu\nu a}W_{\mu\nu}^a - \frac{1}{4}B^{\mu\nu}B_{\mu\nu} + \sum_{f=q,u,d,l,e} i\bar{f}\not{D}f + (D_\mu H)(D^\mu H)^\dagger. \quad (7)$$

where  $G^{\mu\nu a}$ ,  $W^{\mu\nu a}$  and  $B^{\mu\nu}$  are the  $SU(3)_c \times SU(2)_L \times U(1)_Y$  field strengths. The covariant derivative  $D$  is defined as

$$D_\mu = \partial_\mu - ig_s \lambda_a G_\mu^a - ig \tau^a W_\mu^a - ig' Y B_\mu, \quad (8)$$

with  $\lambda^a$  and  $\tau^a$  the generators of  $SU(3)_c$  and  $SU(2)_L$  algebras and  $g_s$ ,  $g$  and  $g'$  the various gauge couplings. The term  $\mathcal{L}_H$  contains the Higgs potential

$$\mathcal{L}_H = -\lambda_h \left( H^\dagger H - \frac{v^2}{2} \right), \quad (9)$$

and  $\mathcal{L}_Y$  describes the Yukawa interactions among the Higgs and the fermions

$$-\mathcal{L}_Y = Y_u^{ij} \bar{q}_L^i \tilde{H} u_R^j + Y_d^{ij} \bar{q}_L^i H d_R^j + Y_e^{ij} \bar{l}_L^i H e_R^j + h.c.. \quad (10)$$

## Introduction

---

Here  $\tilde{H} \equiv i\sigma_2 H^*$ , with  $\sigma_i$  the Pauli matrices. The non zero Higgs doublet vacuum expectation value

$$\langle H \rangle = \begin{bmatrix} 0 \\ \frac{v}{\sqrt{2}} \end{bmatrix}, \quad (11)$$

generates the masses for the gauge bosons and the various fermions. through the well-known spontaneous symmetry breaking mechanism. Given the unitary transformation that diagonalizes the up and down Yukawas

$$\frac{v}{\sqrt{2}} U_u^\dagger Y_u V_u = \text{Diag}[m_u, m_c, m_t], \quad \frac{v}{\sqrt{2}} U_d^\dagger Y_d V_d = \text{Diag}[m_d, m_s, m_b], \quad (12)$$

the Cabibbo–Kobayashi–Maskawa (CKM) matrix is given by

$$U_u^\dagger U_d = V_{CKM} = \begin{bmatrix} 1 - \frac{1}{2}\lambda^2 & \lambda & A\lambda^3(\rho - i\eta) \\ -\lambda & 1 - \frac{1}{2}\lambda^2 & A\lambda^2 \\ A\lambda^3(1 - \rho - i\eta) & -A\lambda^2 & 1 \end{bmatrix} + \mathcal{O}(\lambda^4), \quad (13)$$

where in the second equality we expressed the CKM in the so-called Wolfenstein parametrization. Finally, the last term in eq. (6) contains the topological term

$$\mathcal{L}_\theta = \frac{\theta_s}{16\pi^2} G^{\mu\nu a} \tilde{G}_{\mu\nu}^a, \quad \tilde{G}^{\mu\nu a} \equiv \frac{1}{2} \epsilon^{\mu\nu\rho\sigma} G_{\rho\sigma}^a.$$

Finally we remark that what we have just described is the “classical” Lagrangian and that we don’t review in any detail the quantization procedure, for which we refer to standard textbooks [7].

Now, we can turn to the second term in eq. (5). The SM is an Effective Field Theory and, as such, contains all the indirect effects of the degree of freedom that are too heavy to be directly produced. These effects are translated into a infinite tower of irrelevant deformations of the SM, encapsulated in higher dimensional composite operators built out from the SM fields

$$\mathcal{L}_{SM}^{d>4} = \frac{1}{\Lambda_{SM}} \mathcal{L}^{(5)} + \frac{1}{\Lambda_{SM}^2} \mathcal{L}^{(6)} + \dots \quad (14)$$

In the previous expansion  $\Lambda_{SM}$  is the cut-off of the SM, i.e. the energy scale where we can start producing the heavy BSM states. Processes closer and closer to this scale, clearly cannot be accounted by the SM since all the operators in eq. (14) would become more and more relevant and the expansion in eq. (14) would lose any meaning. On the contrary, in the regime where  $\Lambda_{SM}$  is larger than the energies of our processes, the expansion in eq. (14) is meaningful and the SM-EFT is a consistent description for our observations. In the current experimental situation, where no new particles on top of the SM degree of freedom are observed and where  $\mathcal{L}_{SM}^{d\leq 4}$  is found to work remarkably well,



the SM-EFT is the correct theoretical framework.

Following the discussion of the previous pages, the most important question is: what is  $\Lambda_{\text{SM}}$ ? A first indication of where we expect new physics comes from neutrino oscillations. Interactions in  $\mathcal{L}_{\text{SM}}^{d \leq 4}$  can not address such phenomenon which can be described by  $\mathcal{L}_{\text{SM}}^{(5)}$ . Matching the experimental observation with the effects described by the so-called Weinberg operator [8], the only interaction contained in  $\mathcal{L}_{\text{SM}}^{(5)}$ , we can expect  $\Lambda_{\text{SM}} \sim 10^{14}$  GeV.

Another hint comes from the large lifetime of the proton. Again  $\mathcal{L}_{\text{SM}}^{d \leq 4}$  predicts the proton to be stable, just by the fact that all the interactions in  $\mathcal{L}_{\text{SM}}^{d \leq 4}$  have an accidental symmetry conserving the baryon number. Accidental means that higher dimensional interactions can in principle spoil this symmetry, indeed  $\mathcal{L}_{\text{SM}}^{(6)}$  contains operators mediating the decay of the proton. Merging this consideration with experimental constraints, one can infer new physics at  $\Lambda_{\text{SM}} \gtrsim 10^{15}$  GeV.

However, new physics mediating neutrino oscillations and/or proton decay is not in contradiction with new physics at a lower scale. In fact, as the  $\mathcal{L}_{\text{SM}}^{d \leq 4}$  protects the proton from decaying, a similar protection mechanism can arise in hypothetical new physics at scales lower than  $10^{15}$  GeV.

As we discussed at length before, the naturalness argument is pushing for new physics at the TeV scale. At the same time, this is the energy range we are currently exploring at LHC and we plan to explore at future colliders. A SM cut-off of  $\Lambda_{\text{SM}} \sim \text{few TeV}$  can produce potentially measurable effects in  $\mathcal{L}_{\text{SM}}^{d > 5}$ . Therefore insisting in measuring the effects of higher dimensional operators we have the chance to finally understand if or not there is new physics, as suggested by naturalness.

Notice that from a bottom-up perspective the SM as an EFT is an extremely efficient way to search for new physics. Whatever the heavy new physics we are looking for, it generates higher dimensional operators. The coefficients of these operators, the so-called Wilson coefficients, directly parametrize new physics effects. The latter can be computed and matched with data, resulting in constraints or observation on this new physics parameter space defined by the Wilson coefficients. In this sense, the SM, as an EFT, it is not only the correct theoretical way to describe generic heavy new physics effects, but it is also an experimentally valuable tool for BSM searches.

Also from a top-down perspective an EFT description of the SM seems a promising framework. Specific BSM scenarios, at low energy, produce specific signatures described only by certain operators or combinations of operators in  $\mathcal{L}_{\text{SM}}^{d > 4}$ . Therefore, constraining the SM interactions we are effectively constraining the space of UV theories BSM.

At the same time we remark that a completely general SM-EFT contains a so large set of theories to lose any practical application. In fact, if at  $d = 5$  there is only the Weinberg operators, at  $d = 6$  there are more than a thousand operators [9] and they become more and more with the increasing of the scaling dimensions. This makes completely “model independent” searches technically unfeasible and force us to select some class of

operators.

Furthermore, theoretical inputs can drive the experimental searches, through BSM motivated hypotheses that can restrict the space of Wilson coefficients. A remarkable example that we study in details in the rest of the thesis is composite Higgs. The latter admits an EFT description in terms of higher dimensional operators, whose Wilson coefficients can be sized through arguments of dimensional analysis [10].<sup>1</sup> The result is a concrete set of EFTs where the Wilson coefficients are functions of a benchmark model parameters and can be matched with specific BSM models.

## Searching for New Physics far from the EW scale

We just saw that an effective way to search for BSM is through precise measurements of the SM interactions. These are the so-called indirect searches for new physics and they are the common denominator over the three chapter of this thesis. More precisely the material presented in this manuscript is part of a theoretical and experimental program with the final goal to characterize or discover new physics through EFTs. This is a challenging and ambitious program that needs a huge experimental effort and also requires theoretical progress from many different directions. In this thesis we follow some of them as we now shortly summarize.

The results collected in ch. 1 regard the so-called high- $p_T$  searches for EFT interactions at the (HL-)LHC. The key idea we follow is to exploit the large energy provided by our collider to improve the sensitivity to new physics. The logic is very simple and can be easily understood just by dimensional analysis. Probing the effective interactions of eq. (14) at energies  $E \ll \Lambda_{\text{SM}}$ , gives a correction to observables scaling as  $(E/\Lambda_{\text{SM}})^n$ , for some  $n \geq 0$ . For those observables with  $n > 0$ , the energy enhances the accuracy in the determination of the EFT Wilson coefficients.

We focus on dilepton production, via the Drell Yan mechanism, and we identify the most relevant deformations of the SM which give rise to the effects just mentioned. Given that, we study the various kinematic distributions which can improve the sensitivity to new physics and assess the impact of the different sources of theoretical uncertainties.

Furthermore we produced a theoretical tool to obtain theoretical predictions for dim-6 EFT operators in dilepton DY at NLO-QCD and which includes 1-loop EW logs. This tool is aimed to allow the experimental collaborations to have easy access to the theoretical predictions and an efficient way to scan folded and unfolded data into a multi-dimensional new physics parameters space.

Employing this tool, we produce a quantitative theoretical study based on concrete projections for (HL-)LHC. We interpret our results in a simple BSM scenario.

In chapter 2 we turn to future collider and in particular Very High-Energy Lepton Colliders. Here, borrowing the logic presented in ch. 1, we assess the impact of this

---

<sup>1</sup>We refer to chapter 3 for a more detailed discussion.

hypothetical machine to the sensitivity to heavy new physics encoded in EFT operators. The story is, however, quite different than (HL-)LHC. In fact, even if the leptonic environment is cleaner than the messy QCD one, additional challenges arise due to the very high center-of-mass energy (tens of TeV). Radiative EW corrections become  $\mathcal{O}(1)$  effects, at the point to invalidate perturbative calculations and require systematic resummations.

We address this problem resumming Leading-Log effects and we assess the impact of higher order corrections. Moreover the main novelty of our phenomenological study is related to the non trivial interplay between radiation and sensitivity. Concretely we show how the study of the radiation pattern improves the sensitivity to new physics. We conclude this study with the analysis of the projected sensitivity to relevant new physics scenarios, such as composite Higgs.

Finally in chapter 3 we adopt a top-down perspective and we present a phenomenological study mostly based on BSM motivated scenario. In particular we study the interplay of the various flavor and non-flavor observables in a rich-class of composite Higgs EFTs including the description of SM fermions via partial compositeness. We classify the various scenarios based on symmetries and a well-defined set of assumptions. We furthermore assess the impact of the present measurements. We point out the excluded scenario and the ones that could be excluded or confirmed in the next few years. The main goal of the work is to characterize a set of relevant EFTs to guide concrete phenomenological studies of composite Higgs models.

In conclusion in the three chapters we present three different paths toward precision physics, with the common goal to characterize and/or discover heavy new physics far from the EW scale.



# 1 Precision physics from the tail

Accurate measurements of high-energy observables are powerful probes of new physics, and arguably one of the most promising avenues for the continuation of the LHC experimental program. The study of neutral ( $l^+l^-$ ) and charged ( $l\nu$ ) Drell–Yan (DY) differential cross-section measurements offers a clear illustration of this potential [11]. This has also been demonstrated for several other processes, including diboson and boson-plus-Higgs [12–27], dijet [28, 29], di-quark [30, 31] production and also in the context of future colliders (see ref. [32] for a summary).

The competitive advantage of high-energy measurements stems from the fact that the effects of heavy new physics, at a scale  $\Lambda$ , increase with the energy  $E \ll \Lambda$  of the process as a (positive) power of  $E/\Lambda$ . The larger  $E$  the larger the effect and thus, given finite measurements accuracy, new physics could be visible only at high enough  $E$ .

However, precise measurements at high energy, and in particular at the tail of the LHC energy spectrum, are challenging and requires effort from both the experimental and the theoretical sides.

In this chapter we address the various theoretical problems of these “high-energy probes” in the specific framework of the dilepton DY at the LHC. In particular we classify the pertinent deformation of the SM, and we identify the relevant differential measurements that can improve the sensitivity. Moreover we provide the theoretical predictions of the new physics effects via event reweighting of SM Monte Carlo generated events. Our predictions are not only sufficiently accurate, but the reweighting methodology also allows an efficient exploration of the various BSM directions on the multi-differential set of data. Finally we assess the impact of the various sources of uncertainties on concrete sensitivity projections, that we then interpret in simple BSM scenarios.

## 1.1 New Physics in High-Energy dilepton-Drell Yan

Charged ( $l^+l^-$ ) and neutral ( $l\nu_l$ ) DY are in some sense the ideal high energy probes. First of all the large cross-sections together with low systematics allow accurate measurements of the high-energy tail, which is indispensable in order to detect tiny modification from the SM predictions due to heavy new physics. Moreover the dilepton final states represent an “easy” signal, simply characterizable by few kinematic variables that we can exploit in order to improve our sensitivity, as we will explain in detail in sec. 1.4.

The main target of our searches are higher dimensional operator which parametrize irrelevant deformation of the SM, related to heavy new physics. Restricting as customary to dimension-6 operators, with Wilson coefficients  $G \propto 1/\Lambda^2$  of dimension  $-2$ , we immediately identify possible contributions to the scattering amplitudes of order  $G \cdot E^2$  relative to the Standard Model. Even on this aspect dilepton DY is particularly promising, since there is a large set of growing-with-energy amplitudes interfering a tree-level with the SM ones. Therefore we can just focus on the leading effects from the most relevant higher dimensional operators that, as we will see, happen also to describe a large set of BSM motivated EFTs.

These dimension six operators can be easily identified in the so-called Warsaw basis [9]. In particular, among all the quark-lepton interactions, the ones giving rise to growing-with-energy effects in dilepton DY, we can focus only on the “current-current” types, i.e. on operators of the form  $J_l^\mu J_{q,\mu}$ , with  $J_{l(q)}^\mu$  any of the lepton (quark) chiral currents. This is because the fermion chirality structure of the other operators forbids them to interfere with the SM amplitude at tree-level.<sup>1</sup> Therefore the  $\mathcal{O}(G E^2)$  term they produce in the amplitude results in an  $\mathcal{O}((G E^2)^2)$  contribution to the cross-section, relative to the SM one. Since we are interested in probing new physics at scales  $\Lambda$  that are higher than the available energy, so that  $G E^2 \ll 1$ , we can neglect non-interfering operators compared with the interfering (current-current) ones that do instead produce a genuine  $\mathcal{O}(G E^2)$  contribution to the cross-section. The above argument of course fails, and non-interfering operators should be included, if their Wilson coefficients are enhanced relative to the current-current ones. However, if it is hard to find a concrete new physics scenario where this enhancement is structurally motivated, it is easy to find scenarios where the converse happens and non-interfering operators are suppressed. Moreover when targeting quartically energy-growing effects (from the square of the new physics amplitude) one should also worry about the contribution of dimension-8 operators, that can produce similar effects at the interference level. We thus regretless ignore non-interfering operators and focus on the current-current ones. This could of course be reconsidered at a more advanced stage of the global EFT interpretation of LHC data.

The methodology we describe in the rest of the chapter apply to any current-current operators involving light quarks (including the bottom) and lepton, with arbitrary current

---

<sup>1</sup>Also Flavor-Changing Neutral Current (FCNCN) current-current operators, which are in any case irrelevant because of the strong flavor constraints (see however [33]), do not interfere with the SM.

## 1.1. New Physics in High-Energy dilepton-Drell Yan

current-current quark-lepton	W and Y current-current
$\mathcal{O}_{lq}^{(3)} = (\bar{l}_L \sigma_I \gamma^\mu l_L)(\bar{q}_L \sigma_I \gamma_\mu q_L)$	$\mathcal{O}'_{2W} = J_L^{a,\mu} J_{L,\mu}^a \quad J_L^{a,\mu} = \sum_f \bar{f} \gamma^\mu T^a f$
$\mathcal{O}_{lq}^{(1)} = (\bar{l}_L \gamma^\mu l_L)(\bar{q}_L \gamma_\mu q_L)$	$\mathcal{O}'_{2B} = J_Y^\mu J_{Y,\mu} \quad J_Y^\mu = \sum_f \bar{f} \gamma^\mu Y_f f$
$\mathcal{O}_{eu} = (\bar{e}_R \gamma^\mu e_R)(\bar{u}_R \gamma_\mu u_R)$	$G_{Lq}^{(3)} = \frac{1}{2} G'_{2W}$
$\mathcal{O}_{ed} = (\bar{e}_R \gamma^\mu e_R)(\bar{d}_R \gamma_\mu d_R)$	$G_{Lq}^{(1)} = -\frac{1}{6} G'_{2B} \quad G_{eu} = -\frac{4}{3} G'_{2B}$
$\mathcal{O}_{lu} = (\bar{l}_L \gamma^\mu l_L)(\bar{u}_R \gamma_\mu u_R)$	$G_{ed} = \frac{2}{3} G'_{2B} \quad G_{lu} = -\frac{2}{3} G'_{2B}$
$\mathcal{O}_{ld} = (\bar{l}_L \gamma^\mu l_L)(\bar{d}_R \gamma_\mu d_R)$	$G_{ld} = \frac{1}{3} G'_{2B} \quad G_{qe} = -\frac{1}{3} G'_{2B}$
$\mathcal{O}_{qe} = (\bar{q}_L \gamma^\mu q_L)(\bar{e}_R \gamma_\mu e_R)$	

Table 1.1 – Left table: Quark-lepton current-current operators in the Warsaw basis [9]. Right table: The operators related to the W and Y parameters, together with their rewriting in terms of Warsaw basis operators. The operators are flavor universal and thus the generation indices have been suppressed.

chirality and flavor structure. We present, however, concrete results only for two specific new physics scenarios. The first is the “universal” scenario [34], where new effects can be described only as modifications of the SM gauge bosons propagators and can be parametrized through the 8 “oblique” parameters [35].<sup>2</sup> Among them only W and Y give rise to growing-with-energy effects in DY and they are related by equation of motion to the  $\mathcal{O}'_{2W}$  and  $\mathcal{O}'_{2B}$  operators on the right panel of table 1.1. The second scenario is the flavour universal one, where we relax the hypothesis of universality and we allow new physics to couple directly to the SM fermions, assuming, however, that the new effects preserve the SM flavor structure. The choice of restricting our analysis to this two scenarios is motivated in first place by clarity. The expected sensitivity and the impact of the various sources of uncertainties is much more effectively illustrated in a 2 dimensional parameter space. Moreover, as we will see in sec. 1.4, constraining effectively the 7 dimensional parameter space of the flavor universal lepton-quark interactions is technically more challenging and requires a more detailed phenomenological study. In second place, we stress that the subset of EFTs we constrain in this chapter describe a wide and interesting class of UV completion of the SM. Moreover already from the W and Y parameters we can gain information on structurally motivated scenarios such as Composite Higgs [10].<sup>3</sup>

The search for EFT effects in DY data will be most likely based on unfolded differential cross-section measurements, similar to those in refs. [39, 40] for 8 TeV, in ref. [41] for early run-1 and in ref [42] for recent run-2 data, to be compared with the corresponding EFT predictions.<sup>4</sup> We should then provide such predictions as accurately as possible

<sup>2</sup>Or 9 including the  $H$  parameter of [36].

<sup>3</sup>Notice that since the top plays no role in our discussion, W and Y also parametrize the effects of “top-philic” theories [37, 38].

<sup>4</sup>An alternative is to compare the EFT predictions directly with the data distributions at the observed

and, equally importantly, provide reliable estimates of the associated parametrical and theoretical uncertainties. The target accuracy is dictated by the experimental error on the corresponding measurement, which is going to be vastly different in different energy regions. At very high energy the error will unavoidably get large, because of the limited statistics. This reduces the needs for theoretical accuracy, potentially allowing us to cope with the limited knowledge of Parton Distribution Functions (PDF), with the lack of Electroweak (EW) logs resummation, and with other effects that enhance the uncertainties at very high energy. Verifying to what extent this is indeed the case is one of the goals of [1]. A lot of data are instead available at lower energy, and the measurement error will be dominated by systematic uncertainties. While we are unable to quantify them, based on refs. [39, 40] we expect experimental systematics of order few percent in the energy range from 300 GeV to 2 TeV, in line with the first run-2 results in [42] (appeared after the publication of [1, 2]). In section 1.3 we re-analyze this accuracy goal, given state-of-the-art calculations and PDF uncertainties.

As we already mentioned, the DY final state is so simple that it can be characterized completely with fully-differential cross-section measurements. Fully (i.e. triply) differential measurements of the neutral DY process have already been performed by ATLAS with early run-1 data [43].<sup>5</sup> As we will quantify in sec. 1.4 exploiting correctly fully differential measurements improves the sensitivity to the EFT operators with respect to the single differential analysis. In particular, adopting the reweighting procedure described in sec. 1.2 we will show how, starting just from simulation based on the SM-hypothesis, we can efficiently explore the 7-dimensional parameter space defined by the Wilson coefficients of the flavor universal quark-lepton interactions. We stress that the large dimensionality of the EFT parameter space, combined with the large number of analysis bins that are employed for the fully-differential analysis, would have made this project computationally too demanding if employing a Monte Carlo implementation not based on reweighting.

The rest of the chapter is organized as follows. We start in section 1.2 with the technical discussion on the theoretical predictions. Then in sec. 1.3 we present the first sensitivity projections for the W and Y parameters from single-differential measurements, together with a detailed discussion on the statistical analysis and on the impact of the different uncertainties. In sec. 1.4 we turn to the fully-differential measurements and we provide more complete projections for the sensitivity to the quark-lepton interactions. We then employ these results to study the sensitivity to the simple concrete BSM scenario of the minimal  $Z'$ -model. Finally we conclude in sec. 1.6.

---

level. If this strategy is adopted, accurate Monte Carlo events generators are needed, and not only differential cross-sections predictions. The reweighting strategy we discuss in sec. 1.2 does also provide accurate event samples.

<sup>5</sup>Double differential measurements have been performed in Refs. [39, 40].



## 1.2 Theoretical predictions via event reweighting

Precise theoretical predictions for dilepton DY processes have been widely investigated. SM differential cross-section were firstly derived long ago, at NLO-QCD [44, 45] and including NLO-EW effects [46, 47]. Further QCD results have been presented, from some differential distribution at NNLO [48–51] to other predictions up to N<sup>3</sup>LO [52–55]. Moreover, combined NNLO-QCD and NLO-EW corrections to high mass DY pairs have been studied in details [56–62] and state-of-the-art predictions for differential distribution have been automated in FEWZ [63].

At dimension 6 in the SM-EFT, NLO-QCD corrections are automated and consistently interfaced with the parton shower in the POWHEG Monte Carlo event generator [64]. The practical applicability of this tool however is limited by the fact that NLO simulations are long and demanding, and they should be run several times in order to extract, for each bin, the dependence of the cross-section on the EFT parameters. Of course the task is simplified by the fact that the cross-section is a quadratic polynomial in the Wilson coefficients. However extracting the polynomial coefficients (in particular, the linear ones) requires very accurate simulations, to be sensitive to the small correction due to the EFT on top of the SM. Moreover it requires a careful choice of the simulation parameters, which should be such that neither the SM nor the quadratic terms dominate by too many orders of magnitude. Since this parameters choice depends strongly on the bin, a large number of accurate simulations is required. While this approach might perhaps still work in the two-parameters W&Y case, it would definitely be unfeasible in the large parameter space of generic current-current operators.

To solve the problem, in [1] we adopted a different methodology, based on event reweighting. Namely we noticed that the Born, the virtual, and the real helicity amplitudes are all affected by current-current operators through a common multiplicative factor. This factor is a linear polynomial in the Wilson coefficients (which enters squared in the cross-section), with constant term equal one corresponding to the SM contribution and coefficients that depend on the dilepton center-of-mass energy. The coefficients of the polynomial are readily computed for each combination of helicities and of quarks and lepton flavors, and they allow us to model the entire EFT parameter space, at exact NLO accuracy, by reweighting the events of a single Monte Carlo simulation. Namely, for each simulated event we compute the coefficients and we store them in the events file. Once a cross-section binning is defined, the events are binned accordingly and the stored information is used to compute the coefficients of the quadratic polynomial that describes the dependence on the EFT parameters of the cross-section in each bin. Reweighted Monte Carlo events can also be used for the direct comparison of the EFT with the data, or in order to check the possible impact of the EFT effects on the unfolding procedure by which the cross-sections are measured. Notice that the obvious virtues of the reweighting methodology (whenever applicable) are well-recognized in the literature, to the point that reweighting has been automated in MadWeight [65]. However, only recently MadWeight

included quark-lepton four-fermion operators in the EFT MADGRAPH [66] model at NLO<sup>6</sup> [68], which were unavailable when we published [1]. Therefore we produced our own implementation based on the SM POWHEG DY generator [69] as we will describe in the following.

We stress that analytic reweighting is not only more efficient in providing (NLO QCD) EFT predictions, but it also allows one to improve the accuracy by including new effects on what was at time of [1] the state-of-the art prediction. We considered, in particular, the EW single and double logs, which are enhanced at high mass and constitute the dominant NLO EW effects, and we included them in the EFT prediction. We also used reweighting to estimate the effect (on the SM prediction, most importantly) of Sudakov logs of higher orders in the loop expansion.

In rest of the section we describe in detail the reweighting methodology derived in [1] and then employed in [2]. We start, in section 1.2.1, by discussing how fixed-order QCD NLO predictions, in the presence of quark-lepton current-current new physics interactions, can be obtained by analytic reweighting. Next, in section 1.2.2, we illustrate our POWHEG implementation and we show that reweighting is fully compatible with the POWHEG master formula, ensuring that showering effects are consistently included in our reweighted Monte Carlo events. We address in section 1.2.3 the slightly more technical problem of including EW logarithms of IR and UV (RG-running) nature.

### 1.2.1 Fixed-order QCD corrections

We first consider neutral DY, i.e. the process

$$pp \rightarrow l^+ l^- + X, \quad (1.1)$$

with  $l = e, \mu$  or (possibly) a  $\tau$ . We are interested in the high energy regime of the process, with a lower threshold on the dilepton center-of-mass energy that we set for definiteness at  $\sqrt{s} > 300$  GeV. In all the amplitudes that contribute to dilepton production, at the leading order in the EW and in the new physics couplings but at all orders in QCD, it is possible to isolate a common subdiagram, displayed in figure 1.1 with its corresponding Feynman rule. In the figure,  $\chi_q = L, R$  and  $\chi_l = L, R$  denote the chirality of the quark and of the lepton legs, and  $P_{\chi_{q,l}}$  the corresponding chirality projectors acting on the quarks and leptons spinor indices, respectively. Notice that only same-chirality  $q/\bar{q}$  and  $l^+/l^-$  pairs can interact in the SM (Higgs interactions are of course totally negligible), and the same is true for the current-current effective vertices. Also the flavor ( $q = u, d, s, c, b$ ) of the quark must be the same of the anti-quark since we are excluding FCNC new physics interactions as explained in footnote 1.

---

<sup>6</sup>Latest releases of MADGRAPH also includes NLO-EW corrections on SM-EFT, which are also available in explit form in [67] for the neutral DY.

## 1.2. Theoretical predictions via event reweighting

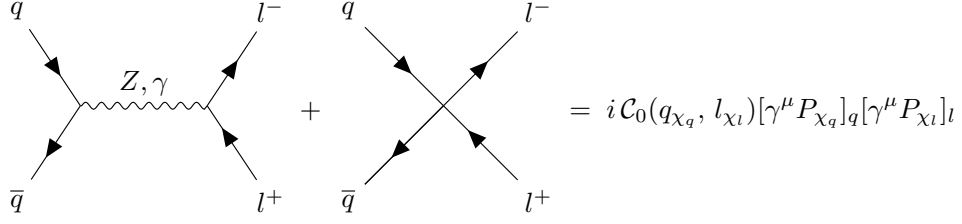


Figure 1.1 – Effective Feynman vertex for neutral DY, including SM EW and the new contact interactions.

The effective coupling  $\mathcal{C}_0$  depends on the quarks and leptons chirality and flavor, and it reads

$$\mathcal{C}_0(q_{Xq}, l_{Xl}) = \mathcal{C}_{\text{SM}}^0(s; q_{Xq}, l_{Xl}) + \mathcal{K}_{q_{Xq}, l_{Xl}}^0, \quad (1.2)$$

where  $\mathcal{K}^0$  are constants that denote the coefficients of the effective neutral current interactions

$$\mathcal{K}_{q_{Xq}, l_{Xl}}^0 (\bar{q}_{Xq} \gamma^\mu q_{Xq}) (\bar{l}_{Xl} \gamma_\mu l_{Xl}). \quad (1.3)$$

The explicit expressions for the  $\mathcal{K}^0$  factors of eq. (1.2) can be found in tab. A.2 and A.1, respectively for the  $O'_{2W}$  and  $O'_{2B}$  operators or for the flavor universal ones. The SM contribution depends on the dilepton invariant mass and it can be concisely written as

$$\mathcal{C}_{\text{SM}}^0(s; q_{Xq}, l_{Xl}) = \frac{g^2 T^3(q_{Xq}) T^3(l_{Xl}) + g'^2 Y(q_{Xq}) Y(l_{Xl})}{s - m_Z^2} + \frac{e^2 Q(q) Q(l) m_Z^2}{s(m_Z^2 - s)}, \quad (1.4)$$

where  $g$  and  $g'$  denote the  $\text{SU}(2)_L$  and  $\text{U}(1)_Y$  couplings,  $e$  is the electric charge,  $T^3$  is the third  $\text{SU}(2)_L$  generator,  $Y$  and  $Q$  are the hypercharge and the fractional charge.<sup>7</sup>

Based on the above discussion, it is obvious that at tree-level the dependence on the new physics parameters  $\mathcal{K}^0$  can be obtained by reweighting the SM ( $\mathcal{K}^0 = 0$ ) predictions. The dilepton production cross-section (fully differential in the dilepton 4-momenta) is the sum of the polarized  $q\bar{q} \rightarrow l^+ l^-$  partonic cross-sections convoluted with the corresponding PDF. The quarks and the leptons being effectively massless, each term in the sum depends on new physics through the square of the corresponding  $\mathcal{C}_0(q_{Xq}, l_{Xl})$  coefficient. The differential cross-section is thus the sum of the SM cross-sections in each helicity and quark flavor channel, each weighted by the factor

$$\rho_n(s, \mathcal{K}^0; q_{Xq}, l_{Xl}) = \left( \frac{\mathcal{C}_0(q_{Xq}, l_{Xl})}{\mathcal{C}_{\text{SM}}^0(s; q_{Xq}, l_{Xl})} \right)^2 = \left( 1 + \frac{\mathcal{K}_{q_{Xq}, l_{Xl}}^0}{\mathcal{C}_{\text{SM}}^0(s; q_{Xq}, l_{Xl})} \right)^2. \quad (1.5)$$

Starting from a SM Monte Carlo simulation where quark and lepton flavors and helicities are stored in the events file (or, equivalently, from simulations of the individual channels),

<sup>7</sup>We follow the exact same conventions as in ref. [9], apart from the sign (irrelevant in the above equation) of the coupling in the covariant derivatives and in the field-strengths definition.

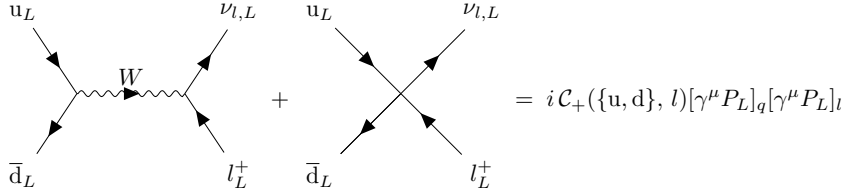


Figure 1.2 – Effective Feynman vertex for charge plus DY. The subscript “ $L$ ” denotes chirality, not helicity.

Monte Carlo events implementing the differential cross-section calculation are readily obtained by assigning to each event its reweighting factor  $\rho$  as defined above. Of course we do not need to commit ourselves to a specific value of the  $\mathcal{K}^0$  parameters and reweight the SM sample as the first step. Since  $\rho$  is merely a linear polynomial (squared) in  $\mathcal{K}^0$ , with unit constant term, we just need to compute and store its coefficient  $1/\mathcal{C}_{\text{SM}}^0$  (plus the information of the helicity and flavor channel of the event) in the events file. The actual reweighting can be performed at a later stage, or one can use eq. (1.5) to compute the dependence on  $\mathcal{K}^0$  of the cross-sections in the analysis bins.

The reweighting formula in eq. (1.5) also holds at NLO in QCD, because the gluon-quark coupling preserves the quark flavor and chirality. Therefore the one-loop  $q_{\chi_q} \bar{q}_{\chi_q} \rightarrow l_{\chi_l}^+ l_{\chi_l}^-$  amplitude is proportional to the same  $\mathcal{C}_0(q_{\chi_q}, l_{\chi_l})$  factor as the tree-level one, and the same is true for  $q_{\chi_q} \bar{q}_{\chi_q}$ -initiated real emission amplitudes with one final gluon and for  $g q_{\chi_q}$ - and  $g \bar{q}_{\chi_q}$ -initiated real emissions. The dilepton differential cross-section is thus the linear combination, with  $\rho$  reweighting coefficients as in eq. (1.5), of Born plus virtual plus real contributions in each individual channel labeled by the flavor and chirality of the initial quark or anti-quark and by the ones of the leptons. Notice that the IR divergencies consistently cancel in each channel. The UV divergencies also cancel, with no renormalization needed for the new physics coupling because the new interaction involves a QCD-neutral vector current. Monte Carlo events reweighting can thus be carried out at NLO in the exact same way described above for the tree level case. It should be possible in principle to extend the reweighting approach also to NNLO accuracy. The main difference is that at NNLO new channels appear (like for instance the  $ud \rightarrow ud l^+ l^-$  real correction) whose amplitude is not proportional to one specific  $\mathcal{C}_0(q_{\chi_q}, l_{\chi_l})$  effective coupling, but to a linear combination of them. New reweighting factors should thus be computed and used to deal with these new channels. We do not explore this possibility because NLO accuracy will turn out to be more than sufficient for our purposes. NNLO corrections to the SM contribution are instead important, but those are easily added on top of our NLO new physics predictions.

Analogous considerations hold for the charged DY process

$$pp \rightarrow l^\pm \bar{\nu}_l + X. \quad (1.6)$$

## 1.2. Theoretical predictions via event reweighting

The effective Feynman diagram is reported in figure 1.2 for charge-plus dilepton production, with  $u = u, c$  and  $d = d, s, b$  representing up- and down-type quark flavor indices. The effective coupling  $\mathcal{C}_{\pm}(\{u, d\}, l)$  depends now on a pair of quark flavor indices denoted as “ $\{u, d\}$ ”, and on the lepton flavor. It does not instead depend on the chirality, because all fermions are left-handed as indicated in the figure. This is obviously the case in the SM, but also for new physics since the only relevant operator (i.e.,  $O_{lq}^{(3)}$ , see table 1.1) is purely left-handed. We readily obtain the reweighting factors

$$\rho_c(s, \mathcal{K}^0; q_{\chi_q}, l_{\chi_l}) = \left| \frac{\mathcal{C}_+(\{u, d\}, l)}{\mathcal{C}_{\text{SM}}^+(s; \{u, d\}, l)} \right|^2 = \left| 1 + \frac{\mathcal{K}_{\{u, d\}, l}^+}{\mathcal{C}_{\text{SM}}^+(s; \{u, d\}, l)} \right|^2, \quad (1.7)$$

for both charge plus and minus DY processes. Explicitly, the SM effective coupling reads

$$\mathcal{C}_{\text{SM}}^+(s; \{u, d\}, l) = \frac{g^2}{2} \frac{V_{ud}^*}{s - m_W^2}, \quad (1.8)$$

where  $V$  is the CKM quark mixing matrix. New physics is encapsulated in the couplings of the effective charged current interactions

$$\mathcal{K}_{\{u, d\}, l}^+(\bar{d}_L \gamma^\mu u_L)(\bar{\nu}_{l, L} \gamma_\mu l_L) + \text{h.c.} \quad (1.9)$$

Charged DY NLO events reweighting can be performed, using eq. (1.7), with the exact same logic we described in the neutral case. Notice that we can regretless apply the charged reweighting factor to all the events in the simulation, in spite of the fact that it was derived for the Left-Left (LL) chirality subprocesses, because all the SM events are indeed of the LL type. The only (very minor) subtlety with charged DY reweighting is associated with real NLO corrections producing a top quark in the final state, through for instance the SM  $bg \rightarrow t l^- \bar{\nu}_l$  subprocess. Given that the top is massive, and since we are excluding effective interactions involving the top quark, we cannot deal with this process with our strategy. However its contribution is totally negligible in the SM and we do not expect that new physics effects in the top sector could be large enough to make it detectable. Otherwise, the final states with an extra top quark could be isolated experimentally and studied separately.

For concreteness, we now specialize the general reweighting formulas to the subset of operators that are associated to the  $W$  and the  $Y$  parameters. The latter are defined as the coefficients of the four-fermion operators  $O'_{2W}$  and  $O'_{2B}$  reported in table 1.1. More precisely, we write

$$G'_{2W} = -\frac{g^2 W}{2m_W^2}, \quad G'_{2B} = -\frac{g'^2 Y}{2m_W^2}. \quad (1.10)$$

By performing a field redefinition (i.e., by using the equations of motion),  $O'_{2W}$  and  $O'_{2B}$  can be traded for the gauge/gauge operators  $O_{2W}$  and  $O_{2B}$  of ref. [10]. In turn,  $O_{2W}$  and  $O_{2B}$  generate “oblique” corrections to the  $Z$  and photon propagators that can be

encapsulated in the phenomenological parameters  $\hat{W}$  and  $\hat{Y}$  probed at LEP [35]. The normalization is chosen in eq. (1.10) such that  $\hat{W} = W$  and  $\hat{Y} = Y$  at tree-level. The relevance of  $O_{2W}$  and  $O_{2B}$  (and in turn of  $O'_{2W/2B}$ ) stems from the fact that they are the only dimension-6 operators that grow with the energy in DY to be generated by a new physics scenario where the light quarks and the leptons communicate with the new physics sector only through the SM gauge interactions. For more details, also on the correspondence between  $O_{2W/2B}$  and  $O'_{2W/2B}$ , see ref. [11].

By employing eq. (1.10), table 1.1, and the almost direct correspondence between the  $\mathcal{K}^{0,+}$  couplings and the Warsaw basis operator coefficients (see tab. A.2), we immediately derive the neutral and charged DY reweighting factors.

$$\begin{aligned}\rho_n(s, W, Y; q_{\chi_q}, l_{\chi_l}) &= (1 + a_W^n(s; q_{\chi_q}, l_{\chi_l})W + a_Y^n(s; q_{\chi_q}, l_{\chi_l})Y)^2, \\ \rho_c(s, W) &= (1 + a_W^c(s)W)^2,\end{aligned}\tag{1.11}$$

where the neutral and charged  $a^{n,c}$  coefficients are

$$\begin{aligned}a_W^n(s; q_{\chi_q}, l_{\chi_l}) &= -\frac{g^2 T^3(q_{\chi_q}) T^3(l_{\chi_l})}{m_W^2 \mathcal{C}_{\text{SM}}^0(q_{\chi_q}, l_{\chi_l})}, & a_Y^n(s; q_{\chi_q}, l_{\chi_l}) &= -\frac{g'^2 Y(q_{\chi_q}) Y(l_{\chi_l})}{m_W^2 \mathcal{C}_{\text{SM}}^0(q_{\chi_q}, l_{\chi_l})}, \\ a_W^c(s) &= -\frac{s - m_W^2}{m_W^2},\end{aligned}\tag{1.12}$$

with  $\mathcal{C}_{\text{SM}}^0$  as in eq. (1.4). The neutral DY reweighting coefficients are independent of the lepton flavor and of the quark family, because  $O'_{2W/2B}$  are quark- and lepton-family independent. The  $a_W^n$  and  $a_Y^n$  coefficients can thus be computed for each SM Monte Carlo event based on the quark type (u or d) and on the quark/lepton (LL, LR, RL or RR) chirality combinations, for a total of 8 options. Actually  $a_W^n$  is non-vanishing only for LL-chirality events, which are thus the only ones bringing the dependence on  $W$ . This is because  $O_{2W}$  can be viewed as a modification of the  $W_3/W_3$  component, which only couples to left-handed fermions, of the neutral vector bosons propagators. By similar considerations it is easy to understand why the charged DY reweighting does not depend on  $Y$  ( $O_{2B}$  does not affect the charged  $W$ -boson propagator) and why  $a_W^c$  is flavor-independent (i.e., the CKM factor drops). Notice that these features make reweighting for charged DY trivial, in the sense that all events have to be scaled with the same (but dependent on the dilepton mass) factor. Namely the charged dilepton differential cross-section is equal to the SM one, summed over all channels, times the overall factor  $\rho_c(s, W)$  that brings the entire dependence on new physics. This is of course not the case for neutral DY, where different flavor and helicity channels are weighted by different  $W$ & $Y$ -dependent factors.

### 1.2.2 Reweighting POWHEG

We applied our reweighting strategy to the POWHEG SM DY generator [69]. For the charged process, our procedure merely consists in computing and storing the reweighting coefficient  $a_W^c(s)$  in eq. (1.12) for each SM Monte Carlo event. The invariant mass  $s = (p_l + p_\nu)^2$  is obtained from the lepton and neutrino momenta before the showering Monte Carlo (PYTHIA 8 [70], in our case) is applied to the event. The augmented SM Monte Carlo sample can be used to produce histograms, with the cross-section (or, more generally, the total weight) of each bin obtained as the (positive or negative) SM weight of the event, times the reweighting factor (1.11), summed over the events that fall in the bin. Notice that the cross-section in the bin can be evaluated as a function of  $W$ . Namely one can expand  $\rho_c$  in  $W$ , evaluate the coefficient of the linear and of the quadratic term and sum them up (with the appropriate SM weights) separately over the events in the bin. We thus obtain the linear and quadratic coefficients of the polynomial that describes the cross-section in the bin as a function of  $W$ . The constant term of the polynomial is of course the SM prediction for the cross-section.

The procedure is only slightly more complicated in the neutral DY case, because subprocesses with different quark and lepton helicities must be reweighted with different factors, while the SM Monte Carlo collects them in a single (one for each quark flavor) unpolarized channel. This is not a problem for charged DY because the amplitudes are non-vanishing only for the LL polarization subprocess as previously explained. Therefore even if the Monte Carlo evaluates unpolarized cross-sections, the result is effectively the polarized one. Fortunately in the code implementing the SM neutral DY calculation of ref. [69] it is easy to access and modify the  $Z$  and the photon chiral couplings to quarks and leptons. We can thus produce four SM generators, labeled as LL, LR, RL and RR, in which only the corresponding quark/lepton chiral couplings are present (and set to the SM value) while the others are set to zero. POWHEG evaluates the unpolarized cross-sections in each of the four cases, however the results are effectively polarized as discussed above for the charged process. The four Monte Carlo samples obtained by the four generators represent the contribution of the four helicity subprocesses, to be reweighted with the corresponding factor. For each event in each sample we compute  $a_W^n(s; q_{\chi_q}, l_{\chi_l})$  and  $a_Y^n(s; q_{\chi_q}, l_{\chi_l})$  as in eq. (1.12), using the information of the quark flavor in the event. Finally we combine the four samples in the calculation of the cross-section as a function of  $W$  and  $Y$  similarly to what previously explained for the charged case.

The procedure outlined above is exact (in the limit of massless leptons and quarks) from the viewpoint of a fixed-order NLO QCD calculation. However POWHEG [71] also describes the hardest parton showering emission, producing events that can be further showered without introducing double-counting. It is thus legitimate to ask if and how our procedure interferes with the POWHEG approach, possibly invalidating its consistency. In order to answer, we sketch below the implementation of the POWHEG method, in the presence of new physics, on each individual helicity subprocess. This is a trivial extension



of refs. [69, 71], from which we borrow all notations.

The Born ( $B$ ), the real ( $R_{q\bar{q},g}$ ,  $R_{g\bar{q},q}$  and  $R_{qg,\bar{q}}$ , summed/averaged over the gluon helicity) and the “bare” virtual ( $V_b$ ) contributions, for given helicities, are equal to the appropriate  $\rho$  factor times the corresponding SM expressions. The same applies to the bare factorization counterterms  $G_{\oplus,b}$  and  $G_{\ominus,b}$ , since they emerge from the bare parton distribution functions in the tree-level term and are therefore proportional to  $B$ . The Catani–Seymour counterterms are also equal to  $\rho$  times their SM expressions, again because they are proportional to the Born term. One might want to cross-check the latter statement because the Catani–Seymour formalism was developed [72] to deal with unpolarized processes, while here we are considering a polarized one. The statement can be readily verified by direct calculation or by noticing that the Catani–Seymour formulas hold for a completely generic unpolarized process with arbitrary Born term, and that our polarized cross-sections are effectively the unpolarized cross-sections as computed in a theory where the  $Z$  and the photon only couple to specific quark and lepton chiralities. The Catani–Seymour formulas must thus apply.<sup>8</sup> A last potential subtlety is associated with the fact that the  $\rho$  reweighting factor depends on the dilepton invariant mass  $\sqrt{s}$  and that the Catani–Seymour counterterms are evaluated on an “underlying-Born”  $2 \rightarrow 2$  kinematics that is obtained from the true  $2 \rightarrow 3$  kinematics by a prescription that is, to some extent, arbitrary. Fortunately with the choice of ref. [69] the underlying Born dilepton invariant mass is identical to the true one, therefore the exact same  $\rho(s)$  factor appears in the Born, virtual and real contributions and in all counterterms. The dilepton invariant mass is of course also consistently preserved in the reconstruction of the 3-body kinematics out of the underlying Born 2-body variables.

We conclude that the elements that appear in the POWHEG master formula (see eq. (4.17) of ref. [71]), including the subtracted virtual and the real contribution decomposition in the two singular regions, all depend on new physics through the same  $\rho(s)$  multiplicative factor. The same thus holds for the  $\bar{B}$  term, which is a linear combination of the latter terms. The rescaling instead cancels in the Sudakov exponent, which contains the “R/B” ratio of real over Born, and in the real radiation term of the formula for the same reason. Consequently, the POWHEG master formula for the cross-section is also equal to  $\rho(s)$  times the corresponding SM object. Each of the LL, LR, RL and RR generators described above implements the POWHEG formula for the corresponding helicity subprocess with  $\rho = 1$  (i.e., in the SM), and in each of them the contributions from different quark flavors are treated separately. By reweighting based on the quark flavor of each event and joining the four helicity samples we thus obtain events that rigorously implement the POWHEG calculation of the Drell–Yan process in the presence of new physics. After passing them through a showering Monte Carlo program, these events consistently include showering effects at the NLO in QCD.

---

<sup>8</sup>A similar argument also holds for counterterms in the so-called Frixione-Kunszt-Signer approach [73, 74].



## 1.2. Theoretical predictions via event reweighting

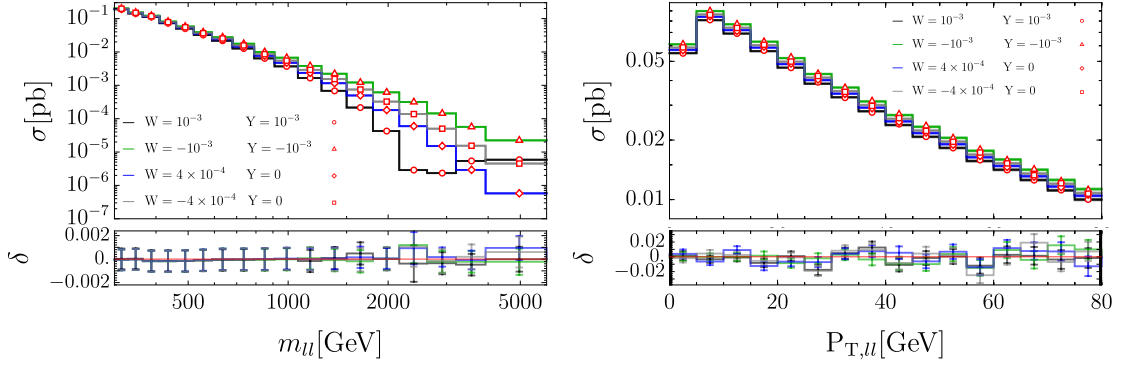


Figure 1.3 – Dilepton invariant mass ( $m_{ll}$ , left panel) and total transverse momentum of the dilepton pair ( $P_{T,ll}$ , right panel) distributions.  $\delta$  is the ratio between our prediction and the one of ref. [64] minus one, with its error obtained by combining the Monte Carlo errors of the predictions.

Our reweighting strategy is one consistent implementation of the POWHEG method for the Drell–Yan calculation, but it is slightly different from the one of ref. [64] (where SM EFT effects are included), and from the SM calculation [69]. This is because in these implementations, different helicity subprocesses are grouped into unpolarized channels as previously mentioned. Of course we eventually sum the four helicity contributions, but this is not sufficient to make our implementation identical to the other ones, because of the R/B ratio that appears in the Sudakov and in the real radiation term of the master formula. Our R/B is the ratio of real and Born terms where the external quarks and leptons have fixed helicity, while those of refs. [64, 69] are summed over the helicities. On inclusive observables the two implementations (after we sum over helicities, of course) give the same prediction at NLO, owing to the NLO accuracy of the POWHEG formula. The predictions are also identical at the leading log order where the real term in the Sudakov exponent and the real radiation term (for low- $k_T$  emissions) factorize as the product of the Born, which drops in the R/B ratio, times the appropriate splitting functions. Since the splitting functions are the same (notice that the gluon helicity sum is performed also in our case), the same expressions are found for R/B in the two implementations. The latter property clearly follows from the fact that the first POWHEG showering emission is consistent at the leading log level. The residual difference between the two implementations is thus beyond NLO and leading log accuracy, and too small to be appreciable in practice, as the results below demonstrate.

A validation of our reweighting is readily obtained by comparing with ref. [64], as in figure 1.3 and in table 1.2. The left panel of the figure shows the neutral dilepton invariant distribution at four selected points in the W and Y parameter space as computed with our strategy, compared with those obtained with the code of ref. [64], represented as points. One minus the ratio between our prediction and the one of ref. [64], denoted as  $\delta$ , is displayed below the plot with the corresponding Monte Carlo error. A similar

		$c_*$ bin		
		$[-1, -0.33]$	$[-0.33, 0.33]$	$[0.33, 1]$
$m_{ll}$ bin [GeV]	[330, 365]	$(-2 \pm 8)10^{-3}$	$(4 \pm 8)10^{-3}$	$(0 \pm 6)10^{-3}$
		$(-4 \pm 8)10^{-3}$	$(3 \pm 8)10^{-3}$	$(0 \pm 6)10^{-3}$
		$(-2 \pm 8)10^{-3}$	$(0 \pm 8)10^{-3}$	$(0 \pm 6)10^{-3}$
		$(0 \pm 8)10^{-3}$	$(4 \pm 8)10^{-3}$	$(0 \pm 6)10^{-3}$
	[910, 1070]	$(-6 \pm 8)10^{-3}$	$(7 \pm 8)10^{-3}$	$(6 \pm 5)10^{-3}$
		$(-12 \pm 8)10^{-3}$	$(6 \pm 8)10^{-3}$	$(8 \pm 5)10^{-3}$
		$(-15 \pm 8)10^{-3}$	$(0 \pm 8)10^{-3}$	$(6 \pm 5)10^{-3}$
		$(-6 \pm 8)10^{-3}$	$(6 \pm 8)10^{-3}$	$(6 \pm 5)10^{-3}$
	[2620, 3200]	$(-8 \pm 8)10^{-3}$	$(2 \pm 7)10^{-3}$	$(2 \pm 5)10^{-3}$
		$(3 \pm 8)10^{-3}$	$(0 \pm 8)10^{-3}$	$(-1 \pm 5)10^{-3}$
		$(2 \pm 7)10^{-3}$	$(-9 \pm 7)10^{-3}$	$(4 \pm 5)10^{-3}$
		$(-6 \pm 9)10^{-3}$	$(8 \pm 8)10^{-3}$	$(-2 \pm 6)10^{-3}$

Table 1.2 – Comparison with ref. [64] in 9 bins of the doubly-differential  $m_{ll}$  and  $c_* = \cos \theta_*$  distribution. The relative discrepancy  $\delta$  is reported for the four values of the W&Y parameter employed in figure 1.3.

comparison is shown in table 1.2 for 9 bins of the double-differential invariant mass and  $\cos \theta_*$  (with  $\theta_*$  the dilepton center-of-mass angle defined boosting the dilepton system along the center-of-mass direction of motion in the LAB frame) distribution. The relative discrepancy  $\delta$  is in all cases compatible with zero within the error. Notice that the error on  $\delta$  is tiny in the invariant mass distribution plot because the cross-sections result from dedicated simulations in each bin. The error is larger in the doubly-differential distribution comparison because the cross-sections are obtained in this case by cutting the dedicated simulation events (of  $10^5$  events each) in the 3  $\cos \theta_*$  bins. In the right panel of the figure we consider instead the transverse momentum of the dilepton pair, integrated over the dilepton mass above 300 GeV and over the angles. Although measuring this distribution is not relevant to probe W and Y, the comparison is interesting because of the slightly different implementation of the POWHEG radiation emission in the two approaches. Also in this distribution, no difference is found within the Monte Carlo error. Notice that the  $P_{T, ll}$  distribution includes showering with PYTHIA 8 [70], while the other results described above are obtained with pure POWHEG events before showering. Other comparison plots were made, also for charged DY production, and no significant difference was found.

### 1.2.3 Electroweak logarithms

High-energy DY measurements target growing-with-energy new physics effects. Thus it is imperative to keep under control any SM contribution that might result in a similar behavior, such as EW double and single logarithms of both IR and UV (RG-running) origin. One-loop EW NLO corrections, including in particular the corresponding EW logs, are present in the neutral DY SM predictions of FEWZ [63] (together with QCD at

## 1.2. Theoretical predictions via event reweighting

NNLO), and in POWHEG both for charged and for neutral DY [75, 76]. New physics must also be modeled correctly if we want to discover it by exploiting correlated deviations from the SM of the measurements in multiple bins. Clearly the new physics term is itself a correction to the SM, therefore it needs not to be predicted as accurately as the SM one. However one should still carefully monitor the impact of high-order corrections on the new physics contribution and include them if possible, as we did above for the NLO QCD corrections. We now show how to add, again through reweighting, EW logs at the one-loop order in the EW coupling expansion.

The relevant IR logs have been computed in ref. [77] (see also refs. [78–81]) up to two loops, and they have been recently implemented in Sherpa [82] (at one loop). Restricting to one loop, and defining

$$L = \log \frac{s}{m_W^2}, \quad L_{t(u)} = 2L \log \frac{-t(u)}{s} + \log^2 \frac{-t(u)}{s}, \quad (1.13)$$

the Feynman amplitudes for the fully exclusive  $2 \rightarrow 2$  Drell–Yan processes at Next to Leading Logarithm (NLL) accuracy read <sup>9</sup>

$$\begin{aligned} \mathcal{M}_{11,\text{NLL}}^{\text{u}\bar{\text{u}} \rightarrow l^- l^+} &= \mathcal{F}_D \mathcal{M}_B^{\text{u}\bar{\text{u}} \rightarrow l^- l^+} + \frac{g^2}{(4\pi)^2} L_u \Re \left[ V_{\text{u}d'} \mathcal{M}_B^{\text{u}d' \rightarrow \nu_l l^+} \right], \\ \mathcal{M}_{11,\text{NLL}}^{\text{d}\bar{\text{d}} \rightarrow l^- l^+} &= \mathcal{F}_D \mathcal{M}_B^{\text{d}\bar{\text{d}} \rightarrow l^- l^+} - \frac{g^2}{(4\pi)^2} L_t \Re \left[ \mathcal{M}_B^{\text{u}'\bar{\text{d}} \rightarrow \nu_l l^+} V_{\text{u}'d} \right], \\ \mathcal{M}_{11,\text{NLL}}^{\text{u}\bar{\text{d}} \rightarrow \nu_l l^+} &= \mathcal{F}_D \mathcal{M}_B^{\text{u}\bar{\text{d}} \rightarrow \nu_l l^+} + \frac{g^2}{2(4\pi)^2} L_u \left( \mathcal{M}_B^{\text{u}\bar{\text{u}}' \rightarrow l^- l^+} V_{\text{u}'d}^* + V_{\text{u}d'}^* \mathcal{M}_B^{\text{d}'\bar{\text{d}} \rightarrow \nu_l \bar{\nu}_l} \right) \\ &\quad - \frac{g^2}{2(4\pi)^2} L_t \left( V_{\text{u}d'}^* \mathcal{M}_B^{\text{d}'\bar{\text{d}} \rightarrow l^- l^+} + \mathcal{M}_B^{\text{u}\bar{\text{u}}' \rightarrow \nu_l \bar{\nu}_l} V_{\text{u}'d}^* \right). \end{aligned} \quad (1.14)$$

In the equation,  $\mathcal{M}_B$  denote the Born (tree-level) amplitudes, including their dependence on new physics encapsulated in the  $\mathcal{C}_0$  and  $\mathcal{C}_\pm = (\mathcal{C}_\mp)^*$  effective couplings defined in section 1.2.1. The charged process amplitudes are of course only non-vanishing for the LL chirality process. Neutral amplitudes for  $\text{u}\bar{\text{u}}' \rightarrow \nu_l \bar{\nu}_l$  are equal to those for  $\text{d}\bar{\text{d}}' \rightarrow l^- l^+$  and similarly for down-initiated neutrino production. We denote as  $q_1, \bar{q}_2, l_1$  and  $\bar{l}_2$  the four particles involved in the scattering with the corresponding chiralities, such that the generic Drell–Yan partonic subprocess is

$$q_1 \bar{q}_2 \rightarrow l_1 \bar{l}_2. \quad (1.15)$$

With this notation, the Mandelstam variables are defined as

$$s = (p_{q_1} + p_{\bar{q}_2})^2, \quad t = (p_{q_1} - p_{l_1})^2, \quad u = (p_{q_1} - p_{\bar{l}_2})^2. \quad (1.16)$$

<sup>9</sup>The equations that follow assume that the charge-minus amplitude is the conjugate of the charge-plus amplitude, as it is the case in the SM and for generic current-current New Physics operators. The sum over the  $\text{u}'$  and  $\text{d}'$  flavor indices is understood. Log-enhanced terms with imaginary coefficient are not reported because they do not interfere with the Born amplitudes.

The “diagonal”  $\mathcal{F}_D$  factors in eq. (1.14) depend on the fermion species and chiralities. They contain angular independent (a.i.) and angular dependent (a.d.) contributions. The latter ones emerge, together with the other angular-dependent terms in eq. (1.14) (those proportional to  $L_t$  and  $L_u$ ), from the double logarithms of  $t/m_W^2$  and of  $u/m_W^2$  rewritten in terms of  $L = \log s/m_W^2$ . The a.d. contributions which are not proportional to  $L$  (e.g., the last term in eq. (1.13)), are normally not retained at the NLL accuracy. We do include them because they are enhanced in the forward and backward regions. We have verified that they considerably improve the quality of the NLL approximation, not only in the angular but also in the invariant mass dilepton distribution.

We write  $\mathcal{F}_D$  as

$$\mathcal{F}_D = f_{\text{a.i.}} + f_{\text{a.d.}}(t/s, u/s) + f_{\text{a.i.}}^{\text{qed}} + f_{\text{a.d.}}^{\text{qed}}(t/s, u/s), \quad (1.17)$$

where the (IR-divergent) angular-independent and angular-dependent contributions from soft and collinear photon loops have been isolated in the corresponding  $f^{\text{qed}}$  terms, to be discussed later. The others can be written concisely as

$$\begin{aligned} f_{\text{a.i.}} &= \frac{1}{2(4\pi)^2} \sum_{f=q_{1,2}, l_{1,2}} \left[ (-L^2 + 3L) (g^2 C_f + g'^2 y_f^2 - e^2 q_f^2) + 2L g_{Z,f}^2 \log \frac{m_Z^2}{m_W^2} \right] \quad (1.18) \\ f_{\text{a.d.}} &= \frac{1}{(4\pi)^2} \left[ (g_{Z,q_1} g_{Z,l_2} + g_{Z,q_2} g_{Z,l_1}) \left( L_u + 2 \log(-u/s) \log \frac{m_Z^2}{m_W^2} \right) \right. \\ &\quad \left. - (g_{Z,q_1} g_{Z,l_1} + g_{Z,q_2} g_{Z,l_2}) \left( L_t + 2 \log(-t/s) \log \frac{m_Z^2}{m_W^2} \right) \right], \end{aligned}$$

in terms of the  $T^3$  eigenvalue ( $t_f^3$ ), the Casimir ( $C_f = 0, 3/4$ ), the charge and hypercharge ( $y_f$  and  $q_f$ ) of each of the four fermions  $f = q_1, q_2, l_1, l_2$ . The coupling of the  $Z$  boson  $g_{Z,f} = g(t_f^3 - s_w^2 q_f)/c_w$  is used in place of  $t_f^3$  for more compact expressions.

The results above are in  $D = 4 - 2\epsilon$  dimensions and the UV singularities are subtracted in the  $\overline{\text{MS}}$  renormalization scheme. The photon and the fermions are exactly massless, therefore soft and collinear divergences appear in the  $f^{\text{qed}}$  terms

$$\begin{aligned} f_{\text{a.i.}}^{\text{qed}} &= -\frac{e^2}{2(4\pi)^2} \left( \frac{2}{\epsilon^2} + \frac{3}{\epsilon} \right) \sum_{f=q_{1,2}, l_{1,2}} q_f^2, \quad (1.19) \\ f_{\text{a.d.}}^{\text{qed}} &= \frac{2e^2}{(4\pi)^2} \frac{1}{\epsilon} \left[ (q_{q_1} q_{l_1} + q_{q_2} q_{l_2}) \log(-u/s) - (q_{q_1} q_{l_2} + q_{q_2} q_{l_1}) \log(-t/s) \right]. \end{aligned}$$

Notice that the  $f^{\text{qed}}$  terms diverge, but they do not depend on  $L = \log(s/m_W^2)$ . This is because they are defined as the contribution to the loop integrals from the region where the virtual photon is soft and/or collinear to an external leg, and these regions are insensitive to  $m_{W/Z}$  up to  $m_{W/Z}^2/s$  power corrections.

## 1.2. Theoretical predictions via event reweighting

The  $\epsilon$  poles get canceled by real corrections and by PDF renormalization in the calculation of the dilepton differential cross-section, provided extra emissions are allowed and provided the charged leptons momenta are defined by recombining collinear photons. If the energy (or  $p_T$ ) threshold for extra photons, the  $k_T^{\text{rec}}$  transverse momentum threshold for recombination, and the factorization scale are a considerable fraction of  $\sqrt{s}$ , no large finite contributions emerge from the cancellation and the  $f^{\text{qed}}$  terms can simply be dropped in the cross-section calculation. We construct our reweighted Monte Carlo samples targeting the “fully-inclusive” differential cross-section as defined above. More exclusive results, incorporating in particular the effect of a lower (or absent)  $k_T^{\text{rec}}$  threshold (or of a small  $\Delta R^{\text{rec}}$  recombination cone), are easily obtained by passing the events through a QED showering Monte Carlo code.

Rewighted Monte Carlo samples implementing the calculation described above are easily obtained from a LO generator, which employs the SM Born matrix element  $\mathcal{M}_{\text{B,SM}}$ . Provided of course that the fermion chirality channels are treated separately, or based on LL, LR, RL, and RR polarized generators constructed as in section 1.2.2, one can compute the reweighting factor

$$\begin{aligned} \rho_{\text{NLL}}^{q_1\bar{q}_2 \rightarrow l_1\bar{l}_2}(s, t, u) &= \frac{|\mathcal{M}_{\text{B}}^{q_1\bar{q}_2 \rightarrow l_1\bar{l}_2}|^2}{|\mathcal{M}_{\text{B,SM}}^{q_1\bar{q}_2 \rightarrow l_1\bar{l}_2}|^2} + \frac{2 \Re \left[ \mathcal{M}_{\text{11,NLL}}^{q_1\bar{q}_2 \rightarrow l_1\bar{l}_2} (\mathcal{M}_{\text{B}}^{q_1\bar{q}_2 \rightarrow l_1\bar{l}_2})^* \right]}{|\mathcal{M}_{\text{B,SM}}^{q_1\bar{q}_2 \rightarrow l_1\bar{l}_2}|^2} \\ &\equiv \rho_{\text{n(c)}}^{q_1\bar{q}_2 \rightarrow l_1\bar{l}_2} + \Delta\rho_{\text{NLL}}^{q_1\bar{q}_2 \rightarrow l_1\bar{l}_2}, \end{aligned} \quad (1.20)$$

for each event, as a function of the new physics couplings, and use it in a way similar to that described in the previous sections for the NLO QCD reweighting. Up to running effects, to be discussed below, the first term on the first line of the equation coincides with  $\rho_{\text{n,c}}$  in eqs. (1.5) and (1.7) for the neutral and charged processes, respectively. Namely, it can be expressed in terms of the  $\mathcal{C}_0$  and  $\mathcal{C}_{\pm}$  neutral and charged amplitude coefficients and the corresponding SM expressions. It is a perfect square and, restricting to the W&Y case for concreteness, its dependence on new physics can be parametrized by the reweighting coefficients  $a_{W/Y}^{\text{n}}$  and  $a_W^{\text{c}}$  as in eq. (1.11). The second term in eq. (1.20) contains NLL effects. It can also be expressed in terms of the  $\mathcal{C}$ ’s using eq. (1.14) and noticing that the spinor current matrix elements drop in the amplitude ratio. The  $\Delta\rho_{\text{NLL}}$  term is still a quadratic polynomial in the new physics parameters, but it is not a perfect square and its constant term is not equal to zero. This is due to the fact that NLL corrections are introduced also on the SM term, therefore the reweighting is non-trivial even in the absence of new physics. The 6 coefficients of the  $\Delta\rho_{\text{NLL}}$  polynomial have to be computed and stored in the events file, together with  $a_{W/Y}^{\text{n}}$  and  $a_W^{\text{c}}$ , in order to obtain the analytical W&Y predictions at NLL EW accuracy.

Notice that the NLL corrections are often negative, so that  $\rho$  can become negative in certain regions of the phase space. If this had to result in a negative cross-section after the weights are summed up in some bin, it would mean that the EW IR corrections are

too large to be treated perturbatively in that bin. Fortunately this does not occur in the energy range of interest for the LHC measurements. Finally, we remark that the NLL corrections in the LL chirality channel make neutral contact interaction operators contribute to the charged DY process, because of the amplitude mixing in eq. (1.14). Therefore, at least in principle, charged DY measurements are actually also sensitive to the Y parameter and not only to W.

So far we only discussed EW logs of IR origin. UV logs do not appear explicitly in eq. (1.14) because we are applying the results of ref. [77] with the  $\overline{\text{MS}}$  renormalization scale set to the center-of-mass energy  $\sqrt{s}$ . At one loop order this is irrelevant for the one-loop corrections in eq. (1.14), which can still be computed at a fixed scale. However the tree-level amplitudes need to be evaluated with running couplings, RG-evolved at the scale  $\sqrt{s}$ . When expanding at one-loop, this produces single logarithms of  $s$ . The running of the SM couplings  $g$  and  $g'$  starts at the  $Z$ -boson mass  $m_Z \simeq m_W$ , where these parameters are defined. Therefore the SM couplings renormalization produces “IR-type” logarithms of  $s/m_W^2$ . These are readily computed by replacing

$$g^2 \rightarrow g^2(s) \simeq g^2 + \delta g^2 = g^2 + \frac{g^4}{16\pi^2} b_g L, \quad g'^2 \rightarrow g'^2(s) \simeq g'^2 + \delta g'^2 = g'^2 + \frac{g'^4}{16\pi^2} b_{g'} L, \quad (1.21)$$

in the  $C_{\text{SM}}^{\pm,0}$  effective couplings as they appear in the effective Feynman vertices in figures 1.1 and 1.2. The factors  $b_g = -19/6$  and  $b_{g'} = 41/6$  in the above equation are the SM  $g$  and  $g'$  couplings  $\beta$ -functions.

The RG running of the new physics couplings is the last source of enhanced logarithms. However these are not logarithms of  $s/m_W^2$ , but rather of  $\Lambda^2/s$ , where  $\Lambda$  is the scale where the EFT operators are renormalized. The explicit form of these terms depends on the definition of the renormalized W and Y parameters. These are given by eq. (1.10), in terms of the  $G'_{2W/2B}$  four-fermion operator coefficients renormalized at  $\Lambda$ . The SM parameters ( $g$ ,  $g'$ , and  $m_W$ ) that appear in the equation are evaluated at  $m_Z$ , therefore they do not contribute to the running. Insertions of  $O'_{2W/2B}$  in EW loops generates RG-running logarithmic contributions to a number of dimension-six operators. However, only the current-current quark-lepton non-FCNC operators listed in table 1.1 produce quadratically energy-growing effects in the DY cross-section and need to be retained. The effect of the others is power-suppressed relative to the leading energy-growing terms. It should be noted that  $O'_{2W/2B}$  generate generic quark-lepton operators, namely the universality relations on the right panel of table 1.1 are violated by RG-running. In order to include running effect we thus need to go back to eqs. (1.5) and (1.7), evaluated with the  $\mathcal{K}$ 's obtained by solving the evolution equations at the leading log. The final expression for the reweighting factors takes the form

$$\rho_{\text{NLL}}^{q_1 \bar{q}_2 \rightarrow l_1 \bar{l}_2}(s, t, u) \equiv \rho_{\text{n(c)}, \Lambda}^{q_1 \bar{q}_2 \rightarrow l_1 \bar{l}_2} + \Delta \rho_{\text{NLL}, \Lambda}^{q_1 \bar{q}_2 \rightarrow l_1 \bar{l}_2}. \quad (1.22)$$

## 1.2. Theoretical predictions via event reweighting

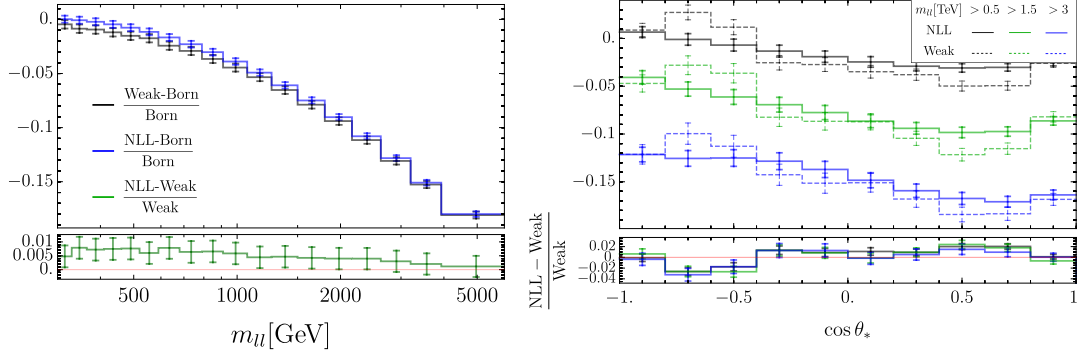


Figure 1.4 – Dilepton invariant mass ( $m_{ll}$ , left panel) and center of mass angle ( $\cos \theta_*$ , right panel) distributions.  $\delta$  is the discrepancy relative to the Born.

Explicit results, obtained with the `DsixTools` [83] calculation of the relevant  $\beta$ -functions for the new physics couplings, and including the running of the SM couplings, are presented in appendix A.1.

The RG EFT logs are found to have a marginal impact on the phenomenological analysis of the DY data, but they introduce conceptually novel aspects that is worth clarifying. First, they introduce a dependence on the EFT operators renormalization scale  $\Lambda$ . Technically,  $\Lambda$  is arbitrary and we conventionally set it to  $\Lambda = 10$  TeV in our projections for the W and Y parameters sensitivity. On the other hand, for the interpretation of the results in the microscopic UV theory the EFT operators emerge from, setting  $\Lambda$  to the cutoff scale of the EFT would have been preferable. The EFT cutoff intrinsically depends on the UV theory. The choice  $\Lambda = 10$  TeV corresponds to the estimated cutoff scale in the Composite Higgs UV scenario with moderate  $g_*$ , for values of W and Y close to the LHC reach [11]. Naively, one could consider employing the results with  $\Lambda = 10$  TeV also for EFT's with much higher cutoff, by running the operator coefficients down to 10 TeV. However this would not be correct in general because running produces many operators at 10 TeV, while our calculation assumes that  $O'_{2W/2B}$  are the only non-vanishing current-current operators at  $\Lambda = 10$  TeV. Therefore our results are strictly speaking inapplicable even to theories where  $O'_{2W/2B}$  are the only operators that emerge at the cutoff scale, if the cutoff scale is much higher than 10 TeV. Furthermore even in theories with 10 TeV cutoff, the presence of other operators, even if not of the current-current type, does influence the current-current operators running below  $\Lambda$  and our calculation does not apply. While of limited practical relevance (since the RG logs are very small and the cutoff is unlikely to be much higher than 10 TeV), this issue is readily addressed by including in the reweighting all the current-current quark-lepton non-FCNC operators, with coefficients RG-evolved starting from the most general  $d = 6$  operators content at the scale  $\Lambda$ . Since current-current operators are the only relevant ones in DY up to power-suppressed effects, this will produce complete NLL predictions in the general EFT parameter space. We will come back on this point in sec. 1.4.



We can not fully validate our implementation of the EW logarithms because EW radiative corrections in the presence of the EFT operators have not been computed. However we can validate the SM EW logarithms using the POWHEG calculation of neutral DY including the complete one-loop EW correction [76]. We employ the “weak-only” POWHEG routine, that implements only the virtual corrections involving massive vector bosons, obtaining excellent agreement as figure 1.4 shows. The logarithms reproduce the exact one-loop result up to  $\mathcal{O}(1\%)$  accuracy, relative to the tree-level, in the entire mass spectrum. In particular they reproduce very accurately the  $\mathcal{O}(20\%)$  enhancement of the corrections in the very high mass tail. Somewhat larger discrepancies are found as expected in the forward and backward regions of the angular distribution. As previously mentioned, the agreement would significantly deteriorate if we had not fully retained the angular-dependent logs. Given the expected statistics and experimental errors, 1% accuracy in the predictions would probably be sufficient in the analysis, therefore one might even consider using the reweighted Monte Carlo in place of POWHEG for the Standard Model prediction. The same level of accuracy is expected in the prediction of the new physics EFT effects, relative to the exact one-loop calculation. Since new physics is itself a small correction to the SM (never more than 10% in the relevant configurations), the reweighted prediction of the new physics term is fully equivalent to the exact one-loop result to all practical purposes. A technical aspect worth mentioning is that, since the “weak-only” POWHEG routine does not implement the box diagrams involving the exchange of a photon and of a  $Z$ -boson, the corresponding EW logs due to the soft/collinear  $Z$ -boson region need to be consistently removed from our reweighting formulas for the comparison. A successful comparison also relies on a judicious choice of the SM input parameters. The most accurate predictions are obtained using tree-level input parameters in the  $G_\mu$ -scheme [84, 85].

Up to now we discussed pure EW corrections, obtained by reweighting tree-level Monte Carlo events. We can straightforwardly combine EW corrections with NLO QCD effects by reweighting the POWHEG DY generator [69]. The reweighting strategy is similar to the one described in section 1.2.2, with the reweighting factors given by eq. (1.22). The only difference is that reweighting now depends also on the  $t$  and  $u$  Mandelstam variables, and not only on  $s$ . These are computed on the POWHEG events, before showering, with the following prescription. If a gluon is present in the final state, we assume that it is emitted from the initial parton moving along the positive  $z$ -axis if it moves in the right hemisphere (in the center of mass frame), and the converse for left-hemisphere gluons. Concretely, we compute  $t$  and  $u$  using the four-momentum of the incoming quark or anti-quark that travels in the  $z$  direction opposite to the final-state gluon. For gluon-initiated process, the momentum of the initial quark or anti-quark is employed. There is of course no ambiguity in events without emissions. At the leading log in QCD, where the emissions are collinear or soft and factorize, this prescription is exact. It is not exact at NLO, for hard emissions. However the  $t$ - and  $u$ -dependent terms in the reweighting are EW corrections, therefore we do not need to model them precisely at



NLO in QCD since mixed (two-loops order) QCD and EW corrections are not included in our calculation.

Summarizing, our reweighting produces NLO QCD events, consistently matched with QCD parton showering, and including NLL EW corrections on the SM and on the new physics contributions. The NLL QED accuracy for partially exclusive quantities, like lepton momenta defined with a narrow recombination cone, or “bare” muons momenta, is obtained by the PYTHIA 8 QED showering. We validated QED showering effects by comparing with the literature [63, 76, 85, 86]. In particular we reproduced table 1 of ref. [85], with  $\Delta R^{\text{rec}}=0.1$  recombination cone,  $p_{T,\min}^{\gamma}=10$  GeV, and  $|\eta|_{\max}^{\gamma}=3$  thresholds for photons. The thresholds on the recombined leptons are  $p_{T,\min}^l=25$  GeV and  $|\eta|_{\max}^l=2.5$ . We also recombine to the nearest lepton the lepton pairs produced by photon splitting. The same recombination strategy is adopted for the predictions reported in the following sections.

Before concluding this section, it is worth emphasizing that our result does not include real emissions of massive vector bosons. Namely we target a final state without  $W$  or  $Z$  bosons. While theoretically well-defined, this final state is not experimentally accessible because the vector bosons might not be detectable if they are soft, or collinear to the beam, or if they decay to neutrinos. We could straightforwardly account for real emissions, including new physics by reweighting, because at the NLL order the real emissions factorize. Therefore they can be generated through splitting, starting from Monte Carlo events without emissions, duly weighted to include new physics. We did not implement this strategy because it is much simpler to use MADGRAPH. For a tree-level process such as the massive vector bosons emission, reweighting is automated and can be used to include the EFT effects. The effect of real corrections depends strongly on the exact definition of the cross-section that is measured experimentally, which in turn is also dictated by experimental considerations. Therefore we ignore real corrections in the analysis of the following section, having in mind an hypothetical measurement of the exclusive cross-section as defined above. However it should be emphasized that these effects should be properly taken into account in the experimental analysis because they are as relevant as the virtual EW logs [87], as expected.

Two more processes are not included in our results. One is the photon-quark dilepton production, which does depend on new physics but is extremely small [84, 85]. The other is photon-photon initiated production, which is not sensitive to new physics and thus can be easily added on top by a tree-level SM simulation.

### 1.3 The Drell-Yan Likelihood

We now turn to phenomenological applications. In this section we discuss the parametrization of the predicted cross-section as a function of the new physics parameters and with

the associated uncertainties. We use it to build the binned Likelihood function needed for the interpretation of the DY measurements in the EFT and this will be the starting point for the LHC sensitivity projections presented at the end of this section and in the rest of the chapter.

In this section we specialize again on the universal new physics scenario and we discuss quantitative results only in the W and Y parameters space. Extending our analysis to the 7-dimensional parameter space of the flavor universal quark lepton interaction is straightforward and it will be briefly discussed in sec. 1.4.

### 1.3.1 Cross-section parametrization

Suppose the neutral and charged DY cross-sections are measured in bins, labeled by the index  $I$ . The theoretical expected cross-section, denoted by  $\sigma_I^{\text{th}}$ , is a quadratic polynomial in the parameters of interest W and Y. The cross-section is positive, so it can be parametrized as

$$\begin{aligned} \sigma_I^{\text{th}}(W, Y) &= \bar{\sigma}_I^{\text{SM}} c_{0,I}^2 \left| \begin{pmatrix} 1 & c_{1,I} & c_{3,I} \\ 0 & c_{2,I} & c_{4,I} \\ 0 & 0 & c_{5,I} \end{pmatrix} \cdot \begin{pmatrix} 1 \\ W \\ Y \end{pmatrix} \right|^2 \\ &= \bar{\sigma}_I^{\text{SM}} c_{0,I}^2 [1 + 2c_{1,I}W + 2c_{3,I}Y + (c_{1,I}^2 + c_{2,I}^2)W^2 + (c_{3,I}^2 + c_{4,I}^2 + c_{5,I}^2)Y^2 \\ &\quad + 2(c_{1,I}c_{3,I} + c_{2,I}c_{4,I})WY]. \end{aligned} \quad (1.23)$$

by employing the Cholesky decomposition for positive  $3 \times 3$  matrices, in terms of six dimensionless coefficients  $c_{k,I}$ , with  $k = 0, \dots, 5$ . The decomposition is unique provided  $c_{0,I}$ ,  $c_{2,I}$  and  $c_{5,I}$  are positive, while both signs are allowed for the other coefficients. In the equation,  $\bar{\sigma}_I^{\text{SM}}$  denotes the prediction for the SM cross-section in each bin evaluated with central-value inputs. Namely, with the strong coupling constant  $\alpha_s$  set to the central value  $\alpha_s = 0.1180$  and with central-value PDF and renormalization/factorization scales. Consequently, the central value of the  $c_{0,I}$  coefficients is equal to one by definition:  $\bar{c}_{0,I} = 1$ .

The central values of the other coefficients,  $\bar{c}_{k,I}$ , are readily computed with our reweighted samples, starting from central-value SM Monte Carlo data. As explained in the previous section, the reweighted events contain the coefficients of the weights as a polynomial in W and Y. These are summed up in each bin producing the polynomial coefficients in the bin, out of which the Cholesky decomposition coefficients can be computed, provided the cross-section is a positive polynomial as it must be by consistency. This is always the case in the kinematical regimes accessible at the LHC, because the negative EW logs are still sufficiently small. The only subtlety is associated with the dependence on Y of the charged DY cross-section. Since the latter emerges only through the EW logs, which we expanded at fixed order in our reweighting formulas, no  $Y^2$  term is present and the

cross-section polynomial becomes negative at  $W = 0$  for very large  $Y$ . While such large values of  $Y$  are phenomenologically irrelevant, we solved the problem by adding the  $Y^2$  term to the charged DY reweighting for a fully consistent combined expansion in the new physics and in the EW loop parameters.

#### 1.3.2 Parametric and theoretical uncertainties

We now discuss the estimate of the uncertainties on the theoretical predictions for the  $c_{k,I}$  coefficients.

These are described statistically, and included in the Likelihood, in terms of nuisance parameters, with an approach that can fit both in a frequentist and in a Bayesian inference framework. From the frequentist point of view the nuisance are related to parameters the  $c_{k,I}$  predictions depends on, such as for instance the value of  $\alpha_s$  or the PDF. The results of auxiliary measurements (e.g.,  $\alpha_s$  or PDF measurements) are incorporated in the Likelihood as multiplicative terms that depend on the nuisance parameters but not on the parameters of interest (i.e.,  $W$  and  $Y$ ). From the Bayesian perspective, the nuisance are random variables (and so in turn the  $c_{k,I}$ 's), and the likelihood of the auxiliary measurements can be interpreted as their statistical distribution. In what follows we adopt the Bayesian language to describe the auxiliary likelihood associated with the nuisance parameters, but we eventually employ it for a frequentist inference on the  $W$  and  $Y$  parameters.

Notice that the discussion above applies only to systematic uncertainties with an underlying statistical origin. The uncertainties from scale variation instead, and more in general all the uncertainties associated with missing higher order corrections in the predictions, do not possess a robust statistical interpretation. As customary we will nevertheless include them as nuisance parameters, but fortunately we will see that they do not play a dominant role in our sensitivity projections.

We now examine the different sources of uncertainties individually, discuss their parametrization in terms of nuisance parameters, and start quantifying their impact.

#### Uncertainty from Monte Carlo statistic

No nuisance parameters must be included for Monte Carlo statistical uncertainties, which are completely negligible. More precisely, the uncertainties on the new physics terms are negligible provided the Monte Carlo statistics is sufficient to provide accurate enough (well below 1%) predictions of the SM terms. This is because new physics is included by reweighting, hence the relative accuracy on the new physics  $c_{k,I}$  parameters is the same one of the SM terms. Since new physics is itself a correction to the SM in the kinematical regime of interest and for the relevant values of the  $W$  and  $Y$  parameters,

the resulting cross-section uncertainty is completely negligible. Accurate SM predictions for unfolded differential cross-section measurements are easy to obtain. If instead the analysis had to be performed on the observed distribution, producing large enough detector simulations might be problematic. However once this is achieved, new physics effects could be included by reweighting with negligible Monte Carlo error. As discussed in the Introduction, it would have been harder to bring the uncertainties on the new physics prediction to a negligible level if employing Monte Carlo predictions that are not obtained by reweighting.

### Uncertainty from $\alpha_s$

The uncertainty coming from the value of the QCD coupling  $\alpha_s$  is, by construction, determined by a single parameter. It is thus included through a single nuisance parameter  $\theta^{\alpha_s}$  affecting all bins in a correlated way. The nuisance is distributed as a standard normal, i.e.

$$f_{\alpha_s}(\theta^{\alpha_s}) = \frac{1}{\sqrt{2\pi}} e^{-\frac{1}{2}(\theta^{\alpha_s})^2}. \quad (1.24)$$

We can regard  $\theta^{\alpha_s}$  as a variable related to the physical  $\alpha_s$  (which is Gaussian-distributed by assumption) by a suitable linear transformation that brings its distribution to the standard normal.

The POWHEG SM DY [69] Monte Carlo samples include the weights of each event when  $\alpha_s$  is set to the lower and upper ( $\alpha_s^l = 0.1165$  and  $\alpha_s^u = 0.1195$ ) boundaries of the  $1\sigma$  confidence interval, plus of course the weight for  $\alpha_s$  equal to its central value  $\alpha_s = 0.1180$ . From the latter, we obtain the central-value coefficients  $\bar{c}_{k,I}$  (with  $\bar{c}_{0,I} = 1$  as previously discussed). From the former, we obtain the values of  $c_{k,I}$  for  $\alpha_s = \alpha_s^l$  and for  $\alpha_s = \alpha_s^u$ . The resulting relative variations are shown in the left panel of figure 1.5 for the neutral DY invariant mass distribution, with the binning employed for the LHC projections in section 1.3.4.

We see that the  $\alpha_s$  uncertainties are rather small, compared with the expected experimental (statistical and systematic) uncertainties of the cross-section measurements (see figure 1.7). Also notice that the  $\alpha_s$  uncertainties are much smaller for the new physics  $c_{k,I}$ 's (for  $k = 1, \dots, 5$ ) than for the overall multiplicative  $c_{0,I}$  coefficient, which encapsulate in particular the uncertainty on the SM term of the prediction. Moreover, the new physics contribution to the cross-section is small, suggesting that all the  $\alpha_s$  uncertainties apart from those on  $c_{0,I}$  can safely be ignored in the analysis. This is confirmed by the right panel of figure 1.5, which quantifies the relative impact of the new physics terms to the total expected cross-sections  $\sigma_I^{\text{th}}$ . Large values of the W and Y parameters are chosen in the figure, well above the projected LHC sensitivity with only  $100 \text{ fb}^{-1}$ . Even for these values, new physics is a small correction to the SM up to around 2 TeV energies. At this high energy,  $\alpha_s$  uncertainties are anyhow irrelevant because of

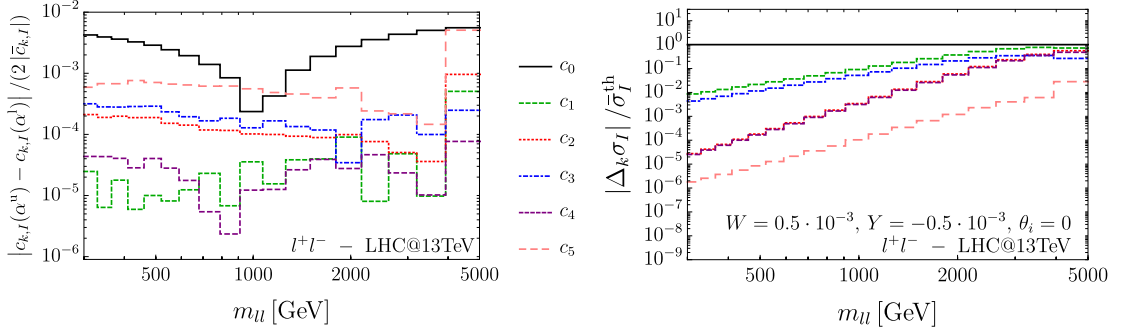


Figure 1.5 – Left: Uncertainties on the  $c_{k,I}$  coefficients from variation of the value of  $\alpha_s$ , computed as  $|c_{k,I}(\alpha_s^u) - c_{k,I}(\alpha_s^l)| / (2|\bar{c}_{k,I}|)$ . Right: Relative impact of the  $c_{k,I}$  coefficients on the total  $\sigma_I^{\text{th}}$  for  $W = 5 \cdot 10^{-4}$ ,  $Y = -5 \cdot 10^{-4}$ , and all nuisance parameters  $\theta_i = 0$ . This is computed as  $|\Delta_k \sigma_I| / \bar{\sigma}_I^{\text{th}}$ , with  $\Delta_k \sigma_I$  the difference between the central-value cross-section  $\bar{\sigma}_I^{\text{th}}$  and the value of  $\sigma_I^{\text{th}}$  obtained by setting “ $c_k$ ” to zero in eq. (1.23).

the large statistical uncertainties (see again figure 1.7). Similar conclusions are reached by studying the charged DY transverse mass distribution we consider in section 1.3.4 for the LHC projections.

In light of the above discussion, we include the dependence on  $\theta^{\alpha_s}$  only on  $c_{0,I}$ , with a linear parameterization

$$c_{0,I} = c_{0,I}(\theta^{\alpha_s}) = \bar{c}_{0,I} + \kappa_I^{\alpha_s} \theta^{\alpha_s} = 1 + \kappa_I^{\alpha_s} \theta^{\alpha_s}, \quad (1.25)$$

where the  $\kappa_I^{\alpha_s}$ ’s are computed as

$$\kappa_I^{\alpha_s} = \max \left( |c_{0,I}(\alpha_s^u) - \bar{c}_{0,I}|, |c_{0,I}(\alpha_s^l) - \bar{c}_{0,I}| \right). \quad (1.26)$$

If the dependence of the coefficients on  $\alpha_s$  was exactly linear, the upper and lower variations would be exactly equal and opposite, and eq. (1.25) would describe exactly the dependence of  $c_{0,I}$  on  $\alpha_s$ . We have verified that the variations are equal and opposite to good approximation, and the maximal variation was selected for conservative results. Notice that the parameterization in eq. (1.25) does not respect the condition  $c_{0,I} > 0$  for the unicity of the Cholesky decomposition. This does not produce negative cross-sections, but (formally) results in a double coverage of the space of the predictions in terms of  $\theta^{\alpha_s}$ . However the problem is irrelevant in practice because the uncertainties are so small that  $c_{0,I}$  will never change sign in the Likelihood marginalization (or profiling) process.

### Uncertainty from the parton distribution functions

The PDF uncertainties on the  $c$ ’s are computed using POWHEG, with the same strategy outlined above for the  $\alpha_s$  uncertainties. We employed the 30 PDF in the set

PDF4LHC15\_NLO\_30\_PDFAS (code 90400 in the LHAPDF database [88]) [89–92], which correspond to the Hessian reduction of the PDF uncertainties to 30 nuisance parameters  $\theta_i^{\text{PDF}}$ , with  $i = 1, \dots, 30$ . The nuisance are uncorrelated and normally distributed:

$$f_{\text{PDF}}(\theta_i^{\text{PDF}}) = \frac{1}{\sqrt{2\pi}} e^{-\frac{1}{2}(\theta_i^{\text{PDF}})^2}, \quad i = 1, \dots, 30. \quad (1.27)$$

The use of an Hessian set is legitimated by the fact that we look for small deviations from the SM, rather than to on-shell new physics. In this context, the Hessian parametrization allows for a simpler treatment of the PDF uncertainties including correlations between different bins and different process such as the neutral and charged DY. Our choice of the set with 30 replicas, in alternative to the one with 100 replicas, is motivated by a study we performed for neutral DY using the PDF4LHC15\_NLO\_MC\_PDFAS Monte Carlo ensemble set, where we identified less than 20 eigenvectors of the  $c$ 's covariance matrix with uncertainties above ‰.

The following dependence of the  $c_{k,I}$  coefficients on the PDF nuisance parameters is assumed. The  $c_{0,I}$ ,  $c_{2,I}$  and  $c_{5,I}$ , which need to be positive for the unicity of the Cholesky decomposition, are parametrized with an exponential:

$$X(\theta_i^{\text{PDF}}) = \bar{X} \exp \left[ \sum_{i=1}^{30} \frac{X^{(i)} - \bar{X}}{\bar{X}} \theta_i^{\text{PDF}} \right], \quad \text{for } X = \{c_{0,I}, c_{2,I}, c_{5,I}\}. \quad (1.28)$$

The others are parameterized linearly

$$X(\theta_i^{\text{PDF}}) = \bar{X} + \sum_{i=1}^{30} (X^{(i)} - \bar{X}) \theta_i^{\text{PDF}}, \quad \text{for } X = \{c_{1,I}, c_{3,I}, c_{5,I}\}. \quad (1.29)$$

In the equation, we indicate with a bar the central value predictions, while the superscript  $(i)$  denotes the value of the parameter obtained with each of the 30 PDF replicas in the set. The parametrization is such that  $X$  equals (approximately, in the case of eq. (1.28))  $X^{(i)}$  when  $\theta_i^{\text{PDF}}$  is at its one-sigma value and all the other  $\theta_i^{\text{PDF}}$ 's vanish, compatibly with the definition of the Hessian set.

The PDF uncertainties are larger than those on  $\alpha_s$ , and eventually turn out to be the dominant component of the total theoretical uncertainties shown in figure 1.7. Furthermore these uncertainties grow with the energy like the new physics effects. Therefore in our analysis we account for them fully, both in the SM and in the new physics contributions to the cross-section.

### Uncertainty from missing higher orders

The uncertainties due to the truncation of the perturbative series in the cross-section prediction are harder to quantify, and impossible to incorporate rigorously in any statis-

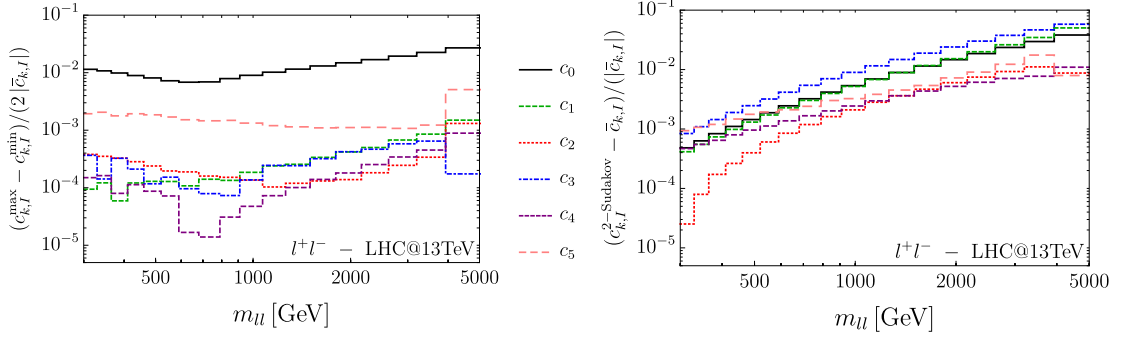


Figure 1.6 – Left: Uncertainties from scale variation computed as  $(c_{k,I}^{\max} - c_{k,I}^{\min}) / (2\bar{c}_{k,I})$ . Right: Uncertainties from missing EW loops estimated as explained in the main text.

tical framework. Nevertheless we can estimate their impact as follows. Missing higher orders in the QCD loop expansion are estimated by varying the factorization ( $\mu_F$ ) and QCD-coupling renormalization ( $\mu_R$ ) scales independently around the central values  $\bar{\mu}_F = \bar{\mu}_R = \sqrt{s}$ . The scales are varied by multiplicative factors equal to  $2^{\pm 1}$ ,  $2^{\pm 1/2}$  and 1, in a grid with a total of 24 entries plus the central value configuration. The maximal and the minimal values of the  $c_{k,I}$  coefficients in this grid, denoted as  $c_{k,I}^{\max}$  and  $c_{k,I}^{\min}$  below, are used for the uncertainty estimate. Missing higher order in the EW loop expansion are instead estimated by adding the leading IR logarithmic terms at two loops to our reweighting formulas. All IR logs have been computed in ref. [77] at two loops, however only the leading (i.e.,  $L^4$  angular-independent) terms are retained in the estimate of the uncertainties. Compatibly with Sudakov resummation formulas, these are straightforwardly included by replacing  $f_{\text{a.i.}} \rightarrow f_{\text{a.i.}} + f_{\text{a.i.}}^2/2$  in eq. (1.17). The predictions for the  $c_{k,I}$  coefficients that include this contribution are denoted as  $c_{k,I}^{2\text{-Sudakov}}$ .

The uncertainties from missing higher orders in QCD (left panel) and in EW (right panel) are displayed in figure 1.6. We discuss them in turn. NLO QCD scale variation effects are known (see, e.g., ref. [93]) to be sizable in the SM. Correspondingly we see in the figure that the uncertainties on the  $c_{0,I}$ 's are relatively big. On the other hand, the scale uncertainties on the new physics  $c_{k,I}$ 's (with  $k \neq 0$ ) are extremely small and completely negligible. Namely, we find that the NLO QCD scale variations mostly affect  $\sigma_I^{\text{th}}$  in eq. (1.23) as an overall new physics-independent multiplicative factor. The uncertainties due to the missing higher-orders in the EW loop-expansion are smaller than the QCD scale variation, and they become sizable only at high energy where the statistical error gets big. They are definitely irrelevant for the new physics term, but they could play a role for the SM contribution, in particular for the charged DY process where they are slightly larger than what shown in the figure for the neutral case.

The previous results show that our predictions for the new physics contribution to the cross-section are sufficiently accurate, and the associated theoretical uncertainties can be neglected. On the SM term instead, NLO QCD scale variations and missing higher

orders in the EW expansion are potentially relevant. However the SM predictions are available at NNLO [63], and 2-loops enhanced EW logarithms can be easily included in by analytic reweighting. By replacing the SM term of our prediction with the NNLO SM, and including 2-loops logs, we could thus lower the NLO scale variations to the NNLO level, and make higher order EW corrections completely negligible. In what follows we will thus ignore EW effects and include NNLO-sized QCD scale variations which we estimate, following ref. [63], to be one tenth of the NLO ones. These uncertainties are modeled by introducing one nuisance parameter  $\theta_I^{\text{TU}}$  for each bin, following a standard normal distribution. Linear dependence on  $\theta_I^{\text{TU}}$  is assumed for  $c_{0,I}$

$$c_{0,I} = \bar{c}_{0,I} + \frac{(c_{k,I}^{\text{max}} - c_{k,I}^{\text{min}})}{2} \theta_I^{\text{TU}}. \quad (1.30)$$

### 1.3.3 Statistical inference

In the following section we will present sensitivity estimates for the W&Y parameters at the LHC with the standard [94] frequentist approach based on the profile Likelihood ratio and employing Asymptotic formulas and the “Asimov dataset”. Namely, we define the “ $t_\mu$ ” test statistic (with  $\mu = (\text{W}, \text{Y})$  the parameters of interest), with the Likelihood in the numerator maximized over the nuisance parameters for fixed W and Y and the one in the denominator maximized also on the parameters of interest. The Asymptotic ( $\chi_2^2$ ) distribution is assumed for  $t_\mu$  in the EFT hypothesis in order to set the 95% (or 68%) CL boundaries, while the median  $t_\mu$  in the SM hypothesis is obtained by setting the observed data to the central-value SM prediction.

The treatment of experimental (statistical and systematical) uncertainties would be completely straightforward if the experimental result was presented as a measurement of the unfolded cross-section in the bins. Namely, the complete Likelihood will be merely obtained by plugging  $\sigma_I^{\text{th}}$  in the experimental Likelihood, expressed as a function of the “truth-level” cross-sections  $\sigma_I$ , including the dependence on the parameters of interest and on the nuisance, and multiplying by the nuisance parameters constraint terms. The simplest way to mimic the complete Likelihood would be to employ a Gaussian guess for the experimental Likelihood, which should include an estimate of the uncertainties on the measurement emerging from the combination of statistical and systematic errors. Since it is unclear how the statistical and systematic errors should be combined, a slightly more sophisticated approach is considered in what follows. However it should be emphasized that this adds nothing to the accuracy of our modeling of the experimental errors, given the lack of basic information on the systematic uncertainties expected in the measurement and of the (potentially very important) correlations between the errors in different bins and in neutral and charged DY. One advantage of the strategy we follow is that it could be adapted to the direct comparison of the W and Y prediction with the observed-level distributions without unfolding.



### Experimental uncertainties

The experimental Likelihood for the  $\sigma_I$  cross-sections emerges from the number of events,  $n_I$ , observed in each bin. These are Poisson-distributed independent variables with means  $\mu_I$  that are related to the theoretical predictions  $\mu_I^{\text{th}} = L \cdot \sigma_I^{\text{th}}$  (with  $L$  the integrated luminosity) up to experimental uncertainties which we encapsulate in normal-distributed nuisance parameters  $\theta_I^{\text{exp}}$ , and to the luminosity uncertainty. Namely, the  $\mu_I$  are defined as

$$\mu_I = \mu_I^{\text{th}} \left( 1 + \sum_J \left[ \sqrt{\Sigma^{\text{exp}}} \right]_I^J \theta_J^{\text{exp}} + 0.02 \theta^{\text{L}} \right), \quad (1.31)$$

where  $\Sigma^{\text{exp}}$  is the covariance matrix associated with the systematic experimental uncertainties in the relation between the truth-level expected countings  $\mu_I^{\text{th}}$  and the observed-level expectations  $\mu_I$ . Notice that the expression above does not take into account event migrations from the truth- and observed-level bins, which should be encapsulated in the response matrix that multiplies the  $\mu_I^{\text{th}}$  term. However it can model realistically the effect of uncertainties on the determination of the response matrix, provided a reasonable guess is made for the covariance matrix  $\Sigma^{\text{exp}}$ . The simple choice we consider in the next session is based on current experimental results. The error on the luminosity measurement, at the 2% level, is described by the normally distributed nuisance parameter  $\theta^{\text{L}}$ .

The complete Likelihood we will employ for the statistical inference finally reads

$$\mathcal{L} \left( W, Y, \theta^{\alpha_s}, \theta_i^{\text{PDF}}, \theta_I^{\text{TU}}, \theta_I^{\text{exp}}, \theta^{\text{L}} \right) = \prod_{I=1}^N \text{Poisson} \left[ n_I | \mu_I \left( W, Y, \theta^{\alpha_s}, \theta_i^{\text{PDF}}, \theta_I^{\text{TU}}, \theta_I^{\text{exp}}, \theta^{\text{L}} \right) \right] \quad (1.32)$$

$$\times f_{\alpha_s}(\theta^{\alpha_s}) f_{\text{PDF}}(\theta^{\text{PDF}}) f_{\text{TU}}(\theta_I^{\text{TU}}) f_{\text{exp}}(\theta^{\text{exp}}) f_{\text{L}}(\theta^{\text{L}}). \quad (1.33)$$

The dependence of  $\mu_I$  (through  $\sigma_I^{\text{th}}$ , as in eq. (1.31)) on the parametric and theoretical uncertainties is introduced by combining additively the correction terms in eqs. (1.25), (1.28), (1.29), and (1.30).

#### 1.3.4 LHC projections

We base our projection on hypothetical measurements of the neutral DY invariant mass ( $m_{ll}$ ) and of the charged DY transverse mass ( $m_T$ ) distributions in logarithmically-spaced bins

$$\{.3, .33, .365, .41, .46, .52, .59, .68, .79, .91, 1.07, 1.26, 1.5, 1.8, 2.16, 2.62, 3.20, 3.93, 13\} \text{ TeV}.$$

The LHC collider energy is set to 13 TeV, and integrated luminosities of  $100 \text{ fb}^{-1}$ ,  $300 \text{ fb}^{-1}$ , and  $3 \text{ ab}^{-1}$  are considered. The former luminosity is roughly the one that has been

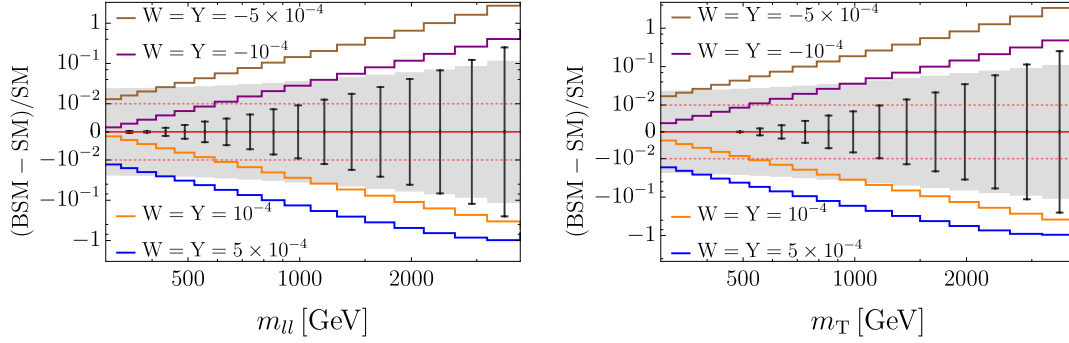


Figure 1.7 – Invariant and transverse mass distribution of the relative discrepancy between BSM and SM predictions, for neutral (left panel) and charged (right panel) Drell-Yan. The gray band represents the uncertainties (at  $1\sigma$ ) in the theoretical predictions, while the black bars denote the statistical uncertainties estimated as one over the square root of the number of expected events. The HL-LHC integrated luminosity ( $L = 3 \text{ ab}^{-1}$ ) is assumed.

collected as of today. The two latter ones are those that will be available at the end of the LHC and of the HL-LHC programs, respectively. We incorporate in the projections 65% identification efficiency for electrons and 80% for muons, which effectively reduces the luminosity by a factor of 2 in neutral DY and by around 40% for the charged process.

The projections are obtained with the Likelihood described in the previous section, where all the relevant sources of parametrical and theoretical uncertainties in the cross-section predictions are taken into account. However they are not fully realistic because the experimental systematic uncertainties in the cross-section measurements (and the correlation of these uncertainties across different bins) can only be estimated by the experimental collaboration. Based on run-1 results, in our “baseline” scenario we set to 2% and to 5% the experimental relative uncertainties in the measurement of the neutral and of the charged cross-sections, respectively. No correlation is assumed across different bins, i.e.  $\Sigma^{\text{exp}} \propto \mathbb{1}$  in eq. (1.31), aiming to a conservative result.

The results are illustrated in the rest of this section, starting from those in the baseline configuration for the uncertainties. We next consider departures from the baseline setup and discuss the impact of the various sources of uncertainties separately.

A first qualitative assessment of the sensitivity can be obtained by looking at figure 1.7. The figure shows the corrections to the cross-section, relative to the SM, at 4 points in the W&Y parameter space, overlaid with the total uncertainties in the theoretical predictions, represented as a gray shaded region. As discussed in the previous section, these uncertainties are dominated by the PDF contribution. The black bars correspond to the statistical uncertainties in each bin at the HL-LHC. The 1% uncertainty level is

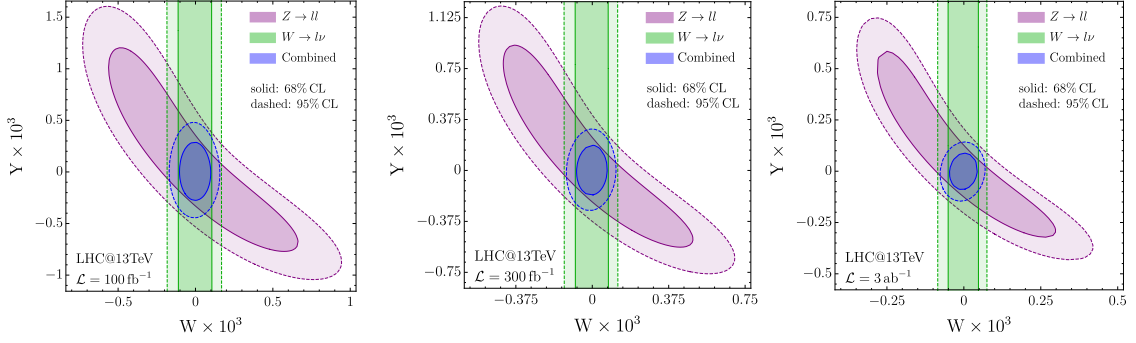


Figure 1.8 – Projected 68% and 95% exclusions in the  $W$ & $Y$  plane for different luminosities from neutral (purple) and charged (green) Drell-Yan measurements at 13 TeV LHC.

marked with horizontal dotted lines because it provides a reasonable absolute lower bound to the systematic component of the experimental error on the cross-section measurements, on top of the statistical one. Based on the figure, we expect values of  $W$ & $Y$  of the order of  $1 \cdot 10^{-4}$  or less to be within the reach of the HL-LHC. This is confirmed by the contours in the  $W$ & $Y$  plane, at 68 and 95% CL, displayed in figure 1.8 for the 3 integrated luminosities we considered. The neutral and charged DY sensitivities are shown separately and combined.

We further inspect our results, following ref. [11], from the viewpoint of the validity of the EFT modeling of new physics. The first three plots in figure 1.9 show single-parameter 95% CL sensitivities as a function of the maximal energy (invariant or transverse mass) of the data employed in the analysis. These are obtained considering only one ( $W$  or  $Y$ ) parameter of interest, with the other set to zero. The first two panels refer to neutral and charged DY, respectively, and the third one to the combination of the two channels. Consistently with ref. [11], we see that the reach sits comfortably below the “Derivative Expansion Breakdown” region, showing that the usage of the EFT is justified and the resulting limits are valid. More quantitatively, we see that the energy region which is relevant for the limit does not exceed 2 or 3 TeV. The value of the  $W$ & $Y$  parameters we are sensitive to can easily be due to new physics particles which are much heavier than that. For instance in Composite Higgs theories the new physics scale could easily be at 10 TeV or more, justifying the usage of the EFT at few TeV energies. A more simple examples is the one of a  $Z'$ , such as the “Universal  $Z'$  model” employed in ref. [32] for future colliders performance assessments. The sensitivity projection on the  $Y$  parameter (which is the only one generated by this model), once translated in the mass-coupling plane of the  $Z'$  model as in figure 1.9, reveals that the HL-LHC could be sensitive to values of the  $Y$  parameter induced by a  $Z'$  which is as heavy as 30 TeV. The projected direct reach on the  $Z'$  particle at the HL-LHC, from ref. [32], is overlaid to the figure in order to outline that the sensitivity to the model is dominated by the neutral DY measurement of  $Y$  in a wide region of the parameter space.

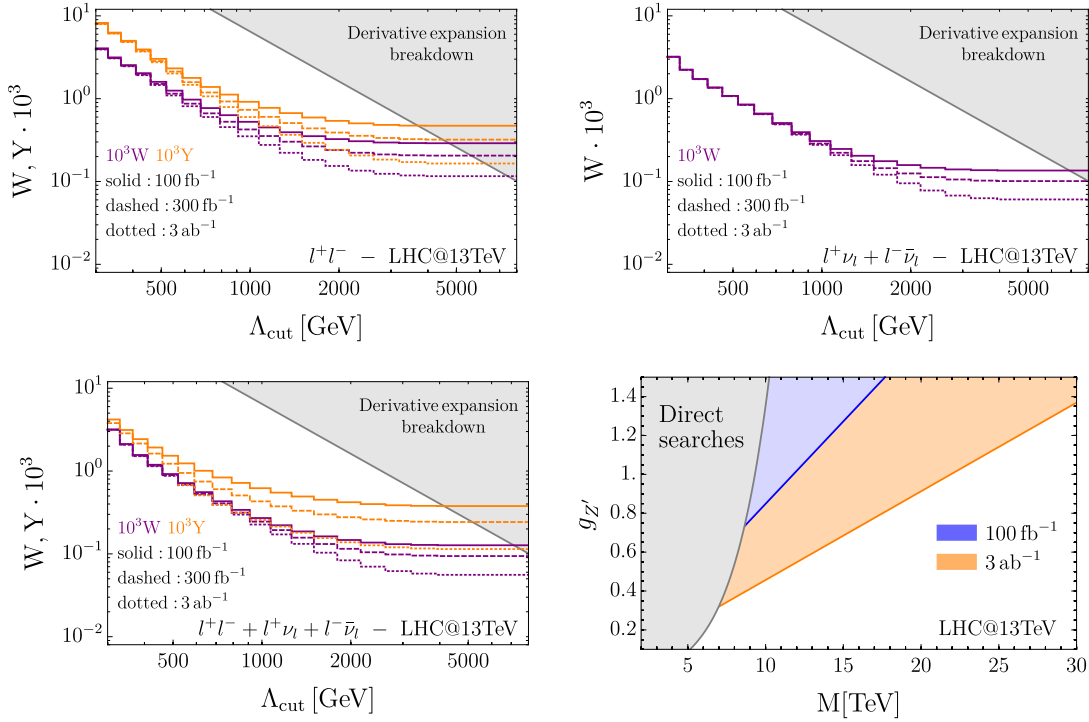


Figure 1.9 – Projected bounds as a function of a cutoff on the mass variable. Bottom right: Projected exclusions on a simple  $Z'$  model (defined as in ref. [32]) from the measurement of the  $Y$  parameter. The exclusion reach from direct  $Z'$  searches, at the HL-LHC, is also shown.

It is interesting to investigate the impact of each source of uncertainty on the sensitivity. We report in figure 1.10 the projected single-operator limits obtained with different assumptions on the errors, compared with the baseline configuration. Eliminating the uncertainties from  $\alpha_s$  and from missing higher orders in the perturbative expansion is found not to improve the sensitivity appreciably, and for this reason the corresponding reach is not reported in the figure. On the other hand, we have verified that the reach would significantly deteriorate with respect to the baseline, especially at the HL-LHC, if the theory uncertainties on the SM prediction were increased to the level estimated by the NLO scale variation in figure 1.6. Incorporating uncertainties from missing 2-loops EW Sudakov effects degrades instead the reach by 10% at most at the HL-LHC. The baseline reach projections thus rely on the availability of NNLO predictions, while it is less relevant to include the enhanced EW logarithms at the 2-loops order.

As expected, PDF are the most relevant source of uncertainties in the theoretical predictions. However we see in figure 1.10 that halving or eliminating these uncertainties does not improve the sensitivity radically. We now turn to the uncertainties of experimental origin, i.e. the luminosity and the  $\Sigma^{\text{exp}}$  uncertainty of eq. (1.31). Removing the latter (as in the “No Syst” bars) has a moderate impact on the reach, while the former is

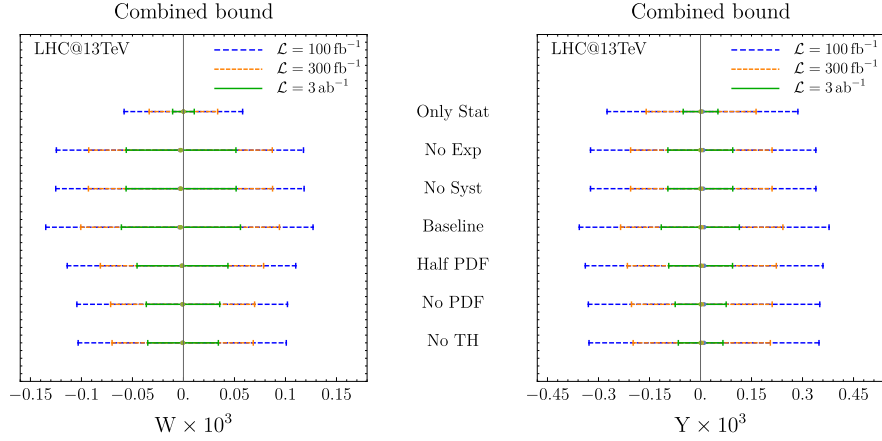


Figure 1.10 – Single-parameter 95% reach on  $W$  (left) and on  $Y$  (right), with different integrated luminosities and for different uncertainty configurations.

completely irrelevant. Indeed, by removing also the luminosity uncertainty (“No Exp” bar), the reach does not improve further.

The picture emerging from the previous discussion is that the experimental accuracy assumed in the baseline configuration is sufficient, given the state-of-the art accuracy of the theoretical predictions, to exploit at best the LHC and HL-LHC potential to probe the  $W$ & $Y$  parameters, and vice versa. A more accurate determination of the PDF could improve the sensitivity, but only slightly. On the other hand, it should be emphasized that our estimate of the experimental uncertainties is a mere guess, which in particular does not take into account correlations between the experimental errors in the different bins and in the different processes, which might reduce the impact of these uncertainties on the reach. If this was the case, the adequacy of the theoretical predictions should be reconsidered, and an improvement of the PDF determination could entail a much more significant progress in the sensitivity. The absolute lower bound for the reach is provided by the “Only Stat” bars in figure 1.10, where all sources of theoretical and experimental systematic error are eliminated.

Before concluding, we compare our results with the findings of ref. [11]. Our projected limits are weaker by around 30%, due to a different estimate of the PDF uncertainties. In [1, 2], we used LHAPDF, which combines several PDF sets, while the estimate in ref. [11] was based on ref. [95], where only one set (NNPDF) was considered. The PDF uncertainties of ref. [95] are a factor of around 2 smaller than ours in the relevant kinematical range, making the uncertainties employed in ref. [11] effectively correspond to our “Half PDF” configuration. With this configuration we could indeed accurately reproduce the results of ref. [11] which are in line with the first run-2 findings in [42].

## 1.4 Fully differential measurements

We have considered so far only the invariant (transverse) mass distribution of the dilepton pairs. The DY final state is however so simple that it can be characterized completely with fully-differential cross-section measurements.<sup>10</sup> In this section we generalize the previous phenomenological analysis to fully-differential DY measurements, quantifying its impact on the sensitivity to EFT operators.

Moreover, we improve the results of sec. 1.3.4 including all the 7 flavor universal current-current quark-lepton interactions. As we will explain the reweighting methodology introduced in sec. 1.2 now becomes crucial. In fact, the large dimensionality of the EFT parameter space, combined with the large number of analysis bins that are employed for the fully-differential analysis, would have made our tasks computationally too demanding if employing a Monte Carlo implementation not based on reweighting.

We start our investigation of the fully-differential DY dilepton production and its sensitivity to new physics by developing a semi-analytic qualitative understanding based on the structure of the tree-level distributions. Quantitative estimates of the sensitivity are performed in Sections 1.4.2 and 1.4.3.

### 1.4.1 Tree-level distributions

Consider the neutral process  $q\bar{q} \rightarrow \ell^+\ell^-$ . The fully-differential cross-section is given by

$$\begin{aligned} \frac{d^3\sigma}{dm_{\ell\ell}^2 dc_* dy} = \frac{\tau}{3 \cdot 64 \pi m_{\ell\ell}^4} \sum_q \left\{ \left[ (1 + c_*)^2 \mathcal{L}_q(\tau, y) + (1 - c_*)^2 \mathcal{L}_q(\tau, -y) \right] P_s^q(m_{\ell\ell}) \right. \\ \left. + \left[ (1 - c_*)^2 \mathcal{L}_q(\tau, y) + (1 + c_*)^2 \mathcal{L}_q(\tau, -y) \right] P_o^q(m_{\ell\ell}) \right\}, \end{aligned} \quad (1.34)$$

where  $m_{\ell\ell} = \sqrt{\hat{s}}$  is the dilepton invariant mass and  $\tau = \hat{s}/S$  (with  $\sqrt{S}$  the collider energy), while  $y$  is the absolute value of the rapidity (relative to the beam axis) of the dilepton system. We define  $c_* = \cos\theta_*$  as the cosine of the angle formed, in the rest frame of the dilepton pair, by the charge-minus lepton and the direction of motion of the dilepton rest frame relative to the lab frame. At tree-level,  $\theta_*$  as defined above is the angle between the  $\ell^-$  and the most energetic incoming parton.<sup>11</sup> The detailed definition of the kinematical variables beyond tree-level is reported in Appendix A.2.

---

<sup>10</sup>Fully (i.e. triply) differential measurements of the neutral DY process have already been performed by ATLAS with early run-1 data [43]. Double differential measurements have been performed in Refs. [39, 40].

<sup>11</sup>It is essential *not* to define  $\theta_*$  with respect to a fixed beam-axis orientation. With that definition, the fully-differential cross-section in eq. (1.34) would depend only on the combination  $(P_s^q + P_o^q)$  like the single-differential cross-section in eq. (1.37), and all the advantages of the fully-differential analysis would be lost.

The sum in eq. (1.34) spans over the light quarks  $q = \{u, d, c, s, b\}$ , and, for each quark species  $q$ ,  $\mathcal{L}_q$  is the product of the corresponding  $q$  and  $\bar{q}$  parton distribution functions (PDFs), namely

$$\mathcal{L}_q(\tau, y) = f_q(\sqrt{\tau} e^y; m_{\ell\ell}^2) f_{\bar{q}}(\sqrt{\tau} e^{-y}; m_{\ell\ell}^2). \quad (1.35)$$

The coefficient functions  $P_s^q$  ( $P_o^q$ ) parametrize the contributions, including both SM and new physics, from the subprocesses where the chirality of the incoming quarks is the same (opposite) one of the outgoing leptons. Our target new physics operators are flavor-universal, like the SM contribution to the scattering amplitudes. Therefore the coefficient functions are the same for all the up-type and for all the down-type quarks, for a total of four independent functions  $P_s^{u,d}$  and  $P_o^{u,d}$ . In the high energy regime  $m_{\ell\ell} \gg m_Z$ , and at the linear interference level in the new physics contribution, the coefficient functions read

$$\begin{aligned} P_s^{u,d}(m_{\ell\ell}) &\simeq P_{\text{SM},s}^{u,d} + m_{\ell\ell}^2 \left( \vec{V}_s^{u,d} \cdot \vec{G} \right) \equiv P_{\text{SM},s}^{u,d} + m_{\ell\ell}^2 G_s^{u,d}, \\ P_o^{u,d}(m_{\ell\ell}) &\simeq P_{\text{SM},o}^{u,d} + m_{\ell\ell}^2 \left( \vec{V}_o^{u,d} \cdot \vec{G} \right) \equiv P_{\text{SM},o}^{u,d} + m_{\ell\ell}^2 G_o^{u,d}, \end{aligned} \quad (1.36)$$

where  $\vec{G}$  denotes the Wilson coefficients of the seven effective four-fermion operators defined in Table 1.1. In these expressions both the SM terms  $P_{\text{SM},s}^{u,d}$  and  $P_{\text{SM},o}^q$ , and the vectors  $\vec{V}_{s,o}^{u,d}$ , are kinematics-independent numerical coefficients, reported in Appendix A.1. At the linear level, and up to tiny effects suppressed by  $m_Z^2/m_{\ell\ell}^2$ , the neutral DY cross-section depends on new physics only through the four linear combinations  $G_{s,o}^{u,d} = \vec{V}_{s,o}^{u,d} \cdot \vec{G}$  of the seven Wilson coefficients. With the fully-differential analysis we can probe each of these four directions in the new physics parameters space independently, at least in line of principle.

Consider for comparison the single-differential cross-section  $d\sigma/dm_{\ell\ell}^2$ . By integrating eq. (1.34) over  $c_*$  and  $y$ , we get

$$\frac{d\sigma}{dm_{\ell\ell}^2} = \frac{\tau}{72\pi m_{\ell\ell}^4} \sum_q \frac{d\mathcal{L}_q}{d\tau} [P_s^q(m_{\ell\ell}) + P_o^q(m_{\ell\ell})], \quad (1.37)$$

where the parton luminosities are defined as

$$\frac{d\mathcal{L}_q}{d\tau} = \int_{-y_{\max}}^{y_{\max}} dy \mathcal{L}_q(\tau, y), \quad y_{\max} = -\frac{1}{2} \log \tau. \quad (1.38)$$

We see that the single-differential cross-section only depends on the sum of the “ $s$ ” and “ $o$ ” coefficient functions. At linear level, using eq. (1.36), it is thus only sensitive to  $G_s^u + G_o^u$  and  $G_s^d + G_o^d$ , i.e. to two combinations of the four directions in the EFT parameter space that the fully-differential analysis can probe. Actually it is not difficult to see that the single-differential analysis is not even sensitive to  $G_s^u + G_o^u$  and  $G_s^d + G_o^d$  independently,

but only to the combination

$$(G_o^u + G_s^u) + 0.5(G_o^d + G_s^d). \quad (1.39)$$

This is because the ratio between the up and the down quarks luminosities (that dominate over the one of the other quark flavors) is nearly constant in  $\tau$  in the most sensitive energy range  $m_{\ell\ell} \sim 1 - 2$  TeV. The ratio is approximately equal to 2 owing to the valence quarks content of the proton.

The advantages of performing a fully-differential measurement can now be appreciated by analyzing the various regions in the  $(c_*, y)$  kinematic space. In the kinematical regime with small center of mass rapidity ( $y \simeq 0$ ), one has  $\mathcal{L}_q(\tau, y) \simeq \mathcal{L}_q(\tau, -y)$ , and the cross-section in eq. (1.34) becomes proportional to  $(1 + c_*^2)\mathcal{L}_q(\tau, 0)(P_s^q + P_o^q)$ . Hence this region provides sensitivity to the same combination of Wilson coefficients that can be probed through the  $d\sigma/dm_{\ell\ell}^2$  distribution. On the other hand, in the region with large  $y$  we have  $\mathcal{L}_q(\tau, y) \gg \mathcal{L}_q(\tau, -y)$  for the (dominant) up and down quarks because the valence quarks are typically more energetic than the sea anti-quarks. Therefore the cross-section is proportional to  $(1 + c_*)^2 P_s^q + (1 - c_*)^2 P_o^q$  and it is sensitive to both  $P_s^q$  and  $P_o^q$  for  $c_* \simeq +1$  and  $c_* \simeq -1$ , respectively.

Measuring the fully-differential distribution can also mitigate the degeneracy between the up and down quark contributions that is due, as previously discussed, to the similar shape of the parton luminosities. Indeed the dependence of  $\mathcal{L}_q(\tau, y)$  on  $y$  is significantly different for the two quark species. In particular the up quark distribution is peaked at larger values of  $y$  than the one of the down quark.<sup>12</sup>

The discussion above shows that the fully-differential cross-section measurement has the potential to disentangle the four  $G_{s,o}^{u,d}$  linear combinations of Wilson coefficients. This is a significant improvement relative to the single-differential measurement that is sensitive to one combination only. The quantitative assessment of this improvement is postponed to Section 1.4.3.

It should be stressed that our findings are based on the dependence of the cross-section on the Wilson coefficients at the linear order. At the quadratic level, all Wilson coefficients enter in the  $P_{s,o}^q$  functions with comparable coefficients (see the explicit expression for the amplitudes in Appendix A.1). Therefore also the combinations of parameters that do not enter or are suppressed in the linear term can be determined through their quadratic contributions. These combinations are all expected to be tested less effectively than the ones contributing to the linear terms, but with similar precision among them.

A similar analysis can be performed for the charged DY process  $q\bar{q}' \rightarrow \ell\nu$ . In this case, however, a fully-differential measurement has a milder impact. The reason for this is

---

<sup>12</sup>A detailed discussion of this feature can be found in Ref. [96] (see in particular Figure 3).



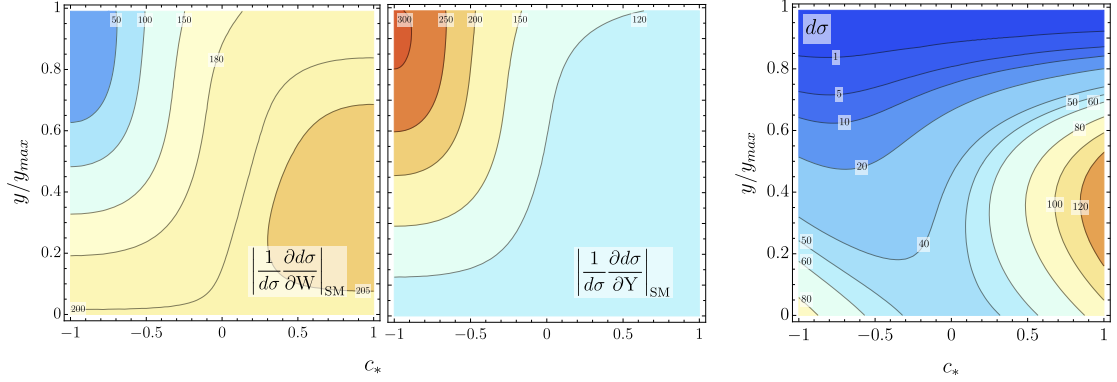


Figure 1.11 – Left panel: Absolute value of the logarithmic derivative of the tree-level differential cross-section with respect to the W and Y parameters in the  $(c_*, y)$  plane. Right panel: Level contours of the tree-level SM differential cross-section (in arbitrary units). Both plots are obtained at fixed  $m_{\ell\ell} = 1$  TeV.

twofold. First, the charged process is only affected by one operator, namely  $\mathcal{O}_{lq}^{(3)}$ , so that no issue in disentangling various new physics contributions is present. Second, due to the presence of a neutrino, only two independent kinematic variables can be accessed, for instance the transverse momentum of the charged lepton  $p_{T,\ell}$  and its rapidity  $\eta_\ell$ . The new-physics contributions depend on the center of mass energy  $\sqrt{\hat{s}}$ , which is closely correlated with  $p_{T,\ell}$ , but has a very mild correlation with  $\eta_\ell$ . The additional benefit of considering both kinematical variables rather than only  $p_{T,\ell}$  is therefore expected to be small. However it should be taken into account that more differential information in the charged channel might help reducing the impact of PDF uncertainties in the combination with the fully-differential neutral DY measurements. Indeed some advantage of the doubly-differential measurement in charged DY will be observed in the analyses presented below.

#### 1.4.2 Bounds on the Universal parameters W and Y

As a first quantitative analysis we focus again on the specific set of dimension-6 operators related to the Universal parameters W and Y. There are some crucial differences between the W and the Y parameter, which make the latter more difficult to test. While W can be probed in both the charged and the neutral DY channels, Y only affects the neutral DY process. Furthermore, if the neutral channel is analyzed by fitting only the invariant mass distribution, the single combination of Wilson coefficients that is probed at the linear level, in eq. (1.39), turns out to be proportional to  $W + 0.6 Y$  (using Table A.4). Therefore the sensitivity to Y is almost two times weaker than to W.

As we discussed above, a fully-differential analysis in the neutral channel can help to disentangle different new physics contributions. This happens also for the W and Y

parameters. To illustrate this point we show in the left panel of Figure 1.11<sup>13</sup> the logarithmic derivatives of the tree-level differential cross-section with respect to  $W$  and  $Y$ , namely

$$\left. \frac{1}{d\sigma} \frac{\partial d\sigma}{\partial W} \right|_{\text{SM}}, \quad \left. \frac{1}{d\sigma} \frac{\partial d\sigma}{\partial Y} \right|_{\text{SM}}, \quad (1.40)$$

evaluated at the SM point  $W = Y = 0$ . For definiteness the dilepton invariant mass has been set to  $m_{\ell\ell} = 1$  TeV in the figure. The logarithmic derivative scales like  $m_{\ell\ell}^2$  as a function of the mass. As expected, in most of the kinematic space, i.e. for small rapidity and for  $c_* \gtrsim 0$ , the cross-section dependence on  $W$  is roughly twice stronger than on  $Y$ . In particular this happens in the regions with larger cross-section, as can be seen from the plot in the right panel of Figure 1.11.

The behavior, however, drastically changes in the corner with  $c_* \lesssim -0.5$  and  $y/y_{\text{max}} \gtrsim 0.5$ . For these configurations the differential cross-section mostly depends on  $Y$ , while the sensitivity to  $W$  is small. This feature can be easily understood from the analysis we performed in the previous section. For large rapidity and  $c_* \sim -1$  the differential cross-section is controlled by  $P_o^q$ , which gets contributions from subprocesses with opposite fermion chiralities. Since  $W$  corresponds to an operator with only left-handed fields, it can contribute only to the same-chirality subprocesses and not to  $P_o^q$ . Exploiting the fully-differential distribution for the fit is thus expected to improve the determination of  $Y$ . It must be however noticed that the differential cross-section in the  $y \sim y_{\text{max}}$  and  $c_* \sim -1$  corner is somewhat suppressed, and is an order of magnitude smaller than in the  $c_* > 0$  region. This means that a significant improvement in the  $Y$  determination can be obtained only when a high number of signal events are collected, so that the  $y \sim y_{\text{max}}$  and  $c_* \sim -1$  region is sufficiently populated at high  $m_{\ell\ell}$ . To give an idea, at the HL-LHC, out of  $\sim 12000$  SM events with  $m_{\ell\ell} > 1.1$  TeV, only 210 events are expected in the region with  $y/y_{\text{max}} > 0.4$  and  $c_* < -0.6$ .

We show in Figure 1.12 the comparison of the projected exclusion reach on the  $W$  and  $Y$  parameters obtained from a fit taking into account the fully-differential distribution or the single-differential (invariant mass or transverse momentum for neutral and charged DY, respectively) distributions. To obtain the bounds we considered the HL-LHC benchmark, with collider energy 14 TeV and  $\mathcal{L} = 3 \text{ ab}^{-1}$  integrated luminosity, and we assumed that the experimental measurements of the cross-section coincide with the SM predictions.<sup>14</sup> The fit of the charged DY process was obtained by considering a set of bins in the transverse momentum and rapidity of the charged lepton, whose boundaries are

$$p_{T,\ell} : \quad \{150, 180, 225, 300, 400, 550, 750, 1000, 1300, 7000\} \text{ GeV}, \quad (1.41)$$

$$\eta_l/\eta_{\text{max}} : \quad \{0, 1/3, 2/3, 1\}, \quad (1.42)$$

where  $\eta_{\text{max}}$  is the minimum between the acceptance cut of 2.5 and the maximal kinemat-

<sup>13</sup>We employed the package of Ref. [97] to obtain semi-analytic expressions for the PDF.

<sup>14</sup>Results for the LHC run 3 benchmark are reported in Appendix A.4.

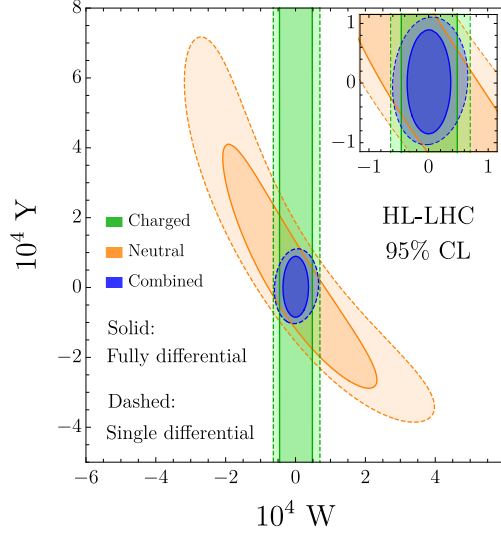


Figure 1.12 – 95% CL allowed regions for  $W$  and  $Y$  at the 14 TeV HL-LHC. The green and orange shaded regions correspond to the bounds from charged and neutral DY, respectively, whereas the combined bounds are given by the blue shaded regions. The fully-differential analysis results are reported with solid contours while the dashed contours represent the sensitivity of the single-differential measurements.

ically allowed rapidity  $\text{arctanh}[(1 - 4p_{T,\ell}^2/S)^{1/2}]$ . For the neutral DY channel we instead used a binning in  $m_{\ell\ell}$ ,  $c_*$  and  $y$ , with boundaries

$$m_{\ell\ell} : \quad \{300, 360, 450, 600, 800, 1100, 1500, 2000, 2600, 14000\} \text{ GeV} , \quad (1.43)$$

$$c_* : \quad \{-1, -0.6, -0.2, 0.2, 0.6, 1\} , \quad (1.44)$$

$$y/y_{\text{max}} : \quad \{0, 0.2, 0.4, 0.6, 1\} . \quad (1.45)$$

The cross-section predictions are obtained as explained in sec. 1.2, at NLO in QCD combined with parton showering (based on POWHEG and PYTHIA 8) and at the NLL order in the EW expansion. The effects due to the  $W$  and  $Y$  parameters (and the EW logarithms) are included through reweighting, which enables fast and accurate Monte Carlo predictions in the relatively large number of bins (a total of 234) that we consider in the fully-differential analysis. The  $O'_{2W}$ ,  $O'_{2B}$  operators have been defined at the renormalization scale of 10 TeV.

The projected bounds take into account, as explained in sec. 1.3, the PDF uncertainties and a 2% luminosity uncertainty. We considered an 80% reconstruction efficiency for each muon and 65% for each electron. The results now, do not take into account any additional experimental systematic uncertainty. This is because we expect that the size and the correlation of these uncertainties will strongly depend on the binning and it will be quite different in the fully-differential measurement and in the single-differential one.

Since a quantitative estimate of the uncertainties is not available, we set them to zero for a fair comparison of the two analysis procedures. A qualitative assessment of their potential impact is presented in Section 1.4.4.

From Figure 1.12 we see that the fully-differential analysis gives a strong boost to the sensitivity of the neutral DY channel, improving in particular the sensitivity along the  $W + 0.6 Y = 0$  line that is weakly probed by the single-differential analysis as previously discussed. The charged DY sensitivity also improves. However it should be taken into account that the single-differential analysis is performed (like in Refs. [1, 11]) on the sum of the charge plus and charge minus cross-sections in each  $p_{T,\ell}$  bin. The two charges are instead separately measured and combined in the fully-differential analysis, which is helpful to mitigate the impact of PDF uncertainties. The improvement we observe in the charged channel is partly due to this effect.

Interestingly, the improvement of the fully-differential analysis is quite significant for the combination of the neutral and charged DY channels. The 95%CL single-parameter bounds from the combined fit are given by

$$\begin{aligned} W : \quad & [-2.9, 3.0] \times 10^{-5} \quad ([-4.9, 5.2] \times 10^{-5}), \\ Y : \quad & [-6.8, 7.1] \times 10^{-5} \quad ([-8.3, 8.8] \times 10^{-5}), \end{aligned} \tag{1.46}$$

where the numbers in parentheses correspond to the single-differential fit. The constraint on  $W$  becomes nearly a factor 2 more stringent, whereas the determination of  $Y$  improves more mildly. It is interesting to notice that part of the improvement in the  $W$  determination does not come from the naive sum of the log likelihood for the neutral and charged processes, but is instead a consequence of the reduced impact of the PDF uncertainties. The PDF errors, in fact, are strongly correlated in the two channels, so that including both of them simultaneously in the fit allows one to distinguish their effects from the contributions due to new physics.

### 1.4.3 General quark-lepton interactions

We now consider the impact of the fully-differential analysis on the determination of the complete set of lepton-quark current-current operators listed in Table 1.1. In order to make the comparison with the single-differential analysis more straightforward, it is convenient to choose a basis in the space of Wilson coefficients which is aligned with the directions that appears in the invariant mass distribution for the neutral dilepton channel. As we discussed in Section 1.4.1, the  $d\sigma/dm_{\ell\ell}^2$  distribution depends at the linear level only on two particular combinations of parameters,  $G_s^u + G_o^u$  and  $G_s^d + G_o^d$ , with  $G_{s,o}^{u,d}$  defined as in eq. (1.36). Moreover the ratio of up and down parton luminosities singles out one combination of Wilson coefficients (1.39) that is most effectively probed

in the invariant mass distribution. We thus include in our basis the combination

$$G_E^+ = (G_o^u + G_s^u) + 0.5 (G_o^d + G_s^d), \quad (1.47)$$

and the orthogonal one, which we denote by

$$G_E^- = 0.5 (G_o^u + G_s^u) - (G_o^d + G_s^d). \quad (1.48)$$

We further consider the two remaining combinations of parameters, which contribute to the fully-differential distribution at the linear level but not to the invariant mass distribution

$$G_O^+ = (G_o^u - G_s^u) + 0.5 (G_o^d - G_s^d), \quad G_O^- = 0.5 (G_o^u - G_s^u) - (G_o^d - G_s^d). \quad (1.49)$$

Finally, we complete the seven-dimensional basis with the  $\tilde{G}_{lq}^{(3)} = G_{lq}^{(3)}$  coefficient and two additional combinations,  $G_s^\perp$  and  $G_o^\perp$ , that are orthogonal to all the others. The explicit expressions are reported in Appendix A.1. The  $G_s^\perp$  and  $G_o^\perp$  coefficients contribute (at the quadratic level) to the same-chirality and opposite-chirality subprocesses, respectively. It is important to stress that the change of basis we are performing is not orthogonal. In particular this means that the  $G_{lq}^{(3)}$  coefficient of the Warsaw basis not only gives rise to  $\tilde{G}_{lq}^{(3)}$  (with the same value), but also gives a correlated contribution to the  $G_{E,O}^\pm$  coefficients.

Fully-differential measurements improve the determination of the different parameters defined above, relative to the single-differential analyses, to different extents. The  $\tilde{G}_{lq}^{(3)}$  coefficient is mainly tested in the charged DY process, where the impact of the differential analysis is less pronounced. Its (single-operator) determination can thus improve only mildly from the combination with the neutral channel and the associated possible reduction of the impact of the PDF uncertainties. The  $G_s^\perp$  and  $G_o^\perp$  coefficients contribute only at quadratic order or through very small subleading terms in the  $m_Z^2/m_{\ell\ell}^2$  expansion, both to the single and to the fully-differential cross-section. Therefore they will be tested with lower accuracy and they will not improve significantly with the fully-differential analysis. We thus focus on the remaining four coefficients  $G_{E,O}^\pm$ . Among those,  $G_E^+$  will not improve much, since it is already effectively probed in the invariant mass distribution. A significant improvement is instead possible for the other ones.

For a first assessment of the perspectives for progress we show in Figure 1.13 the logarithmic derivative of the tree-level fully-differential cross-section for the neutral DY channel with respect to the four  $G_{E,O}^\pm$  parameters. In the low-rapidity region ( $y/y_{\max} \lesssim 0.5$ ) the cross-section is sensitive dominantly to  $G_E^+$ . This is not surprising since, as we saw in Section 1.4.1, the distribution in the low-rapidity region depends on the same combination of coefficient functions that enter in the invariant-mass distribution. The high-rapidity configurations, on the contrary, show very different sensitivity patterns to the  $G_{E,O}^\pm$  coefficients. One can see, in particular, that the  $c^* > 0$  region, which has

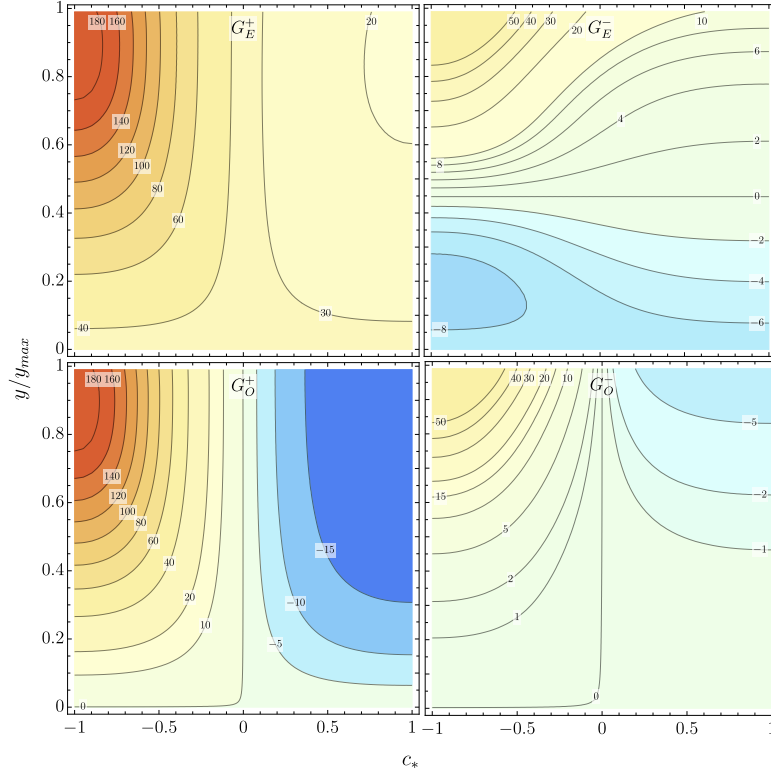


Figure 1.13 – Logarithmic derivative of the tree-level differential cross-section with respect to the  $G_{E,O}^{\pm}$  coefficients in the  $(c_*, y)$  plane. The plots are obtained setting  $m_{\ell\ell} = 1$  TeV.

a high SM cross-section (see the right panel of Figure 1.11), shows a relatively large logarithmic derivative with respect to  $G_O^+$ . The fully-differential analysis is therefore expected to improve significantly the determination of this coefficient and to disentangle it from  $G_E^+$ , which gives a different dependence of the logarithmic derivative as a function of  $y$ .

On the other hand, the  $G_O^-$  coefficient affects the distribution mainly in the  $c_* \sim -1$ ,  $y \sim y_{\max}$  corner, in which the cross-section is rather small. For this reason we expect its determination to remain relatively poor. Finally the  $G_E^-$  coefficient is in an intermediate situation. The related logarithmic derivative is significantly smaller than for  $G_E^+$  and  $G_O^+$ , but nevertheless shows a distinctive pattern in the region with  $y/y_{\max} \lesssim 0.5$ , which has a good cross-section. We thus expect that the fully-differential analysis could provide some improvement on its determination.

To estimate the sensitivity to  $G_{E,O}^{\pm}$  we performed the same analysis presented in Section 1.4.2 for the W and Y parameters. The two-dimensional 95% CL contours for each pair of coefficients, setting the others to zero, are shown in Figure 1.14.<sup>15</sup> Different sets

<sup>15</sup>The plots are obtained by combining the neutral and charged DY channels. Notice that the charged channel does not depend on the  $G_E^{\pm}$  and  $G_O^{\pm}$  coefficients, so its contribution is only indirect, through a

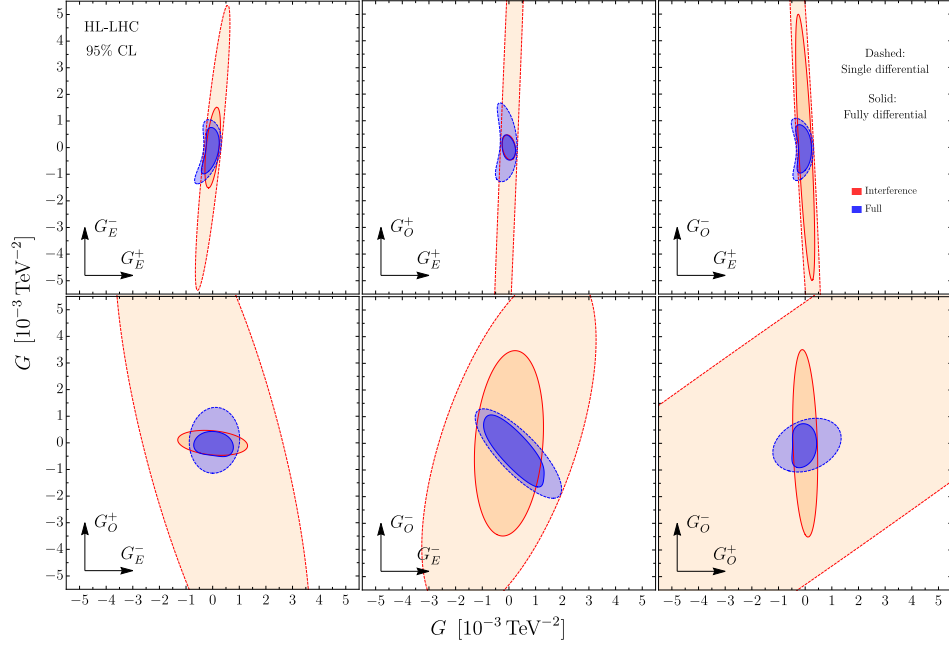


Figure 1.14 – Allowed regions at 95% CL on the six coordinate planes along the four  $G_{E,O}^{\pm}$  coefficients. Solid contours correspond to the fully-differential analysis, while the dashed ones are obtained with the single-differential measurements. The blue shaded regions include the full dependence on the Wilson coefficients in the cross-section, while only the linear terms are retained in the orange shaded regions.

of bounds are compared in the plots. The solid contours correspond to the 95% CL constraints from the fully-differential analysis, whereas the dashed ones are obtained exploiting the invariant-mass distribution in the neutral channel and the transverse-momentum distribution (summed over the two charges as discussed in Section 1.4.2) in the charged channel. The blue shaded regions are obtained by considering the full dependence on the Wilson coefficients in the cross-section, while the orange shaded regions are found by taking into account only the linear terms. The axes of the ellipses for the fully-differential analysis at the linear level are aligned with the reference axes of each plane, owing to our judicious choice of the basis.

We also report, in Table 1.3, the expected sensitivity to all the seven parameters  $G_{E,O}^{\pm}$ ,  $G_{s,o}^{\perp}$  and  $\tilde{G}_{lq}^{(3)}$ . We list both the single-parameter bounds obtained by setting all the others to zero and the bounds profiled over the other parameters. In the case of the fully-differential analysis we also report the results of the linearized fit.

We see from the figure and the table that the single-operator determination of  $G_E^+$  is only marginally modified, with a modest improvement or order 10%. This was expected, as previously discussed, since the determination of  $G_E^+$  from the invariant-mass distribution

---

reduction of the impact of the PDF uncertainties. This effect is however small.

95%CL [ $10^{-3} \text{ TeV}^{-2}$ ]	single parameter			profiled		
	fully diff.	fully diff. lin.	single diff.	fully diff.	fully diff. lin.	single diff.
$\tilde{G}_{lq}^{(3)}$	[-0.36, 0.35]	[-0.36, 0.36]	[-0.49, 0.50]	[-0.53, 0.48]	[-0.57, 0.57]	[-0.97, 0.77]
$G_E^+$	[-0.20, 0.19]	[-0.20, 0.20]	[-0.27, 0.25]	[-0.55, 0.32]	[-0.60, 0.60]	[-1.19, 0.45]
$G_E^-$	[-0.61, 0.65]	[-1.02, 1.02]	[-0.77, 0.90]	[-1.52, 1.30]	[-1.62, 1.62]	[-3.31, 1.94]
$G_O^+$	[-0.38, 0.35]	[-0.37, 0.37]	[-1.01, 1.19]	[-0.44, 0.60]	[-0.82, 0.82]	[-1.32, 2.17]
$G_O^-$	[-0.77, 0.65]	[-2.74, 2.74]	[-0.95, 0.79]	[-1.58, 1.80]	[-5.85, 5.85]	[-2.06, 3.20]
$G_s^\perp$	[-2.14, 1.44]	[-3.74, 3.74]	[-2.24, 1.59]	[-2.46, 2.19]	[-10.5, 10.5]	[-2.91, 2.41]
$G_o^\perp$	[-0.69, 0.67]	[-18.6, 18.6]	[-0.85, 0.84]	[-0.98, 0.89]	[-25.5, 25.5]	[-1.26, 1.31]

Table 1.3 – 95% CL projected bounds (in  $10^{-3} \text{ TeV}^{-2}$  units) for the seven coefficients  $\tilde{G}_{lq}^{(3)}$ ,  $G_{E,O}^\pm$  and  $G_{s,o}^\perp$ . The first three bounds correspond to single-operator fits, in which all other parameters are set to zero, while the last three are profiled over the other parameters. For each set of bounds the three columns correspond to the complete fully-differential fit, the linearized one and the single-differential measurement fit.

is already quite good. Since  $G_E^+$  contributes at the linear level and it is well probed, no significant difference is present between the full fit and the linearized one in this direction.

A strong improvement is instead found in the sensitivity to  $G_O^+$ , as anticipated. The bound from the full fit (i.e. including both the linear and quadratic dependence on the Wilson coefficient in the cross-section) improves roughly by a factor of 3. The improvement in the linearized fit is even more dramatic, since  $G_O^+$  does not contribute to the invariant mass distribution at the linear level up to small effects, as previously discussed. Correspondingly, an approximate flat direction is present for  $G_O^+$  (see for instance the middle plot on the top row of Figure 1.14) in the single-differential linearized contour. The fully-differential analysis is instead strongly sensitive to  $G_O^+$  at the linear level and the linearized and the full fit agree very well.

The impact of the fully-differential analysis on the  $G_E^-$  and  $G_O^-$  parameters follows a slightly different pattern. In the full fit a mild improvement of the bounds, of order 15%, is found. The results, however, change drastically at the linearized level. In this case the fully-differential analysis is able to significantly improve the constraints on both parameters (see for instance the middle plot on the second row of Figure 1.14).

The profiled bounds reported in Table 1.3 are more difficult to interpret. They significantly differ from the single operator ones, signaling the presence of non-negligible correlations among the various parameters. We notice that for many parameters the fully-differential analysis improves the profiled bound more than the single-operator one. This pattern is particularly visible for the  $\tilde{G}_{lq}^{(3)}$ ,  $G_E^+$  and  $G_E^-$  parameters, and, to a lesser degree, for  $G_O^+$  and  $G_O^-$ . The origin of this behavior can be traced back to the reduction of flat directions in the fully-differential fit, which helps in reducing the correlations among the various Wilson coefficients.



#### 1.4. Fully differential measurements

95%CL [ $10^{-3} \text{ TeV}^{-2}$ ]	single parameter			profiled		
	fully diff.	fully diff. lin.	single diff.	fully diff.	fully diff. lin.	single diff.
$G_{lq}^{(3)}$	[-0.46, 0.44]	[-0.45, 0.45]	[-0.80, 0.75]	[-0.53, 0.48]	[-0.57, 0.57]	[-0.97, 0.77]
$G_{lq}^{(1)}$	[-1.95, 2.42]	[-2.15, 2.15]	[-2.42, 3.55]	[-4.69, 5.28]	[-12.8, 12.8]	[-5.93, 8.75]
$G_{qe}$	[-2.13, 3.29]	[-2.56, 2.56]	[-3.19, 6.19]	[-4.31, 5.35]	[-139, 139]	[-7.11, 7.05]
$G_{lu}$	[-1.76, 2.12]	[-1.92, 1.92]	[-2.87, 4.22]	[-3.18, 5.41]	[-69.2, 69.2]	[-7.38, 8.57]
$G_{ld}$	[-8.98, 5.01]	[-7.09, 7.09]	[-11.9, 6.92]	[-9.89, 8.95]	[-148, 148]	[-12.6, 14.0]
$G_{eu}$	[-1.22, 1.30]	[-1.26, 1.26]	[-1.51, 1.65]	[-3.38, 5.75]	[-16.3, 16.3]	[-4.46, 7.29]
$G_{ed}$	[-4.74, 3.55]	[-4.03, 4.03]	[-7.12, 4.47]	[-9.25, 9.33]	[-41.3, 41.3]	[-10.7, 12.7]

Table 1.4 – 95% CL projected bounds for the four-fermion operator coefficients in the Warsaw basis. The bounds are given in  $10^{-3} \text{ TeV}^{-2}$  units.

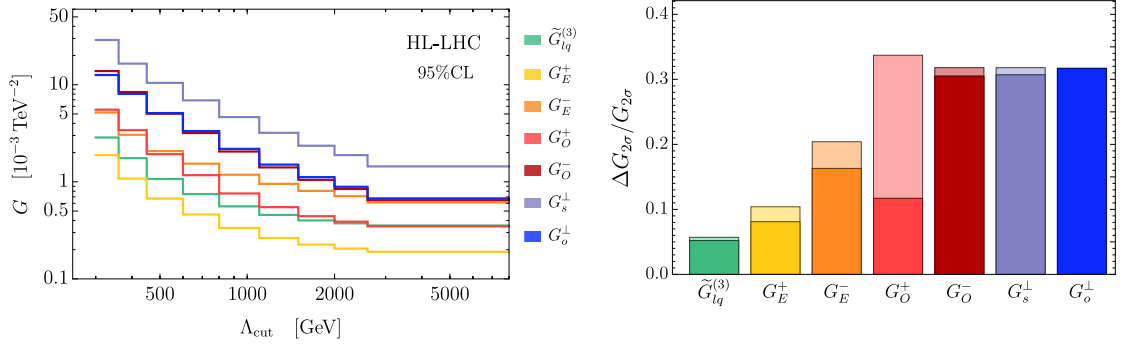


Figure 1.15 – Left panel: Expected bounds on the Wilson coefficients as a function of the upper cut on the energy of the events  $\Lambda_{\text{cut}}$ . Right panel: Relative change in the bounds in the last two bins in  $\Lambda_{\text{cut}}$ . The darker shadowing corresponds to the fully-differential analysis, while the lighter shadowing corresponds to the single diff. analysis.

For completeness, we report in Table 1.4 the bounds on the four-fermion operators in the Warsaw basis. In this basis we find that  $G_{lq}^{(3)}$  is expected to be determined with much higher precision than the other parameters. Moreover its determination is only mildly affected by profiling, differently from the bounds on the other coefficients that significantly degrade in the profiled fit. This behavior is clearly due to the fact that  $G_{lq}^{(3)}$  is tested with high precision in the charged DY channel, which is not affected by the other effective operators. The impact of a fully-differential analysis is quite large for many Warsaw operators. In particular the bounds on  $G_{lq}^{(3)}$ ,  $G_{qe}$  and  $G_{lu}$  become roughly 40% tighter, while the constraints on the other operators improve by an amount of order 10 – 20%.

As a last point, we investigate the dependence of our results on the maximal energy scale,  $\Lambda_{\text{cut}}$ , of the measurements included in the fit. This gives useful indications on the measurements that contribute more to the final sensitivity and on the energy range of validity of the EFT description of new physics that is theoretically required for the

bounds to apply. Following Refs. [1, 11], we show on the left panel of Figure 1.15 how the single-operator bounds change by retaining in the fit only the bins where  $m_{\ell\ell} < \Lambda_{\text{cut}}$  in the neutral channel and  $p_{T,\ell} < \Lambda_{\text{cut}}/2$  in the charged one. We see that the bounds on the Wilson coefficients with more stringent constraints, namely  $\tilde{G}_{lq}^{(3)}$ ,  $G_E^+$  and  $G_O^+$ , saturate around  $\Lambda_{\text{cut}} \sim 2$  TeV. In particular, removing the last bin (starting at 2600 GeV) has an extremely mild impact. The constraints on the other coefficients, on the contrary, receive sizable contributions from the events in the last bin. This behavior can be explained by recalling that the bounds on the  $\tilde{G}_{lq}^{(3)}$ ,  $G_E^+$  and  $G_O^+$  coefficients in the fully-differential analysis are mainly driven by the linear interference terms in the cross-section prediction. These terms grow linearly with the partonic  $\hat{s}$  so that the energy region with good sensitivity, which we find to be  $\sqrt{\hat{s}} \sim 1 - 2$  TeV, is where this growth starts being balanced by the decrease of the quark luminosity. For the other parameters, instead, the bounds are driven mostly by the square of the BSM contributions, which grow like  $\hat{s}^2$ . The faster growth pushes the sensitive region to higher energies.

To appreciate better this point, we show in the right panel of Figure 1.15 the relative change in the bounds on the various parameters when the last bin is removed. For the fully-differential fit (darker shadowing), a variation below around 10% is observed for  $\tilde{G}_{lq}^{(3)}$ ,  $G_E^+$  and  $G_O^+$ . The  $G_O^-$ ,  $G_s^\perp$  and  $G_o^\perp$  coefficients, instead, show a relatively large change in the bounds ( $\simeq 30\%$ ). Finally, the  $G_E^-$  coefficient shows an intermediate behavior, which is explained by the fact that for its determination the linear interference terms and the quadratic terms have comparable weight. It is interesting to notice that the sensitivity to the last bin of  $G_O^+$  is quite lower in the fully-differential fit than in the single-differential one (displayed with lighter shadowing in the figure). This is because in the former case the bound is driven by the linear terms, while in the latter it is mainly driven by the quadratic terms. This difference can be also seen in the single-parameter bounds on  $G_O^+$ , which improve by roughly a factor 3 with the fully-differential analysis (see Figure 1.14 and Table 1.3).

### Running Effects

Our cross-section predictions include EW corrections at the single-log accuracy, among which the ones associated with the Renormalization Group evolution of the EFT operators. Therefore, as we already mentioned before, our results depend, in line of principle, on the operator renormalization scale. This has been set to 2 TeV because the measurements at that scale dominate the sensitivity as previously shown. However the running effects are extremely small and our results do not depend on this choice in practice. This has been verified by repeating the fit in two ways. In one case we switched off completely the running, while in the other one we fixed the values of the Wilson coefficients at an energy scale  $E = 10$  TeV. In both cases the bounds on the Wilson coefficients, both single-operator and the profiled ones, change at most by *few* %. Our results can thus be safely applied even to EFT operators defined at several tens of TeV.

It is important to keep in mind that only quark-lepton current-current operators are included in our calculation. Other EFT operators do not produce growing-with-energy effects in high-energy DY, therefore their contribution is very suppressed relative to the quark-lepton ones and completely negligible if their size is not anomalously large. In particular this means that operators induced by the quark-lepton ones through running are completely negligible because running is itself a small effect. The contribution to the running of the quark-lepton operators by the other ones is also negligible, for the same reason. On the other hand, one cannot firmly exclude the presence of other EFT operators with anomalously large coefficients that are not already excluded or that can not be probed with other LHC measurements. Such operators, if found to exist after a more systematic global exploration of the LHC EFT potential, should be included in the predictions.

### 1.4.4 Experimental uncertainties

This section is devoted to uncertainties that are not included in the analysis presented above, namely the presence of systematic uncertainties in the experimental cross-section measurements other than the luminosity uncertainty that was already taken into account.

As explained in sec. 1.3, our fits are based on the Poisson likelihood, which takes automatically into account the statistical component of the cross-section measurement errors. The systematic component of the experimental error is instead incorporated by nuisance parameters on the expected Poisson countings. Only the nuisance corresponding to a 2% luminosity uncertainty has been included in the analysis and its effect is very small as expected. The dominant experimental errors are indeed those that, unlike the luminosity, distort the shape of the differential distributions. We cannot rely on any estimate of the size of these uncertainties, nor of their correlations across different analysis bins which on the other hand are expected to have a major impact on the sensitivity to new physics. In order to get a feeling of their possible impact, we adopt now a crude parametrization of these effects by introducing a fully-uncorrelated 2% error in all bins, both for the fully-differential and for the single-differential fit.<sup>16</sup>

Including these uncorrelated systematic errors, the combined 95% CL bound on the W and Y parameters become

$$\begin{aligned} W : & \quad [-3.6, 3.7] \times 10^{-5} \quad ([-5.3, 5.8] \times 10^{-5}) \\ Y : & \quad [-8.4, 8.9] \times 10^{-5} \quad ([-10.9, 12.0] \times 10^{-5}) \end{aligned} \quad \text{with 2\% uncorr. syst..} \quad (1.50)$$

The numbers in parentheses refer to the single-differential fit. Comparing with the results in eq. (1.46), we see that the bounds from the fully-differential analysis become roughly 25% weaker. In the case of the single-differential analysis, the bounds on Y suffer from

<sup>16</sup>Notice that this choice is slightly different from the one of sec. 1.3.3.

## Chapter 1. Precision physics from the tail

95%CL [ $10^{-3} \text{ TeV}^{-2}$ ]	single parameter			profiled		
	fully diff.	fully diff. lin.	single diff.	fully diff.	fully diff. lin.	single diff.
$\tilde{G}_{lq}^{(3)}$	[-0.46, 0.46]	[-0.46, 0.46]	[-0.62, 0.63]	[-0.68, 0.59]	[-0.72, 0.72]	[-1.06, 0.84]
$G_E^+$	[-0.25, 0.23]	[-0.24, 0.24]	[-0.38, 0.32]	[-0.67, 0.36]	[-0.73, 0.73]	[-1.51, 0.51]
$G_E^-$	[-0.67, 0.70]	[-1.45, 1.45]	[-0.85, 0.95]	[-1.80, 1.61]	[-1.96, 1.96]	[-3.73, 2.24]
$G_O^+$	[-0.41, 0.37]	[-0.40, 0.40]	[-1.07, 1.24]	[-0.48, 0.72]	[-0.97, 0.97]	[-1.43, 2.49]
$G_O^-$	[-0.79, 0.67]	[-3.01, 3.01]	[-0.99, 0.83]	[-1.84, 2.00]	[-6.21, 6.21]	[-2.33, 3.61]
$G_s^\perp$	[-2.18, 1.50]	[-4.21, 4.21]	[-2.31, 1.70]	[-2.59, 2.44]	[-11.9, 11.9]	[-3.17, 2.85]
$G_o^\perp$	[-0.71, 0.69]	[-22.2, 22.2]	[-0.89, 0.88]	[-1.03, 0.91]	[-31.8, 31.8]	[-1.47, 1.46]

Table 1.5 – 95% CL projected bounds for the seven coefficients  $\tilde{G}_{lq}^{(3)}$ ,  $G_E^\pm$ ,  $G_O^\pm$  and  $G_{s,o}^\perp$ , including a 2% uncorrelated systematic uncertainty.

95%CL [ $10^{-3} \text{ TeV}^{-2}$ ]	single parameter			profiled		
	fully diff.	fully diff. lin.	single diff.	fully diff.	fully diff. lin.	single diff.
$G_{lq}^{(3)}$	[-0.57, 0.55]	[-0.56, 0.56]	[-0.89, 0.82]	[-0.68, 0.59]	[-0.72, 0.72]	[-1.06, 0.84]
$G_{lq}^{(1)}$	[-2.21, 2.97]	[-2.50, 2.50]	[-2.90, 6.60]	[-5.28, 5.88]	[-14.9, 14.9]	[-6.65, 9.92]
$G_{qe}$	[-2.39, 4.33]	[-3.02, 3.02]	[-3.78, 7.83]	[-4.40, 5.67]	[-174, 174]	[-7.70, 8.19]
$G_{lu}$	[-1.98, 2.53]	[-2.21, 2.21]	[-3.49, 8.10]	[-3.29, 5.74]	[-86.7, 86.7]	[-7.95, 9.81]
$G_{ld}$	[-10.1, 5.58]	[-8.83, 8.83]	[-13.1, 8.00]	[-10.57, 9.19]	[-179, 179]	[-15.0, 15.3]
$G_{eu}$	[-1.48, 1.63]	[-1.55, 1.55]	[-1.95, 2.30]	[-3.46, 6.58]	[-18.7, 18.7]	[-4.65, 8.67]
$G_{ed}$	[-7.83, 4.39]	[-5.42, 5.42]	[-12.7, 5.62]	[-11.0, 9.81]	[-46.5, 46.5]	[-13.3, 13.5]

Table 1.6 – 95% CL projected bounds for the four-fermion operator coefficients in the Warsaw basis, including a 2% uncorrelated systematic uncertainty.

a similar change, while the ones on  $W$  are less affected and are only 10% weaker. The advantage of a fully-differential analysis is however still evident also in these results.

In Tables 1.5 and 1.6 we give the bounds on the lepton-quark four-fermion operators including the uncorrelated systematic uncertainty (the corresponding correlation matrices for the fully-differential linearized fit are reported in Appendix A.3). The impact of the uncertainty is relatively large on  $\tilde{G}_{lq}^{(3)}$  and  $G_E^+$ , whose determination becomes roughly 25% weaker. The reduction in sensitivity on the other coefficients is instead milder, at most of order 10%. Similar results are found for the operators in the Warsaw basis (Table 1.6). In this basis the most affected operators are  $G_{lq}^{(3)}$ ,  $G_{eu}$  and  $G_{ed}$ , with a loss of sensitivity of order 25%, while the bounds on the other operators are quite stable. One can also see that the impact of the systematic uncertainty on the fully-differential fit and on the single-differential one is comparable.

## 1.5 Sensitivity to Minimal $Z'$ models

For a concrete assessment of the benefits of the fully-differential analysis, we consider in this section a minimal BSM scenario featuring a single additional vector boson that gauges a generic linear combination of the hypercharge  $U(1)_Y$  and  $B - L$ . The Lagrangian describing the new vector boson is

$$\mathcal{L}_{Z'} = -\frac{1}{4}F_{\mu\nu}^2 + \frac{1}{2}M^2 A^2 + A_\mu J^\mu, \quad (1.51)$$

with the current

$$J^\mu = \sum_f [g_Y Y(f) + g_{BL}(B - L)(f)] \bar{f} \gamma^\mu f + g_Y \frac{i}{2} H^\dagger \overleftrightarrow{D} H, \quad (1.52)$$

where  $f$  denote the SM fermions and  $H$  is the Higgs doublet. In the above formula  $g_Y$  and  $g_{BL}$  are free parameters, while  $Y(f)$  and  $B(f)$  and  $L(f)$  are the hypercharge, the baryon and the lepton numbers of the various fermions, respectively. This model has been studied extensively in the literature and in particular in Ref. [98] (see also Refs. [99–107]), where a first projection of LHC direct searches sensitivity was given, and compared with the indirect constraints from precision measurements (EWPT) performed at LEP and other experiments.<sup>17</sup>

When integrated out at tree-level, the massive  $Z'$  produces all the flavor-universal lepton-quark operators in Table 1.1 except  $\mathcal{O}_{lq}^{(3)}$ , with Wilson coefficients that are readily computed in terms of the three free parameters  $g_Y$ ,  $g_{BL}$  and  $M$  (see Eq. (A.7)). Clearly the Wilson coefficients are quadratic polynomials in the ratios  $g_Y/M$  and  $g_{BL}/M$ , which are therefore the only two parameter combinations that can be probed by indirect searches.<sup>18</sup> Furthermore the indirect constraints are symmetric under an overall change of sign of the couplings  $(g_Y, g_{BL}) \rightarrow (-g_Y, -g_{BL})$ . The 95% CL reach on the model at the HL-LHC is displayed in Figure 1.16 on the  $(g_Y/M, g_{BL}/M)$  plane (left panel) and on the  $(g_Y, g_{BL})$  plane for a fixed mass  $M = 7$  TeV (right panel). The bounds are obtained from the fully and single-differential analyses described in the previous section, but including in this case a 2% uncorrelated experimental uncertainty in the measurements, aiming at a more conservative result.

The advantage of the fully-differential analysis over the single-differential one is mainly in the region  $g_{BL} \simeq -g_Y$ . This region is particularly difficult to probe as it entails the

<sup>17</sup>For the model to be free of gauge anomalies, 3 right handed neutrinos with  $B - L$  coupling must be present. We take these states to be light, so that  $Z' \rightarrow \nu_R \nu_R$  is allowed. Heavy  $\nu_R$ 's would only modify the  $Z'$  width  $\Gamma$  and the direct searches, strengthening the reach on the coupling by a factor  $\sqrt{\Gamma_{\text{light}}/\Gamma_{\text{heavy}}}$ . This factor is in the interval  $[1, 1.2]$  in the entire range of couplings.

<sup>18</sup>This statement is true only at tree level. In fact, already at our level of accuracy (NLL), the RG flow induces an additional logarithmic dependence on  $M$  in our observables. However these effects are extremely small as can be appreciated in Figure 1.17, where the indirect searches contours are well approximated by straight lines.

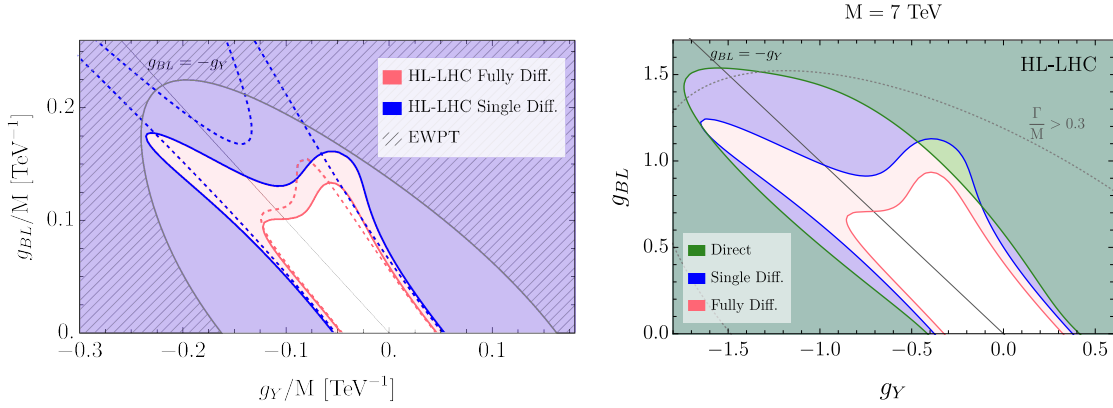


Figure 1.16 – Left panel: 95% CL exclusion reach in the  $(g_Y/M, g_{BL}/M)$  plane from EWPT (gray shaded region) [98] and projected exclusion at the HL-LHC (blue and orange shaded regions). Right panel: Comparison of direct (green shaded region) and indirect (blue and orange shaded regions) exclusions at the HL-LHC for a heavy vector of mass  $M = 7$  TeV. In both panels the blue shaded region corresponds to the fully-differential fit, while the orange shaded region is obtained with the single-differential one. In the left panel, the dashed lines correspond to the exclusion reach obtained including only the linear terms in the fit, while the solid ones correspond to the full fit taking into account also the quadratic terms.

cancellation of the  $Z'$  coupling to the right-handed electrons as well as the suppression of the couplings to the left handed quark doublets, the right-handed up-type quarks and the left-handed lepton doublets. Therefore in this region  $G_{qe}$ ,  $G_{eu}$  and  $G_{ed}$  vanish and  $G_{lq}^{(1)}$ ,  $G_{lu}$  and  $G_{ld}$  are suppressed (and  $G_{lq}^{(3)}$  is always zero). We notice in passing that the suppression of the couplings to quarks also determines a reduction of the direct production cross-section at the LHC, which makes direct searches less effective. The fully-differential analysis not only improves the sensitivity along the  $g_{BL} = -g_Y$  direction, it also mitigates the impact of the quadratic terms in the cross-section prediction. This is shown by the dashed lines in the left panel of Figure 1.16, reporting the results of the linearized fits. The single-differential linearized analysis possesses two very pronounced flat directions that correspond to directions in the  $(g_Y, g_{BL})$  plane where the  $G_E^+$  coefficient cancels. The fully-differential analysis linearized contour is instead quite close to the full fit thanks to the improved sensitivity to  $G_O^+$  at the linear level.

In the left panel of Figure 1.16 we also compare our result with existing EWPT constraints, extracted from Ref. [98]. With the fully-differential analysis, the progress of the HL-LHC is of a factor around 3 in  $g/M$  in most of the directions in the  $(g_Y/M, g_{BL}/M)$  plane, which corresponds to an improvement of one order of magnitude in the sensitivity to the Wilson coefficients that scale like  $(g/M)^2$ . Furthermore, notice that the EWPT bounds in the figure are based on actual experimental measurements whose central value, while compatible with the SM, disfavors the  $Z'$  model. This is easily verified in the direction  $g_{BL} = 0$ , where integrating out the  $Z'$  produces only the  $\mathcal{O}'_{2B}$  operator with

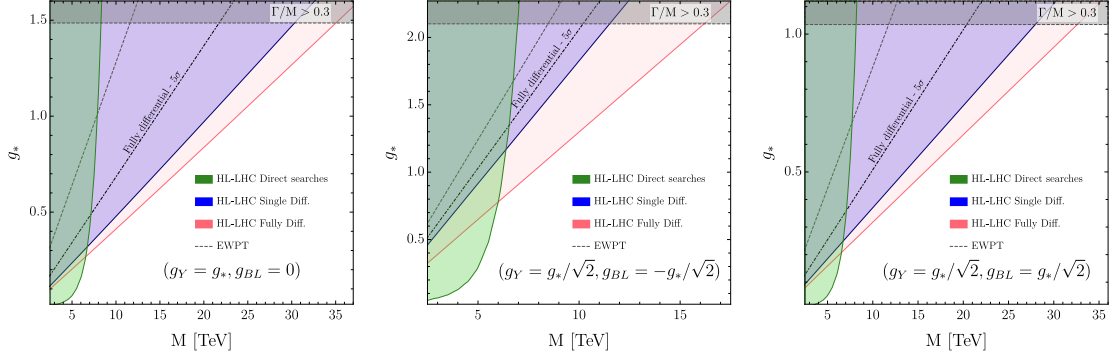


Figure 1.17 – HL-LHC 95% CL (1 d.o.f) exclusion reach in the mass/coupling plane for three different  $Z'$  benchmark models, namely  $g_{BL} = 0$ ,  $g_{BL} = -g_Y$  and  $g_{BL} = g_Y$ . The blue shaded region can be excluded through the fully-differential di-lepton DY analysis, while the orange one can be probed with the invariant-mass fit. The green shaded region corresponds to the exclusion from direct searches.

negative coefficient, that corresponds to a positive  $Y$  parameter. The central value of  $Y$  measured at LEP is instead negative (see e.g. Ref. [11]) making the EWPT exclusion on the model stronger. Our HL-LHC projections assume instead a central value at the SM point. Depending on the sign of central value that will be eventually observed the actual sensitivity to the model could be stronger or weaker than the projection.

We turn now to the comparison of our findings with the projected HL-LHC sensitivity for direct searches of the  $Z'$  particle, which are most effectively performed in the dilepton final state. The exclusion on the resonant production cross-section times branching ratio is obtained from the projections in Ref. [108], slightly improved to take into account the more recent and refined results in Ref. [109]. The  $Z'$  production cross-section is obtained by two MADGRAPH [66] simulations (at each  $Z'$  mass) with the  $Z'$  coupling only to up- or to down-type quarks, rescaled based on the analytical calculation of these couplings as a function of  $g_Y$  and  $g_{BL}$ . The branching ratio is also computed analytically. The results are reported in Figure 1.17, in the mass/coupling plane for three benchmark models ( $g_Y = g_*$ ,  $g_{BL} = 0$ ), ( $g_Y = g_*/\sqrt{2}$ ,  $g_{BL} = -g_*/\sqrt{2}$ ) and ( $g_Y = g_*/\sqrt{2}$ ,  $g_{BL} = g_*/\sqrt{2}$ ). Notice that the plot extends up to the maximal  $g_*$  coupling for which, depending on the model, the width over mass ratio  $\Gamma/M$  of the  $Z'$  is reasonably small ( $< 0.3$ ) enabling a perturbative treatment. The indirect reach from our analyses, and from EWPT, is also reported in the plots. We find a substantial improvement of the mass reach for relatively large  $g_*$ , up to around 30 TeV in the first and in the second benchmark model. Finally, in the right panel of Figure 1.16 we compare direct and indirect searches in the  $(g_Y, g_{BL})$  plane at a fixed mass  $M = 7$  TeV, slightly below the threshold of around 8 TeV after which direct searches become ineffective. The direction  $g_{BL} = -g_Y$  is difficult to probe also directly, as anticipated. The sensitivity improvement of the fully-differential analysis along this direction is significant.



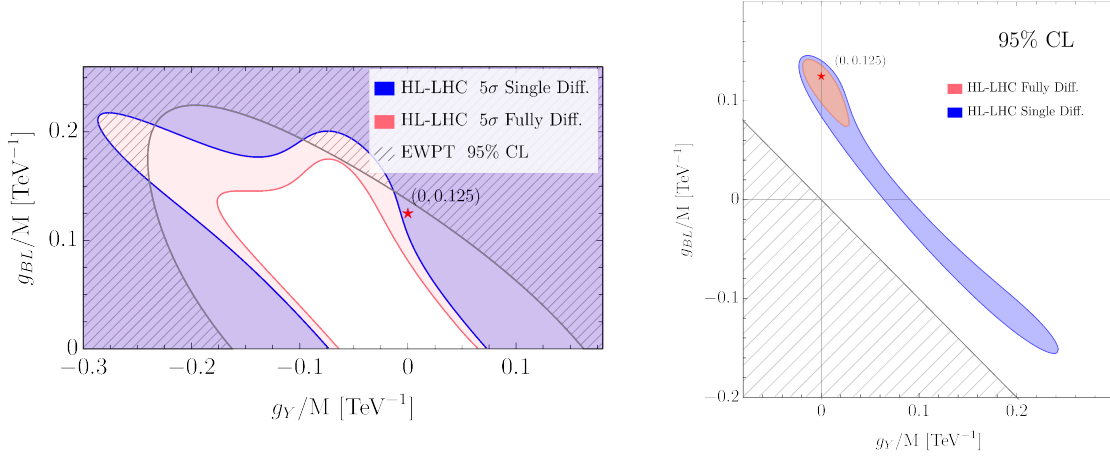


Figure 1.18 – Left panel:  $5\sigma$  discovery reach for HL-LHC and 95% CL EWPT exclusions. Right panel: 95% CL likelihood contours assuming the presence of a  $Z'$  with  $g_{BL}/M = 0.12$  TeV<sup>-1</sup> in the measurements.

### Discovery and characterization

High-energy measurements have the potential to discover the  $Z'$ . This is shown on the left panel of Figure 1.18 by comparing the HL-LHC  $5\sigma$  discovery reach with the current exclusion bound from EWPT in the  $(g_Y/M, g_{BL}/M)$  plane. For  $M$  of several TeV or more, direct searches are ineffective and high-energy measurements will provide the only evidence for the existence of the  $Z'$ . While “indirect”, i.e. not based on the detection of a resonant peak, this evidence would be a conclusive and convincing proof of the existence of new physics thanks to the peculiar behavior (growing with energy) of the observed signal and to the possibility of getting confirmations on its nature by the study of angular distributions. The fully-differential analysis would clearly play a major role in this context, on top of course of enabling the discovery itself in a larger region of the parameter space.

We illustrate the benefits of the fully-differential analysis for the characterization of a putative signal by picking up a point ( $g_{BL}/M = 0.12$  TeV<sup>-1</sup> and  $g_Y = 0$ ) which is discoverable at the HL-LHC, but close enough to the boundary of the discovery region to make characterization more difficult. We assume the presence of the corresponding signal in the data and we obtain the 95% CL likelihood contours on the right panel of Figure 1.18. A simple question related to characterization is whether we can establish that the underlying  $Z'$  couples to the  $B - L$  current, rather than for instance to the hypercharge current. The figure shows that this is possible only with the fully-differential analysis.



## 1.6 Conclusion and outlook

We have shown that the effect of the most relevant dimension-6 operators (i.e., those that grow quadratically with the energy at the interference level) can be incorporated in the high-energy Drell–Yan predictions by analytic reweighting, up to the NLO accuracy in QCD and including double and single log-enhanced EW corrections at one loop. Our method allows to compute the dependence on the new physics parameters of the cross-section in any phase-space bin without performing a scan on the parameters space. It can also generate events that include QCD and QED showering effects consistently, based on the POWHEG method.

Two operators in this set, associated with the  $W$  and  $Y$  parameters, are particularly interesting because they are generated in universal new physics scenarios including Composite Higgs. We focused in sec. 1.3 on these operators for an illustration of the methodology, and performed LHC (and HL-LHC) sensitivity projections. Our results confirm and strengthen the findings of ref. [11], where less accurate predictions and systematic uncertainties estimates were employed. Our finding for  $W$  is also in line with the very recent charged DY measurement in CMS [42]. The result in [42] is, however, slightly stronger than our and this can be traced back to the different PDF set they use. Moreover, as soon as the ATLAS measurement for the charged DY and the neutral measurements are published we plan to reconsider our analysis including the updated data.

The accuracy of our predictions for the new physics contribution to the cross-sections is found to be totally adequate, and the associated uncertainties are negligible. The relevant uncertainties are those on the SM term, and PDF are the dominant source. Theoretical uncertainties are under control provided NNLO QCD predictions are employed for the SM term. One-loop EW radiative corrections should also be included, possibly exactly rather than at the single-log order using our strategy. The impact of two-loops EW logarithms on the reach has been found to be marginal, also at the HL-LHC. Nevertheless, these terms could be included straightforwardly by analytic reweighting.

In sec. 1.4 We studied the potential of fully-differential DY measurements to probe the seven flavor-universal current-current operators listed in Table 1.1. We found (see Table 1.3) that five directions in this parameter space can be probed effectively at the linear interference level with the fully-differential analysis, while with single-differential measurements this is possible for only two directions. At the HL-LHC, the strongest single-parameter sensitivity improvement, by a factor of 3, is for the parameter  $G_O^+$  because of the reasons explained in Section 1.4.1. Improvements in the ballpark of 30% or 10% are observed for the other single-parameter bounds. The improvement is significantly more pronounced for the profiled bounds, owing to the reduction of correlations in the fully-differential fit. The augmented sensitivity at the interference level makes the fully-differential results generically more stable when the quadratic new physics terms are excluded from the predictions. This is beneficial for considerations

related to the validity of the EFT, as it lowers the scale of the measurements that drive the sensitivity and reduces the impact of removing the highest-energy cross-section bins as shown in Figure 1.15.

The observed sensitivity improvement is due to two distinct factors. The one with the strongest impact is the extended linear-level sensitivity mentioned above and explained in Section 1.4.1 in details. The second, which is also quite a strong effect, is the reduction of the impact of PDF uncertainties due to their correlations across different analysis bins. These correlations are typically different from the ones of the EFT differential cross-section predictions, making harder for the PDF nuisance parameters to mimic the signal and to reduce the sensitivity. Of course the effect is quantitatively so important because the PDF are among the dominant sources of uncertainties in our fit. Correspondingly, the benefits of the fully-differential analysis are (mildly) reduced when other sources of systematic uncertainties are assumed to be present, lowering the relative impact of PDF uncertainties in the total error budget. We have verified this fact in Section 1.4.4 by including a 2% systematic uncertainty uncorrelated across all bins, on top of the fully correlated luminosity uncertainty that is present (but has a totally negligible impact) in the results of Sections 1.4.2 and 1.4.3.

The dependence (at the 10% or 20% level) of our results on the assumed patterns of experimental systematic uncertainties outlines the need of detailed experimental projections for DY measurements. Experimental uncertainties that are fully correlated in all bins as in Sections 1.4.2 and 1.4.3 are definitely unrealistic. However assuming the uncertainties to be fully uncorrelated, as in Section 1.4.4, is equally unrealistic. We do expect correlations, especially in the fully-differential measurements, whose impact could be beneficially for the sensitivity analogously to what we have found happening for the PDF. The final HL-LHC sensitivity could thus be closer to the one in Sections 1.4.2 and 1.4.3 than to the one in Section 1.4.4. Furthermore, our findings are based on the statistically sub-optimal strategy of comparing cross-section measurements with EFT predictions, rather than comparing directly the EFT with the observed data. More sophisticated and unbinned strategies could be considered to further improve the sensitivity.

A significant improvement in the sensitivity is also found in the LHC run 3 projections (see Appendix A.4). The gain is however much milder than for the HL-LHC, mostly because the number of expected events is too low to efficiently reconstruct the full angular distributions at high energy (i.e. to populate enough all the bins required for a fully-differential analysis).

The sensitivity improvement of fully-differential measurements has a direct impact on concrete putative new physics scenarios, as we discussed in Section 1.5 for a simple minimal  $Z'$  model. The point is that in models where the charged current  $\mathcal{O}_{lq}^{(3)}$  operator is absent, the single-differential DY analysis is mostly sensitive to a single EFT parameters

combination:  $G_E^+$ . In the new physics model it will be generically possible to suppress  $G_E^+$  without particular fine-tuning, making the single-differential analysis loose sensitivity in a large region of the parameter space as in Figure 1.16. The fully-differential analysis will boost the sensitivity in that region.

The results of Section 1.5 also outline the effectiveness of high- $p_T$  probes on a well-established new physics benchmark that has been investigated since the beginning of the LHC program. High- $p_T$  probes by high energy DY measurements extend (see Figure 1.17) the projected HL-LHC exclusions well beyond the reach of direct searches in a large region of the parameter space, with sensitivity to masses from 10 to 30 TeV. Discovery is also possible up to around 20 TeV. In the event of a discovery, fully-differential measurements will play a crucial role in the characterization of the observed signal as illustrated in Figure 1.18.



## 2 Precision physics from Very High Energy Leptons collisions

The perspective of a future muon collider with high energy and high luminosity [110–113], has triggered a growing interest in the physics potential of lepton colliders with a center of mass energy of 10 TeV or more [112–153]. Such a Very High Energy Lepton Collider (VHEL) could greatly advance the post-LHC knowledge of fundamental physics [110] by directly searching for new heavy particles (see e.g. [114–117]), and by precise measurements of EW scale processes taking advantages from the high luminosity of virtual vector bosons pairs (see e.g. [117–119]).

Moreover, a third strategy of investigation can be carried at VHEL [3, 110, 118], exploiting hard processes at energies comparable with the collider energy  $E_{\text{cm}} \sim 10$  TeV. These searches aim at indirect effects of heavy new particles enhanced by  $E_{\text{cm}}$ , which represent extremely sensitive probes of new physics. With the target integrated luminosity of  $10 \text{ ab}^{-1}$ ,  $2 \rightarrow 2$  scattering processes at  $E_{\text{cm}} = 10$  TeV can be generically measured within percent or few-percent precision, opening the possibility to test new physics up to a scale  $\Lambda \sim 100$  TeV.

In this chapter we focus on this last strategy, studying the potential of lepton collisions with about 10 TeV center of mass energy to probe Electroweak, Higgs and Top short-distance physics. Such precise measurements, so far from the EW scale, are particularly challenging due to the phenomenon of Electroweak radiation. The reason is two-fold: first of all sufficiently accurate theoretical predictions require the resummed inclusion of radiation effects. Secondly, short-distance physics does influence the emission of Electroweak radiation, implying that the radiation pattern can become an important signal of new short-distance physical laws.

In the following, we illustrate these aspects by studying di-fermion and di-boson production at VHEL as probes of Effective Field Theory contact interactions. Furthermore, we will show that the complementary measurements of processes with or without the inclusion of soft massive Electroweak bosons enhances the sensitivity to the new interactions.

## 2.1 Learning from radiation at VHEL

One of the strengths of a VHEL is represented by the opportunity of precise indirect searches of energy growing new physics effects. Through this kind of searches we can fully exploit the large amount of energy provided by the collider and thanks to a clean lepton environment we can target a 1% precision in many 2-to-2 processes. In this way, with  $E_{\text{cm}} \sim 10$  TeV we would have access, for the first time, to the unexplored  $\Lambda \sim 100$  TeV energy scale.

The logic of these searches is strictly analogous the so-called “high-energy” probes at LHC, described in Chapter 1. Low energy interactions due to heavy new physics can be parametrized according to the SM-EFT paradigm and can give rise to growing-with-energy effects. Certain operators can produce deviations from the SM scaling like  $E_{\text{cm}}^2/\Lambda^2$ , in 2-to-2 processes with enough statistics to reach the percent precision we can aim at touching the aforementioned 100 TeV new physics scale. The VHEL sensitivity to these probes vastly and generically exceeds the potential of any other future project that is currently under consideration. In particular it exceeds the sensitivity of precision measurements of EW-scale processes at future Higgs factories, where new physics at  $\Lambda \sim 100$  TeV produces effects at the unobservable level of one part per million. It also exceeds the potential sensitivity of a 100 TeV proton collider, because the effective luminosity for partonic collisions above 10 TeV is significantly lower than that of the VHEL. The possibility of probing new physics at the 100 TeV scale, and in particular of probing new physics that is either flavor-universal or endowed with a flavor protection mechanism, is thus a unique feature of the VHEL that deserves an extensive investigation.<sup>1</sup>

The above mentioned high-energy strategy exploits simple  $2 \rightarrow 2$  processes with extremely low or negligible background, whose target accuracy is statistically limited to 1%. At a superficial look, it might thus seem that its implementation will not pose any specific challenge, neither concerning the feasibility of the measurements, nor as concerns the theoretical predictions that are needed for their interpretation. However the situation is slightly more complex, both experimentally and theoretically, owing to the phenomenon of EW radiation [154–174], which becomes prominent at 10 TeV or above. This happens because of the existence of a large separation between the hard scale  $E$  of the process and the vector boson mass scale  $m_W$ , which acts as an IR cutoff. As the hard scale is increased, large logarithms  $\log E^2/m_W^2$  (squared) enhance both virtual corrections and real emissions, up to the point where fixed-order perturbation theory becomes insufficient and resummation is needed.

EW radiation obviously displays some similarities with QCD radiation, but also remarkable differences. First, EW scattering processes violate the KLN theorem assumptions [175, 176] because the initial state particles are not EW singlets. Therefore no

---

<sup>1</sup>Hard processes are also useful to investigate flavor non-universal effects, as we will see in Section 2.4.3 for Top Compositeness. See also Ref. [148] for a study of new physics potentially responsible for the  $g - 2$  muon anomaly.

cancellation takes place between virtual and real contributions, not even in “fully-inclusive” cross-sections [154, 155]. Moreover the observables that are fully inclusive in the sense of Ref. [154] are insufficient to characterize new physics because they require summing over the “color” of the hard final-state particles. In the EW context, color sum means, for instance, including transversely-polarized  $W$  and  $Z$  bosons and photons (or, longitudinal  $W$ ,  $Z$  and Higgs) in the same observable, while we need to keep them separate for a comprehensive exploration of new physics. Unlike QCD (and QED), EW radiation effects cannot be eliminated or systematically mitigated with a judicious choice of the observables. They unavoidably play an crucial role in the predictions and it is necessary to assess their importance at VHEL as we will explain in detail later on. In particular in sec. 2.3 and sec. 2.4 we will assess the impact of EW radiation respectively on the theoretical prediction and on the sensitivity to new physics.

The second peculiarity of EW radiation is that the IR cutoff scale is physical, and the theory is weakly-coupled at the IR scale. It should thus be possible to characterize the radiation fully by first-principle suitably resummed perturbative calculations. Unlike QCD and QED, one can consider observables with an arbitrary degree of radiation exclusiveness, among which “exclusive” scattering cross-sections with a fixed number (2, in  $2 \rightarrow 2$  processes) of hard partons in the final state and no extra massive vector bosons.<sup>2</sup> Fully-inclusive cross-sections can be also considered, however they are not sufficiently informative on new physics as previously mentioned.

Several approaches have been considered in the literature for the resummation of the effects of EW radiation. Double logarithm (DL) contributions, of the form  $(\alpha \log^2 E^2/m_W^2)^n$  with arbitrary  $n$ , have been resummed in fully-inclusive and exclusive cross-sections, using respectively Asymptotic Dynamics [154, 155] and the so-called InfraRed Evolution Equation (IREE) [156, 157]. In Soft-Collinear Effective Theory (SCET) the expansion is already organized in exponential form. In that case the resummation of leading logarithms (LL)<sup>3</sup> as well as its extension to next-to-leading (NLL) logarithm [163] has been studied. The study of EW parton distribution or fragmentation functions [166–170] is obviously connected, but not directly relevant for very high energy processes, where the main role is played by the emission of EW radiation that is both collinear and soft. Notice however that in some framework [166–170] soft effects are partially or completely included in parton distributions and fragmentation functions.

In our analysis, in sec.s 2.3, 2.4, we employ “semi-inclusive” final states, consisting of 2 hard partons with fixed EW color and flavor, carrying a large fraction of the total available energy  $E_{\text{cm}}$  and accompanied by an arbitrary number of massive vectors, photons and other light particles.<sup>4</sup>

<sup>2</sup>In order to cope with QED and QCD radiation, the observable must still be inclusive over the emission of photons and other light particles. The cross-section we define as “exclusive” coincides with the “semi-inclusive” cross-section of Ref. [156]. Correspondingly, the “semi-inclusive” cross-section we will readily introduce was not considered in Ref. [156]. See Section 2.2.2 for details.

<sup>3</sup>These include but do not coincide with the pure DL, as explained, for instance, in Ref. [163].

<sup>4</sup>A similar observable is discussed in [177] to show the impact of weak gauge boson emission at LHC.

We restrict the accuracy of our predictions for semi-inclusive observables at the double logarithm (DL) accuracy. The latter are obtained by extending the IR Evolution Equation (IREE) treatment of EW radiation developed in Ref. [156], the explicit derivation is presented in sec. 2.2. Similarly, we employ the IREE to compute the more standard exclusive cross-sections. Single-logarithmic terms turn out to be relevant, and they are included at fixed one-loop order in the exclusive cross-sections using the results of Ref. [178].

Finally we must comment on the remarkable interplay between EW radiation and short-distance physics that has no analog in QED and QCD [118]. Based on a simplistic fixed order intuition, this interplay can be exemplified by noticing that the emission of a soft  $W$  from one initial lepton changes the total charge of the initial state of the hard  $2 \rightarrow 2$  scattering process. By allowing for the charged  $W$  emission one thus obtains a scattering cross-section that is sensitive to charged current new physics interactions, while the exclusive process where no radiation is allowed is only sensitive to neutral currents.<sup>5</sup> The combined measurement of the two types of cross-section thus enables a more effective and complete exploration of new physics. In reality the situation is slightly more complex, because the neutral and the charged current hard amplitudes both contribute to the resummed expression of the neutral exclusive and of the charged and neutral semi-inclusive cross-sections. However, since they appear in different combinations in the different cross-sections, the conclusion is unchanged.

At a more quantitative level, we will see that the VHEL energy sits in an interestingly “intermediate” regime for EW radiation. The energy is on one hand large enough for the radiation effects to be important and require resummation. Accurate resummation techniques, more accurate than the one considered in [3], will thus be needed to fully exploit the potential of the machine. On the other hand, the energy is not yet in the asymptotic regime where the Sudakov exponentials entail a strong suppression of the non-emission probability. Therefore in this regime the exclusive cross-sections are still large, and comparable with the semi-inclusive (and fully-inclusive) ones. Observables with a different degree of radiation inclusiveness can thus be measured with comparable statistical accuracy and combined, potentially boosting, as previously explained, the indirect sensitivity to heavy new physics.

The rest of the chapter is organized as follows. We start, in Section 2.2, by reviewing the general idea beyond the method of the asymptotic dynamics [179] to address the problem of IR radiation. We report explicit results only for the case of abelian gauge theories and we comment on the leading effects in the more general non-abelian setup. The main goal of that section is to develop some intuition before the discussion on the more pragmatic

---

The final state they consider is somehow intermediate between the “fully-inclusive” of [154] and the “semi-inclusive” we study in [3]

<sup>5</sup>More precisely, the charged and neutral current process depend on different linear combinations of the Wilson coefficients of the operators parametrizing new physics.



approach to the DL resummation based on the IREE. We discuss the latter in sec. 2.2.2. In section 2.3 we present the calculation of the exclusive and semi-inclusive di-fermion and di-boson production processes, to be employed in Section 2.4 to estimate the sensitivity to dimension-6 EFT current-current contact interactions of muon colliders with a center of mass energy ranging from 3 to 30 TeV. The estimates include experimental reconstruction efficiencies at the level expected for the CLIC detector at 3 TeV, which we extract from Ref. [180]. Our results do not depend on the nature of the colliding leptons. In particular they do not include the effect of Beamstrahlung, which is expectedly small at muon colliders but large at  $e^+e^-$  colliders of the same energy. Up to this caveat, our results thus also apply to hypothetical linear  $e^+e^-$  collider based on plasma wake field acceleration [181].<sup>6</sup> In Section 2.4.3 we then study the impact of the EFT sensitivity projections on concrete scenarios for Beyond-the-SM (BSM) physics such as Higgs and Top Compositeness and a minimal  $Z'$  extension of the EW sector. A conclusions to the chapter and an outlook on future work are reported in Section 2.5.

## 2.2 All-orders IR Double Logs

Infrared effects play a ubiquitous and unavoidable role in our description of nature. How to deal with them in QFT has been widely investigated in the past and it represents nowadays the main focus of much ongoing research, from their theoretical understanding to their phenomenological applications.

An intuition can be built by simple arguments based on scale separation. At energy  $E$  the exchange of soft quanta, of characteristic scale  $\delta \ll E$ , becomes a probable and messy phenomenon. In general, the larger the scale separation the more important are the effects, up to a point where they cannot be ignored. Moreover, these effects are governed by the IR dynamics and therefore we expect them to be in some sense universal, i.e. independent of the process/theory under consideration.

The approach to the IR problem, that better clarifies this space-time picture, is the so-called method of the Asymptotic Dynamics [179]. This method “solved” the IR catastrophe in QED and was further generalized to systematically improve perturbation theory in non-abelian gauge theories [182–184] and gravity [185]. In sec. 2.2.1 we present the main idea and the calculation of the leading DL effects in QED. We furthermore give a qualitative description of the generalization to the non-abelian case, pointing out the peculiarities of high-energy EW processes.

While conceptually clean, the method of the asymptotic dynamics becomes extremely complicated at the practical level and, moreover, it is not clear whether or not it can address collinear effects. Therefore, in concrete applications, it leaves the stage to more pragmatic diagrammatic approaches [186–188] (see also [189] for a recent review) and to

---

<sup>6</sup>Notice that Beamstrahlung potentially entails a strong depletion of the high-energy luminosity peak, which is the part of the luminosity spectrum that is relevant for the high-energy probes.

more modern techniques based on Effective Field Theory [190–197].

Targeting our concrete goal of sensible theoretical predictions for high energy EW processes at VHEL, in [3] we based our prediction on the methodology of the IREE [156]. In sec. 2.2.2, we review the basic results for exclusive cross-sections and we show our generalization to address semi-inclusive processes.

### 2.2.1 The method of the asymptotic dynamics

The main idea of the method of the asymptotic dynamics [179] is to separate the “strong” IR dynamics, characterized by large IR logarithms, from the “weak” hard one, that can be safely computed order by order in perturbation theory. In concrete, we split the interaction Hamiltonian in two part

$$H_I(t) = H_I^s(t) + H_I^h(t), \quad (2.1)$$

where the soft and hard Hamiltonians,  $H_I^s(t)$  and  $H_I^h(t)$ , describe interactions characterized respectively by exchanges of modes of energies  $\delta < \omega < \Delta$  and  $\Delta < \omega$ . The parameter  $\delta$  is an IR cut-off (we comment on it in a second), while  $\Delta$  is an extra scale we include to separate soft and hard modes. More precisely, given the interaction Hamiltonian

$$H_I(t) \equiv \int_{\delta}^{+\infty} d\nu \left( h_+(\nu) e^{-i\nu t} + h_-(\nu) e^{i\nu t} \right) = H_I^s(t) + H_I^h(t), \quad (2.2)$$

we define the soft and hard Hamiltonians as

$$H_I^s(t) = \int_{\delta}^{\Delta} d\nu \sum_{\sigma=\pm} h_{\sigma} e^{-i\sigma\nu t}, \quad H_I^h(t) = \int_{\Delta}^{+\infty} d\nu \sum_{\sigma=\pm} h_{\sigma} e^{-i\sigma\nu t}, \quad (2.3)$$

where all the previous operators are meant in the interaction picture. The idea, now, is to convert our problem into a two potential problem.<sup>7</sup> In parallel to the Hamiltonian of eq. (2.1) we decompose the Hilbert space as tensor product of the soft and hard Hilbert spaces  $\mathcal{H} = \mathcal{H}_h \otimes \mathcal{H}_s$  and we write our  $S$ -matrix as

$$S = \Omega_{-}^{\dagger} S_h \Omega_{+}, \quad (2.4)$$

where  $\Omega_{I,F}$  are the soft Møller operators, addressing the soft dynamics, and  $S_h$  is the hard  $S$ -matrix responsible for the hard interactions. The operators  $\Omega_{I,F}$  are formally defined as

$$\Omega_{\pm} = T \exp \left( -i \int_{\mp\infty}^0 dt H_I^s(t) \right), \quad (2.5)$$

---

<sup>7</sup>This is analogous to the distorted wave Born approximation used to describe  $\beta$  decays in Quantum Mechanics [198].

with  $T$  the time ordering. Notice that the term  $S_h$  in eq. (2.4) is not just build out of the Hard interactions but also involves the soft ones. However it can be shown to be free of IR divergences (see for instance [199]) when acting on  $\mathcal{H}_h$ .<sup>8</sup>

The arguments so far are just based on scale separation and apply to QED [179] and to some extent to non abelian gauge theories [182, 183] and gravity [185]. Notice that in all our discussion we are considering weakly interacting particles, therefore in the case of QCD the IR cut-off  $\delta$  has to be larger than the scale where QCD becomes strongly coupled. Moreover, we stress that while in QED and QCD this cut-off is fictitious and any sensible IR-free observable will not depend on it, for EW interactions  $\lambda$  is completely physical and it is provided by the masses of the gauge bosons.

Even if eq. (2.5) is general, only in QED one can find an explicit expression for the Møller operators, while for QCD (and gravity as well) this is not possible. In practice, a solution [184] is to work order by order in a sort of improved perturbation theory (Leading Log, Next-to-Leading-Log, etc...) until reaching the needed accuracy. On a practical level this become exponentially complicated and since this approach is limited to soft interactions but not collinear, other techniques seems more promising. In the following we will focus only on the case of QED commenting, when relevant, to the case of non-abelian gauge theories. Furthermore, in order to make the comparison to the EW case more clear, we assume the cut-off  $\lambda$  to be a physical mass term for our photon.

### Abelian gauge theory

The main simplification in QED arises by the basic form of  $H_I(t)$ , that can be easily approximated in case of low energy transfer  $\nu$ . The interaction Hamiltonian is just

$$H_I(t) = e \int d^3x \bar{\psi} A \psi(x), \quad (2.6)$$

where the field can be expanded via the usual mode decomposition for  $\psi(x)$ ,  $\bar{\psi}(x)$  and  $A(x)$

$$\begin{aligned} \psi(x) &= \sum_{\sigma=\pm} \int \frac{d^3\mathbf{k}}{(2\pi)^3 2\omega_{\mathbf{k}}} \left( c_{\sigma}(\mathbf{k}) u_{\sigma}(\mathbf{k}) e^{-ikx} + d_{\sigma}^{\dagger}(\mathbf{k}) v_{\sigma}(\mathbf{k}) e^{ikx} \right)_{\omega_{\mathbf{k}}=\sqrt{\mathbf{k}^2}}, \\ A^{\mu}(x) &= \int \frac{d^3\mathbf{q}}{2\omega_{\mathbf{q}}} \left( A^{\mu}(\mathbf{q}) e^{-iqx} + A^{\dagger\mu}(\mathbf{q}) e^{iqx} \right)_{\omega_{\mathbf{q}}=\sqrt{\mathbf{q}^2}}, \quad A^{\mu}(\mathbf{q}) = \sum_{\sigma=\pm,0} \varepsilon_{\sigma}^{\mu} a_{\sigma}(\mathbf{q}). \end{aligned} \quad (2.7)$$

In the previous equations  $u_{\sigma}$ ,  $v_{\sigma}$  and  $\varepsilon_{\sigma}^{\mu}$  are respectively the massive spin 1/2 and 1 wave functions of helicity  $\sigma$  (for our discussion on soft effects the basis for the wave functions is completely irrelevant) and  $c_{\sigma}$ ,  $d_{\sigma}$  and  $a_{\sigma}$  are the standard annihilation operators. The soft Hamiltonian  $H_I^s(t)$  can be found expanding  $h_{\pm}(\nu)$ , defined in eq.s (2.2, 2.6), for small  $\nu$ . Notice that the conditions for  $\nu$  to be small, in QED, are basically two. First of all

<sup>8</sup>A short discussion can be found on [200].

## Chapter 2. Precision physics from Very High Energy Leptons collisions

we need one incoming particle and an outgoing pair or viceversa. If  $\mathbf{q}$  and  $\mathbf{k}$  are the momenta of the pair we have

$$\nu = \omega_{\mathbf{k}} + \omega_{\mathbf{q}} - \omega_{\mathbf{k}+\mathbf{q}} \simeq \frac{\omega_{\mathbf{k}}\omega_{\mathbf{q}} - \mathbf{k} \cdot \mathbf{q}}{\omega_{\mathbf{k}} + \omega_{\mathbf{q}}}, \quad (2.8)$$

which is small either in the collinear region  $\mathbf{q} \parallel \mathbf{k}$  or if one of the two momenta is soft, for instance  $\omega_{\mathbf{q}} \ll \omega_{\mathbf{k}}$ . Moreover, notice that, in the previous approximation we neglected the masses of the particles, assumed to be small compared to the energy of the parton. A large photon mass would cut-off both the previous regimes and a large mass for the fermion, instead, would just avoid collinear enhancements.

Focusing only in the soft region, we can substitute eq. (2.7) into eq. (2.6) and inverting eq. (2.2) for  $h_{\pm}(\nu)$  it is straightforward to find

$$\begin{aligned} h_+(\nu) &\simeq_{\nu \ll E} e \int \frac{d^3 p}{2\omega_{\mathbf{p}}(2\pi)^3} \frac{d^3 q}{2\omega_{\mathbf{q}}(2\pi)^3} \hat{p}_{\mu} A^{\mu}(\mathbf{q}) \rho(\mathbf{p}) \delta(\hat{p}^{\mu} q_{\mu} - \nu), \\ h_-(\nu) &\simeq_{\nu \ll E} e \int \frac{d^3 p}{2\omega_{\mathbf{p}}(2\pi)^3} \frac{d^3 q}{2\omega_{\mathbf{q}}(2\pi)^3} \hat{p}_{\mu} A^{\dagger \mu}(\mathbf{q}) \rho(\mathbf{p}) \delta(\hat{p}^{\mu} q_{\mu} - \nu), \end{aligned} \quad (2.9)$$

where

$$\hat{p}^{\mu} \equiv \frac{p^{\mu}}{\omega_{\mathbf{p}}}, \quad \rho(\mathbf{p}) \equiv \sum_{\sigma} (c_{\sigma}^{\dagger}(\mathbf{p}) c_{\sigma}(\mathbf{p}) - d_{\sigma}^{\dagger}(\mathbf{p}) d_{\sigma}(\mathbf{p})). \quad (2.10)$$

It is worth to comment on the physics interpretation of the interaction described by eq. (2.9). The action of  $h_{\pm}(t)$  is to excite soft photon quanta (in  $\mathcal{H}_s$ ) out of an energetically moving fermion. Moreover  $h_{\pm}(t)$  act trivially on the hard Hilbert space  $\mathcal{H}_h$ , being the soft photon not enough energetic to affect the motion of the emitting particle. Eq. (2.10) is the so-called Eikonal approximation of the interaction Hamiltonian. Moreover notice that the configuration where the photon is hard and one fermion is soft is suppressed.

We now need to find an explicit form for the soft Møller operators  $\Omega_{\pm}$  in eq. (2.5). A simple strategy is to solve the soft time evolution, defined by

$$i \frac{\partial}{\partial t} \mathcal{U}_s(t, -\infty) = H_I^s(t) \mathcal{U}_s(t, -\infty), \quad (2.11)$$

and extract the Møller operators as  $\Omega_{\pm} = \mathcal{U}_s(0, \mp\infty)$ . This is the point of our discussion the differences of abelian and non-abelian theories become crucial. In general, eq. (2.11) admits a solution in terms of  $H_I^s(t)$  and its commutators. In QED  $H_I^s(t)$  is linear function of the operators  $A^{\mu}(q)$ , acting on the soft Hilbert space  $\mathcal{H}_s$ . Therefore  $\mathcal{U}_s(t)$  can be built out of  $H_s(t)$  and of  $[H_s(t), H_s(t')]$  only. On the contrary, in the non-abelian case, the soft Hamiltonian also include self-interactions among soft gluons generating an infinite algebra of commutator for  $H_s(t)$ . The consequence is that eq. (2.11) cannot be solved analytically and has to be approximated.

A straightforward way to solve eq. (2.11), that is also generalizable to the non-abelian case, is through the so-called energy transfer equation [184]. The idea is just to write  $\mathcal{U}_s(t, \pm\infty)$  as

$$\mathcal{U}_s(t, \pm\infty) = \sum_n^\infty \mathcal{U}_s^{(n)}(t, \pm\infty), \quad (2.12)$$

with

$$\mathcal{U}_s^{(n)}(t, \mp\infty) = \sum_{\sigma_i=\pm} \int d\nu_1 \cdots d\nu_n \frac{e^{-i(\sigma_n\nu_n+\dots+\sigma_1\nu_1)t} h_{\sigma_n}(\nu_n) \cdots h_{\sigma_1}(\nu_1)}{(\sigma_n\nu_n + \dots + \sigma_1\nu_1 \pm i\epsilon) \cdots (\sigma_1\nu_1 \pm i\epsilon)}. \quad (2.13)$$

The leading behavior of the previous integral comes from the region where the integration variables  $\nu_i$  are strongly ordered  $\delta \ll \nu_1 \dots \ll \nu_n$ . In this region we have<sup>9</sup>

$$\frac{1}{(\sigma_n\nu_n + \dots + \sigma_1\nu_1 \pm i\epsilon) \cdots (\sigma_1\nu_1 \pm i\epsilon)} \simeq \prod_{i=1}^n \frac{1}{\sigma_i\nu_i \pm i\epsilon} \quad (2.14)$$

and the Møller operators simply become

$$\Omega_\pm \simeq P_\nu \exp \left( \sum_{\sigma=\pm} \int_\delta^\Delta \frac{d\nu}{\sigma\nu \pm i\epsilon} h_\sigma(\nu) \right), \quad (2.15)$$

where  $\nu$  is the energy ordering operator. Notice that the previous equation is only valid to obtain the leading behavior of the soft effects and it is not exact. As mentioned before the full expression for  $\Omega_\pm$  can be found in QED, in terms of  $H_s(t)$  and  $[H_s(t), H_s(t')]$ . If we forget about the term proportional to  $[H_s(t), H_s(t')]$ , responsible for the so-called Coulomb phase [184], then we are free to commute the  $h_\sigma(\nu)$  in eq. (2.13) and then we can get eq. (2.15) even integrating outside the strong ordering region. Focusing on the leading contribution we get

$$\Omega_\pm \simeq \exp \left( -i \int_\mp^0 dt H_s^I(t) \right), \quad (2.16)$$

We insisted in this quite long derivation in order to show the nature of this approximation. Subleading corrections can be found integrating in the regions where two  $\nu_i$  are of the same order and so on and so forth.

---

<sup>9</sup>To derive this expression a useful identity is

$$\sum_{perm} \frac{1}{(A_1)(A_1 + A_2) \cdots (A_1 + A_2 + \dots + A_N)} = \frac{1}{A_1 \dots A_N},$$

where the sum is extended to all the permutation of the labels  $1, 2, \dots, N$ .

## Chapter 2. Precision physics from Very High Energy Leptons collisions

We finally notice that eq. (2.16) can be rewritten as

$$\Omega_{\pm} = P_{\omega_{\mathbf{q}}} \exp \left( ie \int \frac{d^3 k}{2\omega_{\mathbf{k}}(2\pi)^3} \int_{\delta < \omega_{\mathbf{q}} < \Delta} \frac{d^3 q}{2\omega_{\mathbf{q}}(2\pi)^3} \rho(\mathbf{k}) \frac{k^{\mu} \Pi_{\mu}(\mathbf{q})}{k^{\mu} q_{\mu}} \right), \quad (2.17)$$

where  $\Pi^{\mu} \equiv -i(A_{\mu} - A_{\mu}^{\dagger})$  and again  $P_{\omega}$  is the ordering operator for the energy of photon.

We can now comment on the various properties of the Møller operators. First of all they are unitary on  $\mathcal{H}_s$  and they act diagonally on  $\mathcal{H}_h$  i.e. schematically

$${}_h \langle \psi | \Omega_{\pm} | \psi' \rangle_h \propto \delta_{\psi \psi'}, \quad \forall | \psi \rangle_h | \psi' \rangle_h \in \mathcal{H}_h. \quad (2.18)$$

Notice that the previous property is valid only in QED, since in non abelian theories  $\Omega_{\pm}$  act non trivially on the color indices of the hard states. Secondly, the action of  $\Omega_{\pm}$  factorize leg by leg in multiparticle states, more precisely

$${}_h \langle p_1; \dots; p_n | \Omega_{\pm} | p_1; \dots; p_n \rangle_h = U_{p_1}^{\pm} \dots U_{p_n}^{\pm} \quad (2.19)$$

for each  $n$ -particle state  $|p_1; \dots; p_n\rangle_h$  and where

$$U_p^{\pm} \equiv \mathcal{N} {}_h \langle p | \Omega_{\pm} | p \rangle_h, \quad (2.20)$$

with  $\mathcal{N}$  a normalization constant. Moreover, we stress that the unitary of  $\Omega_{\pm}$ , together with eq. (2.4) and the fact that  $S_h$  is IR finite trivially implies the Bloch-Nordsieck theorem.

We can now use the results found so far to compute, at DL, the two simple observables that we will need for our discussion on the radiative corrections at VHEL.

In particular, we consider a 2-by-2 process  $p_1(k_1) p_2(k_2) \rightarrow p_3(k_3) p_4(k_4)$  among massless ( $k_i^2 = 0$ ) charged particles. We are interested the regime where all the kinematic invariant build out of two different  $k_i$  are large  $|2k_i \cdot k_j| \sim E^2 \gg \delta^2$ , where we remind that in this discussion  $\delta$  is the mass of our photon.

We start with the exclusive process, where no extra particles are allowed on top of the hard state. According to eq. (2.4) the S-matrix element reads

$$({}_s \langle 0 | \otimes {}_h \langle k_3; k_4 |) S(|k_1; k_2\rangle_h \otimes |0\rangle_s) = S_h(k_1 k_2 \rightarrow k_3 k_4) {}_s \langle 0 | (U_{k_3}^{-})^{\dagger} (U_{k_4}^{-})^{\dagger} U_{k_1}^{+} U_{k_2}^{+} |0\rangle_s, \quad (2.21)$$

where with  $|0\rangle_s$  we denote the vacuum on the soft Hilber space. The previous equation show that the contributions from the soft dynamics factorizes with respect to the hard ones in  $S_h(k_1 k_2 \rightarrow k_3 k_4)$  that, at our level of approximation is simply the TL process we compute in standard perturbation theory. The soft factor can be computed according

to the previous results, namely we have

$${}_s\langle 0 | (U_{k_1}^-)^\dagger (U_{k_2}^-)^\dagger U_{k_3}^+ U_{k_4}^+ | 0 \rangle_s = {}_s\langle 0 | \exp \left( \int_{\delta < \omega_{\mathbf{q}} < \Delta} \frac{d^3 q}{(2\omega_{\mathbf{q}})(2\pi)^3} J^\mu(\mathbf{q}) (A_\mu(q) - A_\mu^\dagger(q)) \right) | 0 \rangle_s, \quad (2.22)$$

where

$$J^\mu(\mathbf{q}) \equiv \sum_i e_i \eta_i \frac{k_i^\mu}{k \cdot q}, \quad (2.23)$$

with  $\eta_i = +(-)$  for ingoing (outgoing) particles. Moreover in the previous equation we set  $\Delta = E$ . Through the usual commutation relation among  $A(q)$  and  $A^\dagger(q)$  and noticing that  $J^\mu(\mathbf{q})q_\mu = 0$  just by charge conservation ( $\sum_i e_i \eta_i = 0$ ), we get

$$\begin{aligned} {}_s\langle 0 | (U_{k_1}^-)^\dagger (U_{k_2}^-)^\dagger U_{k_3}^+ U_{k_4}^+ | 0 \rangle_s &= \exp \left( \frac{1}{2} \int_{\delta < \omega_{\mathbf{q}} < E} \frac{d^3 q}{(2\omega_{\mathbf{q}})(2\pi)^3} J^\mu(\mathbf{q}) J_\mu(\mathbf{q}) \right) \\ &= \exp \left( - \frac{\sum_i e_i^2}{32\pi^2} \log^2 \frac{E^2}{\delta^2} \right), \end{aligned} \quad (2.24)$$

where we are taking  $\Delta = E$ . The algebra of the last step is not completely trivial and needs some explanation. However, since we derive the same result in the non-abelian case in sec. 2.2.2 we skip the details.

Eq. (2.24) show that the exclusive process is suppressed by the well known negative DL Sudakov factor. Moreover in the limit of zero photon mass  $\delta$  or infinite energy  $E$ , this factor kills the process, meaning that there is zero probability of emitting no photons.

The second process we consider is the fully-inclusive one, where on top of the hard states we include in our measurement any possible radiation. In practice we consider the cross-section differential on the hard kinematic and integrated over soft final-state radiation

$$d\sigma_{f.i.} \propto \sum_{\psi \in \mathcal{H}_s} |({}_s\langle \psi | \otimes {}_h\langle k_3; k_4 |) S(|k_1; k_2\rangle_h \otimes |0\rangle_s)|^2, \quad (2.25)$$

where with  $\sum_{\psi \in \mathcal{H}_s}$  we indicate that we are integrating over the radiation in  $\mathcal{H}_s$ . Using again eq. (2.4) we simply have

$$d\sigma_{f.i.} \propto |S_h(k_1 k_2 \rightarrow k_3 k_4)|^2, \quad (2.26)$$

where we just exploited the unitarity of the soft Møller operators  $\Omega_\pm$ . As expected by the Bloch-Nordsieck the IR enhancements (in general divergences) cancels after integrating over final state radiation and our inclusive cross-section is just the tree-level one.

### Non-abelian gauge theory

In non-abelian gauge theories, as we already stressed before, eq. (2.5) cannot be solved analytically and only an approximate expression for  $\Omega_{\pm}$  can be found. The main reason is due to the self-interactions among gluons that appear in the soft Hamiltonian. While in the abelian case  $H_s^I(t)$  is linear on  $A_{\mu}^{(\dagger)}$ , this is not the case in a non-abelian framework, since soft-gluons can interact among themselves. A way out to this issue consists in solving eq.s (2.12,2.13) perturbatively.

This procedure was also used to compute observables at DL for high-energy EW interactions and to show the non cancellation of the Sudakov DL suppressions in inclusive observables in [154, 155], as known as Bloch-Nordsieck theorem violation.

Starting from eq. (2.4) we now sketch a qualitative discussion.

Independently from the explicit form of  $H_s^I(t)$  eq. (2.5) can be formally solved according to eq. (2.11) and eq.s (2.12,2.13). Moreover the leading behavior of the radiation effects in non-abelian gauge theories is completely analogous to the QED case. Eq. (2.13) can be approximated keeping only the strong ordering region in the integration variables are we are back again to eq. (2.15). The main difference is that now the Møller operators act non-trivially on the color indices of the hard states, therefore eq.s (2.18,2.27) get modified. More precisely, it can be shown that at DL we still have a factorization similar to eq. (2.27) but now the  $U^{\pm}$  operators, acting on  $\mathcal{H}_s$  carry a non trivial color structure, i.e.

$$_h \langle p_1, \alpha_1; \dots; p_n, \alpha_n | \Omega_{\pm} | p_1, \beta_1; \dots; p_n, \beta_n \rangle_h = U_{p_1; \alpha_1 \beta_1}^{\pm} \dots U_{p_n; \alpha_n \beta_n}^{\pm} \quad (2.27)$$

for each  $n$ -particle state  $|p_1; \dots; p_n\rangle_h$  of color  $\alpha_1, \dots, \alpha_n$  and where now

$$U_{p; \alpha \beta}^{\pm} \equiv \mathcal{N}_h \langle p, \alpha | \Omega_{\pm} | p, \beta \rangle_h, \quad (2.28)$$

is a tensor of the non-abelian group. Moreover the operators  $U_{p, \alpha \beta}^{\pm}$

$$\sum_{\beta} U_{p, \alpha \beta}^{\pm} (U_p^{\pm})_{\beta \gamma}^{\dagger} = \delta_{\alpha \gamma}. \quad (2.29)$$

Starting from the previous expressions and from the  $S$  matrix factorization it is clear how to argue the BN theorem violation. We can consider, for instance, the 2-to-2 reaction, previously considered  $p_1(k_1, \alpha_1) p_2(k_2, \alpha_2) \rightarrow p_3(k_3, \alpha_3) p_4(k_4, \alpha_4) + X$ , where now we have to specify the color of the hard states  $(\alpha_1, \dots, \alpha_n)$ . With  $X$  we mean that we are including all final-state radiation. The fully-inclusive cross-section is obtained by



summing over the color of the final state, i.e.

$$d\sigma_{f.i.} \propto \sum_{\alpha_3\alpha_4} \sum_{\psi \in \mathcal{H}_s} |({}_s\langle\psi| \otimes {}_h\langle k_3, \alpha_3; k_4, \alpha_4|) S(|k_1, \alpha_1; k_2, \alpha_2\rangle_h \otimes |0\rangle_s)|^2 \quad (2.30)$$

$$\propto \sum_{\alpha_3\alpha_4} \sum_{\psi \in \mathcal{H}_s} {}_s\langle 0| (U_{k_1}^+)^\dagger (U_{k_2}^+)^\dagger S_h^{\dagger\beta'_1\beta'_2, \beta'_3\beta'_4} U_{k_1, \beta_1\alpha_1}^- U_{k_2, \beta_2\alpha_2}^- |\psi\rangle_s \quad (2.31)$$

$$\begin{aligned} & \times {}_s\langle\psi| (U_{k_3}^-)^\dagger (U_{k_4}^-)^\dagger S_h^{\beta_3\beta_4, \beta_1\beta_2} U_{k_1, \beta_1\alpha_1}^+ U_{k_2, \beta_2\alpha_2}^+ |0\rangle_s \\ & \propto \sum_{\alpha_3\alpha_4} \sum_{\psi \in \mathcal{H}_s} {}_s\langle 0| (U_{k_1}^+)^\dagger (U_{k_2}^+)^\dagger S_h^{\dagger\beta'_1\beta'_2, \alpha'_3\alpha'_4} |\psi\rangle_s \\ & \times {}_s\langle\psi| S_h^{\alpha_3\alpha_4, \beta_1\beta_2} U_{k_1, \beta_1\alpha_1}^+ U_{k_2, \beta_2\alpha_2}^+ |0\rangle_s, \end{aligned} \quad (2.32)$$

with some abuse of notation and where repeated indices are summed over. In this way we trivially show the BN theorem violation in EW interactions, summing over final state color is not enough to avoid Sudakov DL, not even in fully-inclusive observables. The complication in the previous equation is represented by the factor  $U^\pm$  that have not a simple form, not even in the leading approximation given by eq. (2.15). This is physically related to the fact that *primary* radiation, the one produced by the hard states, can itself radiate *secondary* particles and so forth so on. We will discuss more in detail this aspect in the next section.

There is an additional property of the operators  $U_{p, \alpha\beta}^\pm$  that we have to mention, they commute at DL

$$[U_{p_1, \alpha_1\beta_1}^\pm, U_{p_2, \alpha_2\beta_2}^\pm] = 0. \quad (2.33)$$

Therefore, from eq. (2.32) it is clear that summing over initial state color is sufficient to drop the Soft factors and so to avoid IR effects. While this is guaranteed in QCD by the confinement, in EW reactions and specifically at VHEL it would be meaningless to sum over neutrino and electron, as mentioned already in the previous chapter.

### 2.2.2 The Infrared Evolution Equation

We now turn on the method of the IREE and we discuss directly 2-by-2 EW processes at very high energy.

The basic idea is of the IREE to introduce an unphysical IR regulator  $\lambda$  with dimension (energy)<sup>2</sup> in the calculation of the observables and to write down a differential equation for the evolution with  $\lambda$  of the result. Denoting by “ $E^2$ ” the hardness of the observable under consideration, the choice  $\lambda \sim E^2$  eliminates all the IR enhancements and makes fixed-order perturbation theory well-behaved. For  $\lambda \sim E^2$ , the Born level computation therefore offers a reliable approximation, which can be used as the initial condition for the evolution equation to lower  $\lambda$ . The physical predictions are obtained from the solution of the IREE in the limit  $\lambda \rightarrow 0$ .

## Chapter 2. Precision physics from Very High Energy Leptons collisions

---

In order to define the IR regulator, consider the 4-momenta  $k_i$  of the external hard particles that participate in the scattering process. They will correspond in our setup to the 4 legs of a central energetic  $2 \rightarrow 2$  processes. With the exception of the masses  $k_i^2 \ll E^2$ , all the Lorentz invariants constructed with the  $k_i$ 's are therefore large and of order  $E^2$ . Given a pair  $ij$  of external hard particles and given a radiation particle with 4-momentum  $q$  we define its hardness relative to the  $ij$  pair as

$$\mathfrak{h}^{ij}(q) \equiv 2 \left| \frac{(k_i \cdot q)(k_j \cdot q)}{(k_i \cdot k_j)} \right|. \quad (2.34)$$

The IR regulator is provided by the lower bound  $\lambda$

$$\mathfrak{h}(q) \equiv \min_{i \neq j} \mathfrak{h}^{ij}(q) > \lambda. \quad (2.35)$$

on the “absolute” hardness  $\mathfrak{h}$  of the radiation. Notice that the bound is imposed on the 4-momentum of each individual radiation particle, either virtual or real. Specifically, eq. (2.35) applies to the off-shell loop momenta describing virtual radiation, as well as to the on-shell momenta of real radiation particles in the final state of the process. The specific definition of the radiation hardness in eq. (2.34) is convenient because it reflects the structure of the denominators that appear in the calculation of the IR-enhanced diagrams, as we will readily see. At this stage, it is enough to remark that the lower cut on  $\mathfrak{h}(q)$  in eq. (2.35) is a valid IR regulator as it eliminates both the regions where  $q$  is soft and those where it is collinear to one of the hard partons.

The main peculiarity of the IREE formalism applied to EW radiation stems from the presence of the physical scale  $m_W \sim 100$  GeV associated to the masses of the EW bosons. We will see that  $m_W$  acts as a threshold that separates two different regimes,  $\lambda \gg m_W^2$  and  $\lambda \ll m_W^2$ . In the former regime, the cut on the radiation hardness in eq. (2.35) is so strong that the mass of the radiation particles can be safely neglected and the IREE computed in the unbroken  $SU(2)_L \times U(1)_Y$  EW gauge theory. Starting from the initial condition at  $\lambda \sim E^2$ , the evolution is thus performed with the  $SU(2)_L \times U(1)_Y$  evolution kernel down to  $\lambda \sim m_W^2$ . At  $\lambda \ll m_W^2$ , the massive vector bosons do not contribute to the evolution and the kernel is purely determined by the unbroken  $U(1)_Q$  group of electromagnetism.

### Amplitude evolution

We start, following Ref. [156], from the IREE for the scattering amplitude with purely hard external quanta and with regulator  $\lambda$  on the internal lines. While the discussion holds for an arbitrary number of external legs, we focus for definiteness on  $2 \rightarrow 2$  amplitudes, which we indicate by

$$\mathcal{M}_\lambda^\alpha = \mathcal{M}_\lambda \left[ p_1(k_1, \alpha_1) p_2(k_2, \alpha_2) \rightarrow p_3(k_3, \alpha_3) p_4(k_4, \alpha_4) \right], \quad (2.36)$$

where  $\alpha_i$  denotes the gauge group index of the external state  $p_i$ , which is taken to transform in an irreducible representation of the group. The amplitude is labeled by the 4 indices  $\alpha = \alpha_1\alpha_2\alpha_3\alpha_4$ , and it is IR-regulated according to eq. (2.35). Since no real radiation is involved, the cut acts only on the momenta of virtual vector bosons in loop diagrams. We aim at writing down the IREE for  $\mathcal{M}_\lambda^\alpha$  and to solve it given the initial condition

$$\mathcal{M}_{E^2}^\alpha = \mathcal{B}^\alpha \equiv \text{Born Amplitude}. \quad (2.37)$$

As we explained, for  $\lambda \gg m_w^2$  the effects of EW symmetry breaking (EWSB) can be ignored, and  $\mathcal{M}_\lambda^\alpha$  equals the (IR-regulated) amplitude of the unbroken EW gauge theory. More precisely, EWSB gives negligible relative corrections of order  $m_w/\sqrt{\lambda}$  (or powers thereof) to all those amplitudes that are not forbidden by the  $SU(2)_L \times U(1)_Y$  exact symmetry of the unbroken theory. The other amplitudes are sensitive to EWSB at the leading order and therefore they cannot be studied in the unbroken theory.<sup>10</sup> However their contribution to the physical scattering process is negligible and they can be safely excluded from the discussion.<sup>11</sup> Similarly, for the allowed processes, up to negligible power corrections of order  $m_w/E$ , the amplitude  $\mathcal{M}_\lambda^\alpha$  is an  $SU(2)_L \times U(1)_Y$  invariant tensor satisfying the charge conservation equation

$$(G_{1^c}^A)^\alpha_\beta \mathcal{M}_\lambda^\beta + (G_{2^c}^A)^\alpha_\beta \mathcal{M}_\lambda^\beta + (G_3^A)^\alpha_\beta \mathcal{M}_\lambda^\beta + (G_4^A)^\alpha_\beta \mathcal{M}_\lambda^\beta \stackrel{\lambda \gg m_w^2}{=} 0, \quad \forall A, \alpha. \quad (2.38)$$

In the equation,  $G_i^A$  denotes the generators associated with the representation of each hard particle “ $i$ ” under the EW group, acting only on the corresponding index “ $\alpha_i$ ” of the amplitude tensor. For instance

$$(G_3^A)^\alpha_\beta = \delta_{\beta_1}^{\alpha_1} \delta_{\beta_2}^{\alpha_2} (G_3^A)^{\alpha_3}_{\beta_3} \delta_{\beta_4}^{\alpha_4}. \quad (2.39)$$

Notice that, in our notation,  $(\alpha_3, \alpha_4)$  run in the representations of the outgoing states, while  $(\alpha_1, \alpha_2)$  run in the conjugate representation of the incoming particles. Consequently in eq. (2.38),  $G_{1^c} = -G_1^*$  and  $G_{2^c} = -G_2^*$ .

The IREE is obtained by computing the variation of the amplitude under an infinitesimal variation  $\lambda \rightarrow \lambda + \delta\lambda$  of the IR cutoff in eq. (2.35). This computation dramatically simplifies in the leading DL approximation as one can infer by inspecting diagrams involving a number  $n$  of soft/collinear virtual vector bosons. Indeed the maximal logarithm power arises from the region where momenta are hierarchically separated  $E^2 \gg \mathfrak{h}(q_1) \gg \mathfrak{h}(q_2) \gg \dots \gg \mathfrak{h}(q_n)$  with the softer legs dressing the subdiagrams

<sup>10</sup>For instance the amplitude with 3 transversely- and one longitudinally-polarized  $W$  bosons is suppressed by  $m_w/E$  already at the Born level, owing to the fact that it is impossible to form an  $SU(2)_L$  singlet with one doublet (i.e., the representation of longitudinal  $W$ ’s owing to the Equivalence Theorem) and three triplets.

<sup>11</sup>Regarding power suppressed amplitudes, in [201] it has been found that they can receive positive Sudakov enhancements. However due to the power-like suppression we don’t expect this to affect our discussion.

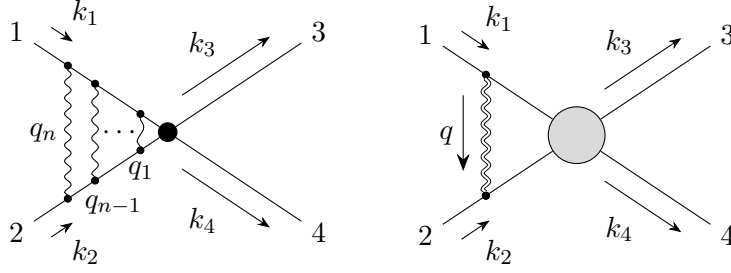


Figure 2.1 – Left panel: the leading Sudakov diagrams topology. Right panel: a diagrammatic representation of the contributions to the amplitude variation that are logarithmically enhanced. The momentum  $q$  is integrated over the infinitesimal strip  $\delta\sigma$  (2.40).

involving the harder legs, as shown in the left panel of Figure 2.1. In this configuration only the outermost virtual vector can reach a virtuality  $\mathfrak{h}(q_n) \sim \lambda$ , the inner ones being much harder in the dominant region of integration. The effect on  $\mathcal{M}_\lambda^\alpha$  of the variation of  $\lambda$  is then computed by considering the variation of the endpoint of the integral over the momentum of such outermost vector. More precisely we have that  $-\delta\mathcal{M}_\lambda^\alpha \equiv \mathcal{M}_\lambda^\alpha - \mathcal{M}_{\lambda+\delta\lambda}^\alpha$  equals the integral over the outermost loop momentum in the infinitesimal strip

$$\delta\sigma = \{q : \mathfrak{h}(q) \in [\lambda, \lambda + \delta\lambda]\}. \quad (2.40)$$

The contribution to the variation from the vector that connects a given pair of hard external legs can be depicted like on the right panel of Figure 2.1. The vector boson is represented with a double line to indicate that its momentum  $q$  must be integrated only over the strip  $\delta\sigma$ .

As we already said the leading contribution comes from the integration region where  $q$  is soft (and also collinear), in which the vector boson emission is described by the eikonal formula

$$\begin{aligned} \mathcal{M} \xrightarrow{q \downarrow \{A, \mu\}} \alpha_i &\simeq \frac{k_i^\mu}{k_i \cdot q} (G_i^A)^\alpha_\beta \mathcal{M}^\beta, & \alpha_i \xrightarrow{q \downarrow \{A, \mu\}} \mathcal{M} &\simeq \frac{k_i^\mu}{k_i \cdot q} (G_{i^c}^A)^\alpha_\beta \mathcal{M}^\beta, \end{aligned} \quad (2.41)$$

with  $G_i$  the group generator acting on particle “ $i$ ” as in eq. (2.39). In line with our conventions, as explained above, the generators of the charge-conjugate representation  $G_{i^c}$  appear in the eikonal formula for vector boson emission from an incoming particle. For brevity, we have included the gauge coupling constants in the definition of the generators  $G_i$ . In terms of the canonical  $\text{SU}(2)_L \times \text{U}(1)_Y$  generators we then have

$$G_i^{1,2,3} = g T_i^{1,2,3}, \quad G_i^Y = g' Y_i. \quad (2.42)$$

The integration over the soft  $q$  momentum factorizes with respect to the integral over the harder lines, represented as a blob in Figure 2.1. Indeed in the eikonal ( $q \rightarrow 0$ ) limit the virtual vector boson momentum can be neglected and the sub-amplitude blob evaluated on the momenta  $k_i$  of the external legs before the virtual vector boson emission/absorption. Therefore the blob gives us back the original amplitude, with one less loop but this is immaterial as  $\mathcal{M}_\lambda^\alpha$  is the all-loops amplitude. We can thus express the amplitude variation in terms of the amplitude itself, eventually obtaining an evolution equation. In covariant gauges, the leading DL contributions only arise from virtual vectors connecting two distinct external lines. Therefore, we have

$$\delta \mathcal{M}_\lambda^\alpha = \frac{-i}{(2\pi)^4} \sum_{j < i} \int_{\delta\sigma} d^4q \frac{1}{q^2 + i\epsilon} \frac{k_i \cdot k_j}{(q \cdot k_i)(q \cdot k_j)} \left[ \sum_A G_i^A \cdot G_j^A \right]_\beta^\alpha \mathcal{M}_\lambda^\beta, \quad (2.43)$$

where the sum extends over the unordered  $ij$  pairs of distinct external legs and it is understood that the conjugate generators must be employed for the incoming legs  $i, j = 1, 2$ , due to eq. (2.41).

The evaluation of the integral in eq. (2.43) is quite straightforward, and it is reported in Appendix B.1 for completeness. This gives

$$\delta \mathcal{M}_\lambda^\alpha = -\frac{1}{8\pi^2} \frac{\delta\lambda}{\lambda} \log \frac{E^2}{\lambda} \frac{1}{2} \sum_{A,i} (G_i^A)^\alpha_\beta \sum_{j \neq i} (G_j^A)^\beta_\gamma \mathcal{M}_\lambda^\gamma, \quad (2.44)$$

up to non logarithmically enhanced terms. Notice that in the equation we traded the sum over unordered  $ij$  pairs for an ordered sum times  $1/2$ . The sum over  $j \neq i$  can be performed using charge conservation according to eq. (2.38), giving

$$\begin{aligned} \delta \mathcal{M}_\lambda^\alpha &= \frac{1}{16\pi^2} \frac{\delta\lambda}{\lambda} \log \frac{E^2}{\lambda} \sum_i \left[ \sum_A G_i^A G_i^A \right]_\beta^\alpha \mathcal{M}_\lambda^\beta \\ &= \frac{1}{16\pi^2} \frac{\delta\lambda}{\lambda} \log \frac{E^2}{\lambda} \sum_i \left[ g^2 c_i + g'^2 y_i^2 \right] \mathcal{M}_\lambda^\alpha, \end{aligned} \quad (2.45)$$

where for any given external particle with weak isospin spin  $t_i$  and hypercharge  $y_i$ , the coefficients  $c_i = t_i(t_i + 1)$  and  $y_i^2$  are nothing but the Casimirs of respectively  $SU(2)_L$  and  $U(1)_Y$ . We thus recovered the familiar result that, in DL accuracy, IR effects are universal for each individual external particle and purely determined by the Casimir of the corresponding gauge group representation.

We finally obtain an IREE

$$\frac{d\mathcal{M}_\lambda^\alpha}{d \log^2(E^2/\lambda)} = -\frac{1}{2} \mathcal{K} \mathcal{M}_\lambda^\alpha, \quad \text{where } \mathcal{K} \stackrel{\lambda \gg m_w^2}{=} \frac{1}{16\pi^2} \sum_i \left[ g^2 c_i + g'^2 y_i^2 \right], \quad (2.46)$$

with, since the Casimir operators are proportional to the identity, an evolution kernel  $\mathcal{K}$  that is a mere multiplicative constant. Solving eq. (2.46) starting from the initial

condition (2.37) gives the amplitude evaluated with an IR cutoff scale  $\lambda = m_W^2$

$$\mathcal{M}_{m_W^2}^\alpha = \exp \left[ - \sum_i \frac{g^2 c_i + g'^2 y_i^2}{32\pi^2} \log^2(E^2/m_W^2) \right] \mathcal{B}^\alpha. \quad (2.47)$$

Notice that the contribution to the previous equation coming from the Abelian  $U(1)_Y$  group matches with the result previously found in eq. (2.24).

In order to continue the amplitude evolution to lower  $\lambda$ , we should now consider the regime  $\lambda \ll m_W^2$ , write the corresponding IREE and solve them using eq. (2.47) as initial condition. This is straightforward, because we have seen that all that matters for the derivation of the IREE are the loop integrals in a strip where the virtual radiation hardness is infinitesimally close to the cutoff  $\lambda$  as in eq. (2.40). In this region, a logarithmic enhancement of the amplitude variation only originates from photon exchange diagrams.<sup>12</sup> The IREE evolution kernel is thus immediately obtained by specifying the previous formulae to the  $U(1)_Q$  gauge group of QED

$$\mathcal{K}^{\lambda \ll m_W^2} = \frac{1}{16\pi^2} \sum_i \left[ e^2 q_i^2 \right]. \quad (2.48)$$

Notice that in order to derive the IREE in this regime, only conservation of electric charge must be employed. The conservation of the full  $SU(2)_L \times U(1)_Y$  charges of eq. (2.38) is not valid for  $\lambda \ll m_W^2$ , where the effects of electroweak symmetry breaking are important.

Solving eq. (2.48) produces the regular QED Sudakov factors, which go to zero in the physical limit  $\lambda \rightarrow 0$  where the IR regulator is removed. Therefore the amplitude  $\mathcal{M}_0^\alpha$  vanishes, and so does the cross-section of the corresponding fully-exclusive scattering process, in which no extra radiation is present in the final state. More inclusive observables need to be considered for a non-vanishing result. One possibility is to allow for the presence of real photon radiation up to an upper threshold of order  $m_W^2$  on the hardness  $\mathfrak{h}$ . This defines a cross-section that we denote as *exclusive* because it indeed excludes the radiation of massive EW bosons. In fact, it is easy to check that  $\mathfrak{h}(q) > m^2$  for the emission of a real radiation quantum with  $q^2 = m^2$ . An upper cut  $\mathfrak{h}(q) < m_W^2$  then excludes the presence of massive EW bosons in the final state, but allows for (sufficiently) soft photons. Ref. [156] considered this same observable (but calling it “semi-inclusive”) showing that it stops evolving with  $\lambda$  below  $m_W^2$ , due to the cancellation of real and virtual IR effects in QED. Cross-sections that are exclusive according to our definition can thus be computed at the DL accuracy by just squaring the  $\lambda = m_W^2$  amplitude (2.47). At the end of the next section we will re-derive the result of Ref. [156] for exclusive cross-sections by a slightly different methodology, which is also suited for the calculation of the other type of cross-sections we are interested in.

---

<sup>12</sup>The calculation of the loop integral in Appendix B.1 shows explicitly that no enhancement emerges from the exchange of vectors with mass  $m_V$  much larger than  $\lambda$ .

### Density matrix evolution

It is possible to extend the IREE methodology to more complex quantities than the hard Feynman amplitude. Specifically, we consider the hard “density matrix”<sup>13</sup>

$$\mathcal{D}_\lambda^{\alpha\bar{\alpha}} \equiv \mathcal{M}_\lambda^\alpha (\mathcal{M}_\lambda^{\bar{\alpha}})^* + \sum_{N=1}^{\infty} \int d\text{Ph}_{N,\lambda}^{\mathcal{H}} \sum_{\rho_1 \dots \rho_N} \mathcal{M}_\lambda^{\alpha;\rho} (\mathcal{M}_\lambda^{\bar{\alpha};\rho})^*, \quad (2.49)$$

which incorporates the emission of an arbitrary number  $N$  of radiation particles, with gauge group indices denoted as  $\rho = \rho_1 \dots \rho_N$ . In the equation,  $\mathcal{M}_\lambda^\alpha$  is the hard amplitude with no extra emissions as in the previous section, while  $\mathcal{M}_\lambda^{\alpha;\rho}$  is the amplitude for the production of the 2 hard particles plus the radiation. The virtual radiation particles exchanged in the Feynman diagrams for the amplitude are subject to the IR hardness cutoff  $\lambda$  as in eq. (2.35). The phase-space volume element  $d\text{Ph}_{N,\lambda}^{\mathcal{H}} = \prod_{k=1}^N d\text{Ph}_{k,\lambda}^{\mathcal{H}}$  for the emission of real radiation is also constrained by eq. (2.35). The  $\mathcal{H}$  superscript refers to the possible presence of an upper cutoff on the radiation hardness  $\mathfrak{h}(q) < \mathcal{H}$ . In what follows we will first consider processes we define as *semi-inclusive*, for which  $\mathcal{H} \sim E^2$ . For these processes the upper radiation cut is effectively absent, and plays no role in the discussion. The exclusive processes defined in the previous section instead simply correspond to  $\mathcal{H} = m_W^2$ .

It should be noted that eq. (2.49) formally violates the conservation of the total energy and momentum, because in the radiation terms we are employing the same hard 4-momenta that obey energy and momentum conservation in the absence of radiation. It is understood that this makes sense only in the presence of an upper cutoff on the total energy and momentum of the radiation, say a one tenth of  $E$ . In this way, the radiation plays a minor role in the total balance of energy and momentum conservation or, equivalently, the hard 4-momenta can be readjusted to balance the radiation emission up to small corrections in the corresponding Feynman amplitudes. In practice, the cutoff allows us to factorize the total phase-space into that for radiation, on one hand, and that for the hard  $2 \rightarrow 2$  process on the other, with the latter also including the delta function of 4-momentum conservation. The density matrix (2.49) can thus be related to the physical scattering cross-section.

An upper cut  $E_{rad} < E/10$  on the total radiation energy and momentum does not affect the predictions at the double logarithm accuracy. Indeed a simple modification of the real radiation integral (see the discussion around eq. (2.51) computation in Appendix B.1 shows that the effect of this cut on the  $q$  momentum of the radiated particle merely entails reduction of the double logarithm from  $\log^2 E^2/\lambda$  to  $\log^2 E_{rad}^2/\lambda$ . The difference is then of order  $\log E^2/\lambda \times \log E^2/E_{rad}^2$  and falls into the same class as single logarithms as long as  $E/E_{rad}$  is not too small, with  $1/10$  qualifying.

<sup>13</sup>The same object was dubbed “overlap matrix” in Ref. [155].

## Chapter 2. Precision physics from Very High Energy Leptons collisions

The hard density matrix (2.49) is a simple generalization of the scattering cross-section in which the conjugated amplitude indices  $\bar{\alpha}$  are not equal to the indices  $\alpha$  of the non-conjugated amplitude. It is a useful generalization because it obeys charge conservation equations similar to eq. (2.38). Namely, in the regime  $\lambda \gg m_w^2$ , we have

$$\sum_{i=1^c, 2^c, 3, 4} \left[ (G_i^A)_{\beta}^{\alpha} \mathcal{D}_{\lambda}^{\beta \bar{\alpha}} + (G_{i^c}^A)_{\bar{\beta}}^{\alpha} \mathcal{D}_{\lambda}^{\alpha \bar{\beta}} \right] \stackrel{\lambda \gg m_w^2}{=} 0, \quad \forall A, \alpha, \bar{\alpha}, \quad (2.50)$$

where the obvious relations  $[1^c]^c \equiv 1$   $[2^c]^c \equiv 2$  should be understood. That way the generators acting on the indices  $\bar{\beta}$  of the complex conjugated amplitude are those of the corresponding charge conjugated representation. Eq. (2.50) holds only for  $\lambda \gg m_w^2$ , because in this regime both the virtual and the real emissions are nearly insensitive to EWSB effects as previously explained. For  $\lambda \ll m_w^2$ , only the electric charge generator is conserved.

The IREE can be obtained like in the previous section by computing the variation of  $\mathcal{D}_{\lambda}$  under  $\lambda \rightarrow \lambda + \delta\lambda$ , taking now also into account also the effect of the IR cutoff on real emission. The contribution of virtual loop momentum integrals is thus accompanied by that of integrals over the momentum of real radiation. All integrals have to be performed over the infinitesimal strip  $\delta\sigma$  defined in eq. (2.40). Logarithmically enhanced terms only arise from the exchange of virtual or real gauge bosons between different external legs ( $i \neq j$ ), like in Figure 2.2. The effects and the corresponding diagrams can be divided into two classes. The first, in the left panel of Figure 2.2, is given by *primary* radiation diagrams where vector bosons are exchanged between the hard legs. The second, in the right panel, is given by *secondary* radiation diagrams where vector bosons connect to at least one real radiation leg.

We will first consider the effects of primary radiation. The virtual radiation integral gives the result already mentioned in eq. (2.44), and, as we show in Appendix B.1, the result is exactly the same for the real radiation integral. The total variation from primary radiation is then

$$\begin{aligned} \delta \mathcal{D}_{\lambda}^{\alpha \bar{\alpha}} = & -\frac{1}{16\pi^2} \frac{\delta\lambda}{\lambda} \log \frac{E^2}{\lambda} \sum_{i=1^c, 2^c, 3, 4} \sum_A \left[ (G_i^A)_{\beta}^{\alpha} \sum_{j \neq i} \left[ (G_j^A)^{\beta}_{\gamma} \mathcal{D}_{\lambda}^{\gamma \bar{\alpha}} + (G_{j^c}^A)_{\bar{\beta}}^{\alpha} \mathcal{D}_{\lambda}^{\beta \bar{\beta}} \right] \right. \\ & \left. + (G_{i^c}^A)_{\bar{\beta}}^{\alpha} \sum_{j \neq i} \left[ (G_j^A)^{\alpha}_{\beta} \mathcal{D}_{\lambda}^{\beta \bar{\beta}} + (G_{j^c}^A)^{\bar{\beta}}_{\bar{\gamma}} \mathcal{D}_{\lambda}^{\alpha \bar{\gamma}} \right] \right]. \end{aligned} \quad (2.51)$$

The argument of the first sum, over the four external legs, collects the contributions of all the radiation emitted from the leg “ $i$ ” of the amplitude and of the conjugated amplitude. A factor 1/2 is included to avoid double-counting. Notice that both virtual and real radiation connecting one leg with itself is excluded from the sum, because, as we already mentioned, no enhancement arises from those diagrams.



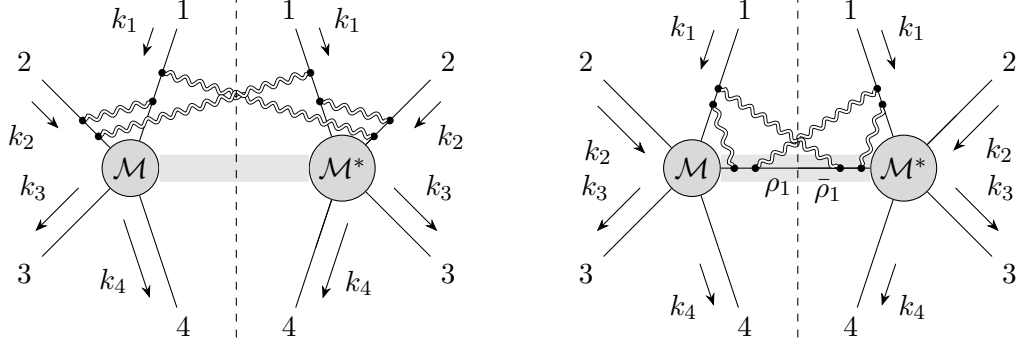


Figure 2.2 – Diagrammatic representation of the contributions to the density matrix variation from primary (left panel) and secondary (right panel) radiation. The vector bosons are represented as double lines to indicate that their momenta have to be integrated over the infinitesimal strip (2.40).

We can now proceed as in the previous section, and use the charge conservation in eq. (2.50) to perform the sum over  $j$  in eq. (2.51). We find the IREE

$$\frac{d\mathcal{D}_\lambda^{\alpha\bar{\alpha}}}{d\log^2(E^2/\lambda)} = -\mathcal{K}_{\beta\bar{\beta}}^{\alpha\bar{\alpha}} \mathcal{D}_\lambda^{\beta\bar{\beta}}, \quad (2.52)$$

with an evolution kernel that is the direct sum of universal terms for each external leg

$$\begin{aligned} \mathcal{K}_{\beta\bar{\beta}}^{\alpha\bar{\alpha}} &\stackrel{\lambda \gg m_w^2}{=} \frac{1}{32\pi^2} \sum_i \left[ \left[ \sum_A G_i^A G_i^A \right]_\beta^\alpha \delta_{\bar{\beta}}^{\bar{\alpha}} + \delta_\beta^\alpha \left[ \sum_A G_{i^c}^A G_{i^c}^A \right]_{\bar{\beta}}^{\bar{\alpha}} + 2 \sum_A (G_i^A)_\beta^\alpha (G_{i^c}^A)_{\bar{\beta}}^{\bar{\alpha}} \right] \\ &= \frac{g^2}{16\pi^2} \sum_i \left[ c_i \delta_{\beta_i}^{\alpha_i} \delta_{\bar{\beta}_i}^{\bar{\alpha}_i} + \sum_{A=1,2,3} (T_i^A)_{\beta_i}^{\alpha_i} (T_{i^c}^A)_{\bar{\beta}_i}^{\bar{\alpha}_i} \right] \left[ \prod_{j \neq i} \delta_{\beta_j}^{\alpha_j} \delta_{\bar{\beta}_j}^{\bar{\alpha}_j} \right] \\ &= \frac{g^2}{16\pi^2} \sum_i \left[ K_i \right]_{\beta_i \bar{\beta}_i}^{\alpha_i \bar{\alpha}_i} \left[ \prod_{j \neq i} \delta_{\beta_j}^{\alpha_j} \delta_{\bar{\beta}_j}^{\bar{\alpha}_j} \right]. \end{aligned} \quad (2.53)$$

The kernel contains one term, provided by the  $SU(2)_L$  Casimir  $c_i = t_i(t_i + 1)$ , which is proportional to the identity in the color indices of the density matrix tensor, plus a non-diagonal term constructed with the  $SU(2)_L$  group generators matrices  $T_i^A$  of the external legs. Notice that the contribution of the  $U(1)_Y$  hypercharge generator cancels.

There is one peculiarity of eq. (2.53) that is worth emphasizing. The semi-inclusive cross-sections we are interested in are the diagonal entries ( $\alpha = \bar{\alpha}$ ) of the density matrix, with no sum performed over the gauge group index  $\alpha$  of the scattering particles.<sup>14</sup> However one can also consider *inclusive* cross-sections, where the sum over the gauge index  $\alpha_i$  is performed for one or several external legs. By setting  $\bar{\alpha}_i = \alpha_i$  and summing

<sup>14</sup>This is true only in a basis where the gauge indices  $\alpha_i$  label the on-shell SM particles, while for the calculation of di-boson cross-sections we work in a different basis. See Section 2.3.2 and Appendix B.2 for details.

over  $\alpha_i$ , the  $SU(2)_L$  generators in eq. (2.53) recombine to form the Casimir operator, and the contribution to the evolution kernel from leg “ $i$ ” cancels. We thus find again that, at DL accuracy, the cancellation between real and virtual IR effects in inclusive cross-sections occurs on a leg-by-leg basis. Namely, the effects of soft/collinear emissions associated to each individual leg cancel in the cross-section (and in the entire density matrix) for processes that are inclusive over the color of the corresponding particle. This result is stronger than the KLN theorem, which foresees a cancellation only when summing over the color of all legs. The reason for the added strength is that we are here considering radiation that is both soft and collinear. Notice however that fully inclusive observables of practical relevance can only involve summation on the color of the final state particles. This retains the IR effects associated with the colliding particles in the initial state (e.g., two left-handed leptons  $\ell_L^+ \ell_L^-$ ) which are not  $SU(2)_L$  singlets. The resulting non-cancellation of IR effects in “fully-inclusive” cross-sections, coincides with the result of Ref. [155].

So far we have ignored the secondary radiation diagrams, depicted in the right panel of Figure 2.2. We show now that their contribution vanishes, giving full justification to eq. (2.53). Secondary radiation diagrams correspond to the effect of the  $\lambda$  cutoff variation on virtual or real vector bosons attached to one of the intermediate “ $\rho$ ” particles in the definition of the density matrix (2.49). Clearly these effects are potentially enhanced only if the intermediate particle is relatively hard, such that a significant separation is present between the IR cutoff  $\lambda$  and the scalar product between the intermediate particle and the external leg momenta. We thus start considering vector bosons attached to the hardest intermediate particle, with gauge index “ $\rho_1$ ” as in the figure. The density matrix is inclusive over the color of the intermediate particle. However we can momentarily define an “extended” density matrix  $\mathcal{D}_\lambda^{\alpha;\rho_1\bar{\alpha};\bar{\rho}_1}$  with labels  $\rho_1$  and  $\bar{\rho}_1$  for the gauge indices of the amplitude and of the conjugate amplitude, as in the figure. The actual density matrix is eventually obtained by first setting  $\rho_1 = \bar{\rho}_1$  and then summing. The effect on the extended density matrix variation of all the radiation emitted from  $\rho_1$  and  $\bar{\rho}_1$  can be written in a form similar to eq. (2.51) and then simplified using the analog of eq. (2.50) for the extended density matrix. The resulting contribution to the evolution kernel from the intermediate  $\rho_1$  leg is the analog of that from the hard external legs in eq. (2.53). But this contribution cancels out in the evolution of the actual density matrix, which is inclusive over the  $\rho_1$  leg, because of the previously explained leg-by-leg cancellation mechanism. The argument can of course be repeated for the diagrams involving the second hardest intermediate particle, showing, as anticipated, that all the secondary radiation diagrams can be ignored in the calculation of the evolution kernel.

It is straightforward to adapt the previous results to the regime  $\lambda \ll m_W^2$ , in which only the exchange of photons contributes to the evolution, as discussed in the previous section. By specifying eq. (2.53) to the Abelian  $U(1)_Q$  group we immediately find that the kernel vanishes, owing to the well-known cancellation between real and virtual IR effects in QED. For the calculation of the physical ( $\lambda \rightarrow 0$ ) density matrix, and in turn of the

semi-inclusive cross-section, we thus only need to solve the IREE with the  $\lambda \gg m_W^2$  kernel (2.53), down to  $\lambda = m_W^2$ .

For  $\lambda = E^2$  the hard density matrix (2.49) is well-approximated by its tree-level expression, which serves as the initial condition for the evolution

$$\mathcal{D}_{E^2}^{\alpha\bar{\alpha}} = \mathcal{B}^\alpha(\mathcal{B}^{\bar{\alpha}})^*. \quad (2.54)$$

The kernel is the direct sum of tensors, denoted as  $K_i$  in eq. (2.53), each acting on the pair  $\alpha_i, \bar{\alpha}_i$  associated to the  $i$ -th external particle. Therefore the solution of the IREE reads

$$\mathcal{D}_{\text{si}}^{\alpha\bar{\alpha}} \equiv \mathcal{D}_{m_W^2}^{\alpha\bar{\alpha}} = \left\{ \prod_i \left[ \exp \left[ -\frac{g^2}{16\pi^2} K_i \log^2(E^2/m_W^2) \right] \right]_{\beta_i \bar{\beta}_i}^{\alpha_i \bar{\alpha}_i} \right\} \mathcal{B}^\beta(\mathcal{B}^{\bar{\beta}})^*, \quad (2.55)$$

where the “si” subscript denotes the density matrix of the semi-inclusive process, with no upper cut on the real radiation hardness. The explicit form of the  $K_i$  exponentials in the above equation is reported in eq.s (B.31) and (B.36) for external legs in the doublet and triplet  $\text{SU}(2)_L$  representations. Applications of eq. (2.55) to specific processes are shown in Sections 2.3.1 and 2.3.2.

We have defined the density matrix (2.49) allowing for the presence of an upper cutoff  $\mathcal{H}$  on the real radiation, but this played no role in the previous discussion because this cutoff is effectively absent ( $\mathcal{H} \sim E^2$ ) in our definition of semi-inclusive processes. In exclusive processes we instead set  $\mathcal{H} = m_W^2$ , namely we veto real radiation particles with hardness above  $m_W^2$ . Obviously, for  $\lambda \gg m_W^2$  this upper cut is in contradiction with the IR cutoff in eq. (2.35) on the radiation phase-space. Therefore in the density matrix for the exclusive process no real radiation is present and in the  $\lambda \gg m_W^2$  regime the result simply equals the square of the hard amplitude in eq. (2.36). The evolution up to  $\lambda = m_W^2$  can thus be obtained from the hard amplitude evolution (2.47) we obtained in the previous section, or easily re-derived by dropping the terms in eq. (2.51) (namely, the second and the third) that are due to real radiation. The contribution of real radiation is instead restored for  $\lambda \ll m_W^2$  and the evolution stops due to the cancellation between virtual and real QED radiation as previously explained. The physical ( $\lambda \rightarrow 0$ ) density matrix for exclusive processes can thus be written in a simple closed form as

$$\mathcal{D}_{\text{ex}}^{\alpha\bar{\alpha}} = \exp \left[ - \sum_i \frac{g^2 c_i + g'^2 y_i^2}{16\pi^2} \log^2(E^2/m_W^2) \right] \mathcal{B}^\alpha(\mathcal{B}^{\bar{\alpha}})^*. \quad (2.56)$$

In Sections 2.3.1 and 2.3.2 we employ this formula to compute exclusive di-fermion and di-boson production cross-sections, and discuss the need of supplementing it with fixed-order single-logarithmic terms, from Ref. [178, 202].

Before concluding this section it is worth commenting on the experimental definition

of the semi-inclusive and exclusive processes, and on the perspectives for their actual experimental detectability. The semi-inclusive process is characterized by two central (specifically, emitted from 30 to 150 degrees from the beam line) energetic particles of specific EW color and flavor. In particular we will require them to carry a total center of mass energy above 85% of the VHEL  $E_{\text{cm}}$ , enforcing in this way the upper cut on the total radiation 4-momentum required for the definition of the hard density matrix as discussed below eq. (2.49). The two particles can be accompanied by the radiation of EW bosons, photons, or any other soft particle.

Notice that in our calculation at the DL order we could ignore all the effects of collinear (rather than soft-collinear) radiation, which emerge at the single logarithm. On the other hand, the single logarithms associated with low-virtuality (below  $m_{\text{W}}$ ) photon splittings are much larger than  $\log E^2/m_{\text{W}}^2$ . In particular, the emission of real photons that are energetic but collinear to a light charged hard particle (e.g., an electron or a muon) with mass  $m_\ell$  produces terms proportional to  $\log E^2/m_\ell^2$ . By the KLN theorem these terms will be canceled by the corresponding virtual contributions, but only in suitably-defined observables that recombine the emitted photons in the experimental definition of the hard particle 4-momentum. With a lower threshold of order  $m_{\text{W}}$  on the energy of the photons to be recombined, the net effect on our prediction should be of the order of a single EW logarithm  $\log E^2/m_{\text{W}}^2$ . A more detailed assessment of this aspect, and of the possible interplay between the QED and the EW bosons collinear emissions, requires the inclusion of single logarithms and goes beyond the scope of this thesis. Similar considerations hold for the collinear emission of QCD gluons to be collected into jets, in the case of colored final states.

Up to the caveats outlined above, there are good perspectives for the actual direct experimental detectability of semi-inclusive cross-sections. The situation is arguably more problematic for the exclusive cross-section. In exclusive final states, we require the presence of the two hard particles defined as above, plus the absence of any massive vector boson (since  $\mathfrak{h}(q) > q^2 = m^2$ , as discussed at the end of the previous section), or photons above the hardness upper threshold  $m_{\text{W}}^2$ . However, it is experimentally impossible to impose this radiation veto strictly because the limited coverage of the detector in the forward and backward regions will not allow to tag EW bosons or photons that are collinear to the beam. Furthermore our definition of the exclusive cross-section is problematic in the case of QCD-colored final states. Indeed if the upper cut  $\mathfrak{h}(q) < m_{\text{W}}^2$  had to be imposed also on gluon radiation, QCD effects should be included in the exclusive density matrix evolution (but not in the semi-inclusive one, where they cancel because of color inclusivity), resulting in a large QCD Sudakov suppression factor in eq. (2.56). This factor is as small as  $\exp[-\alpha_s/(4\pi)(8/3)\log^2 E_{\text{cm}}^2/m_{\text{W}}^2] \sim 0.03$  for di-quark final states at the highest VHEL energy  $E_{\text{cm}} = 30$  TeV, entailing a strong suppression of the cross-section. Avoiding this suppression requires a definition of the exclusive cross-section with a higher threshold on the QCD radiation.

## 2.3 Di-fermion and di-boson production at VHEL

So far we discussed the resummation of DL in generic 2-to-2 semi-inclusive and exclusive EW-processes. We now specify to diboson and difermion production at VHEL.

### 2.3.1 Di-fermion production

The first process we investigate is the production of a highly energetic pair of fermions

$$\ell^+(k_1) \ell^-(k_2) \rightarrow \bar{f}(k_3) g(k_4) + X, \quad (2.57)$$

where  $f$  and  $g$  can be one of the six quarks, a lepton  $\ell' \neq \ell$  or a neutrino  $\nu_{\ell'}$ . We do not discuss explicitly the final states with the same leptonic flavor as the initial state,  $\ell' = \ell$ , but these processes will be employed for the muon collider sensitivity projections in Section 2.4. As previously discussed, the final state is characterized (both for exclusive and semi-inclusive processes) by an invariant mass for the  $(\bar{f}, g)$  pair that is almost equal to the center of mass energy  $E_{\text{cm}}$  of the colliding leptons and by central scattering angle  $\theta_* \in [30^\circ, 150^\circ]$ . Here  $\theta_*$  is the angle between the incoming  $\ell^+$  and the final anti-fermion  $\bar{f}$  in the lab frame. Notice that  $\theta_*$  almost coincides with the scattering angle in the center of mass frame of the hard process, because of the tight cut on the invariant mass of the  $(\bar{f}, g)$  pair.

In order to resum the DL it is convenient to organize the calculation of the cross-section in terms of amplitudes and density matrices whose external legs are canonical irreducible representations of the EW group. This is trivial to achieve for the di-fermion process because the helicity eigenstates of quarks and leptons in the massless limit do indeed transform as canonical representations (doublets and singlets, with specific hypercharge), reported for completeness in Appendix B.2. Furthermore, since we restrict our attention to inelastic processes  $\ell' \neq \ell$ , the only sizable helicity amplitudes are those with the same chirality  $\chi_I$  ( $\chi_O$ ) for the two incoming (outgoing) fermions, corresponding to helicities  $\bar{\psi}_{+1/2}\psi_{-1/2}$  for  $\chi = L$  and  $\bar{\psi}_{-1/2}\psi_{+1/2}$  for  $\chi = R$ . The dominance of such amplitudes holds in the SM because of the vector-like structure of gauge interaction, and it will be preserved by the 4-fermions new physics contact interaction operators we will study in Section 2.4. We thus have to deal with four polarized cross-sections for each di-fermion production process, labeled by  $\chi_I\chi_O = LL, LR, RL, RR$ . Each such cross-section will be obtained from the diagonal  $\alpha = \bar{\alpha}$  entries of the density matrices of Section 2.2.2, times the appropriate phase-space factors.

	3 TeV			10 TeV			30 TeV		
	DL	$e^{\text{DL}}-1$	$\text{SL}(\frac{\pi}{2})$	DL	$e^{\text{DL}}-1$	$\text{SL}(\frac{\pi}{2})$	DL	$e^{\text{DL}}-1$	$\text{SL}(\frac{\pi}{2})$
$\ell_L \rightarrow \ell'_L$	-0.46	-0.37	0.25	-0.82	-0.56	0.33	-1.23	-0.71	0.41
$\ell_L \rightarrow q_L$	-0.44	-0.36	0.25	-0.78	-0.54	0.34	-1.18	-0.69	0.42
$\ell_L \rightarrow e_R$	-0.32	-0.27	0.13	-0.56	-0.43	0.17	-0.85	-0.57	0.21
$\ell_L \rightarrow u_R$	-0.27	-0.24	0.11	-0.48	-0.38	0.15	-0.72	-0.51	0.18
$\ell_L \rightarrow d_R$	-0.24	-0.21	0.10	-0.43	-0.35	0.13	-0.64	-0.47	0.16
$\ell_R \rightarrow \ell'_L$	-0.32	-0.27	0.13	-0.56	-0.43	0.17	-0.85	-0.57	0.21
$\ell_R \rightarrow q_L$	-0.30	-0.26	0.12	-0.53	-0.41	0.16	-0.79	-0.55	0.21
$\ell_R \rightarrow \ell'_R$	-0.17	-0.16	0.07	-0.30	-0.26	0.09	-0.46	-0.37	0.12
$\ell_R \rightarrow u_R$	-0.12	-0.12	0.05	-0.22	-0.20	0.07	-0.33	-0.28	0.08
$\ell_R \rightarrow d_R$	-0.09	-0.09	0.04	-0.17	-0.16	0.05	-0.25	-0.22	0.06

Table 2.1 – Double and single logarithmic corrections to the exclusive processes  $\ell^+ \ell^- \rightarrow \bar{f} f$ . The single-logarithmic corrections are evaluated at  $\theta_* = \pi/2$ .

### Exclusive processes

Exclusive cross-sections are readily obtained from eq. (2.56), and take the form

$$\frac{d\sigma_{\text{ex}}}{d\cos\theta_*} = e^{\text{DL}} \frac{d\sigma_B}{d\cos\theta_*}, \quad (2.58)$$

in terms of the corresponding Born-level differential cross-sections. The Double Log exponent DL is of order  $g^2/16\pi^2 \log^2(E_{\text{cm}}^2/m_W^2)$ , which ranges from 0.14 at  $E_{\text{cm}} = 3$  TeV up to 0.25 (0.38) for  $E_{\text{cm}} = 10(30)$  TeV, times the sum of the four SU(2) Casimir of the external legs. For  $LL$  chirality processes this factor is as large as  $4 \times 1/2(1/2 + 1) = 3$ , showing that DL resummation is mandatory at VHEL energies  $E_{\text{cm}} \geq 10$  TeV, at least for this chirality. Double logs are still considerable for  $LR$  and  $RL$  chirality, while they get smaller in the  $RR$  configuration because  $g'^2 \sim g^2/4$ . Resummation might instead not be necessary for  $E_{\text{cm}} = 3$  TeV. However it will still be needed to include the effects of radiation at fixed order since we aim, eventually, at theoretical predictions with percent-level accuracy.

The DL Sudakov exponents in eq. (2.58) are listed in Table 2.1. The processes are labeled taking into account that electric charge conservation enforces  $g = f$  in eq. (2.57), since a charge mismatch cannot be compensated by the emission of charged  $W$  bosons, which is forbidden in exclusive processes. The table also reports single logarithm (SL) contributions computed at the fixed one loop order, which we extract from Ref.s [178].<sup>15</sup> Specifically, we employ the general formulae of Ref.s [178] to compute the 1-loop log-enhanced cross-section, we subtract the corresponding DL and normalize to the Born cross-section. We also subtract the single logarithms from the Renormalization Group

<sup>15</sup>Two loops NLL results for four-fermion processes are also available in [77, 80].

evolution, because we decided to compute the Born amplitude with the EW couplings at the hard scale  $E_{\text{cm}}$ .<sup>16</sup> Notice that the threshold for photon recombination into the hard final state particles matters at the single-logarithmic order. Here we assume a scale of recombination of order  $m_W$ , for which the SL terms can be easily obtained by adding a fictitious photon mass  $m_\gamma = m_W$  to the calculations of Ref.s [178, 202]. The SL terms obtained in this way can be used for “improved” theoretical predictions

$$\frac{d\sigma_{\text{ex}}^{\text{SL}_1}}{d\cos\theta_*} = e^{\text{DL}}(1 + \text{SL}(\theta_*))\frac{d\sigma_B}{d\cos\theta_*}, \quad (2.59)$$

that include single logarithms at fixed 1-loop order. We see in Table 2.1 that the SL contributions are relatively large. It is unclear whether they require resummation or if including them at fixed order (definitely higher than 1-loop, if we target 1% accuracy) is sufficient.

Notice that, unlike double logarithms, the single logarithm contributions are not proportional to the Born-level amplitude of the same scattering process. Namely the amplitudes of the neutral-current processes in Table 2.1 receive SL corrections that are proportional to Born charged-current amplitudes. Therefore it should be kept in mind the SL terms in eq. (2.59), which we normalized to the Born cross-section of the process, depend on the ratio between charged and neutral current Born amplitudes. We evaluated the amplitude ratio within the SM to produce the results in Table 2.1. However the amplitude ratio depends on the new physics contact interactions we consider in Section 2.4, entailing a dependence of the SL terms on the new physics parameters. This is not the case for the double logarithms, which are completely universal and insensitive to short-distance physics. The single logarithms also carry a non-trivial dependence on the scattering angle  $\theta_*$ , as explicitly indicated in eq. (2.59). In Table 2.1 they are evaluated at central angle  $\theta_* = \pi/2$ , where they are always positive. They can become negative, and typically increase in magnitude, in the forward and backward scattering regions, which we however exclude with the central cut  $\theta_* \in [30^\circ, 150^\circ]$ . Finally, notice that the SL terms are affected by the sizable mass of the top quark, which we do include in the  $t\bar{t}$  production process.

The impact of EW radiation effects on the total (unpolarized) cross-section in the central region, relative to the Born, is displayed in Figure 2.3 as a function of  $E_{\text{cm}}$ . The production of two light up-type quarks is considered for illustration, but the results for the other final states are similar. The blue line is the one-loop DL prediction without exponentiation, while in red we report the resummed DL prediction in eq. (2.58). The green line (labeled  $\text{DL}_1 + \text{SL}_1$ ) represents the fixed-order one loop DL plus SL, while in black we report the SL-improved prediction in eq. (2.59). The dashed lines are semi-inclusive cross-sections computed below. We notice a significant cancellation between

<sup>16</sup>The calculation is similar to the one performed in ch 1. We refer to Section 1.2 for additional details, concerning in particular the inclusion of non-log-enhanced angular-dependent terms.



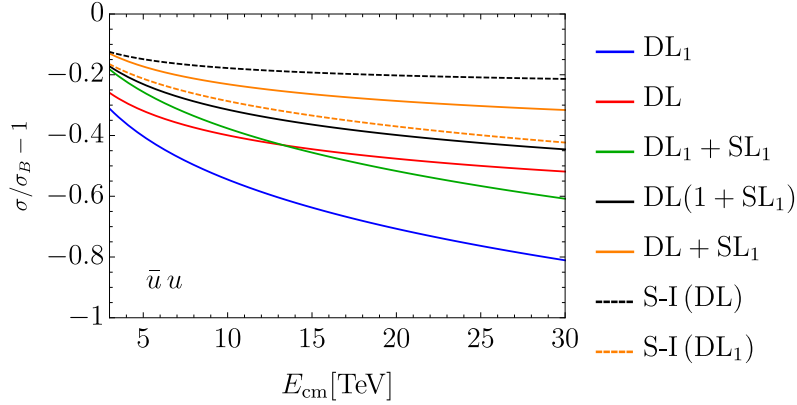


Figure 2.3 – Impact of radiative corrections on the production of two up quarks at the VHEL. The solid lines represent different predictions for the exclusive cross-section. The dashed lines are double-logarithm semi-inclusive cross-sections resummed (in black) or at one loop (in orange).

double and single logarithmic terms. However this cancellation is not expected to be structural and to survive at higher orders in perturbation theory.

We do not try to assign theoretical uncertainties to our predictions. However an upper bound can be obtained by considering the orange line in the figure, in which the resummed DL are combined additively with the SL (i.e., as  $e^{\text{DL}} + \text{SL}$ ), rather than multiplicatively. An alternative estimate of the uncertainties could be obtained by varying the scale of the EW couplings employed for the evaluation of the radiation terms DL and SL. Varying this scale from  $m_W$  (which we employ for our predictions) to  $E_{\text{cm}}$ , the relative change of the radiation effects is rather small, typically at the 10% level or less.

### Semi-inclusive processes

The semi-inclusive cross-sections are the diagonal  $\alpha = \bar{\alpha}$  entries of the semi-inclusive density matrix in eq. (2.55), with the appropriate  $K_i$  exponential factors for each external leg. The factors only depend on the  $\text{SU}(2)_L$  quantum numbers of the legs and not of their hypercharge (and QCD color). They are provided by eq. (B.31) for  $L$ -chirality external legs (which transform as doublets or conjugate-doublets) and they are trivial for the  $R$ -handed singlets. Notice that eq. (B.31) (and the same is true for the triplet exponential factor (B.36)) does not mix diagonal with off-diagonal entries of the density matrix. Namely if we set  $\alpha = \bar{\alpha}$  we obtain a tensor that is diagonal in  $\beta$  and  $\bar{\beta}$ . Therefore the DL resummed cross-sections, collected in a vector  $d\vec{\sigma}_{\text{si}}$ , are linear combinations of the Born cross-sections  $d\vec{\sigma}_B$ . We express this relation as

$$\frac{d\vec{\sigma}_{\text{si}}}{d\cos\theta_*} = e^{\text{DL}} \cdot \frac{d\vec{\sigma}_B}{d\cos\theta_*}, \quad (2.60)$$



where the Double-Logarithm terms “DL” are now matrices connecting the Born cross-sections of different processes unlike for exclusive processes (2.58).

For an explicit illustration of the semi-inclusive cross-section calculation, and of the main features of the result, we consider the  $RL$ -chirality production processes. In this case, we have

$$d\vec{\sigma}_{\text{si}} = \begin{pmatrix} d\sigma_{\text{si}}(\ell_R^+ \ell_R^- \rightarrow \bar{u}_L u_L) \\ d\sigma_{\text{si}}(\ell_R^+ \ell_R^- \rightarrow \bar{u}_L d_L) \\ d\sigma_{\text{si}}(\ell_R^+ \ell_R^- \rightarrow \bar{d}_L u_L) \\ d\sigma_{\text{si}}(\ell_R^+ \ell_R^- \rightarrow \bar{d}_L d_L) \end{pmatrix}, \quad d\vec{\sigma}_B = \begin{pmatrix} d\sigma_B(\ell_R^+ \ell_R^- \rightarrow \bar{u}_L u_L) \\ 0 \\ 0 \\ d\sigma_B(\ell_R^+ \ell_R^- \rightarrow \bar{d}_L d_L) \end{pmatrix} = d\sigma_B(\ell_R^+ \ell_R^- \rightarrow \bar{q}_L q_L) \begin{pmatrix} 1 \\ 0 \\ 0 \\ 1 \end{pmatrix}, \quad (2.61)$$

where “ $u$ ” and “ $d$ ” denote here the up and down components of a  $L$ -handed fermion doublet. The exponentiated DL matrix reads

$$e^{\text{DL}} = \frac{1}{4} e^{-\mathcal{L}} \begin{pmatrix} 4 \cosh^2(\mathcal{L}/2) & 2 \sinh(\mathcal{L}) & 2 \sinh(\mathcal{L}) & 4 \sinh^2(\mathcal{L}/2) \\ 2 \sinh(\mathcal{L}) & 4 \cosh^2(\mathcal{L}/2) & 4 \sinh^2(\mathcal{L}/2) & 2 \sinh(\mathcal{L}) \\ 2 \sinh(\mathcal{L}) & 4 \sinh^2(\mathcal{L}/2) & 4 \cosh^2(\mathcal{L}/2) & 2 \sinh(\mathcal{L}) \\ 4 \sinh^2(\mathcal{L}/2) & 2 \sinh(\mathcal{L}) & 2 \sinh(\mathcal{L}) & 4 \cosh^2(\mathcal{L}/2) \end{pmatrix}, \quad (2.62)$$

where  $\mathcal{L} = g^2/16\pi^2 \log^2(E_{\text{cm}}^2/m_W^2)$ .

We see that DL effects induce a non-vanishing cross-section for charged processes with  $g \neq f$  in eq. (2.57), such as  $\bar{u}_L d_L$  and  $\bar{d}_L u_L$  production. Clearly this stems from the emission of real soft  $W$ -bosons, which is allowed in the semi-inclusive final state. Such charged cross-sections are proportional to the Born cross-section for the corresponding neutral ( $\bar{u}_L u_L$  or  $\bar{d}_L d_L$ ) processes, and they are not drastically smaller than those because the double-logarithm is sizable at VHEL energies. Therefore they can be measured bringing additional sensitivity to the charge-preserving Born amplitudes and to the corresponding short-distance new physics effects. The interplay with short-distance physics is even more interesting for the  $LL$ -chirality process. In that case,  $\vec{\sigma}_{\text{si}}$  is a 16-dimensional vector that contains 4 observable ( $\ell^+ \ell^-$ -initiated) processes with final states  $\bar{u}_L u_L$ ,  $\bar{u}_L d_L$ ,  $\bar{d}_L u_L$  and  $\bar{d}_L d_L$ . DL is a  $16 \times 16$  matrix that relates the observable processes to 16 Born amplitudes, among which those (like, e.g.,  $\bar{\nu}_\ell \ell^- \rightarrow \bar{u}_L d_L$ ) that are sensitive to new charged current interactions. We can thus probe the latter interactions even with the neutral  $\ell^+ \ell^-$  VHEL collisions.

The black dashed lines in Figure 2.3 quantify the impact of the EW radiation effects on the neutral semi-inclusive cross-sections relative to the Born predictions. The effects are smaller than for exclusive cross-sections, as qualitatively expected owing to the partial cancellation between virtual and real radiation. While this suggests that resummation might play a less relevant role in semi-inclusive predictions, we point out that one-loop double logarithms are insufficient for accurate predictions. This is shown in the purple dashed line in the figure, which is obtained by truncating at the one-loop order the

exponentiated DL matrix. It would be interesting to study the impact of single logarithms on the predictions. This could be achieved by combining the single radiative logs from Ref.s [178, 202] with the factorized formulas for real emissions in Ref.s [171, 203] (which however would have to be extended to include also the soft radiation region), but is left to future work.

As a final technical note, we remark that the DL matrix is negative semi-defined with a single vanishing eigenvector that corresponds to the “fully-inclusive” cross-section, further averaged over the  $SU(2)_L$  color of the initial states. Specifically the vanishing eigenvector of eq. (2.62) is  $(1, 1, 1, 1)^t$ , which corresponds to the sum of the cross-sections over the  $SU(2)_L$  gauge indices of the final states. Therefore in this case the double logarithmic effects cancel on the “fully-inclusive” cross-section, in accordance with the KLN theorem since the right-handed initial leptons are  $SU(2)_L$  singlets. Clearly this does not happen for the  $LL$ -chirality processes (nor for  $LR$ -chirality) and the average over leptons and neutrinos in the initial states would be necessary for the cancellation. The vanishing eigenvalue controls the behavior of the DL exponential at asymptotically high energies. In the case of eq. (2.62), we have

$$e^{\text{DL}} \xrightarrow{E_{\text{cm}} \rightarrow \infty} \frac{1}{4} \begin{pmatrix} 1 & 1 & 1 & 1 \\ 1 & 1 & 1 & 1 \\ 1 & 1 & 1 & 1 \\ 1 & 1 & 1 & 1 \end{pmatrix}, \quad (2.63)$$

and all the semi-inclusive cross-section listed in eq (2.61) become equal. Notice however this only holds at asymptotic energies, way above the VHEL energies. Cross-sections equality becomes a reasonable (better than order-one) approximation only for if  $g^2/16\pi^2 \log^2(E_{\text{cm}}^2/m_W^2)$  is as large as  $\sim 1.5$ , i.e.  $E_{\text{cm}} \gtrsim 10000$  TeV.

### 2.3.2 Di-boson production

We now turn to the production of two energetic vector or Higgs bosons. We are interested in reactions that are not power-like suppressed at high energy, therefore we restrict our attention to “longitudinal” processes entailing the production of zero-helicity  $W$  and  $Z$  bosons and Higgs, and to “transverse” di-boson processes where the  $W$  and the  $Z$  (or, the photon) have  $\pm 1$  helicities. Indeed the “mixed” longitudinal/transverse production processes are suppressed by  $m_W/E_{\text{cm}}$  at the amplitude level, as readily understood (see e.g. [174, 203]) by combining the Goldstone Boson Equivalence Theorem with the selection rules associated with the  $SU(2)_L \times U(1)_Y$  SM group.

The new physics interactions we consider in Section 2.4 only affect longitudinal di-boson production cross-sections, which thus play the role of the signal in our analysis. We nevertheless also need the transverse cross-sections for an estimate of the background. We discuss the calculation of the (exclusive and semi-inclusive) cross-sections for the two

type of processes in turn.

#### Longitudinal di-boson

We consider the production, out of  $\ell^+\ell^-$ , of one of the following hard final states

$$W_0^+W_0^-, \quad Z_0h, \quad W_0^\pm Z_0, \quad W_0^\pm h, \quad (2.64)$$

where the subscript “0” refers to the helicity of the massive vectors, and “ $h$ ” denotes the physical Higgs particle. Obviously only the first two final states can be produced in an exclusive process, while the latter ones require the emission of at least one charged  $W$  and therefore they only occur at the semi-inclusive level. Notice that the ones listed above are the only hard final states with longitudinal bosons and Higgs that can be produced by soft EW bosons radiation out of sizable Born-level  $2 \rightarrow 2$  cross-sections. Therefore they are the only longitudinal di-boson processes that can be considered for precise VHEL measurements in the high-energy regime.

At energies much above  $m_W$ , the adequate description of longitudinally-polarized massive vectors is provided by the charged and neutral Goldstone boson scalars  $\pi^\pm$  and  $\pi_0$  (see Appendix B.2). Together with the Higgs, they form a canonical  $SU(2)_L \times U(1)_Y$  doublet  $H$  with  $1/2$  hypercharge, reported in eq. (B.26). We thus need to consider amplitudes and density matrices associated with the hard processes

$$\begin{aligned} \ell_{-1/2}^+(k_1)\ell_{+1/2}^-(k_1) &\rightarrow \bar{H}(k_3, \alpha_3^{\bar{d}}) H(k_4, \alpha_4^d), \\ \bar{\ell}_{+1/2}(k_1, \alpha_1^{\bar{d}})\ell_{-1/2}(k_2, \alpha_2^d) &\rightarrow \bar{H}(k_3, \alpha_3^{\bar{d}}) H(k_4, \alpha_4^d), \end{aligned} \quad (2.65)$$

for, respectively,  $L$ -handed and  $R$ -handed production.<sup>17</sup> For the gauge group indices we employ the same notation as in eq. (2.36), supplemented by the superscripts  $d$  ( $\bar{d}$ ) to indicate that the indices belong to the doublet (conjugate-doublet) representation. With a slight abuse of notation we are denoting as  $\ell_{-1/2} = (\nu_{\ell,-1/2}, \ell_{-1/2}^-)^t$  the lepton doublet with  $-1/2$  helicity and with  $\ell_{+1/2}$  the conjugate-doublet with helicity  $+1/2$ . Notice that final states with two  $H$  or two  $\bar{H}$  need not to be included because they are power-like suppressed at high energy by hypercharge conservation.

The relevant density matrices are obtained as a straightforward application of the results in Section 2.2.2. The need for employing  $H$  and  $\bar{H}$  as external states does not pose any additional difficulty (relative to the di-fermion processes) in the evaluation of exclusive cross-sections. That is because the double logs are mere multiplicative factors in front of the Born-level density matrix (2.56). Therefore the exclusive cross-sections still take the form of eq. (2.58) and are proportional to the corresponding Born-level predictions. For

---

<sup>17</sup>The production from opposite-chirality leptons is negligible, both in the SM and in the presence of the new contact interactions we investigate in the following section.

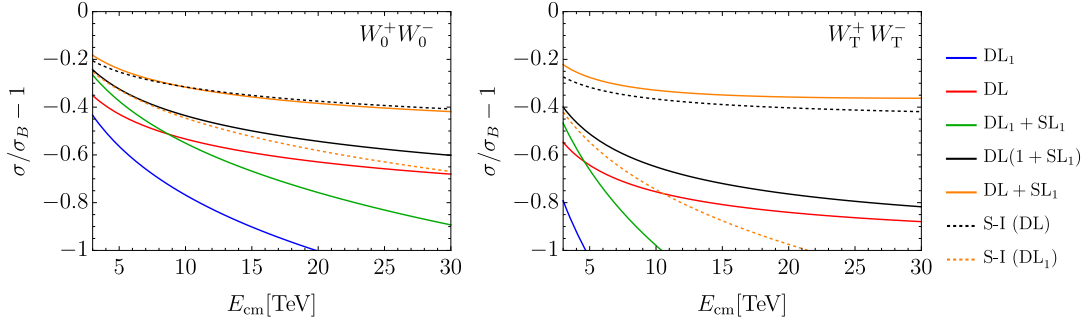


Figure 2.4 – Same as Figure 2.3, but for di-boson production. As explained in Section 2.4.2, the cross-sections for  $W^+W^-$  production are integrated in the angular region  $\theta_* \in [67^\circ, 150^\circ]$ .

the semi-inclusive cross-section, we can proceed as for di-fermions in the determination of the  $K_i$  exponential factors, using in particular eq. (B.31) which also holds in the present case because  $H$  and  $\bar{H}$  are doublets. However in order to apply eq. (2.55) we must first express the  $\mathcal{D}_{\text{si}}^{\alpha\bar{\alpha}}$  density matrix, which is written in the isospin basis ( $H$  and  $\bar{H}$ ), in the physical basis of the charge and CP eigenstates  $h$ ,  $Z_0 = \pi_0$  and  $W_0^\pm = \pi^\pm$ . This is achieved by simply inverting eq. (B.26). The final result can again be expressed in terms of the Born-level cross-sections in the form of eq. (2.60).

The results display the same qualitative features as di-fermions. In particular we observe the same interplay between short-distance physics affecting the neutral- and the charged-current Born amplitudes, which we investigate in Section 2.4 in details. Also at the quantitative level, the relative impact of radiation radiation is similar, as expected because  $\text{SU}(2)_L$  doublets are involved also in these processes. This is shown in the left panel of Figure 2.4, where we show the exclusive and semi-inclusive cross-section predictions for  $W_0^+W_0^-$ . The different predictions are obtained as explained in the previous section for the di-fermion processes. Notice in particular the exclusive predictions that include one-loop single logarithms as in eq. (2.59). We employ these predictions for exclusive cross-section in the phenomenological studies of Section 2.2.2.

### Transverse di-boson

Vector bosons ( $W$ ,  $Z$ , or  $\gamma$ ) with transverse helicity  $T = \pm 1$  have zero hypercharge and they decompose as a real triplet plus a singlet under the SM  $\text{SU}(2)_L$ , as in eq. (B.27). Therefore three non-power-suppressed hard processes have to be considered for  $L$ -handed

production

$$\begin{aligned}
\bar{\mu}_{+1/2}(k_1, \alpha_1^{\bar{d}})\ell_{-1/2}(k_2, \alpha_2^d) &\rightarrow B(k_3) B(k_4), \\
\bar{\mu}_{+1/2}(k_1, \alpha_1^{\bar{d}})\ell_{-1/2}(k_2, \alpha_2^d) &\rightarrow W(k_3, \alpha_3^t) B(k_4), \\
\bar{\mu}_{+1/2}(k_1, \alpha_1^{\bar{d}})\ell_{-1/2}(k_2, \alpha_2^d) &\rightarrow W(k_3, \alpha_3^t) W(k_4, \alpha_4^t),
\end{aligned} \tag{2.66}$$

while only one is relevant for the production initiated by  $R$ -handed leptons <sup>18</sup>

$$\ell_{-1/2}^+(k_1)\ell_{+1/2}^-(k_2) \rightarrow B(k_3) B(k_4), \tag{2.67}$$

The “t” superscript in eq. (2.66) refers to the triplet nature of the  $W$  indices.

Unlike for di-fermion and longitudinal di-boson, the transverse di-boson cross-sections for  $L$ -handed initial leptons are linear combinations of several distinct density matrices with different  $SU(2)_L$  quantum numbers. Therefore the exclusive cross-sections are not proportional, unlike in eq. (2.58), to the corresponding Born cross-sections in general. For instance in the  $\gamma\gamma$  cross-section the contribution from the  $WW$  final state experiences a stronger Sudakov suppression (2.56) than one from the  $BB$  (or  $WB$ ) final state, owing to the higher  $SU(2)_L$  Casimir of the final states.

The evaluation of the semi-inclusive cross-sections proceeds as for the longitudinal di-bosons. Namely we derive the cross-sections for the physical states by inverting eq. (B.27) and we compute the double-logarithm exponentials using eq. (B.36) on the  $SU(2)$  triplet subspace. Clearly the need of combining different density matrices complicates the calculation, but it does not introduce any novel conceptual aspect. At the quantitative level instead, the situation is significantly different than for di-fermions and longitudinal di-bosons. As shown on the right panel of Figure 2.4, EW radiation effects are much larger due to the larger Casimir  $c_t = 2$  of the triplet representation. A sufficiently accurate modeling of these effects will probably require resummation even at the lowest VHEL energy  $E_{\text{cm}} = 3$  TeV.

The figure reports the cross-section of the  $W_T^+ W_T^-$  final state. This final state, together with  $W_T^+ Z_T$ , is the only transverse di-boson process we will consider in Section 2.4 (as a background to the corresponding longitudinal processes). Notice however that there are many other transverse di-boson processes (namely  $ZZ$ ,  $Z\gamma$ ,  $\gamma\gamma$ , and  $W\gamma$ ) that can be measured at the VHEL. These processes probe heavy new physics in the EW sector. In particular, as shown in Refs. [149, 150, 153], they are sensitive (together with di-fermions) to minimal Dark Matter in large-multiplets. The large effects of EW radiation might have a strong impact on these studies.

<sup>18</sup>The Born process  $\ell_{-1/2}^+(k_1)\ell_{+1/2}^-(k_2) \rightarrow W(k_3, \alpha_3^t) W(k_4, \alpha_4^t)$  is power-suppressed in the SM.

## 2.4 Sensitivity projections

As described in the Introduction, we target effects from short-distance new physics that grow quadratically with the collision energy, to be probed in  $\ell^+\ell^-$  collisions at the highest available energy  $E = E_{\text{cm}}$ . In this section we consider the dimension-6 EFT operators listed in Table 2.2, and we estimate the sensitivity of muon colliders of energies  $E_{\text{cm}} = 3, 10, 14$  or  $30$  TeV to their Wilson coefficients. We assume a baseline integrated luminosity [110]

$$\hat{\mathcal{L}} = 10 \text{ ab}^{-1} \left( \frac{E_{\text{CM}}}{10 \text{ TeV}} \right)^2. \quad (2.68)$$

Semi-quantitative comments on the impact of a reduced luminosity target are postponed to the Conclusions. We base our projections on statistically-dominated measurements of exclusive and semi-inclusive cross-sections for the processes listed in Table 2.3. In the table, for each process we label with a check mark the operators that produce a quadratically growing-with-energy correction to the SM cross-section.

The target EFT operators are selected to represent generic manifestations, at energies much below the new physics scale, of the BSM scenarios we investigate in Section 2.4.3. These are Composite Higgs, Composite Top and a minimal  $Z'$  model, which we select as concrete examples of new physics in the Higgs, Top and EW-gauge sectors. Among the many operators that emerge in these scenarios, we focused our attention on those that display energy growth in  $2 \rightarrow 2$  scattering processes at the muon collider. We will see in Section 2.4.3 that other operators offer a weaker sensitivity to the same BSM scenarios.

The phenomenological analysis of the various processes listed in Table 2.3 is described in Sections 2.4.1 and 2.4.2, focusing respectively on the effects of the “W&Y” and of the “Di-boson” operators of Table 2.2. In an attempt to mimic realistic experimental results, we include reconstruction (and, in some case, mistag) efficiencies at a level that is comparable with the CLIC detector performances, which we extract, whenever possible, from Refs. [37, 180]. Table 2.3 displays surprisingly low efficiencies for certain processes (e.g.,  $t\bar{t}$ ), entailing a considerable degradation of the measurement uncertainty. In Sections 2.4.1 and 2.4.2 we also present our results for the sensitivity of muon colliders to the corresponding set of operators, with the main aim of outlining the impact of the EW radiation effects on the analysis. The operators in the last class, dubbed “3<sup>rd</sup> family” in Table 2.2, are not discussed explicitly but the sensitivity projection results are reported in Appendix B.3. The relevant final states,  $t\bar{t}$ ,  $b\bar{b}$  and  $t\bar{b}$  are discussed in Section 2.4.1.

### 2.4.1 W&Y operators

The first two operators we consider are those associated with the W and Y parameters of LEP EW precision tests [35], namely  $O_{2W}$  and  $O_{2B}$  defined as in Table 2.2. These operators arise in the so-called *universal* scenarios [34, 35], that is new physics that couples

## 2.4. Sensitivity projections

	SILH basis	Warsaw-like basis
W&Y	$O_{2W} = (D_\mu W^{\mu\nu,a})^2$ $O_{2B} = (\partial_\mu B^{\mu\nu})^2$	$O'_{2W} = J_L^{a,\mu} J_{L,\mu}^a \quad J_L^{a,\mu} = \frac{1}{2} \sum_f \bar{f} \gamma^\mu \sigma^a f$ $O'_{2B} = J_Y^\mu J_{Y,\mu} \quad J_Y^\mu = \sum_f Y_f \bar{f} \gamma^\mu f$
Di-boson	$O_W = \frac{ig}{2} (H^\dagger \sigma^a \overleftrightarrow{D}_\mu H) D^\nu W_{\mu\nu}^a$ $O_B = \frac{ig'}{2} (H^\dagger \overleftrightarrow{D}_\mu H) \partial^\nu B_{\mu\nu}$	$O'_W = \frac{g^2}{4} (H^\dagger i \overleftrightarrow{D}_\mu \sigma^a H) (\bar{L}_L \gamma^\mu \sigma^a L_L)$ $O'_B = -\frac{g'^2}{4} (H^\dagger i \overleftrightarrow{D}_\mu H) (\bar{L}_L \gamma^\mu L_L)$ $-\frac{g'^2}{2} (H^\dagger i \overleftrightarrow{D}_\mu H) (\bar{l}_R \gamma^\mu l_R)$
3 <sup>rd</sup> family	$O_{qD}^{(3)} = (\bar{q} \gamma^\mu \sigma^a q) (D^\nu W_{\mu\nu}^a)$ $O_{qD}^{(1)} = (\bar{q} \gamma^\mu q) (\partial^\nu B_{\mu\nu})$ $O_{tD} = (\bar{t} \gamma^\mu t) (\partial^\nu B_{\mu\nu})$	$O'_{qD}^{(3)} = (\bar{q} \gamma^\mu \sigma^a q) J_{L,\mu}^a$ $O'_{qD}^{(1)} = (\bar{q} \gamma^\mu q) J_{Y,\mu}$ $O'_{tD} = (\bar{t} \gamma^\mu t) J_{Y,\mu}$

Table 2.2 – The operators under consideration in their “SILH” [10] form and, after using the equations of motion, expressed as a linear combination of Warsaw [9] operators.  $Y_f$  is the hypercharge of the fermionic field  $f$ . In the operators involving the 3<sup>rd</sup> family the fields  $t$  and  $q$  denote respectively the right-handed and left-handed top quark.

Process	$N$ (Ex)	$N$ (S-I)	Eff.	$O'_{2W}$	$O'_{2B}$	$O'_W$	$O'_B$	$O'_{qD}^{(3)}$	$O'_{qD}^{(1)}$	$O'_{uD}$
$e^+ e^-$	6794	9088	100%	✓	✓					
$e \nu_e$	—	2305	100%	✓	✓					
$\mu^+ \mu^-$	206402	254388	100%	✓	✓					
$\mu \nu_\mu$	—	93010	100%	✓	✓					
$\tau^+ \tau^-$	6794	9088	25%	✓	✓					
$\tau \nu_\tau$	—	2305	50%	✓	✓					
$jj$ (Nt)	19205	25725	100%	✓	✓					
$jj$ (Ch)	—	5653	100%	✓	✓					
$c \bar{c}$	9656	12775	25%	✓	✓					
$c j$	—	5653	50%	✓	✓					
$b \bar{b}$	4573	6273	64%	✓	✓			✓	✓	
$t \bar{t}$	9771	11891	5%	✓	✓			✓	✓	✓
$b t$	—	5713	57%	✓	✓			✓	✓	✓
$Z_0 h$	680	858	26%			✓	✓			
$W_0^+ W_0^-$	1200	1456	44%			✓	✓			
$W_T^+ W_T^-$	2775	5027	44%							
$W^\pm h$	—	506	19%			✓	✓			
$W_0^\pm Z_0$	—	399	23%			✓	✓			
$W_T^\pm Z_T$	—	2345	23%							

Table 2.3 – The exclusive and semi-inclusive processes employed for the sensitivity projections. The operators that give a growing-with-energy contribution to each operator are labeled with a check mark. The expected number of events (before efficiencies) is for  $E_{\text{cm}} = 10$  TeV with the integrated luminosity (2.68).

dominantly to the bosonic sector of the SM. Employing  $O_{2W}$  and  $O_{2B}$  is convenient in the low-energy context of the LEP experiment, however for our purpose it is better to trade them for the current-current operators  $O'_{2W}$  and  $O'_{2B}$  (see again Table 2.2), using the SM equations of motion. In doing so, we neglect the contribution to the  $O'_W$  and  $O'_B$  operators, which are expected to have no impact on the sensitivity. In what follows we parameterize the  $O'_{2W}$  and  $O'_{2B}$  operator coefficients

$$G'_{2W} = -\frac{g^2 W}{2m_W^2}, \quad G'_{2B} = -\frac{g'^2 Y}{2m_W^2}, \quad (2.69)$$

in terms of the dimensionless parameters  $W$  and  $Y$ .

The relevant scattering processes, listed in Table 2.3, are the production of two energetic fermions in the central region of the detector. Specifically, as explained at the end of Section 2.3, we have in mind the two hard particles whose invariant mass is higher than around 85% of the total collider  $E_{\text{cm}}$ , and a scattering angle  $\theta_* \in [30^\circ, 150^\circ]$ . We assume perfect detector sensitivity to massive  $W$  and  $Z$  bosons of arbitrary low 3-momentum, enabling the measurement of exclusive scattering cross-sections where the emission of massive vectors (and of photons with hardness above  $m_W^2$ ) is vetoed. The exclusive cross-section measurements are combined with the semi-inclusive cross-sections, where the emission of an arbitrary number (including zero) of massive vectors or hard photons is allowed.

For each inclusive and semi-inclusive final state, we employ cross-section measurements in 10 equally-spaced bins of  $\cos \theta_*$  in the range  $[-\sqrt{3}/2, \sqrt{3}/2]$ . In processes (e.g.,  $jj$ , or  $b\bar{b}$ ) where the two final states are effectively indistinguishable,  $\cos \theta_*$  is defined to be positive and 5 bins are employed. We assume cross-section measurements with purely statistical uncertainties, which we estimate based on the number of events that are expected in the SM.

Of course in order to combine the exclusive and semi-inclusive cross-sections for the same (neutral) hard final state we must take into account that the exclusive events are also counted in the measurement of the semi-inclusive cross-section. It is thus convenient to consider a cross-section *with radiation*, defined as the difference between the semi-inclusive and the exclusive cross-sections

$$\sigma_{\text{rad}} \equiv \sigma_{\text{si}} - \sigma_{\text{ex}}. \quad (2.70)$$

The measurement of  $\sigma_{\text{rad}}$  can be combined with the one of  $\sigma_{\text{ex}}$  since they are statistically independent. For charged hard final states there is instead only one type of cross-section, which necessarily involves EW radiation emission by charge conservation. We will refer to the charged cross-section as “semi-inclusive” or “with radiation” interchangeably.

We now discuss the di-fermion processes individually.



- **$e^+e^-$ ,  $\mu^+\mu^-$  and  $\tau^+\tau^-$ :** We assume 100% reconstruction efficiency for muon and electrons, and an efficiency of 50% [180] for each  $\tau$  lepton. Notice that the cross-section for muons is around 30 times larger than for the other leptons. This is mostly due to the  $t$ -channel enhancement of the elastic  $\mu^+\mu^-$  scattering.
- **$c\bar{c}$  and  $b\bar{b}$ :** We assume 50% and 80% efficiency for tagging respectively charm and bottom quark jets [180]. We ignore the mis-tag of light jets, as well as  $c/b$  misidentification. No information on the charge of the tagged quark is employed.
- **$jj$ :** We consider the production of two light quarks  $u$ ,  $d$  or  $s$ , which we suppose to be reconstructed as jets with 100% efficiency. In Table 2.3 we report separately the production of a neutral (Nt) and of a charged (Ch) quark/anti-quark pair, but the two processes are collected into a single 2-jets final state. We also include the contribution from mistagged  $b$  and  $c$  quarks.
- **$t\bar{t}$ :** Based on Ref.s [37, 204], we estimate as 5% the total efficiency for the reconstruction of the  $t\bar{t}$  pair. This (somewhat low) efficiency estimate only includes the semi-leptonic  $t\bar{t}$  final states, in which the charge of the tagged top quarks can be measured.
- **$tb$  and  $cj$ :** We use 50% and 80% tag efficiency for the charm and the bottom, respectively, and  $\sqrt{0.05} = 20\%$  efficiency for the top. The charge of the top quark is assumed to be reconstructed.
- **$e\nu_e$ ,  $\mu\nu_\mu$  and  $\tau\nu_\tau$ :** The efficiency is 100% for muons and electrons, and 50% for the  $\tau$ . It should be noted that, because of the invisible neutrino, the hard scattering region of this final state can not be selected with a cut on the invariant mass of the two particles. The selection will have instead to be performed on the energy and the transverse momentum of the observed charged lepton.

The different dependence on  $W$  and  $Y$  of the neutral- and charged-current Born amplitudes entails (see Section 2.3.1) a different dependence on these parameters of the exclusive and semi-inclusive cross-sections. The statistical combination of the two types of cross-sections can thus increase the sensitivity, as illustrated in Figure 2.5. The left panel displays the 95% CL sensitivity of  $c\bar{c}$  production to  $W$  and  $Y$ , comparing the impact of the exclusive cross-section (in green) to that (in orange) of the cross-section with radiation. The two measurements probe different regions of the  $W$  and  $Y$  parameter space, and a significant sensitivity gain is observed in their combination (in blue). The green and blue lines on the right panel of Figure 2.5 display a similar complementarity pattern for the  $e^+e^-$  final state. There also appears an even stronger complementarity with the measurement of the  $e\nu$  cross-section, reported as a gray dashed line. The emergence of the  $e\nu$  process, as well as the other charged final states in Table 2.3, is entirely due to EW radiation. Nevertheless its (semi-inclusive) cross-section is large, because EW radiation is indeed a prominent phenomenon at  $E_{\text{cm}} \simeq 10$  TeV. Furthermore the cross-section displays a peculiar dependence on new physics, producing a sensitivity contour that is different from

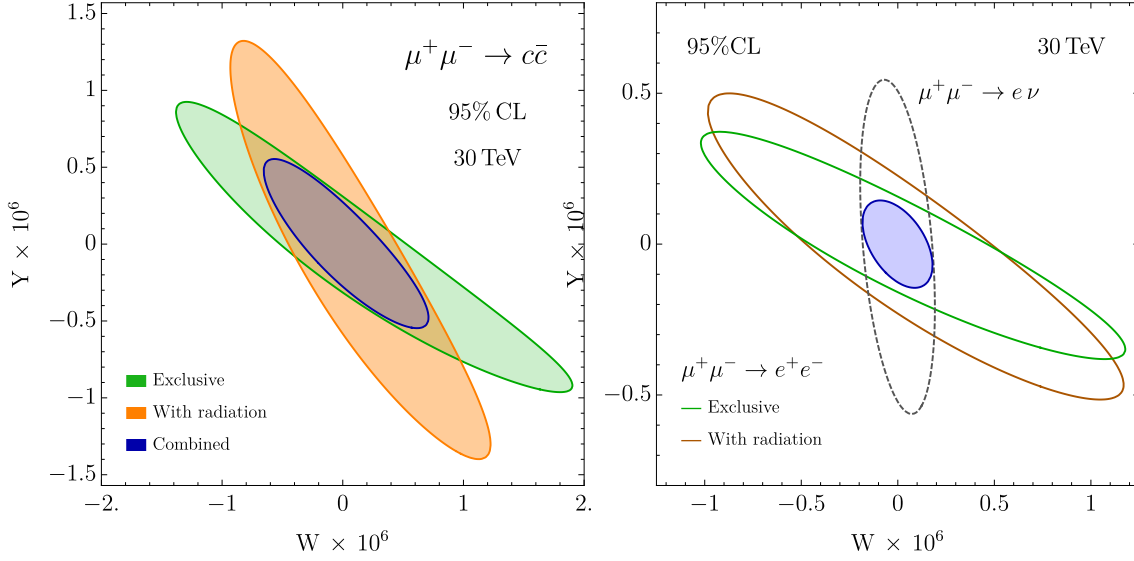
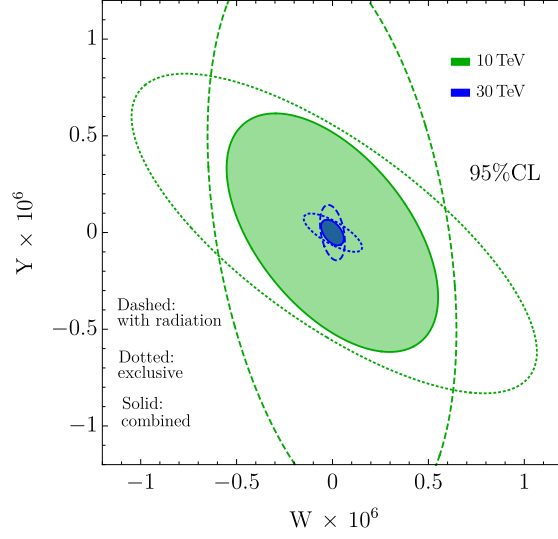


Figure 2.5 – 95% CL sensitivities to the  $W$  and  $Y$  parameters of the 30 TeV muon collider. Exclusive and “with radiation” (i.e., semi-inclusive minus exclusive) cross-section measurements of the  $c\bar{c}$  process are considered in the left panel. The right panel shows the impact of  $e^+e^-$  (exclusive and “with radiation”) and  $e\nu$  (that only exists at the semi-inclusive level) final states.

that of the  $e^+e^-$  measurements. The statistical combination of the three measurements (in blue) improves the sensitivity significantly.

The final results of our analysis including all channels are summarized in Figure 2.6 and in Table 2.4. The figure displays the sensitivity contours of exclusive measurements as dotted lines, and the combined impact of charged and of neutral “with radiation” cross-sections, in dashed. The combination of all measurements is also shown. The table reports the results for 3, 10, 14 and 30 TeV, comparing the sensitivity of exclusive cross-sections alone with the total combination.

At the High-Luminosity LHC (HL-LHC), it will be possible to probe the  $W$  and  $Y$  parameters at the level of  $4 \cdot 10^{-5}$  and  $8 \cdot 10^{-5}$ , respectively, at 95% CL [1, 2, 11]. Table 2.4 shows that the 3 TeV muon collider would improve by one order of magnitude or more, and the sensitivity improves quadratically with the muon collider energy. Among the other future collider projects [205], CLIC at 3 TeV has the best sensitivity, of around  $4 \cdot 10^{-6}$  for both parameters [180]. This is of course comparable with the 3 TeV muon collider sensitivity, and a factor 10 worst than that of the muon collider at 10 TeV. The comparison with FCC-hh projections is even more favorable to the muon collider.


 Figure 2.6 – 95% CL sensitivities to the  $W$  and  $Y$  at the 10 and 30 TeV muon collider.

	Exclusive-only [95% CL]			Combined [95% CL]		
	$W \times 10^7$	$Y \times 10^7$	$\rho_{W,Y}$	$W \times 10^7$	$Y \times 10^7$	$\rho_{W,Y}$
3 TeV	$[-53, 53]$	$[-48, 48]$	-0.72	$[-41, 41]$	$[-46, 46]$	-0.60
10 TeV	$[-5.71, 5.71]$	$[-4.47, 4.47]$	-0.74	$[-3.71, 3.71]$	$[-4.16, 4.16]$	-0.54
14 TeV	$[-3.11, 3.11]$	$[-2.31, 2.31]$	-0.74	$[-1.90, 1.90]$	$[-2.13, 2.13]$	-0.52
30 TeV	$[-0.80, 0.80]$	$[-0.52, 0.52]$	-0.75	$[-0.42, 0.42]$	$[-0.47, 0.47]$	-0.48

 Table 2.4 – Single-operator 95% CL reach and correlation for the  $W$  &  $Y$  parameters at different muon collider energies including only exclusive cross-sections and combining all measurements. Since the likelihood is dominated by the linear terms in the new physics parameters, the single parameter reach plus the correlation characterizes our results completely.

### 2.4.2 Diboson operators

The setup for this analysis is similar to that of Ref. [118]. Namely we consider the SILH operators  $O_W$  and  $O_B$ , we convert them into the current-current interactions  $O'_W$  and  $O'_B$  as in Table 2.2, and we study their effect on the production of high-energy vector bosons and Higgs. Notice that, by the equivalence theorem,  $O'_W$  and  $O'_B$  only significantly affect the production of longitudinally polarized vector bosons. We are therefore here studying the production of high-energy longitudinally vector bosons and Higgs, with the production of transversely polarized vector bosons playing merely the role of background. Since the effects are quadratically enhanced by the energy, such high-energy di-boson processes are by far the best probe of these operators at the muon collider [118].

We thus consider, among those in Table 2.3, the following final states

- **$Zh$** : Following Ref. [118], we consider an efficiency of 26% for tagging the two hard and central final state particles, with a selection that reduces the background to a manageable level. Notice that this final state is dominated by the longitudinal helicity channel  $Z_0h$ .
- **$W^+W^-$** : Again like in [118], we assume a 44% efficiency for the detection of the two  $W$  bosons in the semi-leptonic decay channel, where the charge of the  $W$ 's can be reconstructed. Transverse  $WW$  production plays here the role of background.
- **$Wh$** : We consider an efficiency of 19%, having in mind the leptonic  $W$  decay, and  $h \rightarrow b\bar{b}$ . Like for  $Zh$ , there is no relevant background from transverse production.
- **$WZ$** : We apply an efficiency of 23%, which corresponds to the leptonic  $W$  and the hadronic  $Z$  decay. The background from transverse  $WZ$  production is considerable, and is taken into account.

In our analysis we do not consider the possibility of employing the decay angles of the bosons to extract information on their polarization. Therefore the transverse di-bosons processes  $W_T^+W_T^-$  and  $W_T Z_T$  are effectively irreducible backgrounds to the corresponding longitudinal processes, and the scattering angle  $\theta_*$  is the only discriminating variable. An increased lower cut on  $\theta_*$  benefits the sensitivity, as it suppresses the  $t$ -channel enhancement of the transverse background processes. After optimization we find, like in Ref. [118], that a good signal sensitivity is obtained by the measurement of fiducial  $WW$  and  $WZ$  cross-sections in the range

$$\theta_* \in [67^\circ, 150^\circ]. \quad (2.71)$$

The possibility of binning  $\theta_*$  has been considered, but found not to improve the sensitivity. Our analysis will thus be only based on the measurement of the fiducial  $WW$  and  $WZ$  cross-sections in the above region, and of the  $Zh$  and  $Wh$  cross-sections for  $\theta_* \in [30^\circ, 150^\circ]$ . As in the previous section, both exclusive and semi-inclusive cross-sections will be employed for the neutral processes  $WW$  and  $Zh$ , plus the semi-inclusive charged cross-sections for  $Wh$  and  $WZ$ .

The results of our analysis are reported in Table 2.5 and on the left panel of Figure 2.7, in terms of the dimensionful coefficients ( $C_B$  and  $C_W$ ) of the  $O'_B$  and  $O'_W$  operators of Table 2.2. Our findings are quantitatively similar to the ones of Ref. [118]. We can thus refer to that article for the (very favorable) assessment of the muon collider sensitivity to  $C_B$  and  $C_W$  in comparison with current knowledge and with other future colliders. We devote the rest of this section to discuss the approximate flat direction of the likelihood in the  $(C_B, C_W)$  plane, which we observe in Figure 2.7 (left panel).

The flat direction entails a strong degradation of the marginalized sensitivity, as in Table 2.5. Furthermore this degradation brings the marginalized  $C_B$  and  $C_W$  limits to large values, in a region where the likelihood is considerably affected by the contributions

## 2.4. Sensitivity projections

Single Operator (Exclusive-only) [95% CL]				
$C_B[10^{-4} \text{ TeV}^{-2}]$		$C_W[10^{-4} \text{ TeV}^{-2}]$		
	Linear	Quadratic	Linear	Quadratic
3 TeV	$[-170, 170]$	$[-189, 157]$	$[-77.4, 77.4]$	$[-81, 74.4]$
10 TeV	$[-15.3, 15.3]$	$[-17, 14.2]$	$[-8.18, 8.18]$	$[-8.62, 7.82]$
14 TeV	$[-7.86, 7.86]$	$[-8.69, 7.25]$	$[-4.40, 4.40]$	$[-4.65, 4.20]$
30 TeV	$[-1.73, 1.73]$	$[-1.92, 1.6]$	$[-1.1, 1.1]$	$[-1.16, 1.04]$

Single Operator (Combined) [95% CL]				
$C_B[10^{-4} \text{ TeV}^{-2}]$		$C_W[10^{-4} \text{ TeV}^{-2}]$		
	Linear	Quadratic	Linear	Quadratic
3 TeV	$[-153, 153]$	$[-169, 142]$	$[-65.8, 65.8]$	$[-68.2, 63.6]$
10 TeV	$[-12.8, 12.8]$	$[-13.9, 11.9]$	$[-6.14, 6.14]$	$[-6.37, 5.93]$
14 TeV	$[-6.40, 6.40]$	$[-6.95, 5.99]$	$[-3.17, 3.17]$	$[-3.29, 3.06]$
30 TeV	$[-1.34, 1.34]$	$[-1.44, 1.25]$	$[-0.71, 0.71]$	$[-0.737, 0.686]$

Marginalized (Exclusive-only) [95% CL]				
$C_B[10^{-4} \text{ TeV}^{-2}]$		$C_W[10^{-4} \text{ TeV}^{-2}]$		
	Linear	Quadratic	Linear	Quadratic
3 TeV	$[-478, 478]$	$[-352, 596]$	$[-217, 217]$	$[-583, 125]$
10 TeV	$[-53.2, 53.2]$	$[-35.2, 50]$	$[-28.4, 28.4]$	$[-53.5, 14.2]$
14 TeV	$[-29.4, 29.4]$	$[-18.6, 25]$	$[-16.5, 16.5]$	$[-27.5, 7.82]$
30 TeV	$[-7.98, 7.98]$	$[-4.45, 5.19]$	$[-5.04, 5.04]$	$[-6.16, 2.05]$

Marginalized (Combined) [95% CL]				
$C_B[10^{-4} \text{ TeV}^{-2}]$		$C_W[10^{-4} \text{ TeV}^{-2}]$		
	Linear	Quadratic	Linear	Quadratic
3 TeV	$[-442, 442]$	$[-341, 535]$	$[-189, 189]$	$[-426, 115]$
10 TeV	$[-44, 44]$	$[-33.4, 43.4]$	$[-21.1, 21.1]$	$[-35.1, 12.3]$
14 TeV	$[-23.1, 23.1]$	$[-17.6, 21.6]$	$[-11.4, 11.4]$	$[-17.6, 6.6]$
30 TeV	$[-5.24, 5.24]$	$[-4.12, 4.43]$	$[-2.79, 2.79]$	$[-3.70, 1.62]$

Table 2.5 – Single operator and marginalized 95% reach on  $C_B$  and  $C_W$ , at different muon collider energies. The sensitivity of exclusive cross-section measurements alone is shown separately from the combination of all the measurements. The significant degradation of the marginalized bounds relative to the single-operators ones, and the strong sensitivity to the quadratic terms at the marginalized level, is due to the approximately flat direction displayed in Figure 2.7

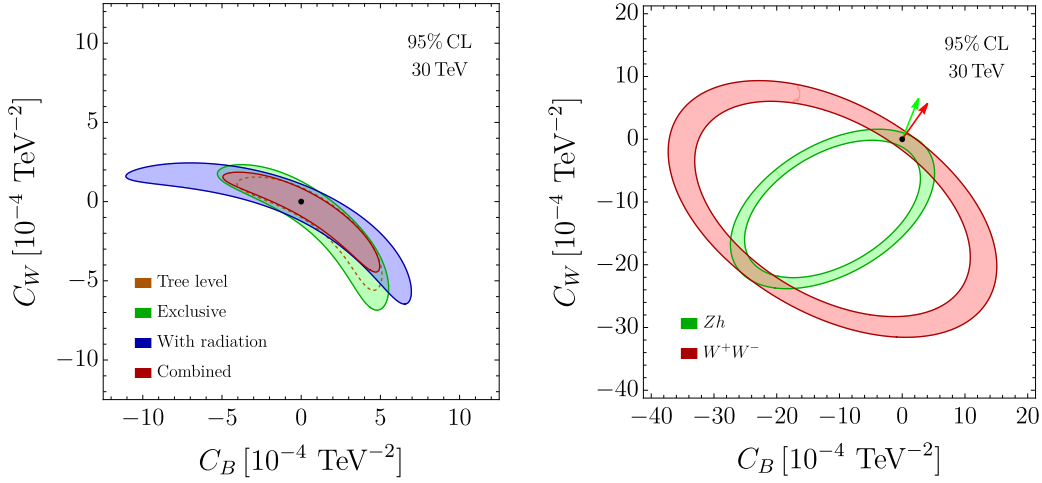


Figure 2.7 – Left: 95% sensitivity contours in the  $(C_B, C_W)$  plane at the 30 TeV muon collider. A second allowed region, not shown in the figure, can be eliminated by other measurements [118]. Right:  $Zh$  and  $WW$  likelihood contours at tree-level. Notice that the ellipses for  $WW$  and  $Zh$  are tangent in two points, one being the SM, the other being the point where the amplitudes have the same magnitude as in the SM but opposite sign.

to the cross-sections of the terms that are quadratic in the new physics parameters. In theories like Composite Higgs where  $C_{B,W} \sim 1/m_*^2$ , this fact implies that the marginalized limits correspond to a new physics scale  $m_*$  not much above the collider energy. In fact, looking at Table 2.5 we notice that the 30 TeV  $C_B$  reach corresponds to  $m_* = 43$  TeV. Thus, if new physics happened to sit along the flat direction in Figure 2.7, diboson processes would fail to extend the muon collider sensitivity well above the direct mass-reach. We do not have reasons to expect new physics to lie in that direction. Actually in certain Composite Higgs models one expects it to lie in the nearly orthogonal direction  $C_B = C_W$  [118]. However the presence of the flat direction is an obstruction to the broad exploration of new physics and to the characterization of a putative discovery. It is thus worth explaining its origin and discussing strategies to eliminate it.

The origin of the flat direction in the tree-level sensitivity contour (showed dashed, on the left panel of Figure 2.7) is readily understood analytically, by considering the gradients “ $\nabla$ ” of the Born-level cross-sections in the  $(C_B, C_W)$  plane, around the SM point  $(0,0)$ . Using the results for  $WW$  and  $Zh$  shown in Figure 2.8 and rescaling the gradients by the common factor  $2 E_{\text{cm}}^2 \sigma_0$  one finds

$$\nabla_L^{Zh} = (1-t_w^2)\{-t_w^2, +1\}, \quad \nabla_L^{WW} = (1+t_w^2)\{+t_w^2, +1\}, \quad \nabla_R^{Zh} = \nabla_R^{WW} = 4t_w^4\{1, 0\}, \quad (2.72)$$

where sup- and sub-scripts refer respectively to the final states and to the chirality of the incoming fermions. Notice that the  $Zh$  and  $WW$  gradients for right-handed initial states are perfectly aligned, so that this contribution to the cross sections has

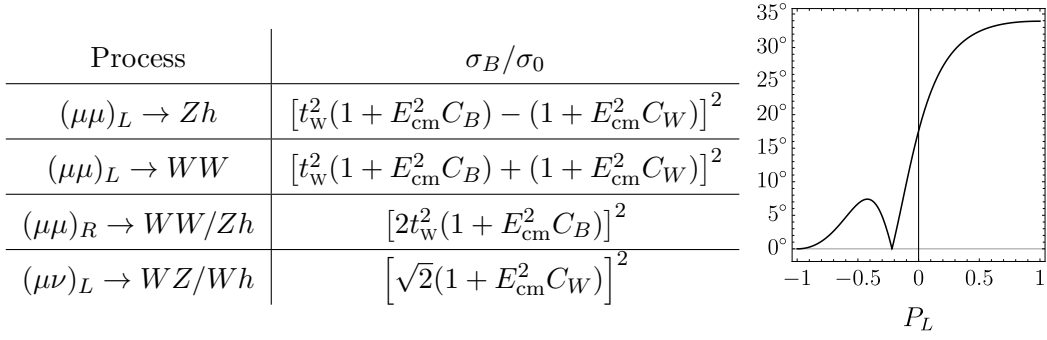


Figure 2.8 – Left: Born-level cross-sections, with  $t_w$  the tangent of the Weinberg angle, normalized to a common  $\sigma_0$  (whose expression is irrelevant). Right: the angle between the  $Zh$  and  $WW$  cross-section gradients as a function of the beam polarization fraction.

a flat direction (orthogonal to the gradient). The degeneracy can only be lifted by the left-handed contribution to the cross sections. However, given the small value of  $t_w^2 \simeq 0.3$ , the gradients  $\nabla_L^{Zh}$  and  $\nabla_L^{WW}$  also form a relatively small angle,  $\sim 30^\circ$ . They are thus not very effective in lifting the flat direction when considering the total  $(L + R)$  contribution to the  $WW$  and  $Zh$  cross-section. Indeed, the angle between  $\nabla_L^{Zh} + \nabla_R^{Zh}$  and  $\nabla_L^{WW} + \nabla_R^{WW}$  is in the end only  $\sim 17^\circ$  and thus the flat directions of the two cross-section measurements essentially coincide, as the right panel of Figure 2.7 shows. The combined likelihood is consequently also flat, in the same direction.

As evident in eq. (2.72), the  $L$ -gradients form a large angle with the  $R$ -gradient. Therefore, if one could use polarized beams, the degeneracy would be eliminated by measuring the contribution of each chirality. Considering a polarization fraction  $-P_L$  for the muon, and  $+P_L$  for the anti-muon beam, the cross-section gradients read (we indicate by  $\nabla_R$  the identical  $\nabla_R^{Zh}, \nabla_R^{WW}$ )

$$\nabla_{P_L}^{Zh} = \frac{(1 + P_L)^2}{4} \nabla_L^{Zh} + \frac{(1 - P_L)^2}{4} \nabla_R, \quad \nabla_{P_L}^{WW} = \frac{(1 + P_L)^2}{4} \nabla_L^{WW} + \frac{(1 - P_L)^2}{4} \nabla_R. \quad (2.73)$$

The angle between the two gradients steeply increases for positive  $P_L$ , as indicated by the plot in the right panel of Figure 2.8. Correspondingly, even a modest amount of polarization has a considerable impact on the sensitivity. The left panel of Figure 2.9 displays our sensitivity projections in a scheme where the VHEL integrated luminosity is equally split between positive and negative  $P_L = \pm 30\%$ . The likelihood contour (in green) corresponding to  $P_L = +30\%$  is significantly smaller than that (in blue) for  $P_L = -30\%$ , owing to the lifting of the flat direction achieved for positive  $P_L$ . On the other hand, the measurements at  $P_L = -30\%$  probe a direction complementary to that probed at  $P_L = +30\%$ . The combination of the two measurements thus benefits the sensitivity. The impact of beam polarization was emphasized already in Ref. [118]. Here we confirm that result, using more accurate predictions and including the entire set of exclusive and semi-inclusive cross-section measurements previously described.

Up to this point, we discussed the flat direction in the un-polarized likelihood (left panel of Figure 2.7) by employing the tree-level cross-sections. When considering also EW radiation, the predictions are significantly affected, but the flat direction is not fully eliminated. For the exclusive  $Zh$  and  $WW$  cross-sections this is easily understood, since virtual radiation suppresses the  $L$ -processes more than the  $R$  ones, owing to the larger Sudakov for incoming left-handed muons. The exclusive  $Zh$  and  $WW$  cross-sections gradients are thus even more aligned than the gradients of the corresponding tree-level predictions. The semi-inclusive cross-sections for  $Zh$  and  $WW$  production are also quite aligned, among them and with the exclusive cross-sections. This was expected because the partial cancellation between real and virtual logarithms make semi-inclusive cross-sections not vastly different from the tree-level ones.

On the contrary, the measurement of the charged processes  $WZ$  and  $Wh$  could have been expected to eliminate or mitigate the flat direction, because they are strongly sensitive to the Born cross-section of the charged scattering  $(\mu\nu)_L \rightarrow WZ/Wh$  (see the left panel of Figure 2.8). The associated gradient

$$\nabla_L^{\text{ch}} = 2\{0, +1\}, \quad (2.74)$$

points in a different direction than  $\nabla_L^{Zh}$ ,  $\nabla_L^{WW}$  and  $\nabla_R$ . Therefore the gradient of  $\sigma^{Wh/WZ}$  could in principle point in a direction that is completely different from that of the (nearly parallel) gradients of the  $Zh$  and  $WW$  cross-sections. However, by expanding at the first order in  $\mathcal{L} = g^2/16\pi^2 \log^2(E_{\text{cm}}^2/m_W^2)$ , the unpolarized (longitudinal)  $WZ$  and  $Wh$  cross-sections are approximately equal and read

$$\sigma^{WZ} \simeq \sigma^{Wh} \simeq \frac{1}{4} \mathcal{L} \cdot (\sigma_B^{Zh} + \sigma_B^{WW} + \sigma_B^{\text{ch}}), \quad (2.75)$$

where  $\sigma_B^{\text{ch}}$  is the charged Born cross-section reported on the left panel of Figure 2.8 (times 1/4, from the polarization average) and  $\sigma_B^{Zh, WW}$  are the Born cross-sections of the neutral processes. Therefore, the charged cross-section gradient  $\nabla_L^{\text{ch}}$  must compete with the (nearly parallel) gradients of  $Zh$  and  $WW$ , and its size happens to be insufficient to produce a large misalignment angle between the  $\sigma^{Wh/WZ}$  and  $\sigma^{Zh/WW}$  gradients.

The situation would be improved, if we could tailor an observable in which the  $\sigma_B^{Zh}$  and  $\sigma_B^{WW}$  contributions in eq. (2.75) are eliminated or reduced. Notice, for that purpose, that the  $Zh$  and  $WW$  terms in eq. (2.75) can be interpreted as due to one hard  $\mu\mu$  neutral-current scattering, followed by the radiation of one charged  $W$  boson from the final legs of the hard process. The  $W$  is thus preferentially collinear to the final states. The  $\sigma_B^{\text{ch}}$  term comes instead from the radiation of a  $W$  from the initial state, collinear to the beam axis, followed by a hard  $\mu\nu$  scattering.<sup>19</sup> This suggests to consider alternative

---

<sup>19</sup>This interpretation would straightforwardly correspond to Feynman diagrams in a physical gauge, where DL's are associated to emissions from individual legs. We already remarked that in covariant gauges instead they arise from the interference between emission from strictly different legs.



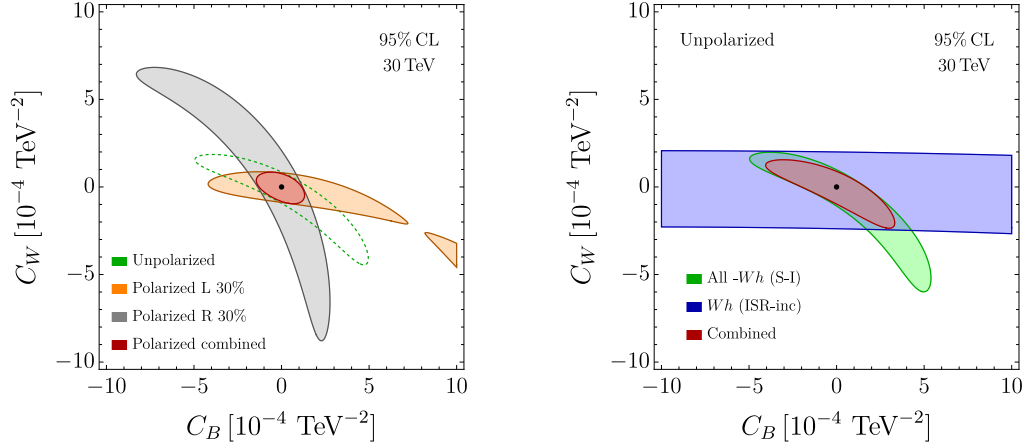


Figure 2.9 – Left Panel: 95% CL contours in for  $P_L = \pm 30\%$  beam polarization. Right Panel: the impact of the ISR-inclusive  $Wh$  cross-section measurement.

$Wh$  and  $WZ$  cross-sections that exclude final state radiation (FSR) while being inclusive on initial state radiation (ISR). FSR consists of soft radiation collinear to the hard particles in the final state, which is precisely the source of the first two terms in eq. (2.75). Excluding FSR, the resulting “ISR-inclusive” cross-sections are expected to be roughly

$$\sigma_{\text{ISR-inc}}^{WZ/Wh} \simeq \frac{1}{4} \mathcal{L} \sigma_B^{\text{ch}}. \quad (2.76)$$

This observable should thus be mostly sensitive to  $C_W$ , and its measurement should produce a nearly horizontal band in the  $(C_B, C_W)$  plane, thus eliminating the flat direction.

Unfortunately we are unable to produce resummed predictions for the ISR-inclusive cross-sections with the IREE methodology. We can however illustrate the impact of such measurements using tree-level **MadGraph** [66] predictions with the SMEFT@NLO model [68], focusing in particular on the  $Wh$  channel. Specifically, we simulate the process

$$\mu^+ \mu^- \rightarrow W^+ W^- h, \quad (2.77)$$

at  $E_{\text{cm}} = 30 \text{ TeV}$ , with the following selection cuts. First, we identify as “hard” the  $W$  boson that forms, together with the Higgs, the pair with the highest invariant mass. Secondly we ask this mass to be above  $0.85 \cdot E_{\text{cm}} = 25.5 \text{ TeV}$  and the hard  $W$  and  $h$  to be within the central region  $\theta_* \in [30^\circ, 150^\circ]$ . These selections enforce the occurrence of a hard scattering, and correspond to our definition of a “semi-inclusive” process. We further restrict to the “ISR-inclusive” region by asking the other (“soft”)  $W$  to be parallel to the beam, in a cone of  $20^\circ$ . Since the emission of at least one soft  $W$  is required for  $Wh$  production, the latter cut effectively corresponds to a veto on central EW radiation.<sup>20</sup>

<sup>20</sup>The attempt made in Ref. [118] to exploit the  $WW h$  process did not impose the crucial angular cut that defines the ISR-inclusive region.

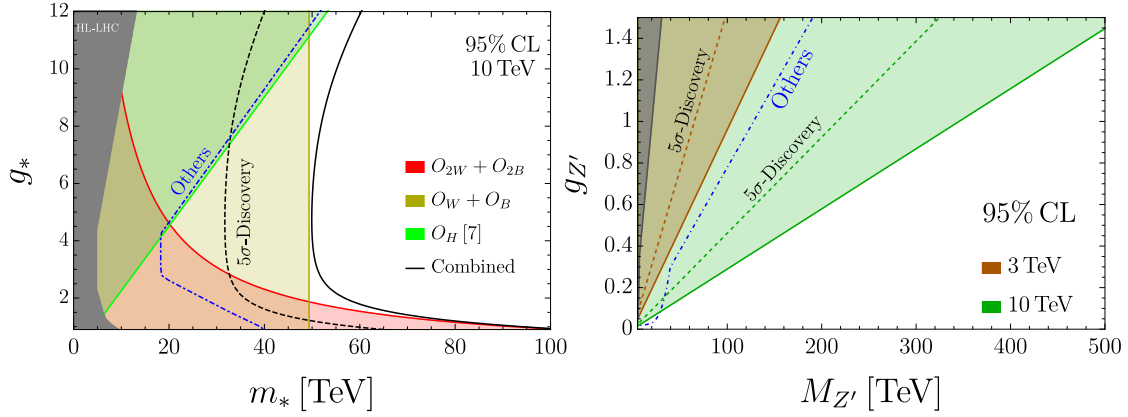


Figure 2.10 – Left Panel: 95% exclusion reach on the Composite Higgs coupling-mass parameter space. The reach for  $O_H$  is taken from [118]. Right Panel: sensitivity projections for a  $Y$ -universal  $Z'$  model. The gray band and the blue dash-dot line represent respectively the region probed by the HL-LHC program and the sensitivity projections for all other future collider projects [206].

The above estimate of the ISR-inclusive cross-section produces the blue band on the right panel of Figure 2.9. As expected, the band is nearly horizontal. In the figure we also display, in green, the 95% CL contour of the likelihood including all the measurements discussed in the present section, apart from the measurement of the semi-inclusive  $Wh$  cross-section which is correlated with the ISR-inclusive measurement. The combination of the two contours, shown in red, strongly mitigates the flat direction issue. Notice however that our tree-level estimate of the ISR-inclusive cross-section could be subject to large errors, and resummed predictions should be employed for a conclusive assessment of the sensitivity gain.

### 2.4.3 BSM sensitivity

**Composite Higgs.** As a first concrete scenario of new physics we consider Composite Higgs [207–209]. In this scenario, the Higgs is a composite Pseudo-Nambu-Goldstone boson emerging from some strong dynamics at a scale  $m_*$ . In principle the underlying dynamics could arise from gauge interactions, like in QCD. However the only concrete realistic constructions, accounting for the origin of both the fermion masses and the scale  $m_*$  itself, have been obtained in the context of warped compactifications. In these constructions, compositeness occurs in a holographic sense. Within the Composite Higgs scenario, the size of the Wilson coefficients in the resulting low energy EFT, can be estimated, under simple but robust dynamical assumptions, in terms of the mass scale  $m_*$  and overall coupling strength  $g_*$  of the underlying strong dynamics [10]. Furthermore, simple considerations suggest  $g_* \lesssim 4\pi$ , while the existence of  $\mathcal{O}(1)$  couplings within the SM implies  $g_* \gtrsim 1$ . More details on Composite Higgs can be found in sec. 3.1. Using the

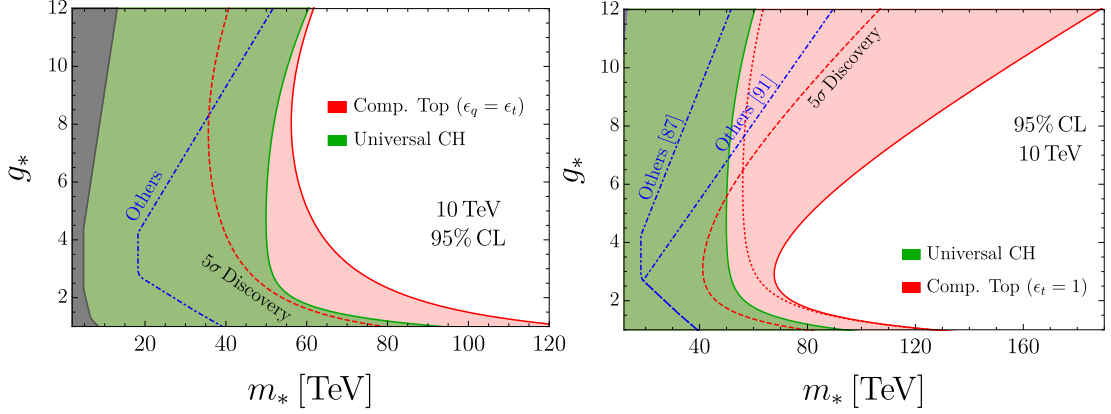


Figure 2.11 – 95% exclusion reach for the two partial compositeness scenarios under consideration. The green shapes represent the combined bound from the flavor universal measurements, while the red contours also includes the di-top and di-bottom constraints. The projected sensitivity of other future collider projects and the gray band of HL-LHC are taken from Ref. [206]. The right panel ( $\epsilon_t = 1$ ) also includes the stronger CLIC sensitivity estimated in Ref. [210].

power-counting rules we review there, we find the Wilson coefficients of the operators in the left column of Table 2.2 to scale as

$$C_{2W} = -\frac{c_{2W}}{2} \frac{g^2}{g_*^2 m_*^2}, \quad C_{2B} = -\frac{c_{2B}}{2} \frac{g'^2}{g_*^2 m_*^2}, \quad C_W = c_W \frac{1}{m_*^2}, \quad C_B = c_B \frac{1}{m_*^2}, \quad (2.78)$$

where the dimensionless coefficients  $c_{2W}$ ,  $c_{2B}$ ,  $c_W$ ,  $c_B$  are expected to be of order 1. Even though it does not affect the processes studied in this section, an important role is also played by

$$O_H = \partial_\mu (H^\dagger H) \partial^\mu (H^\dagger H), \quad C_H = \frac{c_H}{2} \frac{g_*^2}{m_*^2}. \quad (2.79)$$

In our sensitivity projections we will report the corresponding bounds, as obtained in [118] by studying the process  $\mu^+ \mu^- \rightarrow hh\nu\nu$  at tree level. Other probes of  $C_H$  at the muon collider, from Higgs coupling measurements, are superior or competitive at the lower energy muon colliders [118], but they are not considered in the sensitivity plots.

Using the above scalings, and setting all the  $c$  coefficients to 1, we can translate the bounds of Section 2.4 for a 10 TeV muon collider into sensitivity estimates in the plane  $(m_*, g_*)$ , as in Figure 2.10. In the same plot we also report the HL-LHC sensitivity projections, the envelope of the 95% CL sensitivity contours of all the future collider projects that have been considered for the 2020 update of the European Strategy for Particle Physics [206]. The advantage of the muon collider is evident. Results at muon colliders with different energies, with an integrated luminosity scaling as in eq. (2.68), are reported in Appendix B.4.

**Composite top.** The results for purely bosonic operators we just discussed apply robustly to basically all composite Higgs scenarios. Operators involving fermions are more sensitive to the assumptions on the flavor dynamics, but one convenient option is offered by the mechanism of partial compositeness [211], under which the elementary fermions mix linearly with heavy partners in the strong sector. Due to its large Yukawa coupling, the top quark is expected to have a large mixing with its partners and therefore precise measurements involving the third family represent an appealing opportunity to probe new physics.

At the muon collider the most relevant effects are expected in  $t\bar{t}$  and  $b\bar{b}$  production.<sup>21</sup> Indeed the dimension-6 operators in the last block of Table 2.2 gives rise to contributions that grow with  $E_{\text{cm}}$  and which can be exploited at the large energy of the muon collider. In a model-independent approach one can parametrize the “amount of compositeness” of respectively the 3<sup>rd</sup> quark family left-handed doublet and right-handed up-type singlet by  $\epsilon_q$  and  $\epsilon_t$ . These quantities range from 0 to 1. Given the universal coupling strength  $g_*$  of the strong sector the resulting top Yukawa coupling scale as [10]

$$y_t \sim \epsilon_q \epsilon_t g_* . \quad (2.80)$$

The relevant Wilson coefficients are then expected to scale as (see [204] for a short review)

$$C_{qD}^{(3)} = c_{qD}^{(3)} \frac{g \epsilon_q^2}{m_*^2}, \quad C_{qD}^{(1)} = c_{qD}^{(1)} \frac{g' \epsilon_q^2}{m_*^2}, \quad C_{tD} = c_{tD} \frac{g' \epsilon_t^2}{m_*^2}, \quad (2.81)$$

where the  $c_i$  are, as usual, expected to be order 1 coefficient. For concreteness we focus on two benchmark scenarios, where we fix  $\epsilon_t$  and  $\epsilon_q$  and leave  $g_*$  and  $m_*$  free. In the first scenario, the right-handed top quark is assumed to be fully composite, corresponding to  $\epsilon_t = 1$  and  $\epsilon_q = y_t/g_*$ . In the second, the two top chiralities are assumed equally composite, that is  $\epsilon_q = \epsilon_t = \sqrt{y_t/g_*}$ .

Notice that the contribution of the operator

$$O_{tt} \equiv \frac{1}{2} (\bar{t}_R \gamma^\mu t_R) (\bar{t}_R \gamma_\mu t_R), \quad (2.82)$$

to the Wilson coefficients of the  $O_{tD}$ , through Renormalization Group (RG) evolution, is not negligible in the scenario of total right-handed top quark compositeness [210]. Using the power-counting estimate

$$C_{tt} = \epsilon_t^4 \frac{g_*^2}{m_*^2} c_{tt}, \quad (2.83)$$

---

<sup>21</sup>See [212] for a similar analysis for CLIC.

we obtain a correction [210] to the  $C_{tD}$  coefficient at a scale  $\mu = E_{\text{cm}}$

$$C_{tD}(\mu) = C_{tD}(m_*) + C_{tt}(m_*) \frac{32}{9} \frac{g'}{16\pi^2} \log\left(\frac{m_*^2}{\mu^2}\right) = \epsilon_t^2 \frac{g'}{m_*^2} \left( c_{tD} + c_{tt} \frac{32}{9} \frac{\epsilon_t^2 g_*^2}{16\pi^2} \log\left(\frac{m_*^2}{\mu^2}\right) \right). \quad (2.84)$$

This correction is sizable if  $\epsilon_t \sim 1$ , especially for large  $g_*$ , because the sensitivity of the muon collider extends to a scale  $m_*$  that is significantly larger than  $E_{\text{cm}}$ .

There are in principle three more operators  $O_{Ht}$ ,  $O_{Hq}^{(1)}$  and  $O_{Hq}^{(3)}$  (defined as in the ‘‘Warsaw’’ basis [9]) that mix significantly with those in eq. (2.81) through RG evolution. However, their effects can only be important in the case where  $\epsilon_q \sim 1$ , which we do not contemplate in our analysis. We will therefore neglect the RG effects of the latter three operators and consider only those of  $O_{tt}$ .

Our results are summarized in Figure 2.11, where we report the projected exclusion reach in the  $g_*$  and  $m_*$  plane in the two scenarios under consideration for  $E_{\text{cm}} = 10$  TeV. Additional results can be found in Appendix B.4. Starting from the scenario of equal compositeness (left panel) we notice that at  $g_*$  the additional hypothesis of top compositeness extends the muon collider potential to probe the scale of Higgs compositeness  $m_*$ . The effect is even stronger for fully composite  $t_R$  (right panel), which shows that di-top measurements can cover up to  $m_* \sim 150$  TeV for  $g_* \gtrsim 8$ . We should point out, however, that this result depends on the exact  $\mathcal{O}(1)$  value of the  $c_{tt}$ ,  $c_{tD}$  coefficients in eq. (2.84). This dependence is illustrated in Figure B.4, where we set  $c_{tD} = 1$  and we vary the value of  $c_{tt}$ .

Finally we remark that a detailed analysis of the composite Higgs scenario with partial compositeness would require specific hypotheses on the flavor dynamics and a detailed inspection of the flavor observables. Depending on those hypotheses, principally the maximality or minimality of the underlying flavor symmetry, the resulting flavor constraints on the new physics scale  $m_*$  can vary dramatically. While a comprehensive analysis clearly exceeds the purposes of this work, a perspective can be gained by considering available studies. As shown in Ref. [213], under the strongest assumptions, that is for a symmetry structure offering the best protection from unwanted effects, flavour and CP observables could start exploring the range  $m_* = \mathcal{O}(10)$  TeV in the next decade or so, given the availability of better measurements and assuming better theoretical predictions. This is roughly the same range explored by a 3 TeV muon collider. Moreover the  $m_* \sim 50$  TeV reach of a 10 TeV muon collider vastly surpasses any conceivable improvement of flavour constraints, and competes with the more stringent flavour bounds obtained by making more generic assumptions on the flavor dynamics. Notice also that the present lepton flavor universality anomalies in B-decays, at least the seemingly more prominent ones in neutral currents, suggest a new physics scale in the  $\sim 30$  TeV range, which could be explored both directly and indirectly by the muon collider.

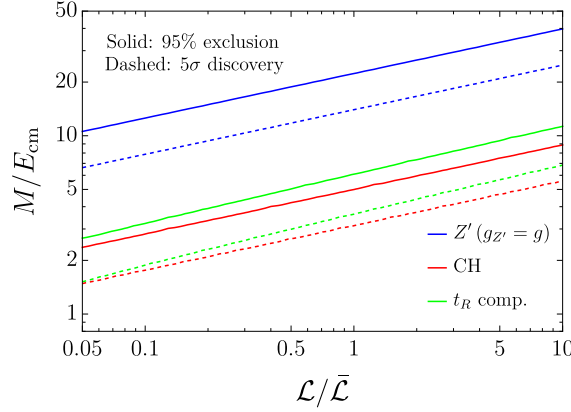


Figure 2.12 – Reach on the new physics scale at  $2\sigma$  (continuous) and at  $5\sigma$  (dashed), relative to the collider energy, as a function of the integrated luminosity normalized to eq. (2.68). The red lines are for Universal manifestations of Higgs compositeness, while the green ones include the effect of Top compositeness in the  $\epsilon_t = 1$ ,  $\epsilon_q = y_t/g_*$  scenario. The blue lines are for the  $Y$ -universal  $Z'$  for a fixed coupling  $g_{Z'} = g$ .

**$Y$ -Universal  $Z'$  model** The  $Y$ -universal  $Z'$  model represents a simple extension of the SM, featuring an additional heavy gauge boson, of mass  $M_{Z'}$ , on top of the SM particles.<sup>22</sup> In this benchmark scenario the new vector charges are aligned with the SM hypercharge with coupling  $g_{Z'}$ . Requiring the width of the  $Z'$  to not exceed  $0.3M_{Z'}$  sets the perturbative limit on the coupling to be  $g_{Z'} \lesssim 1.5$ . At energies below  $M_{Z'}$ , integrating out the  $Z'$  only generates the  $O'_{2B}$  operator of Table 2.2. The Wilson coefficient of the operators corresponds, by eq. (2.69), to

$$Y = \left( \frac{g_{Z'} m_W}{g' M_{Z'}} \right)^2. \quad (2.85)$$

The sensitivity projections are reported in the right panel of Figure 2.10. The orange and green regions are the ones probed by muon colliders at 3 and 10 TeV energy, respectively. The gray band represents the expected exclusion reach from HL-LHC, while the blue line indicates the combined sensitivity from other future collider projects (dominantly FCC, and the 3 TeV stage of CLIC). The 3 TeV muon collider sensitivity is obviously similar to the one of CLIC. A 10 TeV machine would greatly improve this result probing up to 500 TeV for large (but still perturbative) coupling. The dashed lines represent the discovery reach, showing that already at 3 TeV there are vast opportunities for indirect discovery, well above the region that the HL-LHC might exclude. Results at higher muon collider energies are reported in Figure B.2.

<sup>22</sup>See [206] for details. Concrete BSM scenarios featuring additional  $Z'$ s can be found, for instance, in Ref. [99].

## 2.5 Conclusion and outlook

We have studied the interplay between two classes of novel phenomena, which can be observed at future lepton colliders with very large center of mass energy. The first class consists of hard scattering processes induced by new physics at around 100 TeV. The second class consists of the long-distance effects of EW radiation. Both phenomena play a relevant role at lepton colliders with  $E_{\text{cm}} \sim 10$  TeV, with particular focus on muon colliders, which are the main target of our discussion.

The interplay manifests itself in two ways. The first one is simply that EW radiation effects on the SM predictions are large (see Sections 2.3.1 and 2.3.2) and require to be included and resummed with high accuracy in order to isolate the putative BSM contribution to the measurements. EW radiation thus plays for muon colliders a similar role as QCD radiation for the LHC, with the difference that its effects can not be mitigated by the choice of suitable (inclusive) observables. Therefore to some extent, they are even more important for muon colliders than QCD is for the LHC.

The second and possibly more interesting aspect of the interplay is given by the influence on the pattern of EW radiation operated by the presence of new physics in the hard scattering amplitude. This makes observables that require or that exclude the presence of radiation display a different dependence on the new physics parameters, and the sensitivity profits from their combined measurements as illustrated in Sections 2.3 and 2.4.2, and in Appendix B.3.

Our sensitivity projections rely on putative measurements of exclusive and semi-inclusive cross-sections. Both classes of processes are characterized by the occurrence of a hard scattering, with two particles in the final state carrying almost all the available energy. The emission of additional EW bosons and hard photons is vetoed in the exclusive case and allowed in the semi-inclusive one. We computed the resummed semi-inclusive cross-sections in double logarithm (DL) approximation by extending the IREE methodology [156], as described in Section 2.2.2. The exclusive cross-sections were computed at DL, but also including single logarithms at 1-loop, which we found to be sizable.

The studies performed in this chapter should be improved and extended in many directions. Better predictions will be definitely needed in order to approach the percent-level accuracy target that is needed to fully exploit the statistical precision potential of a muon collider. Moreover, given the magnitude of the radiation effects we observed, it is possible that more accurate predictions will considerably affect some of our sensitivity projections. A first step in that direction, which we leave for future work, is the inclusion of single logarithms at fixed leading order in the semi-inclusive predictions. That could be achieved by combining one loop virtual logarithms with a factorized treatment of real emission. That calculation, would possibly also help clarify the connection between soft-collinear effects (studied in this chapter) and the PDF/Fragmentation Function treatment of EW

radiation. It is not unconceivable that the same approach could be extended at the two loop order. In parallel, the impact of resummation beyond DL should be assessed. The SCET methodology currently offers the most promising approaches.

Another priority is to investigate further classes of cross-sections, sensitive to different EW radiation patterns. Our results indicate that investigation should be done on the basis of the structure of short distance new physics. At the end of Section 2.4.2 we took one step in that direction, showing that the approximately flat direction in the  $(C_B, C_W)$  likelihood contours is mitigated, in the absence of polarized beams, by considering an “ISR-inclusive” cross-section. This third cross-section type is inclusive on radiation collinear to the beam, but vetoes centrally emitted radiation. We could not compute the ISR-inclusive cross-section at DL with our IREE methodology and limited ourself to a tree-level estimate. A straightforward direction for progress would be to perform that calculation and verify if and how it impacts our findings.

The definition and study of cross-sections should be also based on experimental considerations. We already pointed out that exclusive cross-sections are problematic in that regard. Indeed imposing the radiation veto requires experimental sensitivity to EW radiation that is emitted in all directions, including the forward and backward regions along the beam line. The angular coverage of the muon collider detector is still to be quantified, however we expect that it will be insufficient for the measurement of exclusive cross-sections.

In view of the above, it is important to emphasize that our sensitivity projections have been verified to not change radically when exclusive cross-section measurements are not available. This conclusion is not in contradiction with (and cannot be inferred from) our sensitivity plots, where (see e.g. Figure 2.6) we observe a strong complementarity between “exclusive” observables and observables “with radiation”. Indeed for neutral processes the latter observables consists of the difference between the semi-inclusive and the exclusive cross-sections. Therefore the impact of eliminating the exclusive measurements can not be estimated by suppressing the “exclusive” cross section measurement in the computation of the likelihood. The proper estimate is obtained by employing the semi-inclusive neutral processes without subtraction, combined with the charged measurements, produces a combined reach that is not much inferior to the one that exploits the exclusive measurements. In essence, the main sensitivity gain due to radiation stems from the emergence of the charged processes and from their complementarity with the neutral ones. The complementarity between neutral measurements with different degrees of radiation inclusiveness (e.g., exclusive versus semi-inclusive) plays instead a less relevant role in our results. This same qualitative behavior can be observed in the comparison between the neutral and charged lepton production processes on the right panel of Figure 2.5.

On the other hand, the complementarity between exclusive and semi-inclusive measurements exists and can benefit the sensitivity as we illustrated on the left panel of



Figure 2.5. It plays a marginal role in the combined fit to the limited number of EFT operators we considered in [3]. It could however be relevant in a more global exploration and characterization of putative new physics. One way to recover sensitivity, if exclusive measurements were indeed unavailable, could be to exploit the ISR-inclusive cross-sections. These are easier to measure because they do not require sensitivity to radiation in the forward and backward regions. This aspect should be investigated.

Our phenomenological results strengthen and extend previous estimates of the muon collider sensitivity to heavy new physics. We have considered a variety of BSM scenarios with new physics coupled to the SM with electroweak strength. We found that a  $E_{\text{cm}} = 10$  TeV muon collider can probe up to a scale ranging from 50 to 200 TeV. The reach improves linearly with  $E_{\text{cm}}$ . These figures are significantly above the potential (direct and indirect) sensitivity of other future collider projects, and above the direct sensitivity reach of the muon collider itself, which is obviously bounded by the collider energy.

The indirect sensitivity to scales that are well above the direct reach is a great addition to the physics case of a muon collider, whose relevance would not be diminished, but on the contrary augmented, by the occurrence of a direct discovery. Indeed, direct hints for new particles observed at the muon collider will turn into a full-fledged discovery of new physics only after unveiling the underlying theoretical description of their dynamics. The possibility of probing this dynamics well above the particle's mass will play a decisive role in this context. Furthermore, the direct manifestation of new physics might be hard to detect. Perhaps, indirect probes will provide the first hint of its existence, to be eventually confirmed by targeted direct searches. Finally, indirect searches for BSM phenomena based on precise measurements guarantee a sound output of the project. The connection with the phenomenon of EW radiation, which is interesting per se, adds scientific value to the program.

Before concluding, we discuss the impact of the integrated luminosity on our results. We employed the baseline luminosity in eq. (2.68), which corresponds to  $90 \text{ ab}^{-1}$  for a 30 TeV muon collider. Since the possibility of reducing the  $90 \text{ ab}^{-1}$  target is under discussion, it is worth assessing the impact of a lower integrated luminosity on our conclusions. An important aspect is associated with the actual experimental feasibility of the relevant measurements. While a conclusive assessment will require dedicated studies, the expected number of events in Table 2.3<sup>23</sup> and the corresponding efficiencies show that, with a factor 10 reduction in luminosity, some of the processes we employed would be left with a handful of observed events, possibly preventing the corresponding measurements. If the reduction in luminosity were less extreme, the sensitivity to the scale of new physics would simply deteriorate as the fourth root of the luminosity, as shown in Figure 2.12 for some of the BSM scenarios we studied in Section 2.4.3. The figure displays the

---

<sup>23</sup>The table is for  $E_{\text{cm}} = 10$  TeV, however with the scaling in eq. (2.68) the results depend weakly on the energy.

exclusion and discovery reach on the new physics scale normalized to the collider energy  $E_{\text{cm}} = 30$  TeV. This is the right figure of merit, since the goal is to extend the muon collider sensitivity above the direct reach. The reduction by a factor of  $10^{1/4} = 1.8$  due to a factor 10 luminosity reduction partially undermines this goal, especially for what concerns the generic manifestations of the Composite Higgs scenario.

## 3 A light composite Higgs vs flavor observables

Flavor physics has always been a driving force for model building and thanks to the huge experimental effort [214, 215] plays nowadays a crucial role in our search for new physics. Moreover flavor measurements can exclude substantial part of our models BSM or even lead to new discoveries.

Among the possible UV completions of the SM, which can solve the hierarchy problem, the composite Higgs, featuring the Higgs to be a composite particle of a new strong dynamics, represents one of the most appealing scenarios. A fundamental ingredient of composite Higgs models is the partial compositeness hypothesis, which includes a description of the SM fermions masses. This task is, however, highly non trivial given the peculiar SM flavor structure and the severe constraints from flavor observables, in particular the CP odd ones.

In this chapter we face the problem of flavor physics in composite Higgs models, focusing on a minimal set of scenarios which include a partial-compositeness [211] description of the SM quarks. In particular we study a class of models where either the left-handed or the right-handed SM quarks belong to the new strong dynamics. Starting from this hypothesis we further assume a flavor symmetry group for the strong dynamics and we classify our models according to the latter.

We find that enough flavor symmetries protect our models from (chromo-)electric dipoles and that there is an optimal flavor group for the strong sector needed to avoid severe flavor constraints. Furthermore we find that, among all the strongest constraints,  $B$  physics observables are particularly important and can be the smoking-gun of the models under consideration.

### 3.1 Composite Higgs

The composite Higgs scenario is a simple and effective solution to the hierarchy problem. The basic idea is that the Higgs boson, rather than being an elementary particle, is a composite object of a new strong dynamics. The size of the Higgs  $\sim 1/m_*$  set the SM cut-off  $\Lambda_{SM} \sim m_*$  in eq. (3) and the integrand  $d\tilde{m}_h^2/dE$  is now localized around  $m_*$ . At low energy  $E$  the latter integrand grows linearly with  $E$ , as predicted from the SM. At energies  $E \gg m_*$  it has a steep fall, being the composite Higgs transparent to wave length much smaller than its characteristic length.

Composite Higgs models have been extensively studied in the literature (see for instance [209, 216, 217] for reviews) and nowadays represent one of the most realistic scenarios that can realize naturalness. In fact, despite of the various constraints from collider searches (see [206] for recent results), a compositeness scale  $m_*$  of few TeV seems compatible with the present data and could solve the hierarchy problem with only 1 or 2 digits of fine tuning.

The mechanism behind the composite Higgs consists of a new strongly interacting sector that completes the SM at high energies. This new dynamic, in analogy to QCD, confines at low energies resulting in a set of bound states, including the SM Higgs. The composite sector itself emerges from a more fundamental theory at a scale  $\Lambda_{UV}$  and that can naturally be larger than  $m_* \sim \text{TeV}$ . This is necessary not to encounter again a naturalness problem for  $m_*$  at the TeV range and it is realized assuming that the strong sector, at  $\Lambda_{UV}$ , is close to an UV fixed point of its renormalization group. Moreover, we also need the strong sector to not flow down “too fast” in the IR. Namely we assume the strong sector to be made just by almost marginal (and irrelevant) interactions, with scaling dimensions not much smaller than 4. In this way we can focus on the dynamics around and below  $m_*$  and we can ignore the details of the UV dynamics at higher scales.

The structural features of composite Higgs models can be encoded in few simple ingredients. The strong sector is symmetric under a global group  $\mathcal{G}$  that it spontaneously broken to a subgroup  $\mathcal{H}$  at the confinement scale  $m_*$ . The group  $\mathcal{H}$  contains the SM EW gauge group  $SU(2)_L \times U(1)_Y$  and the Higgs emerges as pseudo Nambu-Goldstone boson in the  $\mathcal{G}/\mathcal{H}$  coset in this spontaneous symmetry breaking process. The explicit symmetry breaking which makes the Goldstone “pseudo” comes from the mixing of the composite sector with the elementary one<sup>1</sup>, through some interaction encoded in a mixing Lagrangian  $\mathcal{L}_{mix}$ . These interactions are firstly mediated by the gauging of  $SU(2)_L \times U(1)_Y$ , and can contain additional linear mixing between the SM fermions and linear operators belonging to the strong sector. The latter is the core of the so-called partial compositeness construction that we discuss in detail later on.

A crucial aspect of this construction, that we need to emphasize, is that the Higgs is

---

<sup>1</sup>This point is just to simplify the discussion, since it not necessary and there can be, in general, extra sources of symmetry breaking.

a pseudo goldstone boson of an approximate symmetry and as so it is spontaneously lighter of the other bound states. In fact, as it happens in QCD, the confinement process can produce many bound states, usually called resonances at  $m_*$ . The pseudo-goldstone bosons, being related to an approximate symmetry can be lighter than  $m_*$ , allowing a scale separation between the Higgs boson and the other resonances. Moreover through the mechanism of the “vacuum misalignment”, the approximate goldstone symmetry ensures that the Higgs boson is not only light but also looks like an elementary particle, as in the SM (see for instance [209]).

The idea of a composite Higgs dates back to the 80’s [218–220] and attracted renewed interests with extradimensional and holographic models [208, 221–225]. For the present and the next discussions it is enough to recall the general 4D EFT picture that describes the phenomenology of this scenario [10, 226]. By this, we mean that there is not only a specific set of operators related to the Composite Higgs dynamics, it also means that there are a set of rules that reproduce the size of the Wilson coefficients. In the case of Composite Higgs, this rule takes the name of “SILH” power counting, from “Strongly Interacting Light Higgs” [10], the title of the paper that pointed it out.

As we said, the main feature of composite Higgs models is that the Higgs arises as a pseudo Nambu Goldstone boson of  $\mathcal{G} \rightarrow \mathcal{H}$  ( $SO(5) \rightarrow SO(4)$  in case of the minimal model [208]) symmetry breaking pattern, together with other resonance. We now parametrize the Goldstone fields as

$$U = e^{i\frac{\Pi}{f}}, \quad \Pi \equiv \Pi^A \hat{T}^A, \quad (3.1)$$

with  $\hat{T}^A$  the broken generators in  $\mathcal{G}/\mathcal{H}$ , we collectively denote  $\Phi$  the resonances with mass  $\sim m_*$  and the field  $\Pi$  is weighted by the decay constant  $f = m_*/g_*$ . We furthermore assume that the only source of explicit breaking of  $\mathcal{G}$  is absent in the limit  $\mathcal{L}_{mix} \rightarrow 0$  and that the strong sector is characterized by only one scale  $m_*$  and one weak coupling  $g_{SM} < g_* < 4\pi$ .

The most general Lagrangian describing the composite states, in the limit  $\mathcal{L}_{mix} \rightarrow 0$ , is

$$\mathcal{L}_c = \frac{m_*^4}{g_*^2} \hat{\mathcal{L}}_c \left[ \frac{\partial}{m_*}, U, \frac{g_*}{m_*^{d[\Phi]}} \Phi \right], \quad (3.2)$$

where  $\mathcal{L}_c$  is a generic analytic function of its dimensionless arguments in the spirit of Naive Dimensional Analysis (NDA) [227, 228]. In eq. (3.2)  $d[\Phi] = 1$  for spin 0 and 1 field  $\Phi$  and  $d[\Phi] = 3/2$  for spin 1/2 fields (we avoid higher spin fields). Clearly, if the previous is the most general local Lagrangian, the low energy EFT below  $m_*$  for  $U$  (i.e. for the Higgs boson) it is again the most general Lagrangian allowed by the goldstone symmetry. This is captured by a  $\sigma$ -model with decay constant  $f$ .

Yet, as we said, the group  $\mathcal{G}$  is explicitly broken by the interactions with the SM that implies new rules for the operators involving SM fields. In particular the SM gauge

bosons are associated to the respective gauge coupling and not to  $g_*$ . Similarly if the elementary fermions mix linearly to some composite operators  $\lambda O\psi_{SM} \in \mathcal{L}_{mix}$ , then  $\psi_{SM}$  is weighted by a factor  $\lambda$ . Notice that the leading order expansion for  $U$  gives higher dimensional operators among the SM Higgs describing universal composite Higgs dynamics, that we already encountered in the previous chapter. We refer to the original paper [10] for more details on the construction of the effective Lagrangian. We just comment that for the applicability of the previous result it is crucial that the coupling  $g_*$  is  $g_* < 4\pi$ , such that a semiclassical expansion  $\left(\frac{g_*^2}{16\pi^2}\right)^n$  it is meaningful. Moreover, notice that, this expansion is not only compatible with a weakly coupled scenario but also to a strong QCD-like dynamics allowing a large  $N$  expansion. In this case we can identify  $g_* = \frac{4\pi}{\sqrt{N}}$  (see again [209] for a review).

The construction of the effective Lagrangian through NDA is the starting point of all the estimates that we perform in the rest of the chapter. So we repeat once again that the EFT ideology suggests to write down all the higher dimensional operators allowed by gauge and global symmetries and by the goldstone boson nature of the Higgs. Furthermore NDA allows to estimate the size of the Wilson coefficients up to what we assume to be an  $\mathcal{O}(1)$  number.

## 3.2 Partial Compositeness

So far we just described the general logic behind composite Higgs models. A key ingredient, that we now explore more in detail is the partial compositeness paradigm [211].<sup>2</sup> This construction allows to include a description of the SM flavor and in principle an explanation for the SM masses.

The most basic implementation of Partial Compositeness [211] are usually characterized by three sets of mixings

$$\mathcal{L}_{\text{mix}} = \lambda_q^{ia} \bar{q}_L^i O_q^a + \lambda_u^{aj} \bar{O}_u^a u_R^j + \lambda_d^{aj} \bar{O}_d^a d_R^j + h.c. , \quad (3.3)$$

where we are assuming one set of partners ( $O_u, O_d, O_q$ ) for each SM fermions. Notice that in some realization of partial compositeness a second mixing term with the left-handed doublet is introduced. This will be necessary for some of the scenarios we will consider in the following, but in the general case we study here it is unnecessary and leads to further complications. We assume that the operators  $O$  come from the strongly coupled composite dynamics that we take to be characterized by one typical mass scale  $m_*$  and one typical coupling  $g_*$  in the same line of the previous discussion.

We now consider the so-called anarchic partial compositeness scenario (see [209] for a review) where no flavor symmetries are assumed on the strong sector, with the only

---

<sup>2</sup>See [229–232] for extra-dimensional constructions addressing flavor in composite Higgs

requirement for eq. (3.3) to reproduce the SM Yukawas at low energy. The mixing matrices  $\lambda$  can be written as

$$\lambda_q^{ia} = C_q^{ia} \lambda_q^a, \quad \lambda_u^{ai} = \lambda_u^a C_u^{ai}, \quad \lambda_d^{ai} = \lambda_d^a C_d^{ai} \quad (\text{no sum}), \quad (3.4)$$

with all the  $C^{ij}$  a  $O(1)$  anarchic complex matrices and  $\lambda^j$  hierarchical vectors  $\lambda^1 \ll \lambda^2 \ll \lambda^3$ .<sup>3</sup>

The hierarchic structure of the  $\lambda$  vectors allows for a dynamical generation of the masses through the RG running [208] of the theory from the UV scale  $\Lambda_{\text{UV}} \gg \text{TeV}$  to the IR scale  $m_*$ . Qualitatively, the energy scaling of  $\lambda$  is dictated by the anomalous dimension of the composite operators  $\gamma = \dim[O] - 5/2$ , where  $\dim[O]$  is the conformal dimension of the operator  $O$ . For  $\gamma > 0$  the running has the form

$$\lambda(m_*) \sim \lambda(\Lambda_{\text{UV}}) \left( \frac{m_*}{\Lambda_{\text{UV}}} \right)^\gamma, \quad (3.5)$$

leading to a small mixing with the composite sector, while a large mixing can be generated for  $\gamma \lesssim 0$ . However, as we will see in a moment, the SM flavor structure is highly non trivial and a completely anarchic structure leads to severe constraints from flavor observables.

In this scenario, at the scale  $m_*$  the operators  $O^a$  of a given mixing do not have any distinguishable quantum numbers and can be rotated in flavor space together with rotations in the elementary sector in order to rewrite the mixing matrices  $\lambda$  in a more convenient form

$$\mathcal{L}_{\text{mix}} = \lambda_q^i \bar{q}_L^i O_q^i + \lambda_u^i \bar{O}_u^i u_R^i + \lambda_d^i \bar{O}_d^i d_R^i + h.c.. \quad (3.6)$$

At energies smaller than  $m_*$ , integrating out the composite resonances gives rise to the Standard Model Yukawa couplings as

$$Y_u^{ij} = \frac{\lambda_q^i \lambda_u^j}{g_*} c_{ij}, \quad Y_d^{ij} = \frac{\lambda_q^i \lambda_d^j}{g_*} c'_{ij}, \quad (3.7)$$

where  $c$  and  $c'$  are some  $O(1)$  complex anarchic matrices.

The requirement of reproducing the SM masses and the CKM matrix, fixes the hierarchy

---

<sup>3</sup>Notice that some realization of anarchic partial compositeness require two mixings for the SM doublets [233]. However we remark that this is not needed to reproduce the SM and furthermore it requires specific assumption on the UV model.

among the different  $\lambda$ . Namely we have

$$\frac{m_u}{m_c} \sim \frac{\lambda_q^1 \lambda_u^1}{\lambda_q^2 \lambda_u^2}, \quad \frac{m_c}{m_t} \sim \frac{\lambda_q^2 \lambda_u^2}{\lambda_q^3 \lambda_u^3}, \quad \frac{m_d}{m_s} \sim \frac{\lambda_q^1 \lambda_d^1}{\lambda_d^2 \lambda_d^2}, \quad \frac{m_d}{m_b} \sim \frac{\lambda_q^2 \lambda_d^2}{\lambda_d^3 \lambda_d^3}, \quad (3.8)$$

$$V_{\text{CKM}}^{ij} \sim V_{\text{CKM}}^{ji} \sim \frac{\lambda_q^i}{\lambda_q^j} \quad \text{for } i < j. \quad (3.9)$$

The previous conditions fix the parameters of the model up to one undetermined quantity, that in these models is conventionally taken to be

$$x_t = \lambda_q^3 / \lambda_u^3, \quad \text{with } y_t / g_* \lesssim x_t \lesssim g_* / y_t. \quad (3.10)$$

The total lack of a structure in flavor space leads to large tree-level contributions to many of the SM flavor observables that are accidentally suppressed in the SM, especially CP violating ones. For example, the composite dynamics generates an electric dipole moment (EDM) for the neutron. To be compatible with the strong experimental constraint [234], the scale  $m_*$  must be really large. If the dipole is generated at tree-level we can indeed estimate this effect as

$$d_n \sim \frac{m_{u/d}}{m_*^2} \leq 1.8 \times 10^{-26} \text{ cm} \implies m_* \gtrsim 45 - 75 \text{ TeV}. \quad (3.11)$$

In models where the dipoles are only generated at loop level, the bound on  $m_*$  would instead be suppressed by a power of  $g_*/4\pi$ . Assuming a similar anarchic structure also for the lepton sector, gives an even stronger constraint on  $m_*$  coming from the much more precisely measured EDM of the electron. In that case the bound becomes

$$d_e \leq 1.1 \times 10^{-29} \text{ cm} \implies m_* \gtrsim 1300 \text{ TeV}. \quad (3.12)$$

Again, the bound on the mass gets reduced by a factor  $g_*/4\pi$  when the operator is induced at 1-loop level.

Large tree-level contributions also appear to many other flavor observables. A complete and updated analysis of those will be done in sec. 3.4, but we can anticipate some of the stronger results. From the  $K - \bar{K}$  mixing we find  $m_* \gtrsim 25 \text{ TeV}$ , while from  $b \rightarrow s\gamma$  we have  $m_* \gtrsim 29 \text{ TeV}$ .

Finally it is important to note that in models in which we do not make any assumptions on the composite sector, contributions to the neutron EDM might also come from flavor-universal corrections to the Standard Model dynamics. For example, if the composite sector violates CP also in the limit where all the mixing are turned off, we generate the so-called Weinberg operator

$$\mathcal{L} \supset c(m_*) \frac{g_s^3(m_*)}{g_*^2 m_*^2} \frac{1}{3!} f^{abc} G_\mu^{a\nu} G_\nu^{b\rho} \tilde{G}_\rho^{c\mu}, \quad (3.13)$$



that contributes to the neutron EDM [235]. Indeed, we can estimate from NDA up to a dimensionless order one number

$$\frac{d_n}{e} \approx c(1 \text{ GeV}) \frac{g_s^3(m_*)}{g_*^2 m_*^2} \frac{\Lambda_{\text{QCD}}}{4\pi}, \quad (3.14)$$

where  $c(1 \text{ GeV})$  is the value of the Wilson Coefficient  $c(m_*)$  at the  $\Lambda_{\text{QCD}} = 1 \text{ GeV}$  scale.<sup>4</sup> Such a running can be computed by first running from the scale  $m_*$  to 1 TeV and then down to  $\sim 1 \text{ GeV}$  using the results of [236]

$$c(1 \text{ GeV}) \approx 0.3 c(1 \text{ TeV}) \approx 0.3 c(m_*) \left( \frac{\alpha_s(m_*)}{\alpha_s(1 \text{ TeV})} \right)^{15/14}. \quad (3.15)$$

Imposing the current experimental constraint, this translates to a bound on the composite parameters of

$$m_* g_* \gtrsim 110 \text{ TeV}. \quad (3.16)$$

Even though this bound is weaker than the one from the quark dipole moments for large values of  $g_*$ , it is completely independent on the flavor structure of the model and only comes from the assumption of CP violation in the composite sector.

#### 3.2.1 Symmetric strong sector

In the previous section we have seen that the hypothesis of anarchic partial compositeness is incompatible with a small ( $\lesssim \text{few TeV}$ ) value for  $m_*$  as would be required to address the hierarchy problem. The main issues are related to CP odd observables and flavor transitions, especially the ones in the down sector, that are very well experimentally constrained. A possible way out is to invoke some symmetries in the strong dynamics. However, the price to pay if we follow this path is that the flavor hierarchy cannot be explained via RG evolution as it is done in anarchic models. In this chapter we adopt this paradigm and we show how, by motivated and structured assumptions on the strong sector flavor symmetry group, we can maintain  $m_* \lesssim 10 \text{ TeV}$ .

The first hypothesis is directly suggested by eq. (3.16): a TeV scale dynamics which generate the CP odd Weinberg operator  $GG\tilde{G}$  unavoidably produces a large neutron dipole moment. To avoid this, we then have to assume that the composite dynamics respects CP and the only source of its breaking comes from the various mixing of eq. (3.6), that is of course needed to reproduce the SM. This is however not enough to avoid the large CP violating effects mentioned before. Indeed, the  $\mathcal{O}(1)$  phases coming from the mixings  $\lambda$ , in general, imply again the strong bounds of eqs. (3.11) and (3.12) and from the other flavor violating observables. Some flavor symmetry is necessary.

<sup>4</sup>Arguments based on QCD sum-rules [235] estimate a smaller matching coefficient in eq. (3.14). In particular in [235] it was found  $d_n/e = c(1 \text{ GeV}) \frac{g_s^3(m_*)}{g_*^2 m_*^2} ((10 - 30) \text{ MeV})$ .

A very efficient solution to this problem is given by Minimal Flavor Violation (MFV) [237]. The idea is to assume that the only sources of violation of the flavor symmetries of the SM quarks (or in general fermions)  $SU(3)_q \times SU(3)_u \times SU(3)_d$  are given by the SM Yukawas, transforming as spurions as

$$\begin{array}{ccc} & SU(3)_q & SU(3)_u & SU(3)_d \\ Y^u \sim & 3 & \bar{3} & 1 \\ Y^d \sim & 3 & 1 & \bar{3} \end{array} \quad (3.17)$$

and that any new flavor violating contribution is proportional to them. Notice that this hypothesis, together with a CP invariant strong dynamics, not only protect dipoles but also screens (at least partially) flavor transitions, as we will see in detail later on.

In partial compositeness this idea is realized imposing flavor symmetries on the strong sector [238, 239]. Starting from the double mixing Lagrangian

$$\mathcal{L}_{\text{mix}} = \lambda_{qu}^{ia} \bar{q}_L^i O_{qu}^a + \lambda_{qd}^{ia} \bar{q}_L^i O_{qd}^a + \lambda_u^{aj} \bar{O}_u^a u_R^j + \lambda_d^{aj} \bar{O}_d^a d_R^j + h.c. , \quad (3.18)$$

in the absence of the mixings  $\lambda$ , the elementary quarks are symmetric under the flavor group  $\mathcal{F}_e = U(3)_q \times U(3)_u \times U(3)_d$ . Similarly we assume a flavor group  $\mathcal{F}_c$  under which the  $O$  operators transform. To reproduce the SM Yukawas

$$Y_u^{ij} \simeq (\lambda_{qu} \lambda_u)^{ij} , \quad Y_d^{ij} \simeq (\lambda_{qd} \lambda_d)^{ij} , \quad (3.19)$$

it is clear that we need  $O_{qu}$  and  $O_u$  ( $O_{qd}$  and  $O_d$ ) to transform under the same group. At most  $\mathcal{F}_c$  can be  $U(3)_U \times U(3)_D$ , with an obvious notation. The MFV paradigm requires the  $\lambda$ s of eq. (3.18) to be spurions of the breaking of  $\mathcal{F} \equiv \mathcal{F}_e \times \mathcal{F}_c$  to  $U(1)_B$  according to the same pattern of the SM Yukawas. This last point, together with eq. (3.19) selects

only few options, summarized by the following breaking scheme

$$\mathcal{F}_e \times (\mathcal{F}_c \equiv U(3)_U \times U(3)_D) \xrightarrow{\lambda_u \propto \lambda_d \propto \mathbb{1}} U(3)_q \times U(3)_{U+u} \times U(3)_{D+d} \xrightarrow{\frac{\lambda_{qu} \propto Y_u}{\lambda_{qd} \propto Y_d}} U(1)_B, \quad (3.20)$$

$$\mathcal{F}_e \times (\mathcal{F}_c \equiv U(3)_U \times U(3)_D) \xrightarrow{\lambda_{qu} \propto \lambda_{qd} \propto \mathbb{1}} U(3)_{U+D+q} \times U(3)_u \times U(3)_d \xrightarrow{\frac{\lambda_u \propto Y_u}{\lambda_d \propto Y_d}} U(1)_B, \quad (3.21)$$

$$\mathcal{F}_e \times (\mathcal{F}_c \equiv U(3)_{U+D}) \xrightarrow{\lambda_{qu} \propto \lambda_{qd} \propto \mathbb{1}} U(3)_{U+D+q} \times U(3)_u \times U(3)_d \xrightarrow{\frac{\lambda_u \propto Y_u}{\lambda_d \propto Y_d}} U(1)_B, \quad (3.22)$$

$$\mathcal{F}_e \times (\mathcal{F}_c \equiv U(3)_U \times U(3)_D) \xrightarrow{\lambda_{qu} \propto \lambda_d \propto \mathbb{1}} U(3)_{U+q} \times U(3)_u \times U(3)_{D+d} \xrightarrow{\frac{\lambda_{qu} \propto Y_u}{\lambda_d \propto Y_d}} U(1)_B, \quad (3.23)$$

$$\mathcal{F}_e \times (\mathcal{F}_c \equiv U(3)_U \times U(3)_D) \xrightarrow{\lambda_u \propto \lambda_{qd} \propto \mathbb{1}} U(3)_{U+u} \times U(3)_{D+q} \times U(3)_d \xrightarrow{\frac{\lambda_u \propto Y_u}{\lambda_{qd} \propto Y_d}} U(1)_B, \quad (3.24)$$

that we will now review in turns.

### Right-handed compositeness

The first pattern, in eq. (3.20), assumes both right handed quarks mixings to be completely aligned with the composite fermions. Consequently the left handed mixings need to be aligned with the SM Yukawas. This scenario, that we denote  $U(3)_{\text{RC}}^2$ , has been widely explored in the literature [233, 238]. Here we will briefly review it and present updated bounds.

The model is characterized by the following form of the mixing parameters

$$U(3)_{\text{RC}}^2 : \quad \lambda_u^{ia} \equiv \varepsilon_u g_* \delta^{ia}, \quad \lambda_d^{ia} \equiv \varepsilon_d g_* \delta^{ia}, \quad \lambda_{qu}^{ai} \simeq \frac{Y_u^{ai}}{\varepsilon_u}, \quad \lambda_{qd}^{ai} \simeq \frac{Y_d^{ai}}{\varepsilon_d}. \quad (3.25)$$

We will assume that  $\lambda/g_* < 1$  such that a perturbative expansion of the Wilson coefficients can be obtained by counting the insertions of the mixing parameters. From this assumption follows that  $y_t/g_* \lesssim \varepsilon_u < 1$  and  $y_b/g_* \lesssim \varepsilon_d < 1$ .

As we have already anticipated, this scenario trivially protects the neutron EDM. The reason is that the flavor quantum numbers of the dipole interactions are the same as the Yukawa couplings. Therefore, at leading order in the insertion of the  $\lambda$ 's the coefficient of the dipole is necessarily aligned with the SM fermion mass matrix and so, under our assumption of CP-invariance up to  $\lambda$ , in the mass basis it is diagonal and real. Higher order insertions of  $\lambda$  will induce a misaligned correction to the dipole. However, this effect is parametrically suppressed by factors of order  $Y^2/16\pi^2$ .

In this model the strongest constraints come from the interplay of the measurements of the different four-fermion operators. Particularly important are the bounds from the compositeness of the light families and the flavor transition involving down quarks, as we will see in a moment. The  $U(3)$  symmetries of this scenario forces all up (down) right-handed quarks to be equally composite, with a degree of compositeness measured by the parameter  $\varepsilon_u$  ( $\varepsilon_d$ ). The compositeness of the light families can be tested at the (HL-)LHC by studying the dijet angular distributions [28]. In particular we focus on the following two operators

$$\mathcal{O}_{uu}^{(1)} = (\bar{u}_R \gamma^\mu u_R)(\bar{u}_R \gamma_\mu u_R), \quad \mathcal{O}_{dd}^{(1)} = (\bar{d}_R \gamma^\mu d_R)(\bar{d}_R \gamma_\mu d_R), \quad (3.26)$$

whose coefficients are expected to be of order  $g_*^2 \varepsilon_u^4 / m_*^2$  and  $g_*^2 \varepsilon_d^4 / m_*^2$  respectively. The projected 95%-bound for the 14 TeV LHC at  $300 \text{ fb}^{-1}$  integrated luminosity is [29]<sup>5</sup>

$$m_* \gtrsim 12.7 g_* \varepsilon_u^2 \text{ TeV}, \quad m_* \gtrsim 5.8 g_* \varepsilon_d^2 \text{ TeV}. \quad (3.27)$$

Regarding the flavor transitions instead, the most important bounds come from transition involving the  $B$  quark. We firstly consider the rare leptonic decays of  $B_s$  mesons into muons. In our scenarios, if we assume the leptons have a negligible mixing with the composite sector, the dominant transitions come from modifications of the  $Z$  couplings:

$$[\mathcal{O}_Z]^{ij} = \bar{f}^i \gamma^\mu f^j J_\mu^{(Z)}, \quad (3.28)$$

where  $J_\mu^{(Z)}$  is the Standard Model current that couples to the  $Z$ . In our framework these are induced by

$$[\mathcal{O}_{Hq}^{(1)}]^{ij} = (H^\dagger i \overleftrightarrow{D}_\mu H) \bar{q}_L^i \gamma^\mu q_L^j, \quad [\mathcal{O}_{Hq}^{(3)}]^{ij} = (H^\dagger i \overleftrightarrow{D}_\mu \tau^a H) \bar{q}_L^i \gamma^\mu \tau^a q_L^j, \quad (3.29)$$

where  $\tau^a \equiv \sigma^a / 2$  with  $\sigma^a$  the three Pauli matrices and the quarks have free flavor indices. Integrating out the Higgs and the electroweak bosons we get the effective operators of the form of eq. (3.28).

The  $B_s$  decay effective Hamiltonian is conventionally parameterized as

$$\mathcal{H}_{\text{eff}} = -\frac{4G_F}{\sqrt{2}} V_{\text{CKM}}^{tb} (V_{\text{CKM}}^{ts})^* \frac{e^2}{16\pi^2} \left[ C_{10} (\bar{s}_L \gamma^\mu b_L) (\bar{\ell} \gamma_\mu \gamma^5 \ell) + C'_{10} (\bar{s}_R \gamma^\mu b_R) (\bar{\ell} \gamma_\mu \gamma^5 \ell) \right]. \quad (3.30)$$

Notice that eq. (3.28) also contains the operators  $C_9$  and  $C'_9$ , of the same form of the previous ones but coupled with the leptonic current without the  $\gamma^5$ . The latter are suppressed by a factor  $(1 - 4 \sin^2 \theta_w) \sim 0.08$  compared to the ones in (3.30).

---

<sup>5</sup>CMS [240] and ATLAS [241] only released 13 TeV results at  $37 \text{ fb}^{-1}$  at the time of writing. Moreover, both the analyses consider only operators universal on the fermion family. We thus decided to use the projections for the end of Run 3 from [29] for our bounds.

The current neutral anomalies in the rare B decays point towards non-zero values for the  $C_{9/10}^{(\prime)}$  Wilson coefficients involving muons. Moreover the present fit prefers new physics aligned to the direction  $C_9 = -C_{10}$  (see [242]), even if some improvement with the data can be obtained including the effect of only one operator among  $C_9$  and  $C_{10}$ . We report the results from [242], for the best fit in some new physics direction

$$C_9 = -0.73 \pm 0.15, \quad C_{10} = 0.54 \pm 0.12, \quad C_9 = -C_{10} = +0.39 \pm 0.07, \quad (3.31)$$

where for each case all the other operators are set to zero.

The  $U(3)_{\text{RC}}^2$  model we are considering here generates  $C_{10}$  with a coefficient that can be estimated as

$$C_{10} = \frac{\sqrt{2}}{G_F} \frac{4\pi^2}{e^2} \frac{y_t^2}{m_*^2 \varepsilon_u^2} \sim 36.6 \frac{1}{m_*^2 \varepsilon_u^2}. \quad (3.32)$$

The right-handed sector is instead diagonal and thus  $C_{10}'$  is not generated at leading order. Requiring  $C_{10}$  not to exceed twice the  $1\sigma$  error on the single operator best fit in eq. (3.31) we get the following bound on  $m_*$

$$m_* \gtrsim \frac{12.3}{\varepsilon_u} \text{ TeV}. \quad (3.33)$$

With an appropriate choice of the composite group and the representation of the composite operators coupled to the elementary fermions, this bound could become weaker. Indeed, a  $P_{LR}$  symmetry [243] can be invoked to suppress the deviations of the  $Z$  couplings to the left-handed components of the down-type quarks arising from (3.86). In such a case the leading contribution would come from operators of the type

$$\bar{q}_L^i \gamma^\mu q_L^j \partial^\nu B_{\nu\mu}, \quad \bar{q}_L^i \tau^a \gamma^\mu q_L^j (D^\nu W_{\nu\mu})^a, \quad (3.34)$$

and the resulting bound would be parametrically suppressed by a power of  $g_{SM}^{(Z)}/g_* = g/(c_W g_*)$

$$m_* \gtrsim \frac{9.2}{g_* \varepsilon_u} \text{ TeV}. \quad (3.35)$$

The last important bounds come from the  $\Delta F = 2$  transitions in the  $B$  meson system. The right-composite MFV model only generates the  $\mathcal{O}_1$  operator of eq. (3.106) at tree-level. Indeed in this model, the spurions accompanying fermion bilinears involving two quarks of different chiralities ( $LR$ ) or two right-handed quarks ( $RR$ ) are clearly real and diagonal in flavor since they are proportional to a Yukawa matrix or its square respectively. This is not true however for bilinears involving only left-handed quarks ( $LL$ ), since they are proportional to a linear combination of  $Y_u Y_u^\dagger$  and  $Y_d Y_d^\dagger$  that is in general not diagonal.

The strongest bound comes from the  $B_d$  for which we estimate

$$\text{Abs } C_1^{bd} \sim \frac{A^2 y_t^4 \lambda^6}{m_*^2 g_*^2 \varepsilon_u^4}, \quad (3.36)$$

whose corresponding bound on  $m_*$  is

$$m_* \gtrsim \frac{6.5}{g_* \varepsilon_u^2}. \quad (3.37)$$

A complete analysis of all the bounds of this model, including also other observables, is done in sec. 3.4.

Putting together the bounds just discussed, we find that this model requires quite a large value for  $m_*$ . If we do not assume the  $P_{LR}$  symmetry the strongest bounds are in eq. (3.27) from quark compositeness, which tends to require small  $\varepsilon_u$ , and (3.33) from  $\Delta F = 1$  transitions, which require sizable  $\varepsilon_u$ . Marginalizing over  $\varepsilon_u$  we see that the lower bound on the new physics mass scale reads  $m_* \gtrsim 12.4 g_*^{1/3} \gtrsim 12.4$  TeV. If one instead assumes  $P_{LR}$ , the bound from the  $B_s$  decay becomes subdominant. The minimum value for  $m_*$  can then be found by combining eq. (3.27) with eq. (3.37) to give

$$m_* \gtrsim 9 \text{ TeV}. \quad (3.38)$$

This bound is obtained for  $\varepsilon_u = 0.85/\sqrt{g_*}$ , which for not so large  $g_*$  is compatible with the hypothesis of composite  $u$ -type quarks.

It is clear that the origin of this problem is that the mixing in the up-sector  $\varepsilon_u$  is the same for both the light families (that control the quark compositeness bound) and the top-quark (which gives the dominant contribution to flavor-violating processes). In sec. 3.3 we will quantify the improvement obtain when separating the mixing parameters of the first two families from that of the top quark.

#### Left-handed compositeness

The second and third patterns, in eqs. (3.21) and (3.22), feature SM doublets completely aligned with the composite ones. From the flavor point of view, these two scenarios are almost equivalent as long as the left handed mixings are comparable  $\lambda_{q_u} \sim \lambda_{q_d}$ . The main qualitative difference is that imposing the larger symmetry  $\mathcal{F}_c = U(3)_U \times U(3)_D$  suppresses tree-level transitions between right-handed up and down quarks. In other words, the model (3.22) allows the flavor-violating structure  $(Y_u^\dagger Y_d)_{ij} \bar{u}_i \gamma^\mu d_j$ , whereas these can only arise combined with a loop suppression  $g_*^2/16\pi^2$  in (3.21). These transitions are, however, not significantly constrained experimentally, as we see in detail in sec. 3.4. For this reason we will therefore only consider the case of (3.22) that can be realized with a single mixing partner of the left-handed doublets. This scenario, that we denote

$U(3)_{\text{LC}}$ , has been previously explored in [233, 238].

This model thus contains the following mixing parameters

$$U(3)_{\text{LC}} : \quad \lambda_q^{ia} \equiv \varepsilon_q g_* \delta^{ia}, \quad \lambda_u^{ai} \simeq \frac{Y_u^{ai}}{\varepsilon_q}, \quad \lambda_d^{ai} \simeq \frac{Y_d^{ai}}{\varepsilon_q}, \quad (3.39)$$

where  $y_t/g_* \lesssim \varepsilon_q < 1$ .

For the same reasons as  $U(3)_{\text{RC}}^2$ , there is no contribution to the neutron EDM. Yet, this implementation of MFV significantly suppresses flavor-changing transitions at tree-level. This is readily understood since the spurion that controls  $LL$  structures is the identity, while for the  $RL$  and  $RR$  structures we have respectively the Yukawa and its square, which in the mass basis are diagonal. The only exception is the weakly-constrained  $\bar{u}_R - d_R$  structures mentioned above.

The most relevant constraints arise from flavor conserving processes. For example, consider the operator

$$\mathcal{O}_{qq}^{(1)} = (\bar{q}_L \gamma^\mu q_L)(\bar{q}_L \gamma_\mu q_L), \quad (3.40)$$

for left-handed transitions in dijet searches. Using again the bounds from [29], we find

$$m_* \gtrsim 14.2 g_* \varepsilon_q^2 \text{ TeV}, \quad (3.41)$$

that clearly favors a small value for  $\varepsilon_q$ .

The strongest bound for this model however comes from the electroweak sector. The operators in eq. (3.86) indeed generate a flavor universal correction to the  $W$  coupling of the left-handed quarks as

$$\frac{g}{\sqrt{2}}(1 + \delta g_W^L) \bar{u} V_{\text{CKM}} \gamma^\mu P_L d W_\mu^+, \quad (3.42)$$

where we estimate

$$\delta g_W^L \sim v^2 \frac{\varepsilon_q^2 g_*^2}{m_*^2}. \quad (3.43)$$

This correction is constrained by the measured unitarity condition on  $V_{\text{CKM}}$ . Indeed, the experimental condition [244]  $(1 + \delta g_W^L)^2 \sum_i |V_{\text{CKM}}^{ui}|^2 - 1 = (1.5 \pm 0.7) \times 10^{-3}$  in our model (where  $V_{\text{CKM}}$  is in fact unitary) reads  $(1 + \delta g_W^L)^2 - 1 \approx 2\delta g_W^L = (1.5 \pm 0.7) \times 10^{-3}$ . By requiring that this modification does not exceed twice the  $1\text{-}\sigma$  error, we derive the bound

$$m_* \gtrsim 9.3 g_* \varepsilon_q \text{ TeV}. \quad (3.44)$$

Since to reproduce the top Yukawa  $\varepsilon_q$  cannot be smaller than  $y_t/g_*$ , this gives an absolute lower bound on  $m_*$ :

$$m_* \gtrsim 9.3 y_t \text{ TeV} \approx 8 \text{ TeV}. \quad (3.45)$$

Similarly to  $U(3)_{\text{RC}}^2$ , also in this model the origin of the strong lower bound on the new physics scale is the universality of the  $\varepsilon_q$  parameter among the three families.

### Mixed compositeness

Finally the two last scenarios of eqs. (3.23) and (3.24) are somehow hybrid between the pattern previously described [238] and they maintain the same weak spots of the latter. In particular the scenario described in eq. (3.24) has the same strong bounds of  $U(3)_{\text{RC}}^2$ , from  $b \rightarrow s$  transitions and compositeness of the light up families. The model of eq. (3.23), regardless of the flavor structure is excluded up to  $m_* > 8$  TeV from the unitarity of the CKM. For these reasons we will not analyze them further.

## 3.3 Less symmetric strong sector

We now go beyond MFV violation and we show how a smaller strong sector flavor group  $\mathcal{F}_c$  allows to keep  $m_*$  relatively low. The logic we follow is to start from a MFV set-up, identify its weak spots and then try to reduce the tension with the data by downgrading  $\mathcal{F}_c$  to a smaller group. We stress that our goal is not to find the composite Higgs model less constrained by flavor measurements, in fact we can expect that ad-hoc constructions and specific assumptions for the spurions  $\lambda$  can have weaker bounds than the ones we will find in the rest of the section. Our procedure, on the contrary, is systematic and based on two well defined hypotheses: the composite sector respects some flavor symmetry  $\mathcal{F}_c$  and some of the SM quarks belong to the strong sector. The amount of compositeness of the latter are measured by some parameters  $\varepsilon$  and we can check a posteriori if  $\varepsilon \sim 1$  or if  $\varepsilon \ll 1$ , meaning that our hypothesis is inconsistent. Furthermore we take as starting point the Lagrangian of eq. (3.18), including one partner for each right-handed fields and at most two partners for the SM doublets.

### 3.3.1 Right-handed compositeness

We first start from the scenario where the right-handed quarks are aligned with the composite sector. In sec. 3.2.1 we analyzed in detail how MFV can be realized in this hypothesis and why this model is only consistent with data for large values of  $m_*$ . In particular we saw that flavor transitions are enhanced by very composite right-handed top. At the same time composite top means composite up and charm which are very well tested and excluded by LHC measurements. The way out we want to explore is to separate the top from the two lighter families reducing the  $U(3)_U \times U(3)_D$  flavor group to  $U(2)_U \times U(1)_T \times U(3)_D$ . In sec. 3.3.1 we show how this scenario, we denote as  $U(2) \times U(3)_{\text{RC}}$ , has enough freedom to have the right-handed top fully composite, maintaining at the same time mildly composite light quarks and not generating other dangerous (CP odd) effects as electric dipoles. A previous study of this scenario is



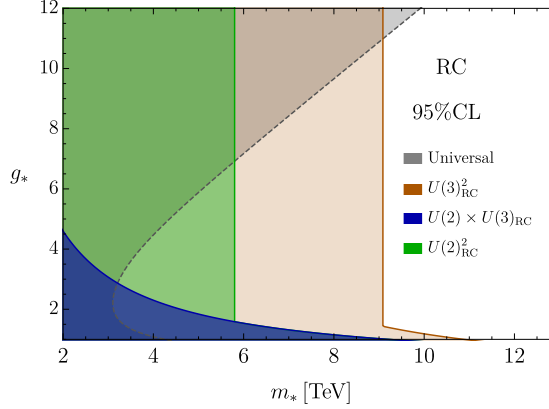


Figure 3.1 – Summary plot for the three right-handed compositeness models under consideration.

presented in [245], that we update and extend in the following. Then, in sec. 3.3.1, we go beyond that and we try to separate also the heaviest family in the down sector. We will see that this scenario, where  $\mathcal{F}_c = U(2)_U \times U(1)_T \times U(2)_D \times U(1)_B$ , does not improve significantly over  $U(2) \times U(3)_{\text{RC}}$ .

Our results are summarized in fig. 3.1. We can see that MFV is excluded up  $m_* \sim 9$ , independently of the other parameters of the model. This bound is obtained by combining the constraints from compositeness and  $\Delta F = 2$  transitions in the  $B$  sector, while the tail at small values of  $g_*$  comes from the  $\Delta F = 1$  leptonic  $B$  decays. The minimal  $m_*$  value is roughly a factor 3 larger than the minimum  $m_*$  allowed by universal constraints. The assumptions of  $U(2)^2_{\text{RC}}$  slightly improve the situation as shown by the green contour, that it is dominated by the  $b \rightarrow s\gamma$  transition. Yet, among the models we studied in this section the mildest flavor-dependent constraints are found in the  $U(2) \times U(3)_{\text{RC}}$  scenario, where the most relevant bound comes from rare  $B$  decays. In some sense this model seems to have the ideal amount of symmetries necessary to avoid indirect searches; more or less symmetries will just increase the tension with the data.

### $U(2) \times U(3)_{\text{RC}}$

This model is characterized by the flavor group  $\mathcal{F}_c = U(2)_U \times U(1)_T \times U(3)_D$  and is described by the following Lagrangian

$$\begin{aligned} \mathcal{L}_{\text{mix}}^{U(3) \times U(2)_{\text{RC}}} = & \lambda_{qu}^{iA} \bar{q}_L^i O_{qu}^A + \lambda_{qd}^{ia} \bar{q}_L^i O_{qd}^a + \lambda_{qt}^i \bar{q}_L^i O_{qt} \\ & + g_* \varepsilon_u \bar{O}_u^A u_R^i \delta_{Ai} + g_* \varepsilon_d \bar{O}_d^a d_R^i \delta_{ai} + g_* \varepsilon_t \bar{O}_t t_R + h.c. . \end{aligned} \quad (3.46)$$

where  $A = 1, 2$  is the index of the  $U(2)_U$  group, while  $a = 1, 2, 3$  is the index of the  $U(3)_D$  group. The mixing parameters  $\lambda$  and  $\varepsilon$  can be identified as spurions of the breaking of the flavor group  $\mathcal{F}$ , transforming as in the table in App. C.1. While in the down sector

this scenario is completely analogous to  $U(3)_{\text{RC}}^2$ , it differs in the up sector, having the top separated from the other two quarks forming a doublet of  $U(2)_U$ . A scheme of the symmetry breaking pattern for this and the other right-handed scenarios is reported in fig. 3.3.

The Yukawa couplings for the up and down sector are written in terms of the mixings as

$$Y_u \sim (\lambda_{qu} \varepsilon_u | \lambda_{qt} \varepsilon_t), \quad Y_d \sim \lambda_{qd} \varepsilon_d \quad (3.47)$$

where the vertical bar means that the  $3 \times 2$  matrix and the  $3 \times 1$  vector should be stacked together to form a  $3 \times 3$  matrix. We parametrize the mixings  $\lambda$  in the most general way that can reproduce the SM Yukawas. We only assume that  $\lambda_{qt} \gg \lambda_{qu}$ , which may be explained by RG effects similarly to anarchic Partial Compositeness. Under this hypothesis  $\lambda_{qt} \sim y_t$  whereas  $\lambda_{qu}$  has the largest size of order  $y_c$ . In order to generate a Yukawa for the up-quark, we have to assume that one component is accidentally small and of the order of  $y_u$ . Using the flavor symmetries of the system, we can reduce them in the following way

$$U(2) \times U(3)_{\text{RC}} : \quad \begin{aligned} \lambda_{qu} &= \frac{1}{\varepsilon_u} \begin{pmatrix} y_u & 0 \\ 0 & y_c \\ a y_c & b y_c \end{pmatrix}, \quad \lambda_{qt} = \frac{1}{\varepsilon_t} \begin{pmatrix} 0 \\ 0 \\ y_t \end{pmatrix}, \\ \lambda_{qd} &= \frac{1}{\varepsilon_d} \tilde{U}_d \begin{pmatrix} y_d & 0 & 0 \\ 0 & y_s & 0 \\ 0 & 0 & y_b \end{pmatrix}. \end{aligned} \quad (3.48)$$

The coefficients  $a$  and  $b$  are assumed to be  $\mathcal{O}(1)$  complex numbers with an arbitrary phase and the matrix  $\tilde{U}$  is a  $3 \times 3$  unitary matrix. Notice that, by field redefinition we can remove all but one phase on  $\tilde{U}_d$  meaning that in this model there are in total three physical phases.

In this basis the Yukawa matrices are not diagonal and can be diagonalized with bi-unitary transformations to go to the mass basis. In particular the two matrices  $U_u$  and  $V_u$  that diagonalize  $Y_u$  can be computed explicitly in the limit  $y_u \ll y_c \ll y_t$  as shown in app. C.1. The matrix  $\tilde{U}_d$  is instead identified in terms of the CKM matrix as

$$V_{\text{CKM}} = U_u^\dagger \tilde{U}_d. \quad (3.49)$$

This model contains in total five additional real free parameters, namely  $\varepsilon_u, \varepsilon_d, \varepsilon_t, |a| \sim 1$  and  $|b| \sim 1$ , and two additional CP violating phases,  $\arg[a]$  and  $\arg[b]$ , compared to the SM. Therefore, even if we assume a CP even strong sector, there are two additional phases giving rise to new potentially measurable effects in electric dipole or CP odd flavor transition. Moreover, notice that, from the Lagrangian in eq. (3.46) it is possible to recover the  $U(3)_{\text{RC}}^2$  model simply by setting  $a = b = 0$  and  $\varepsilon_t = \varepsilon_u$ . This point is also summarized in fig. 3.3.

We now inspect the bounds on this scenario in details.

#### Electric dipole cancellation

As we mentioned before, the new phases in the mixing of eq. (3.46) can in general produce new observables effects. A remarkable property of all the models under exam in this section, is the absence of electric dipole moments at leading order in the spurion insertions. In the specific case of  $U(2) \times U(3)_{\text{RC}}$ , moreover, non-zero electric dipoles are generate at 1-loop only for the up sector and they happen to be extremely suppressed, while contributions from the down quarks come at at least 2-loops.

Contributions to the electric and chromoelectric dipole moments of the neutron are induced by the imaginary part of the Wilson coefficients  $C_{ff\gamma}$  and  $C_{ffg}$  of the following operators

$$\mathcal{O}_{ff\gamma} = e \bar{f}_L \sigma^{\mu\nu} \gamma^5 f_R F_{\mu\nu}, \quad \mathcal{O}_{ffg} = g_s \bar{f}_L \sigma^{\mu\nu} \gamma^5 f_R G_{\mu\nu}. \quad (3.50)$$

In MFV, these are obviously aligned with the SM Yukawas at tree-level and so they are real and diagonal in the mass basis. In the case of  $U(2) \times U(3)_{\text{RC}}$  the same is clearly true for the down sector, which is completely equivalent to MFV, but the cancellation of dipoles in the up sector is less trivial and requires a specific discussion.

Let start from the spurions in eq. (3.46), the flavour structure of the Wilson coefficient of the operators in eq. (3.50) is

$$[C_{uu\gamma}]^{ij} \propto [C_{uug}]^{ij} \propto (\lambda_{qu} \varepsilon_u |x \lambda_{qt} \varepsilon_t)^{ij}, \quad (3.51)$$

where  $x$  is an  $\mathcal{O}(1)$  real number with  $x-1$  measuring the departure from the SM Yukawas, and  $i, j$  denote the SM flavor. To prove the absence of electric dipoles we must show that the coefficients in eq. (3.51), once rotated in the mass basis, have real diagonal entries  $i = j$ . A way to see it is to start from the explicit form for the spurions in eq. (3.48) and remove all the phases from  $\lambda_{qu}$ ,  $\lambda_{qt}$ ,  $\varepsilon_u$  and  $\varepsilon_t$ . This can be done, for instance, rotating the SM fields, in the Lagrangian of eq. (3.46), as

$$u_R^1 \rightarrow u_R^1 e^{-i\arg[a]}, \quad q_L^1 \rightarrow q_L^1 e^{-i\arg[a]}, \quad u_R^2 \rightarrow u_R^2 e^{-i\arg[b]}, \quad q_L^2 \rightarrow q_L^2 e^{-i\arg[b]}. \quad (3.52)$$

This field rotation removes the phases from the two parameters  $a$  and  $b$  and moves them to the down sector. In this way the new up Yukawa in eq. (3.47) is now free of complex entries and can be diagonalized by orthogonal matrices only. As a consequence the dipole Wilson coefficient in eq. (3.51) is build out just starting from real objects and it is clearly real itself. Moreover any additional rotation of the fields which keeps the Yukawas real and diagonal in the mass basis, cannot modify the diagonal entries of eq. (3.51) resulting

in no-tree level electric dipoles.

There is another way to prove the absence of electric dipoles at tree level. Starting again from eq. (3.51) we can see that, at tree level,  $[C_{uu\gamma/g}]^{ij}$  is built out of  $\lambda_{u,t}$  and  $\epsilon_{u/t}$ . Since electric dipoles are observables, and so basis independent, we can search for flavor invariants constructed as combinations of  $\lambda_{u,t}$  and  $\epsilon_{u/t}$ . However, a basis for such invariants is given by

$$\lambda_{qt}^\dagger \lambda_{qt}, \quad \text{Tr}[\lambda_{qu} \lambda_{qu}^\dagger], \quad \text{Tr}[(\lambda_{qu} \lambda_{qu}^\dagger)^2], \quad \lambda_{qt}^\dagger (\lambda_{qu} \lambda_{qu}^\dagger) \lambda_{qt}, \quad \lambda_{qt}^\dagger (\lambda_{qu} \lambda_{qu}^\dagger)^2 \lambda_{qt}, \quad |\varepsilon_t|^2, \quad |\varepsilon_u|^2, \quad (3.53)$$

and it is manifestly real. Therefore, the only way to have a complex invariant is to include also the  $\lambda_{qd}$  spurion, which can only occur at next to leading order.

In the  $U(2) \times U(3)_{\text{RC}}$  model the first diagonal imaginary contribution for the up-sector requires at least one loop of the elementary fields. The Wilson coefficient of eq. (3.50) is given by

$$[C_{uu\gamma}]^{ij} = \frac{1}{16\pi^2} \frac{v}{\sqrt{2}} \left[ \lambda_{qd} \lambda_{qd}^\dagger (\lambda_{qu} \varepsilon_u | x \lambda_{qt} \varepsilon_t) \right]^{ij} \quad (3.54)$$

giving the following leading contribution to the electric dipole moment

$$d_n \sim e \frac{y_b^2}{16\pi^2} \frac{\Re(a) A \eta \lambda^3}{m_*^2 \varepsilon_d^2} m_c \implies m_* > \frac{0.05}{\varepsilon_d} \text{ TeV}. \quad (3.55)$$

The latter is of the same order of the bound on  $Zb_L b_L$  from LEP measurements, reported in tab. 3.1 and it is clearly under control for  $\varepsilon_d \gtrsim 0.05$ . Notice that in the  $a \rightarrow 0$  limit the previous contributions goes to zero.

We also remark that 1-loop contributions to down quarks electric dipole moments are zero, as can be seen by a straightforward calculation. Indeed the contribution reads

$$[C_{dd\gamma}]^{ij} = \frac{1}{16\pi^2} \frac{v}{\sqrt{2}} \left[ (\lambda_{qu} \lambda_{qu}^\dagger + x_1 \lambda_{qt} \lambda_{qt}^\dagger + x_2 \lambda_{qd} \lambda_{qd}^\dagger) \lambda_{qd} \right]^{ij}, \quad (3.56)$$

with  $x_1$  and  $x_2$  some  $O(1)$  real numbers. It is clear that the term proportional to  $x_2$  is real and diagonal in the mass basis. The first two terms in the mass basis instead read

$$(\lambda_{qu} \lambda_{qu}^\dagger + x_1 \lambda_{qt} \lambda_{qt}^\dagger) \lambda_{qd}^\dagger \rightarrow V_{\text{CKM}}^\dagger \left[ \frac{\bar{Y}_u^2}{\varepsilon_u^2} + \left( \frac{x_1}{\varepsilon_t^2} + \frac{1}{\varepsilon_u^2} \right) U_u^\dagger \tilde{Y}_t^2 U_u \right] V_{\text{CKM}} \frac{\bar{Y}_d}{\varepsilon_d} \quad (3.57)$$

with the notation of App. C.1. Since this contribution is written as the product of a Hermitean matrix and a real and diagonal matrix, the diagonal entries are real as well, proving that also at 1-loop there is no contribution to dipoles.

#### Constraints

We just showed that the  $U(2) \times U(3)_{\text{RC}}$  scenario is safe from electric dipoles. Moreover, since the down sector is aligned with the Yukawas, this model is also protected from dipole operators mediating  $b \rightarrow s\gamma$  transitions, which usually give rise to strong bounds. However, this model has a less trivial flavor structure than MFV and the less amount of symmetries in the strong sector open the way to new potentially measurable effects. All the constraints on the model are detailed in sec. 3.4, in the following we just discuss the most important signatures of the model.

The strongest constraints on  $U(2) \times U(3)_{\text{RC}}$  come from the same observables as  $U(3)_{\text{RC}}^2$ . The bound from light fermion compositeness clearly coincides with eq. (3.27), i.e. we have

$$m_* \gtrsim 12.7 g_* \varepsilon_u^2 \text{ TeV}, \quad m_* \gtrsim 5.8 g_* \varepsilon_d^2 \text{ TeV}. \quad (3.58)$$

The bounds from  $\Delta F = 2$  and  $\Delta F = 1$  transitions in the  $B$  sector of eqs. (3.37) and (3.33) are instead now enhanced by a small  $\varepsilon_t$ . They are respectively

$$m_* \gtrsim \frac{6.5}{g_* \varepsilon_t^2}, \quad (3.59)$$

and

$$m_* \gtrsim \frac{12.3}{\varepsilon_t} \text{ TeV}, \quad (\text{w/o } P_{LR}) \quad m_* \gtrsim \frac{9.2}{g_* \varepsilon_t} \text{ TeV} (\text{w/ } P_{LR}). \quad (3.60)$$

It is clear that in this model we can have a small value for  $\varepsilon_u$  and  $\varepsilon_d$  in order to minimize the bounds from compositeness, still keeping  $\varepsilon_t \sim 1$  to minimize the flavor bounds. The ideal scenario has a maximal top compositeness  $\varepsilon_t = 1$  and the  $P_{LR}$  protection, in which case we find  $m_* \gtrsim 10.8 \varepsilon_u \text{ TeV}$ . An order one value  $\varepsilon_u \sim 0.3$  is perfectly compatible with the assumption of composite up-type quarks and would imply the relatively weak bound  $m_* \gtrsim 3 \text{ TeV}$ . Much smaller values of  $\varepsilon_u$  would render the compositeness assumption less plausible. In addition if  $\varepsilon_u \lesssim 0.04 \varepsilon_t$  stronger bounds than the ones considered here would arise from  $s$ -to- $d$   $\Delta F = 2$  transitions (see Tab. 3.4). Apart from what we just mentioned, no other large effects are generated in this model. The strongest bound comes from eq. (3.60) that, in presence of  $P_{LR}$  protection is relatively under control. Moreover, the latter, has to be compared with the universal signatures discussed in sec. 3.4.1, as shown by the summary plot in fig. 3.2.

#### $U(2)_{\text{RC}}^2$

We would like now to see if anything is gained by considering a smaller strong flavor group  $\mathcal{F}_c$ , studying the case where both the right-handed top and bottom possess only an abelian flavor symmetry. The step of separating the bottom is not motivated by the

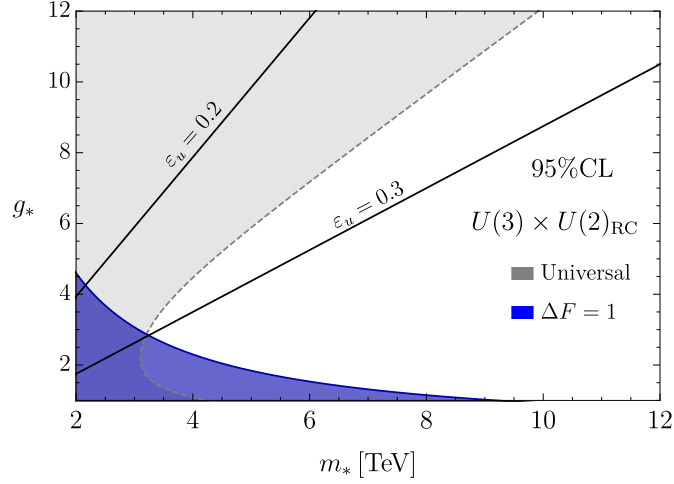


Figure 3.2 – Current constraints on  $U(2) \times U(3)_{\text{RC}}$  model at 95% CL. The blue line is obtained setting  $\varepsilon_t = 1$ . The black lines are the bounds from up quark compositeness for two different values of  $\varepsilon_u$ .

bounds previously discussed, which will not be relaxed. Considering this model is rather aimed to see how much freedom we can leave to the strong sector before it results in unwanted flavor signatures.

The scenario we consider now has so  $\mathcal{F}_c = U(2)_U \times U(1)_T \times U(2)_D \times U(1)_B$  that is then broken by the right-handed mixings to  $U(2)_{u+U} \times U(1)_{t+T} \times U(2)_{d+D} \times U(1)_{b+B}$ . The mixing Lagrangian reads

$$\begin{aligned} \mathcal{L}_{\text{mix}}^{U(2)_{\text{RC}}^2} = & \lambda_{q_u}^{iA} \bar{q}_L^i O_{q_u}^A + \lambda_{q_d}^{iB} \bar{q}_L^i O_{q_d}^B + \lambda_{q_t}^i \bar{q}_L^i O_{q_t} + \lambda_{q_b}^i \bar{q}_L^i O_{q_b} \\ & + g_* \varepsilon_u \bar{O}_u^A u_R^i \delta_{Ai} + g_* \varepsilon_d \bar{O}_d^B d_R^i \delta_{Bi} + g_* \varepsilon_t t_R \bar{O}_t + g_* \varepsilon_b b_R \bar{O}_b + h.c., \end{aligned} \quad (3.61)$$

where the indices  $A, B = 1, 2$  transform respectively under  $U(2)_U$  and  $U(2)_D$ . Analogously to the  $U(2) \times U(3)_{\text{RC}}$  scenario the Yukawas take the following form

$$Y_u \sim (\lambda_{q_u} \varepsilon_u | \lambda_{q_t} \varepsilon_t), \quad Y_d \sim (\lambda_{q_d} \varepsilon_d | \lambda_{q_b} \varepsilon_b), \quad (3.62)$$

and we can parameterize the mixings  $\lambda$  as

$$\begin{aligned} \lambda_{q_u} = \frac{1}{\varepsilon_u} \begin{pmatrix} y_u & 0 \\ 0 & y_c \\ a y_c & b y_c \end{pmatrix}, \quad \lambda_{q_t} = \frac{1}{\varepsilon_t} \begin{pmatrix} 0 \\ 0 \\ y_t \end{pmatrix}, \\ U(2)_{\text{RC}}^2 : \quad \lambda_{q_d} = \frac{1}{\varepsilon_d} \tilde{U}_d \begin{pmatrix} y_d & 0 \\ 0 & y_s \\ d' y_s & b' y_s \end{pmatrix}, \quad \lambda_{q_b} = \tilde{U}_d \frac{1}{\varepsilon_b} \begin{pmatrix} 0 \\ 0 \\ y_b \end{pmatrix}, \end{aligned} \quad (3.63)$$

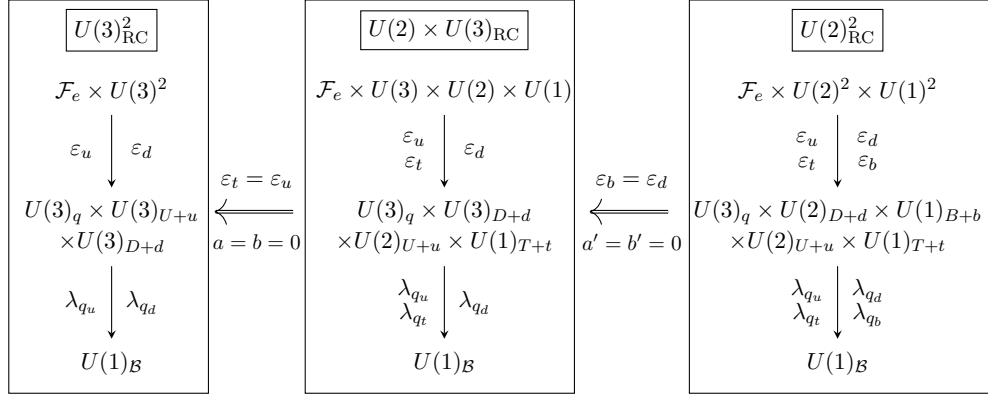


Figure 3.3 – Scheme of the various right-handed compositeness models under consideration. Starting from the less symmetric  $U(2)_{\text{RC}}^2$  on the right, it is possible to recover  $U(3)_{\text{RC}}^2$  switching off some of the parameters.

with  $\tilde{U}_d$  a  $3 \times 3$  unitary matrix.<sup>6</sup> Notice that, even in this model, we can remove all the phases but one from  $\tilde{U}_d$ , with a total of 5 phases in eq. (3.63). The matrices that diagonalize the Yukawas are once again reported in app. C.1 and  $\tilde{U}_d$  is rewritten in terms of the CKM as

$$V_{\text{CKM}} = U_u^\dagger \tilde{U}_d U_d. \quad (3.64)$$

Similarly to before, for this model we assume the parameters  $a, b, a'$  and  $b'$  to be  $O(1)$  with arbitrary phases. The model and its relation to the other Right-handed compositeness scenarios is summarized in fig. 3.3.

### Constraints

This model inherits many features of the  $U(2) \times U(3)_{\text{RC}}$  case just examined. The most important aspect is the absence of the electric dipoles at tree-level. The proof simply follows from the arguments presented for the  $U(2) \times U(3)_{\text{RC}}$ . In that model we showed that one cannot build physical observables using only spurion in the up-sector, the same arguments trivially extends also to the  $U(2)_{\text{RC}}^2$  case for both the down and up sectors. Moreover, notice that, differently from  $U(2) \times U(3)_{\text{RC}}$  now we have one-loop dipoles for both up and down quarks. The latter are totally analogous to eq. (3.55) and are negligible.

The compositeness bound of eq. (3.58) and the flavor bound of eqs. (3.60) and (3.59) apply also here. In this model however we also generate additional flavor transitions. The first one is the  $\Delta F = 2$  transition for right handed quarks. These bounds come from the operator  $\tilde{\mathcal{O}}_1$  of eq. (3.106). The complete list of bounds can be found in sec. 3.4, here

<sup>6</sup>We only need a single  $\tilde{U}_d$  to reach this form: we start from a  $3 \times 3$  unitary matrix that aligns  $\lambda_b$  in the third direction and then we multiply it with a  $2 \times 2$  block diagonal unitary matrix that leaves  $\lambda_b$  invariant but allow to diagonalize the top  $2 \times 2$  block of  $\lambda_d$  together with a  $U(2)_D$  matrix on the right.

we report only the strongest one, related to  $B_d$  system and we get

$$m_* \gtrsim 19.3 g_* \varepsilon_b^2 \text{ TeV} . \quad (3.65)$$

Additional effects are also present in  $\Delta F = 1$  (see sec. 3.4.2 for details), in fact, contrary to  $U(3)_{\text{RC}}^2$  and  $U(2) \times U(3)_{\text{RC}}$  the model  $U(2)_{\text{RC}}^2$  has a less trivial structure in the down sector and generate a non-suppressed  $C'_{10}$  in eq. (3.30)

$$C'_{10}|_{U(2)_{\text{RC}}^2} = \frac{\sqrt{2}}{G_F} \frac{4\pi^2}{e^2} \frac{1}{V_{\text{CKM}}^{tb}(V_{\text{CKM}}^{ts})^*} \frac{g_*^2 y_s (\varepsilon_b^2 - \varepsilon_d^2)}{m_*^2 y_b} \sim 23.9 \frac{g_*^2 (\varepsilon_b^2 - \varepsilon_d^2)}{m_*^2} . \quad (3.66)$$

Still from [242] we can read the bound on  $C'_{10}$ , which implies the following disequality on  $m_*$

$$|C'_{10}| \lesssim 0.2 \implies m_* \gtrsim 10.9 g_* \varepsilon_b \text{ TeV} . \quad (3.67)$$

The previous equation clearly tells that a small  $\varepsilon_b$  is preferred. Moreover there are two effects that are enhanced by a small  $\varepsilon_b$ . The first is the anomalous  $Z b_L b_L$  coupling (see tab. 3.1), the second is the 1-loop contribution to neutron dipole moment. The latter can be simply red from eq. (3.55) replacing  $\varepsilon_d \rightarrow \varepsilon_b$ . Combining eq. (3.67) with the bound from  $Z b_L b_L$  anomalous coupling in tab. 3.1 we find

$$m_* \gtrsim 0.9 \sqrt{g_*} \text{ TeV} , \quad (3.68)$$

obtained marginalizing on  $\varepsilon_b$ . This effect is less relevant than universal constraints on  $C_H$ , as described in sec. 3.85. The lowest value of  $m_*$  outlined in the previous formula is obtained for  $\varepsilon_b = 0.086/\sqrt{g_*}$ . However, values of  $\varepsilon_b$  much smaller than unity are incompatible with the hypothesis of  $b$ -quark compositeness. To defend this hypothesis much larger values of  $\varepsilon_b$  are necessary, and as a result a stronger constraint on  $m_*$  follows.

The  $U(2)_{\text{RC}}^2$  model also generates another  $\Delta F = 1$  effect, the  $B \rightarrow X_s \gamma$  transitions, via the so-called EW dipoles. These interactions are described according to the following effective operators

$$\bar{f}_{L(R)}^i \sigma_{\mu\nu} f_{R(L)}^j F_{SM}^{\mu\nu} , \quad (3.69)$$

with  $F_{SM}^{\mu\nu}$  the field strength of the SM gauge bosons and  $i, j$  the flavor indexes of the fermions.

The strongest constraints on these kind of interactions come from the radiative decay of



$B$  mesons. The effective Hamiltonian relevant for  $b \rightarrow s \gamma$  transition is

$$\mathcal{H}_{\text{eff}} = -\frac{4G_F}{\sqrt{2}} V_{\text{CKM}}^{tb} (V_{\text{CKM}}^{ts})^* \frac{m_b e}{16\pi^2} F^{\mu\nu} (C_7 \bar{s}_L \sigma_{\mu\nu} b_R + C'_7 \bar{s}_R \sigma_{\mu\nu} b_L) , \quad (3.70)$$

and the new physics contribution to the previous Wilson coefficient is constrained to be [246] roughly

$$\text{Re } C_7 \lesssim 0.03 , \quad |C'_7| \lesssim 0.07 \quad (3.71)$$

at 95% CL. In our model we estimate

$$C'_7|_{U(2)_{\text{RC}}^2} \sim \frac{m_s}{m_b} \frac{b' 4\sqrt{2}\pi^2}{G_F V_{\text{CKM}}^{tb} (V_{\text{CKM}}^{ts})^* m_*^2} \sim 2.4 \left( \frac{1 \text{ TeV}}{m_*} \right)^2 , \quad (3.72)$$

while  $C_7$  is suppressed by a further power of  $m_s/m_b$ . This translates into the much stronger bound

$$m_* \gtrsim 5.8 \text{ TeV} . \quad (3.73)$$

Combining all these bounds the largest possible value for  $\varepsilon_b$  is roughly  $\varepsilon_b \lesssim 0.5/g_*$ . The constraints on  $\varepsilon_d$  are much milder and read  $\varepsilon_d \lesssim 1/\sqrt{g_*}$ . Overall, scenarios with composite  $d$ -type quarks seem to require  $g_* \sim 1$ .

To conclude, separating the third family of the down-sector does not seem to offer a significant improvement. Compared to the  $U(2) \times U(3)_{\text{RC}}$  model there are important new signatures. The  $\Delta F = 2$  transition and the new correction to  $C'_{10}$  may be suppressed by taking  $\varepsilon_b$  small. However, the bound in eq. (3.73) gives a robust absolute lower bound on  $m_*$  independent on the other model parameters.

### 3.3.2 Left-handed compositeness

We now move on and we discuss the left-compositeness models. Our starting point is the  $U(3)_{\text{LC}}$  model of sec. 3.2.1, where for concreteness we assume only one mixing for each SM doublet. We have seen that MFV model requires at least  $m_* \gtrsim 8 \text{ TeV}$ , due to the tension with the precise measurement on the CKM matrix unitarity, see eq. (3.42). We now try to relax this constrain assuming a smaller  $\mathcal{F}_c$ .

#### $U(2)_{\text{LC}}$

Following the same logic we adopted so far, we can start from  $U(3)_{\text{LC}}$  and then separate the third family reducing the strong sector flavor symmetries. More explicitly, we take the left-handed mixing to break the composite group  $\mathcal{F}_c = U(2)_{U+D} \times U(1)_{T+B}$  and the elementary flavor group to the diagonal  $U(2)_{q+U+D} \times U(1)_{q^3+T+B}$ , according to the

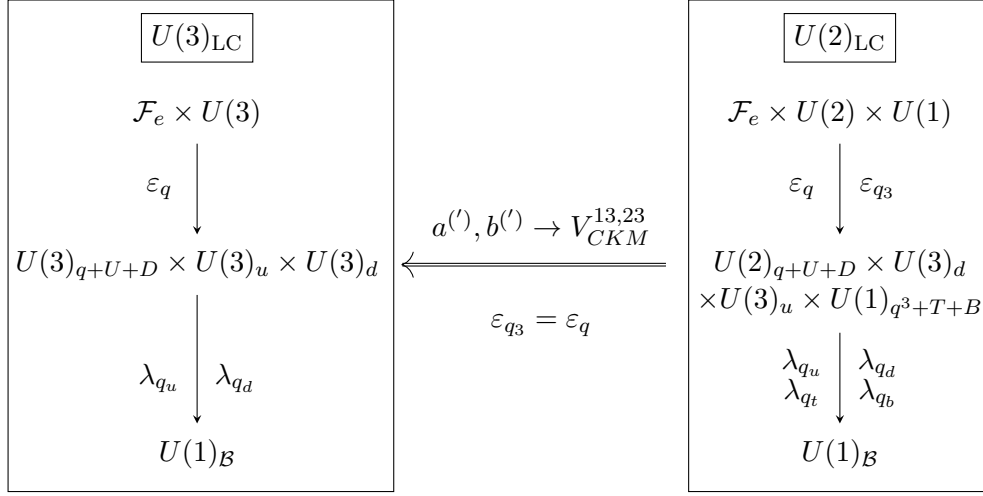


Figure 3.4 – Same as fig. 3.3 for the left-handed compositeness case. We are assuming only one mixing for the SM doublets. There is not an easy way to reproduce MFV by fixing the values of the four parameters  $a^{(')}, b^{(')}$ . In this limit they will be expressed as some functions of the CKM angles and phase.

following Lagrangian

$$\mathcal{L}_{\text{mix}}^{U(2)_{LC}} = g_* \varepsilon_q \bar{q}_L^i O_q^A \delta_{iA} + g_* \varepsilon_{q3} \bar{q}_L^3 O_{q3} + \lambda_u^{Ai} \bar{O}_u^A u_R^i + \lambda_t^i \bar{O}_t u_R^i + \lambda_d^{Ai} \bar{O}_d^A d_R^i + \lambda_b^i \bar{O}_b d_R^i + h.c., \quad (3.74)$$

where the index  $A = 1, 2$  is the index of  $U(2)_{U+D}$ . The SM Yukawas are then obtained as

$$Y_u \sim \left( \frac{\lambda_u \varepsilon_q}{\lambda_t \varepsilon_{q3}} \right), \quad Y_d \sim \left( \frac{\lambda_d \varepsilon_q}{\lambda_b \varepsilon_{q3}} \right), \quad (3.75)$$

where this time the  $2 \times 3$  and  $1 \times 3$  blocks are stacked on top of each other to form the two  $3 \times 3$  matrices. Similarly to before, we can use the flavor symmetries to reduce the  $\lambda$  mixings in the following form

$$U(2)_{LC} : \quad \begin{aligned} \lambda_u &= \frac{1}{\varepsilon_q} \begin{pmatrix} y_u & 0 & a y_c \\ 0 & y_c & b y_c \end{pmatrix}, & \lambda_t &= \frac{1}{\varepsilon_{q3}} \begin{pmatrix} 0 & 0 & y_t \end{pmatrix}, \\ \lambda_d &= \frac{1}{\varepsilon_q} \tilde{U}_d^{(2)} \begin{pmatrix} y_d & 0 & a' y_s \\ 0 & y_s & b' y_s \end{pmatrix}, & \lambda_b &= \frac{1}{\varepsilon_{q3}} \begin{pmatrix} 0 & 0 & y_b \end{pmatrix}, \end{aligned} \quad (3.76)$$

where  $a, b, a'$  and  $b'$  are complex numbers with arbitrary phases and  $\tilde{U}_d^{(2)}$  is a  $2 \times 2$  orthogonal matrix, since it is always possible to remove phases from  $\tilde{U}_d^{(2)}$  by rephasing the elementary quarks.

The matrices  $U_u, V_u, U_d$  and  $V_d$  that diagonalize the two Yukawas are reported in app. C.1

and the CKM matrix is readily obtained as

$$V_{\text{CKM}} = U_u^\dagger \tilde{U}_d U_d, \quad \tilde{U}_d \equiv \begin{pmatrix} \tilde{U}_d^{(2)} & 0 \\ 0 & 1 \end{pmatrix}. \quad (3.77)$$

An important difference with the previous model is that  $\tilde{U}_d$  is now determined in terms of a  $2 \times 2$  orthogonal matrix and thus contains only a single real parameter. This means that three combinations of  $a$ ,  $b$ ,  $a'$  and  $b'$  are determined as function of two remaining CKM angles and the CKM phases. Thus, among  $a$ ,  $b$ ,  $a'$  and  $b'$  there are only 3 phases and 2 real parameters. Given the form of  $U_u$  and  $U_d$ , we can see that for a generic  $2 \times 2$  rotation matrix of angle  $\theta$ ,  $V_{\text{CKM}}$  is roughly

$$V_{\text{CKM}} \sim \begin{pmatrix} \cos \theta & \sin \theta & a \frac{y_c}{y_t} + a' \frac{y_s}{y_b} \\ \sin \theta & \cos \theta & b \frac{y_c}{y_t} + b' \frac{y_s}{y_b} \\ a \frac{y_c}{y_t} + a' \frac{y_s}{y_b} & b \frac{y_c}{y_t} + b' \frac{y_s}{y_b} & 1 \end{pmatrix}. \quad (3.78)$$

For all  $O(1)$  coefficients, the  $(1, 3)$  and  $(3, 1)$  components are one order of magnitude larger than the SM measured value because of the ratio  $y_s/y_b \sim 0.02$ . Thus, to reproduce the CKM mixing angles we assume  $|a| \sim |b| \sim |b'| \sim 1$ ,  $\theta \sim \lambda$  and  $|a'| \sim 0.1$ .

From the previous discussion it emerges that there is not an easy way to recover minimal flavor violation just setting to zero some of the parameters. In general it is necessary to set  $\varepsilon_q = \varepsilon_{q3}$  and to fix  $a$ ,  $b$ ,  $a'$  and  $b'$  as functions of the various CKM entries. A cartoon summarizing the model can be found in fig. 3.4.

### Constraints

The spurion structure of this model is analogous to the one of  $U(2)_{\text{RC}}^2$ . Again this scenario is free from dipole moment at leading order in the mixings  $\lambda$ . The proof follows from the same argument presented for  $U(2) \times U(3)_{\text{RC}}$ . Interestingly this model also does not generate dipoles even at 1-loop. In fact, even at this order it is impossible to build a combination of spurions that contributes to the dipoles and involves both up- and down-type mixings. As we explained this is a necessary requirement to access one of the physical phases of our model.

A first constraint to this model comes from the compositeness bound of eq. (3.41) that gives

$$m_* \gtrsim 14.2 g_* \varepsilon_q^2 \text{ TeV}, \quad (3.79)$$

which can however be satisfied by taking a small value for  $\varepsilon_q$ . The model however faces several constraints from flavor-violating processes, in particular a strong bound comes from the  $b \rightarrow s\gamma$  transitions induced by operators as in eq. (3.69). This effect, in analogy

to  $U(2)_{\text{RC}}^2$ , gives

$$C_7|_{U(2)_{\text{LC}}^2} \sim \frac{m_s}{m_b} \frac{4\sqrt{2}\pi^2 b'}{G_F V_{\text{CKM}}^{tb} (V_{\text{CKM}}^{ts})^* m_*^2} \sim 2.4 \left( \frac{1 \text{ TeV}}{m_*} \right)^2, \quad (3.80)$$

while  $C_7'$  is suppressed by a further power of  $m_s/m_b$ . This translates into an absolute lower bound on  $m_*$  given by

$$m_* \gtrsim 8.8 \text{ TeV}. \quad (3.81)$$

Moreover, the (semi-)leptonic  $B_s$  decays (see sec. 3.4.2) are also enhanced in this model, giving

$$C_{10}|_{U(2)_{\text{LC}}} = \frac{\sqrt{2}}{G_F} \frac{4\pi^2}{e^2} \frac{g_*^2(\varepsilon_{q_3}^2 - \varepsilon_q^2)}{m_*^2} \sim 48.7 \frac{g_*^2 \varepsilon_{q_3}^2}{m_*^2}, \quad (3.82)$$

while the operator  $C_{10}'$  is generated with a negligible coefficient. Again the  $C_{10}$  coefficient can be suppressed in presence of  $P_{LR}$  protections. Imposing the experimental bound we find

$$m_* \gtrsim 14.2 g_* \varepsilon_{q_3} \text{ TeV}, \quad (\text{w/o } P_{LR}) \quad m_* \gtrsim 10.6 \varepsilon_{q_3} \text{ TeV} (\text{w/ } P_{LR}), \quad (3.83)$$

pushing toward the small  $\varepsilon_{q_3}$  direction.

From the previous discussion and from the various bounds reported in sec. 3.4 we find that the strongest constraint is given by eq. (3.81). In fact for each value of  $m_*$  above 8.8 TeV we can always find a compatible values for  $\varepsilon_{q_3}$ . Concretely, the strongest constraint on  $\varepsilon_{q_3}$  comes from the right-handed top coupling in table 3.1. Taking  $\varepsilon_{q_3} \sim y_t/g_*$  this reads  $m_* \gtrsim 0.5 g_*/y_t \text{ TeV} \sim 7.3 g_*/(4\pi) \text{ TeV}$ , which is milder than eq. (3.81).

To conclude, in this section we have found that both  $U(3)_{\text{LC}}$  and  $U(2)_{\text{LC}}$  are not allowed to have  $m_*$  in the few TeV range. While MFV is severely constrained by the CKM unitarity, the less symmetric  $U(2)_{\text{LC}}$  model suffers from large corrections to flavor-violating dipole operators.

### 3.3.3 Other possibilities

In the previous sections we just considered a minimalist set of scenarios of partial compositeness and we need to comment on few more possibilities.

First of all, we remark that our logic was to start from the MFV hypothesis and then lower down the symmetries of the strong sector. We have seen in sec. 3.2.1 that 5 realization of MFV, (summarized in eqs. (3.20, 3.21, 3.22, 3.23, 3.24)), are possible and we considered explicetely how to improve the ones of eq. (3.20) and eq. (3.22), respectively in sec. 3.2.1 and sec. 3.2.1. Nevertheless also the other scenarios might be improved by the right choice of  $\mathcal{F}_c$  and they deserve further investigations. For instance, given that

the strongest bounds are related to the up sector, we expect that the model in eq. (3.24) can be improved following the same pattern we specified for eq. (3.20) resulting in similar constraints.

A more careful discussion it is needed for the models in eqs. (3.23,3.21). In both of them the strongest constraints are related to the unitarity of the CKM put under stress by a large and equal compositeness of all the light families  $\varepsilon_{qu} \gtrsim y_t/g_*$ . This can be relaxed downgrading  $U(3)_U \rightarrow U(2)_U \times U(1)_T$  and the considering smaller  $\varepsilon_{qu}$  to avoid large LEP constrains. At the same time both of these scenarios, differently with  $U(2)_{LC}$  discussed before, are expected not to produce dangerous effects in the down sector, being completely aligned with the SM Yukawas. Yet, we still have to quantify the values of the different  $\varepsilon$  that makes this model compatibles with the various bound.

Moreover, we have to remark that in partial compositeness there can be different realization from the ones we have studied only relying in a small set of hypotheses. For instance one can start from the single mixing Lagrangian in eq. (3.3) and assume an  $U(3)$  symmetry in the strong sector and  $\lambda_q \propto \lambda_d$  [247].

Another possibility has been considered in [233, 248] and relies on an approximated  $U(2)^2$  symmetry. We still need a detailed analysis of this scenarios and a quantitative comparison with the models we presented. We just mention that the minimal model considered in [248] has a structure very similar to our  $U(2)_{RC}^2$  model but on the contrary needs stronger assumptions, namely the absence of some spurions that might cause additional effects. Moreover the  $U(2)^3$  flavor symmetry cannot be justified according to our set of hypothesis where the maximal amount of symmetry of the strong sector is  $U(3)^2$  and, up to the mixings, the SM quarks always respect  $U(3)^3$ .

## 3.4 Experimental constraints

In this section we summarize and extend the analysis performed so far on the various bounds for the different models under consideration. We remark that this section partially overlap with the previous discussion, moreover it aims to collect all the relevant constraints and can be skipped.

In order to make the discussion more systematic we define the tree-level flavor structures  $[S]^{ij}$  as the coefficient that involves the smallest number of mixing  $\lambda$  and  $\varepsilon$  for a given flavor-dependent operators. In the rest of the section we often refer to these tree-level flavor structures, whose explicit expression can be found in App. C.1.

### 3.4.1 Universal constraints

The first class of effects we consider are the universal ones [34], where all the new interactions among the SM fields can be described through higher dimensional operators

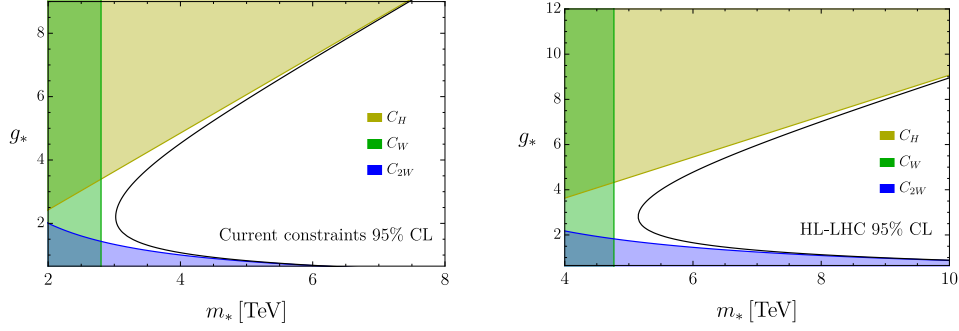


Figure 3.5 – Current and future universal constraints on CH-models at 95% CL. See the main text for details.

involving only SM bosons.

In composite Higgs models we can parameterize the leading effects according to the following Lagrangian [10]

$$\begin{aligned} \mathcal{L}_{SILH} = & \frac{c_H}{2} \left( \partial_\mu (H^\dagger H) \right)^2 + \frac{c_T}{2} \left( H^\dagger \overleftrightarrow{D}_\mu H \right) \left( H^\dagger \overleftrightarrow{D}^\mu H \right) + ig \frac{c_W}{2} \left( H^\dagger \overleftrightarrow{D}_\mu^a H \right) D_\nu W^{a\mu\nu} \\ & + ig \frac{c_B}{2} \left( H^\dagger \overleftrightarrow{D}_\mu H \right) \partial_\nu B^{\mu\nu} - g^2 \frac{c_{2W}}{2} (D^\mu W_{\mu\nu}^a) (D_\rho W^{a\rho\nu}) - g'^2 \frac{c_{2B}}{2} (\partial^\mu B_{\mu\nu}) (\partial_\rho B^{\rho\nu}), \end{aligned} \quad (3.84)$$

where the size of the Wilson coefficient, as function on the new physics parameters, can be estimated according to the so-called “SILH” power-counting. In particular, apart from  $c_T$ , we expect the other Wilson coefficients in eq. (3.84) to be general for composite Higgs models, i.e. to not depend on the detailed flavor structure, and to scale as

$$c_H \sim \frac{g_*^2}{m_*^2}, \quad c_W \sim c_B \sim \frac{1}{m_*^2}, \quad c_{2W} \sim c_{2B} \sim \frac{1}{m_*^2 g_*^2}, \quad (3.85)$$

as functions of  $g_*$  and  $m_*$ .

The operator  $c_W$  and  $c_B$  can be related to the  $S$  parameter [35] which has been constrained by EWPT (see for instance [249]). The operator  $c_{2W}$  and  $c_{2B}$  are very well measured at (HL)-LHC.  $W$  is expected to be stronger than  $Y$  and we can already read the bound on  $W$  from recent run-2 results [42]. We extract the value for  $c_H$  from [250]. We report the results for the current constraints in the left panel of fig. 3.5. In the right panel we report the projections for HL-LHC. The bounds are obtained from [205, 206] and we updated the  $W$  constraint according to the projections of [2].<sup>7</sup>

The size of  $c_T$ , on the contrary, is less generic and strongly depends on the specific assumptions on the strong dynamics. Moreover the  $c_T$  coefficient, usually related to the

<sup>7</sup>Notice that the estimate in [2] assumes conservative hypothesis for the systematic uncertainties, given the recent measurements at  $100 \text{ fb}^{-1}$  in [42].

$\hat{T}$  oblique parameter, is protected by the custodial symmetry that we assume in all our discussion. The main sources of custodial breaking, which generate a non-zero  $\hat{T}$ , are the exchanges of composite fermions, in the case the latter are not singlet under  $SU(2)_R$ .<sup>8</sup> These contributions have been computed in [233] for a defined fermion content. In the various scenarios we consider we don't find them competitive with the other constraints.

### 3.4.2 Anomalous couplings to SM gauge bosons

The first class of non universal effects we consider are the corrections to SM vector bosons couplings. We focus on the following set of operators

$$\begin{aligned} [\mathcal{O}_{Hq}^{(1)}]^{ij} &= (H^\dagger i \overleftrightarrow{D}_\mu H) \bar{q}_L^i \gamma^\mu q_L^j, & [\mathcal{O}_{Hq}^{(3)}]^{ij} &= (H^\dagger i \overleftrightarrow{D}_\mu \tau^a H) \bar{q}_L^i \gamma^\mu \tau^a q_L^j, \\ [\mathcal{O}_{Hu}]^{ij} &= (H^\dagger i \overleftrightarrow{D}_\mu H) \bar{u}_R^i \gamma^\mu u_R^j, & [\mathcal{O}_{Hd}]^{ij} &= (H^\dagger i \overleftrightarrow{D}_\mu H) \bar{d}_R^i \gamma^\mu d_R^j, \end{aligned} \quad (3.86)$$

where  $\tau^a \equiv \sigma^a/2$  with  $\sigma^a$  the three Pauli matrices and the quarks have free flavor indices. The previous operators can be further classified in two categories: the flavor diagonal corrections to  $Z$  and  $W$  bosons couplings and the  $\Delta F = 1$  flavor transitions, that we discuss respectively in sec. 3.4.2 and sec. 3.4.2.

$$\Delta F = 0$$

We already discussed in eqs. (3.42) and below the corrections to the  $W$  couplings, particularly important in the case of left-handed compositeness. Other important bounds come from bottom and top couplings to the  $Z$ . The former is very well constrained by LEP measurements, resulting in the following 95% bounds [251]

$$|[C_{Hq^3}^{(1)} + C_{Hq^3}^{(3)}]^{33}| \lesssim 5.5^{-2} \text{ TeV}^{-2}, \quad |[C_{Hd}]^{33}| \lesssim 1.1^{-2} \text{ TeV}^{-2}. \quad (3.87)$$

The top coupling instead is less precisely constrained by LHC measurements and we estimate it from the individual operators reach on  $O_{Hq^3}^{(3)}$ ,  $O_{Hq^3}^{(1)}$  and  $O_{Ht}$

$$|[C_{Hq}^{(3)}]^{33}| \lesssim 0.8^{-2} \text{ TeV}^{-2}, \quad |[C_{Hq}^{(1)}]^{33}| \lesssim 1.1^{-2} \text{ TeV}^{-2}, \quad |[C_{Hu}]^{33}| \lesssim 0.6^{-2} \text{ TeV}^{-2}, \quad (3.88)$$

extracted at 95% CL from [252]. In the previous equation while we are taking the single operator reach for  $[O_{Hu}]^{33}$ , we are considering the marginalized ones for  $O_{Hq^3}^{(3)}$ ,  $O_{Hq^3}^{(1)}$  since in the two dimensional plane of their Wilson coefficients the direction corresponding to the b couplings is the only very well tested (eq. (3.87)).

We report in table 3.1 the resulting power-counting and bounds on the Composite Higgs parameters space for the various scenarios under consideration. We can notice that the strongest bounds, for all the models, are given by the coupling the left bottom

<sup>8</sup>This contribution usually exceed the so-called IR effects [226].

$\mathcal{F}_c$	$[C_{Hq}^{(1)} + C_{Hq}^{(3)}]^{33}$		$[C_{Hd}]^{33}$		$[C_{Hu}]^{33}$	
	P.C.	Bound	P.C.	Bound	P.C.	Bound
$U(3)_{RC}^2$	$\frac{y_t^2}{m_*^2 \varepsilon_u^2} \left( + \frac{y_b^2}{m_*^2 \varepsilon_d^2} \right)$	$\frac{4.8}{\varepsilon_u} \left( \frac{0.08}{\varepsilon_d} \right)$	$\frac{\varepsilon_d^2 g_*^2}{m_*^2}$	$1.1 g_* \varepsilon_d$	$\frac{\varepsilon_u^2 g_*^2}{m_*^2}$	$0.6 g_* \varepsilon_u$
$U(3) \times U(2)_{RC}$	$\frac{y_t^2}{m_*^2 \varepsilon_t^2} \left( + \frac{y_b^2}{m_*^2 \varepsilon_d^2} \right)$	$\frac{4.8}{\varepsilon_t} \left( \frac{0.08}{\varepsilon_d} \right)$	$\frac{\varepsilon_d^2 g_*^2}{m_*^2}$	$1.1 g_* \varepsilon_d$	$\frac{\varepsilon_t^2 g_*^2}{m_*^2}$	$0.6 g_* \varepsilon_t$
$U(2)_{RC}^2$	$\frac{y_t^2}{m_*^2 \varepsilon_t^2} \left( + \frac{y_b^2}{m_*^2 \varepsilon_b^2} \right)$	$\frac{4.8}{\varepsilon_t} \left( \frac{0.08}{\varepsilon_b} \right)$	$\frac{\varepsilon_b^2 g_*^2}{m_*^2}$	$1.1 g_* \varepsilon_b$	$\frac{\varepsilon_t^2 g_*^2}{m_*^2}$	$0.6 g_* \varepsilon_t$
$U(3)_{LC}$	$\frac{\varepsilon_q^2 g_*^2}{m_*^2}$	$5.5 g_* \varepsilon_q$	$\frac{y_b^2}{\varepsilon_q^2 m_*^2}$	—	$\frac{y_t^2}{\varepsilon_q^2 m_*^2}$	$\frac{0.5}{\varepsilon_q}$
$U(2)_{LC}$	$\frac{\varepsilon_{q3}^2 g_*^2}{m_*^2}$	$5.5 g_* \varepsilon_{q3}$	$\frac{y_b^2}{\varepsilon_{q3}^2 m_*^2}$	—	$\frac{y_t^2}{\varepsilon_{q3}^2 m_*^2}$	$\frac{0.5}{\varepsilon_{q3}}$

Table 3.1 – Constraints from anomalous Z/W coupling for the different scenarios under consideration. For each operator and scenario we report the Naive Power Counting (PC), assuming the operator is produced at TL, and the lower bound on  $m_*$  expressed in TeV.

to the  $Z$ . These effects are partially screened in models featuring  $P_{LR}$  protection.<sup>9</sup> As an example if in our model the up doublets partners transform in the  $(\mathbf{2}, \mathbf{2})_{2/3}$  of  $SU(2)_L \times SU(2)_R \times U(1)_X$  (see [208] for details), then the sum  $C_{Hq^3}^{(3)} + C_{Hq^3}^{(1)}$  is not generated at leading order from the exchanges of  $O_{qu}$ . Notice that, in this case, additional contributions come from the exchanges of the down doublets partners  $O_{qd}$ . These effects are proportional to  $y_b^2$  and are typically small, they are reported in parenthesis in table 3.1. The leading contribution to  $Zb_L b_L$  coupling is then generated through operators of the form

$$[\mathcal{O}_{qD}^{(1)}]^{ij} = \bar{q}_L^i \gamma^\nu q_L^j D^\nu B_{\mu\nu}, \quad [\mathcal{O}_{qD}^{(3)}]^{ij} = \bar{q}_L^i \tau^a \gamma^\nu q_L^j D^\nu W_{\mu\nu}^a, \quad (3.89)$$

giving rise to an anomalous Z coupling suppressed of  $g_{SM}^2/g_*^2$  with respect to the  $\mathcal{O}_{qH}^{(3/1)}$  contributions. We stress that in most of the models  $P_{LR}$  protection is mandatory to avoid large effects from  $\Delta F = 1$   $b$ -to- $s$  transitions. Moreover in presence of these  $P_{LR}$  protection the bounds get weaker, we report them in tab. 3.2.

We also need to remark that in this section we are considering anomalous coupling only to the third family even if Z coupling to light families have comparable experimental bounds [251]. However we find that in LC models the strongest constraints arise from  $V_{CKM}$  unitarity and are slightly stronger than anomalous Z coupling effects. In RC models, moreover, the compositeness of the light families is better constrained by compositeness test at the LHC [238]. Finally, in  $U(3)_{LC}$  and  $U(2)_{LC}$  with only one partner for each SM doublet anomalous right-handed  $DF = 1$  effects are mediated by the operator

$$[O_{Hq}]^{ij} = (H_c^\dagger i D_\mu H) \bar{u}_R^i \gamma^\mu d_R^j. \quad (3.90)$$

<sup>9</sup>Notice that in some minimal models  $P_{LR}$  arises as an accidental symmetry in the lowest order derivative expansion [253].



### 3.4. Experimental constraints

$\mathcal{F}_c$	$[C_{Hq}^{(3)}]^{33}$	$[C_{qD}^{(1)} + C_{qD}^{(3)}]^{33}$	$[C_{Hd}]^{33}$	$[C_{Hu}]^{33}$
$U(3)_{RC}^2$	$\frac{0.7}{\varepsilon_u}$	$\frac{3.5}{g_* \varepsilon_u}$	$1.1 g_* \varepsilon_d$	$0.6 g_* \varepsilon_u$
$U(3) \times U(2)_{RC}$	$\frac{0.7}{\varepsilon_t}$	$\frac{3.5}{g_* \varepsilon_t}$	$1.1 g_* \varepsilon_d$	$0.6 g_* \varepsilon_t$
$U(2)_{RC}^2$	$\frac{0.7}{\varepsilon_t}$	$\frac{3.5}{g_* \varepsilon_t}$	$1.1 g_* \varepsilon_d$	$0.6 g_* \varepsilon_b$
$U(3)_{LC}$	$0.8 g_* \varepsilon_q$	$4.1 \varepsilon_q$	—	$\frac{0.5}{\varepsilon_q}$
$U(2)_{LC}$	$0.8 g_* \varepsilon_{q3}$	$4.1 \varepsilon_{q3}$	—	$\frac{0.5}{\varepsilon_{q3}}$

Table 3.2 – Lower bound on  $m_*$  in TeV from anomalous Z/W coupling for the different scenarios under consideration. We assume custodial protection for the  $Zb_L b_L$  coupling.

Furthermore, the only relevant effect is expected from the third family, generating a Wilson Coefficient scaling as

$$[C_{Hq}]^{33} \sim \frac{y_b y_t}{\varepsilon_q^2} \frac{1}{m_*^2}, \quad (3.91)$$

in case of MFV or  $U(2)_{LC}$  through the replacement  $\varepsilon_q \rightarrow \varepsilon_{q3}$ . Given the present experimental constraints [252],  $|[C_{Hq}]^{33}| \lesssim 3.6 \text{ TeV}^{-2}$  at 95% CL, this effect is clearly negligible.

$$\Delta F = 1$$

#### Rare B-decays

We turn to rare (semi-)leptonic  $B$  decays. As already explained in the main text, we focus on the following effective interaction Hamiltonian

$$\begin{aligned} \mathcal{H}_{\text{eff}} = & -\frac{4G_F}{\sqrt{2}} V_{\text{CKM}}^{tb} (V_{\text{CKM}}^{ts})^* \frac{e^2}{16\pi^2} \left[ C_{10} (\bar{s}_L \gamma^\mu b_L) (\bar{\ell} \gamma_\mu \gamma^5 \ell) + C'_{10} (\bar{s}_R \gamma^\mu b_R) (\bar{\ell} \gamma_\mu \gamma^5 \ell) \right. \\ & \left. + C_9 (\bar{s}_L \gamma^\mu b_L) (\bar{\ell} \gamma_\mu \ell) + C'_9 (\bar{s}_R \gamma^\mu b_R) (\bar{\ell} \gamma_\mu \ell) \right]. \end{aligned} \quad (3.92)$$

In all our models  $C_{9/10}^{(\prime)}$  are generated through the anomalous  $Z$  coupling operator of eq. (3.28) and  $C_9^{(1)}$  is suppressed with respect to  $C_{10}^{(\prime)}$ .

We can express  $C_{10}$  and  $C'_{10}$  through the tree-level flavor structure reported in App. C.1

$$C_{10} \simeq \frac{\sqrt{2}}{G_F} \frac{4\pi^2}{e^2} \left[ \frac{g_*}{m_*^2} S^{d_L d_L} \right]^{sb}, \quad C'_{10} \simeq \frac{\sqrt{2}}{G_F} \frac{4\pi^2}{e^2} \left[ \frac{g_*}{m_*^2} S^{d_R d_R} \right]^{sb}, \quad (3.93)$$

where we remind that the letter on the side of the brackets denote the quark type in the mass basis. Again, in the presence of  $P_{LR}$  protections, the  $C_{10}$  coefficient in eq. (3.93) is suppressed by  $(g_{SM}^{(Z)}/g_*)^2$ . Notice that in App. C.1 we report the factors  $S$  only for  $U(3)_{RC}^2$ ,  $U(2) \times U(3)_{RC}$  and  $U(2)_{LC}$ . The case of  $U(3)_{RC}^2$  can be obtained simply by the

$\mathcal{F}_c$	$C_{10}$	$C_{10} \text{ (w/ } P_{LR})$	$C'_{10}$
$U(3)_{RC}^2$	$\frac{12.3}{\varepsilon_u}$	$\frac{9.2}{g_* \varepsilon_u}$	$\times$
$U(3) \times U(2)_{RC}$	$\frac{12.3}{\varepsilon_t}$	$\frac{9.2}{g_* \varepsilon_t}$	$\times$
$U(2)_{RC}^2$	$\frac{12.3}{\varepsilon_t}$	$\frac{9.2}{g_* \varepsilon_t}$	$10.9 g_* \varepsilon_b$
$U(3)_{LC}$	$\times$	$\times$	$\times$
$U(2)_{LC}$	$14.2 g_* \varepsilon_{q3}$	$10.6 \varepsilon_{q3}$	—

Table 3.3 – Constraints from the leptonic and semi-leptonic  $B$  decays. For each operator and scenario we report the lower bound on  $m_*$  expressed in TeV. With — and  $\times$  we indicate respectively that the bound is negligible or the operator is not generated at leading order.

replacements of figs. 3.3 and  $U(3)_{LC}$  do not generate neither  $C_{10}^{(\prime)}$  nor  $C_9^{(\prime)}$ .

The scaling of the  $C_{10}^{(\prime)}$  Wilson coefficients are summarized in the following equations

$$\begin{aligned}
 U(3)_{RC}^2 : \quad C_{10} &= \frac{\sqrt{2}}{G_F} \frac{4\pi^2}{e^2} \frac{y_t^2}{m_*^2 \varepsilon_u^2}, & C'_{10} &= \times, \\
 U(2) \times U(3)_{RC} : \quad C_{10} &= \frac{\sqrt{2}}{G_F} \frac{4\pi^2}{e^2} \frac{y_t^2}{m_*^2 \varepsilon_t^2}, & C'_{10} &= \times, \\
 U(2)_{RC}^2 : \quad C_{10} &= \frac{\sqrt{2}}{G_F} \frac{4\pi^2}{e^2} \frac{y_t^2}{m_*^2 \varepsilon_t^2}, & C'_{10} &= \frac{\sqrt{2}}{G_F} \frac{4\pi^2}{e^2} \frac{1}{V_{CKM}^{tb}(V_{CKM}^{ts})^*} \frac{y_s g_*^2 (\varepsilon_b^2 - \varepsilon_d^2)}{y_b m_*^2} \\
 U(3)_{LC} : \quad C_{10} &= \times, & C'_{10} &= \times, \\
 U(2)_{LC} : \quad C_{10} &= \frac{\sqrt{2}}{G_F} \frac{4\pi^2}{e^2} \frac{g_*^2 (\varepsilon_{q3}^2 - \varepsilon_q^2)}{m_*^2}, & C'_{10} &= \frac{\sqrt{2}}{G_F} \frac{4\pi^2}{e^2} \frac{1}{V_{CKM}^{tb}(V_{CKM}^{ts})^*} \frac{y_s^2}{m_*^2 \varepsilon_{q3}^2},
 \end{aligned} \tag{3.94}$$

where the  $\times$  means that no tree-level effects are present. Imposing the following constraints [242] on the Wilson Coefficient

$$|C_{10}| \lesssim 0.24, \quad |C'_{10}| \lesssim 0.2, \tag{3.95}$$

we find the bounds on  $m_*$  in table 3.3.

### 3.4.3 Dipole operators

All the model considered in this chapter generate negligible EDMs, as discussed in the main text. Here we summarize the effects related to the so-called EW dipoles, i.e. interactions described according to the effective operators of the form

$$\bar{f}_{L(R)}^i \sigma_{\mu\nu} f_{R(L)}^j F_{SM}^{\mu\nu}, \tag{3.96}$$

with  $F_{SM}^{\mu\nu}$  the field strength of the SM gauge bosons and  $i, j$  the flavor indexes of the fermions.

### The $B$ system

The effective Hamiltonian relevant for  $b \rightarrow s \gamma$  transition is

$$\mathcal{H}_{\text{eff}} = -\frac{4G_F}{\sqrt{2}} V_{\text{CKM}}^{tb} (V_{\text{CKM}}^{ts})^* \frac{m_b e}{16\pi^2} F^{\mu\nu} (C_7 \bar{s}_L \sigma_{\mu\nu} b_R + C'_7 \bar{s}_R \sigma_{\mu\nu} b_L) . \quad (3.97)$$

and the Wilson coefficient can be estimated as

$$C_7 = \frac{4\sqrt{2}\pi^2}{G_F V_{\text{CKM}}^{tb} (V_{\text{CKM}}^{ts})^*} \frac{v}{\sqrt{2}m_b} \left[ \frac{S^{u_L d_R}}{m_*^2} \right]^{sb}, \quad C'_7 = \frac{4\sqrt{2}\pi^2}{G_F V_{\text{CKM}}^{tb} (V_{\text{CKM}}^{ts})^*} \frac{v}{\sqrt{2}m_b} \left[ \frac{S^{u_R d_L}}{m_*^2} \right]^{sb} . \quad (3.98)$$

From the explicit expression of App. C.1 we find

$$\begin{aligned} U(3)_{\text{RC}}^2 : & \quad C_7 = \times, & \quad C'_7 = \times, \\ U(2) \times U(3)_{\text{RC}} : & \quad C_7 = \times, & \quad C'_7 = \times, \\ U(2)_{\text{RC}}^2 : & \quad C_7 = \left( \frac{m_s}{m_b} \right)^2 \frac{4\sqrt{2}\pi^2}{G_F V_{\text{CKM}}^{tb} (V_{\text{CKM}}^{ts})^* m_*^2}, & \quad C'_7 = \frac{m_s}{m_b} \frac{4\sqrt{2}\pi^2}{G_F V_{\text{CKM}}^{tb} (V_{\text{CKM}}^{ts})^* m_*^2}, \\ U(3)_{\text{LC}} : & \quad C_7 = \times, & \quad C'_7 = \times, \\ U(2)_{\text{LC}} : & \quad C_7 = \left( \frac{m_s}{m_b} \right)^2 \frac{4\sqrt{2}\pi^2}{G_F V_{\text{CKM}}^{tb} (V_{\text{CKM}}^{ts})^* m_*^2}, & \quad C'_7 = \left( \frac{m_s}{m_b} \right)^2 \frac{4\sqrt{2}\pi^2}{G_F V_{\text{CKM}}^{tb} (V_{\text{CKM}}^{ts})^* m_*^2}. \end{aligned} \quad (3.99)$$

Imposing the constraints from [246]

$$\text{Re} C_7 < 0.03, \quad |C'_7| < 0.07 \quad (3.100)$$

we get the following bounds

$$U(2)_{\text{RC}}^2 : \quad m_* > 5.8 \text{ TeV} \quad U(2)_{\text{LC}} : \quad m_* > 8.8 \text{ TeV} . \quad (3.101)$$

### The $D$ system

Regarding the  $D$  mesons, the main  $\Delta F = 1$  constraints come from the direct CP violation in the hadronic decays, usually encapsulated in the observable

$$\Delta a_{\text{CP}} \equiv a_{K^+ K^-} - a_{\pi^+ \pi^-} . \quad (3.102)$$

The latest measured value is [254]

$$\Delta a_{\text{CP}} = (-15.4 \pm 2.9) \times 10^{-4}, \quad (3.103)$$

roughly compatible with the expected SM prediction. In our models, such transitions could arise at tree-level from flavor-changing dipole operators

$$\mathcal{H}_{\text{eff}} = \frac{G_F}{\sqrt{2}} \frac{m_c}{4\pi^2} (C_8 \bar{u}_L \sigma^{\mu\nu} g_s G_{\mu\nu} c_R + C'_8 \bar{c}_L \sigma^{\mu\nu} g_s G_{\mu\nu} u_R) . \quad (3.104)$$

These operators are generated at tree-level by the three models in sec. 3.3, while for MFV models they are zero. We estimate for all three models

$$\begin{aligned} & U(2) \times U(3)_{\text{RC}} \\ & U(2)_{\text{RC}}^2 : \quad \text{Im } C_8 \sim \frac{4\pi^2}{m_*^2} \frac{2}{G_F} \frac{y_c^2}{y_t^2} \sim 1.5 \times 10^{-4} \left( \frac{1 \text{ TeV}}{m_*} \right)^2 , \quad (3.105) \\ & U(2)_{\text{LC}} \end{aligned}$$

while  $C'_8$  is further suppressed by  $y_u/y_c$ . The imaginary part of  $C_8$  enters at  $O(1)$  in  $\Delta a_{\text{CP}}$  as shown in [255]. However we see that for  $m_* \gtrsim \text{TeV}$  this contribution is well below the experimental accuracy, leading to no relevant bounds on the models.

### 3.4.4 Four-fermions operators

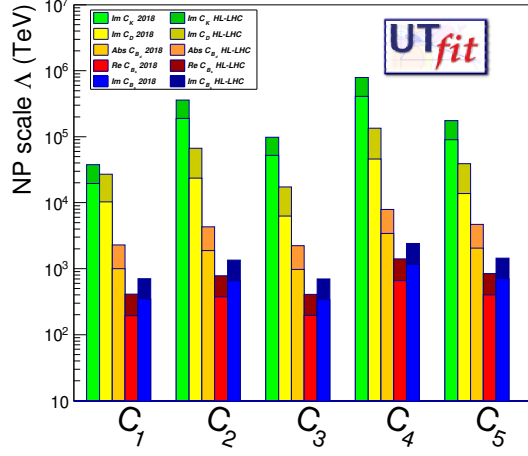
An important set of constraints comes from the  $\Delta F = 2$  transitions. Adopting the convention of [209], the short-distance contact operators mediating the  $\Delta F = 2$  flavor transitions can be reduced to

$$\begin{aligned} \mathcal{O}_1^{ij} &= (\bar{f}_{iL}^\alpha \gamma^\mu f_{jL}^\alpha) (\bar{f}_{iL}^\beta \gamma_\mu f_{jL}^\beta), & \tilde{\mathcal{O}}_1^{ij} &= (\bar{f}_{iR}^\alpha \gamma^\mu f_{jR}^\alpha) (\bar{f}_{iR}^\beta \gamma_\mu f_{jR}^\beta), \\ \mathcal{O}_2^{ij} &= (\bar{f}_{iR}^\alpha f_{jL}^\alpha) (\bar{f}_{iR}^\beta f_{jL}^\beta), & \tilde{\mathcal{O}}_2^{ij} &= (\bar{f}_{iL}^\alpha f_{jR}^\alpha) (\bar{f}_{iL}^\beta f_{jR}^\beta), \\ \mathcal{O}_3^{ij} &= (\bar{f}_{iR}^\alpha f_{jL}^\beta) (\bar{f}_{iR}^\beta f_{jL}^\alpha), & \tilde{\mathcal{O}}_3^{ij} &= (\bar{f}_{iL}^\alpha f_{jR}^\beta) (\bar{f}_{iL}^\beta f_{jR}^\alpha), \\ \mathcal{O}_4^{ij} &= (\bar{f}_{iR}^\alpha f_{jL}^\alpha) (\bar{f}_{iL}^\beta f_{jR}^\beta), & \mathcal{O}_5^{ij} &= (\bar{f}_{iR}^\alpha f_{jL}^\beta) (\bar{f}_{iL}^\beta f_{jR}^\alpha), \end{aligned} \quad (3.106)$$

where  $i$  and  $j$  denote the flavor indices while  $\alpha$  and  $\beta$  denote the color indices. In the following we will neglect the  $\mathcal{Q}_3$ ,  $\tilde{\mathcal{Q}}_3$  and  $\mathcal{Q}_5$  operators, since they have the same power counting in terms of the new physics parameters, but a weaker experimental bound. The bounds we use can be seen in fig. 3.6 and are taken from [215].

### The Kaon system

The strongest bounds for the Kaon system come from the  $K^0 - \bar{K}^0$  mixings and in particular from the observables  $\Delta m_K$  and  $\epsilon_K$ . In terms of the operators defined in


 Figure 3.6 – 95% constraints on  $\Delta F = 2$  operators, from [215]

(3.106), the current and projected for HL-LHC bounds (in parenthesis) are

$$\begin{aligned} |\text{Im } C_1^{sd}| &\sim |\text{Im } \tilde{C}_1^{sd}| \lesssim 2.5 \times 10^{-9} (6.3 \times 10^{-10}) \text{ TeV}^{-2}, \\ |\text{Im } C_2^{sd}| &\sim |\text{Im } \tilde{C}_2^{sd}| \lesssim 2.5 \times 10^{-11} (6.3 \times 10^{-12}) \text{ TeV}^{-2}, \\ |\text{Im } \tilde{C}_4^{sd}| &\lesssim 6.3 \times 10^{-12} (1.6 \times 10^{-12}) \text{ TeV}^{-2}. \end{aligned} \quad (3.107)$$

Using the flavor structures of App. C.1 we find for the various models

$$\begin{aligned} U(3)_{\text{RC}}^2 : \quad & \text{Im } C_1^{sd} = 2 \frac{A^4 y_t^4 \eta \lambda^{10}}{m_*^2 g_*^2 \varepsilon_t^4}, & \text{Im } \tilde{C}_1^{sd} = \times, \\ U(2) \times U(3)_{\text{RC}} : \quad & \text{Im } C_1^{sd} = 2 \frac{A^4 y_t^4 \eta \lambda^{10}}{m_*^2 g_*^2 \varepsilon_t^4}, & \text{Im } \tilde{C}_1^{sd} = \times, \\ U(2)_{\text{RC}}^2 : \quad & \text{Im } C_1^{sd} = 2 \frac{A^4 y_t^4 \eta \lambda^{10}}{m_*^2 g_*^2 \varepsilon_t^4}, & \text{Im } \tilde{C}_1^{sd} = \frac{y_s^4 g_s^2 \varepsilon_b^4}{y_b^4 m_*^2}, \\ U(3)_{\text{LC}} : \quad & \text{Im } C_1^{sd} = \times, & \text{Im } \tilde{C}_1^{sd} = \times, \\ U(2)_{\text{LC}} : \quad & \text{Im } C_1^{sd} = 2 A^4 \eta \lambda^{10} \frac{g_*^2 \varepsilon_{q3}^4}{m_*^2}, & \text{Im } \tilde{C}_1^{sd} = (a')^2 \frac{y_d^2 y_s^6}{y_b^4 g_*^2 \varepsilon_q^4}. \end{aligned} \quad (3.108)$$

The  $U(2) \times U(3)_{\text{RC}}$  and  $U(2)_{\text{RC}}^2$  models also generate a contribution to  $C_1$  that is enhanced for small values of  $\varepsilon_u$ . We estimate this contribution to be

$$\begin{aligned} U(2) \times U(3)_{\text{RC}} : \\ U(2)_{\text{RC}}^2 : \quad & \text{Im } C_1^{sd} = 2 \frac{A^4 y_c^2 y_t^2 \eta \lambda^6}{m_*^2 g_*^2 \varepsilon_u^2} \end{aligned} \quad (3.109)$$

The  $U(2)_{\text{RC}}^2$  and  $U(2)_{\text{LC}}$  models also generate the three mixed chirality operators  $\mathcal{O}_2$ ,  $\tilde{\mathcal{O}}_2$  and  $\mathcal{O}_4$ , but with negligible coefficients compared to the experimental bound. The bound on  $m_*$  coming from all these operators is reported in Tab. 3.4.

$\mathcal{F}_c$	$C_1^{sd}$	$\tilde{C}_1^{sd}$	$C_2^{sd}$	$\tilde{C}_2^{sd}$	$C_4^{sd}$
$U(3)_{RC}^2$	$\frac{4.3(8.6)}{g_*\varepsilon_u^2}$	$\times$	$\times$	$\times$	$\times$
$U(3) \times U(2)_{RC}$	$\frac{4.3(8.6)}{g_*\varepsilon_t^2} \left[ \frac{0.4(0.8)}{g_*\varepsilon_t\varepsilon_u} \right]$	$\times$	$\times$	$\times$	$\times$
$U(2)_{RC}^2$	$\frac{4.3(8.6)}{g_*\varepsilon_t^2} \left[ \frac{0.4(0.8)}{g_*\varepsilon_t\varepsilon_u} \right]$	$7.5(15)g_*\varepsilon_b^2$	—	—	—
$U(3)_{LC}$	$\times$	$\times$	$\times$	$\times$	$\times$
$U(2)_{LC}$	$5.7(11.4)g_*\varepsilon_{q3}^2$	—	—	—	—

Table 3.4 – Constraints from the Kaon system  $\Delta F = 2$  transitions. For each operator and scenario we report the lower bound on  $m_*$  expressed in TeV. In parenthesis the projected bounds for HL-LHC. In square brackets an additional contribution that become large for small values of  $\varepsilon_u$ . With — and  $\times$  we indicate respectively that the bound is negligible or the operator is not generated at leading order.

### The $B_d$ and $B_s$ system

Another important set of constraints from  $\Delta F = 2$  transitions, come from the flavor violating processes involving the neutral  $B_d$  and  $B_s$  mesons. For these operators the current experimental bounds [215] are

$$\begin{aligned}
 |\text{Abs } Q_1^{bd}| \sim |\text{Abs } \tilde{Q}_1^{bd}| &\lesssim 1 \times 10^{-6} (2.5 \times 10^{-7}) \text{ TeV}^{-2}, \\
 |\text{Abs } Q_2^{bd}| \sim |\text{Abs } \tilde{Q}_2^{bd}| &\lesssim 2.5 \times 10^{-7} (6.3 \times 10^{-8}) \text{ TeV}^{-2}, \\
 |\text{Abs } \tilde{Q}_4^{bd}| &\lesssim 1.1 \times 10^{-7} (2.8 \times 10^{-8}) \text{ TeV}^{-2},
 \end{aligned} \tag{3.110}$$

and

$$\begin{aligned}
 |\text{Re } Q_1^{bs}| \sim |\text{Re } \tilde{Q}_1^{bs}| &\lesssim 2.5 \times 10^{-5} (6.3 \times 10^{-6}) \text{ TeV}^{-2}, \\
 |\text{Im } Q_1^{bs}| \sim |\text{Im } \tilde{Q}_1^{bs}| &\lesssim 8 \times 10^{-6} (2 \times 10^{-6}) \text{ TeV}^{-2}, \\
 |\text{Re } Q_2^{bs}| \sim |\text{Re } \tilde{Q}_2^{bs}| &\lesssim 8.1 \times 10^{-6} (1.6 \times 10^{-8}) \text{ TeV}^{-2}, \\
 |\text{Im } Q_2^{bs}| \sim |\text{Im } \tilde{Q}_2^{bs}| &\lesssim 2.8 \times 10^{-6} (6.9 \times 10^{-7}) \text{ TeV}^{-2}, \\
 |\text{Re } \tilde{Q}_4^{bs}| &\lesssim 4 \times 10^{-6} (1 \times 10^{-6}) \text{ TeV}^{-2}, \\
 |\text{Im } \tilde{Q}_4^{bs}| &\lesssim 1 \times 10^{-6} (2.5 \times 10^{-7}) \text{ TeV}^{-2}.
 \end{aligned} \tag{3.111}$$

For these observables we estimate

$$\begin{aligned}
 U(3)_{RC}^2 : \quad \text{Abs } C_1^{bd} &= \frac{A^2 y_t^4 \lambda^6}{m_*^2 g_*^2 \varepsilon_u^4}, & \text{Abs } \tilde{C}_1^{bd} &= \times, \\
 U(2) \times U(3)_{RC} : \quad \text{Abs } C_1^{bd} &= \frac{A^2 y_t^4 \lambda^6}{m_*^2 g_*^2 \varepsilon_t^4}, & \text{Abs } \tilde{C}_1^{bd} &= \times, \\
 U(2)_{RC}^2 : \quad \text{Abs } C_1^{bd} &= \frac{A^2 y_t^4 \lambda^6}{m_*^2 g_*^2 \varepsilon_t^4}, & \text{Abs } \tilde{C}_1^{bd} &= \frac{y_s^2 g_*^2 \varepsilon_b^4}{y_b^2 m_*^2}, \\
 U(3)_{LC} : \quad \text{Abs } C_1^{bd} &= \times, & \text{Abs } \tilde{C}_1^{bd} &= \times, \\
 U(2)_{LC} : \quad \text{Abs } C_1^{bd} &= A^2 \lambda^6 \frac{g_*^2 \varepsilon_{q3}^4}{m_*^2}, & \text{Abs } \tilde{C}_1^{bd} &= (a')^2 \frac{y_d^2 y_s^2}{g_*^2 \varepsilon_q^4},
 \end{aligned} \tag{3.112}$$

### 3.4. Experimental constraints

$\mathcal{F}_c$	$C_1^{bd}$	$\tilde{C}_1^{bd}$	$C_2^{bd}$	$\tilde{C}_2^{bd}$	$C_4^{bd}$
$U(3)_{RC}^2$	$\frac{6.5(13)}{g_*\varepsilon_u^2}$	$\times$	$\times$	$\times$	$\times$
$U(3) \times U(2)_{RC}$	$\frac{6.5(13)}{g_*\varepsilon_t^2}$	$\times$	$\times$	$\times$	$\times$
$U(2)_{RC}^2$	$\frac{6.5(13)}{g_*\varepsilon_t^2}$	$19.3(38.7)g_*\varepsilon_b^2$	—	—	—
$U(3)_{LC}$	$\times$	$\times$	$\times$	$\times$	$\times$
$U(2)_{LC}$	$8.7(17.3)g_*\varepsilon_{q3}^2$	—	—	—	—
$\mathcal{F}_c$	$C_1^{bs}$	$\tilde{C}_1^{bs}$	$C_2^{bs}$	$\tilde{C}_2^{bs}$	$C_4^{bs}$
$U(3)_{RC}^2$	$\frac{5.9(11.8)}{g_*\varepsilon_u^2}$	$\times$	$\times$	$\times$	$\times$
$U(3) \times U(2)_{RC}$	$\frac{5.9(11.8)}{g_*\varepsilon_t^2}$	$\times$	$\times$	$\times$	$\times$
$U(2)_{RC}^2$	$\frac{5.9(11.8)}{g_*\varepsilon_t^2}$	$6.8(13.6)g_*\varepsilon_b^2$	—	—	—
$U(3)_{LC}$	$\times$	$\times$	$\times$	$\times$	$\times$
$U(2)_{LC}$	$7.9(15.8)g_*\varepsilon_{q3}^2$	—	—	—	—

Table 3.5 – Constraints from the  $B_d$  and  $B_s$  systems  $\Delta F = 2$  transitions. For each operator and scenario we report the lower bound on  $m_*$  expressed in TeV. In parenthesis the projected bounds for HL-LHC. With — and  $\times$  we indicate respectively that the bound is negligible or the operator is not generated at leading order.

and

$$\begin{aligned}
U(3)_{RC}^2 : \quad & \text{Re/Im } C_1^{bs} = \frac{A^2 y_t^4 \lambda^4}{m_*^2 g_*^2 \varepsilon_t^4} (1 + i\eta\lambda^2), \quad \text{Re/Im } \tilde{C}_1^{bs} = \times, \\
U(2) \times U(3)_{RC} : \quad & \text{Re/Im } C_1^{bs} = \frac{A^2 y_t^4 \lambda^4}{m_*^2 g_*^2 \varepsilon_t^4} (1 + i\eta\lambda^2), \quad \text{Re/Im } \tilde{C}_1^{bs} = \times, \\
U(2)_{RC}^2 : \quad & \text{Re/Im } C_1^{bs} = \frac{A^2 y_t^4 \lambda^4}{m_*^2 g_*^2 \varepsilon_t^4} (1 + i\eta\lambda^2), \quad \text{Re/Im } \tilde{C}_1^{bs} = \frac{y_s^2 g_*^2 \varepsilon_b^4}{y_b^2 m_*^2}, \\
U(3)_{LC} : \quad & \text{Re/Im } C_1^{bs} = \times, \quad \text{Re/Im } \tilde{C}_1^{bs} = \times, \\
U(2)_{LC} : \quad & \text{Re } C_1^{bs} = A^2 \lambda^4 \frac{g_*^2 \varepsilon_{q3}^4}{m_*^2}, \quad \text{Re/Im } \tilde{C}_1^{bs} = (a')^2 \frac{y_s^4}{g_*^2 \varepsilon_q^4}.
\end{aligned} \tag{3.113}$$

Also in this case the mixed chirality operators are generated only for the  $U(2)_{RC}^2$  and  $U(2)_{LC}$  models but give negligible bounds. The bounds on  $m_*$  can be found in table 3.5.

#### The $D$ system

The final set of  $\Delta F = 2$  constraints we study come from the  $D$  system. These constraints are complementary to the previous ones since they involve up-type quarks. The current experimental bounds are [215]

$$\begin{aligned}
|\text{Im } Q_1^{cu}| &\sim |\text{Im } \tilde{Q}_1^{cu}| \lesssim 1 \times 10^{-8} (1.6 \times 10^{-9}) \text{ TeV}^{-2}, \\
|\text{Im } Q_2^{cu}| &\sim |\text{Im } \tilde{Q}_2^{cu}| \lesssim 2.5 \times 10^{-9} (2 \times 10^{-10}) \text{ TeV}^{-2}, \\
|\text{Im } \tilde{Q}_4^{cu}| &\lesssim 5 \times 10^{-10} (1 \times 10^{-10}) \text{ TeV}^{-2}.
\end{aligned} \tag{3.114}$$

$\mathcal{F}_c$	$C_1^{cu}$	$\tilde{C}_1^{cu}$	$C_2^{cu}$	$\tilde{C}_2^{cu}$	$C_4^{cu}$
$U(3)_{RC}^2$	—	×	×	×	×
$U(3) \times U(2)_{RC}$	—	$0.12(0.31)g_*\varepsilon_t^2$	—	—	—
$U(2)_{RC}^2$	—	$0.12(0.31)g_*\varepsilon_t^2$	—	—	—
$U(3)_{LC}$	×	×	×	×	×
$U(2)_{LC}$	$0.12(0.31)g_*\varepsilon_{q3}^2$	—	—	—	—

Table 3.6 – Constraints from the  $D$  system  $\Delta F = 2$  transitions. For each operator and scenario we report the lower bound on  $m_*$  expressed in TeV. In parenthesis the projected bounds for HL-LHC. With — and × we indicate respectively that the bound is negligible or the operator is not generated at leading order.

In this sector most contributions are negligible compared to the experimental bounds. We report here the only ones that could be potentially relevant

$$\begin{aligned}
 U(2) \times U(3)_{RC} : \quad \text{Im } \tilde{C}_1^{cu} &= \frac{y_c^4}{y_t^4} \frac{g_*^2 \varepsilon_t^4}{m_*^2}, \\
 U(2)_{RC}^2 : \quad \text{Im } \tilde{C}_1^{cu} &= \frac{y_c^4}{y_t^4} \frac{g_*^2 \varepsilon_t^4}{m_*^2}, \\
 U(2)_{LC} : \quad \text{Im } C_1^{cu} &= \frac{y_c^4}{y_t^4} g_*^2 \varepsilon_{q3}^4.
 \end{aligned} \tag{3.115}$$

The bounds on  $m_*$  can be found in table 3.6.

### 3.5 Conclusion and outlook

In this work we have examined several possibilities for the flavor structure in Composite Higgs models that implement Partial Compositeness. The class of models that we studied have either the six right-handed SM quarks or the three left-handed ones strongly composite. The models are further classified according to the flavor group of the composite sector. The remaining mixings are instead taken to be generic, with the only request that the Standard Model can be reproduced. The models we considered are summarized in Fig. 3.3, for the right-handed compositeness models, and Fig. 3.4, for the left-handed compositeness ones. The characteristic common to all of these models is the exact absence of contributions to the neutron EDM at leading order in the number of spurion insertions, assuming no additional CP odd effects arise from the strong sector.

We started from models that realize Minimal Flavor Violation and we then tried to reduce the flavor symmetry group of the composite dynamics in order to relax the tension with the experimental bounds. Regarding the right-handed compositeness models we have seen that there is a clear advantage in going from  $U(3)_{RC}^2$  to  $U(2) \times U(3)_{RC}$  since this removes the strong constraints coming from the interplay of light quark compositeness bounds and  $\Delta F = 2$  transitions in the  $B$  sector. Further reducing the symmetry group to  $U(2)_{RC}^2$  is instead not so convenient, since this model introduces new flavor-violating



processes in the down sector. Most of these can be taken under control for sufficiently small  $\epsilon_b$  with the only exception being  $b \rightarrow s\gamma$ , which is independent on  $\epsilon_b$  and gives an irreducible bound on  $m_*$  that was absent in  $U(2) \times U(3)_{\text{RC}}$ .

We tried to apply the same logic to the left-handed compositeness models (with a single partner for the SM doublets), where the  $U(3)_{\text{LC}}$  MFV model faces strong bounds from combining light quark compositeness and the CKM unitarity constraints. This lead us to consider the  $U(2)_{\text{LC}}$  model that, however, introduces new flavor violating effects, absent in MFV. Even for this model, we found the strongest constraint to come from the  $b \rightarrow s\gamma$  transitions. In Fig. 3.7 we report a summary of the bounds of all the models studied.

It is interesting to notice that from the flavor point of view, in the scenarios considered the strongest bounds always come from the  $B$  mesons mixings and decays. This is different compared to the anarchic scenario where the strongest constraints are due, respectively, to EDMs and to the  $K$  mesons system. We started to assess the projected sensitivity expected from the BELLE II [214] and HL-LHC [215] programs, but we still miss a complete study.<sup>10</sup>

In this direction we also plan to assess the impact of future collider on the different setup we considered. Preliminary projections for a universal and top-philic composite dynamics, in very high-energy lepton colliders, are already present in [3] but a systematic discussion on flavor is still missing.

Our study should also be extended to the lepton sector, already partially addressed in the literature [239, 256]. An unified discussion of all the SM flavor has not yet been presented and can be crucial in light of the foreseen experiments [257, 258].

Our preliminary results show that flavor observables play a remarkable role in the composite Higgs framework. Different flavor structures can indeed completely exclude a strong dynamics accounting for the SM masses or can give specific signatures of it. Research and progress in flavor physics is mandatory in order to exploit the full potential of the next experiments and this can play a major role in our understanding of fundamental physics in the next few years.

---

<sup>10</sup>See also [213].

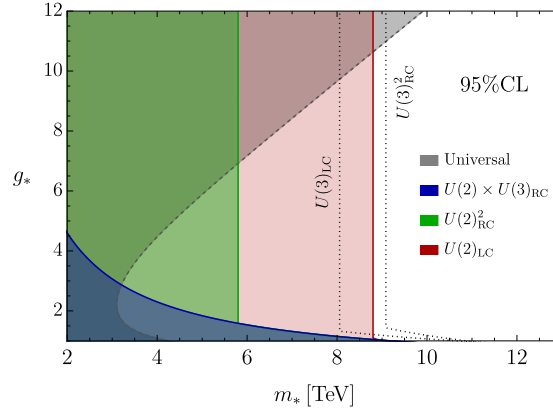


Figure 3.7 – Summary of all the combined bounds for the various models examined in this work. The grey area is for flavor-universal bounds and are common to all models. The dotted lines are the two implementations of MFV for right- and left-handed compositeness models.

# A Appendices for Chapter 1

## A.1 Explicit formulas

In this section we report some explicit formula to complete the discussion of Ch. 1. First of all the  $\mathcal{K}_{q_{\chi q}, l_{\chi l}}^0$  encoding the new physics effects in eq. (1.2) can be found in Table A.1 for the quark-lepton interaction in the Warsaw basis, and in Table A.2 for the  $W$  and  $Y$  parameters.

We now turn to the explicit expression for the reweighting functions in eq. (1.20). We specialize again to the W&Y scenario but the more general flavor universal one is completely analogous. The first term in eq. (1.20) takes the form

$$\rho_{n(c), \Lambda}^{q_1 \bar{q}_2 \rightarrow l_1 \bar{l}_2} = \left(1 + a_{W, \Lambda}^{n(c)} W + a_{Y, \Lambda}^{n(c)} Y\right)^2, \quad (\text{A.1})$$

where

$$\begin{aligned} a_{W, \Lambda}^n &= a_W^n(s; q_{\chi q}, l_{\chi l}) + \frac{\log(\Lambda^2/s)}{16\pi^2 m_W^2} \frac{g^2 \beta_{n, W}(q_{\chi q}, l_{\chi l})}{\mathcal{C}_{\text{SM}}^0(q_{\chi q}, l_{\chi l})}, \\ a_{Y, \Lambda}^n &= a_Y^n(s; q_{\chi q}, l_{\chi l}) + \frac{\log(\Lambda^2/s)}{16\pi^2 m_W^2} \frac{g'^2 \beta_{n, Y}(q_{\chi q}, l_{\chi l})}{\mathcal{C}_{\text{SM}}^0(q_{\chi q}, l_{\chi l})}, \\ a_{W, \Lambda}^c &= a_W^c(s) + \frac{\log(\Lambda^2/s)}{16\pi^2 m_W^2} \frac{V_{ud}^* g^2 \beta_{c, W}}{\mathcal{C}_{\text{SM}}^+(s; \{u, d\}, l)}, \\ a_{Y, \Lambda}^c &= \frac{\log(\Lambda^2/s)}{16\pi^2 m_W^2} \frac{V_{ud}^* g'^2 \beta_{c, Y}}{\mathcal{C}_{\text{SM}}^+(s; \{u, d\}, l)}, \end{aligned}$$

with  $a_{W(Y)}^{n(c)}$  and the  $\mathcal{C}$ 's defined as in section 1.2.1. The  $\beta$ -functions, computed by `DsixTools` [83], are reported in table A.3.

## Appendix A. Appendices for Chapter 1

$(\chi_q, \chi_l)$	(L,L)	(L,R)	(R,L)	(R,R)
$u - \bar{u}$ subprocess	$G_{lq}^{(1)} - G_{lq}^{(3)}$	$G_{qe}$	$G_{lu}$	$G_{eu}$
$d - \bar{d}$ subprocess	$G_{lq}^{(1)} + G_{lq}^{(3)}$	$G_{qe}$	$G_{ld}$	$G_{ed}$

Table A.1 – Explicit expressions for the new physics coefficients  $\mathcal{K}_{q\chi_q, l\chi_l}^0$  defined in eq. (A.3) for the generic quark-lepton operators in the Warsaw basis (Table 1.1).

$(\chi_q, \chi_l)$	(L,L)	(L,R)	(R,L)	(R,R)
$u - \bar{u}$ subprocess	$\frac{3g^2W + g'^2Y}{12m_W^2}$	$\frac{g'^2Y}{6m_W^2}$	$\frac{g'^2Y}{3m_W^2}$	$\frac{2g'^2Y}{3m_W^2}$
$d - \bar{d}$ subprocess	$\frac{-3g^2W + g'^2Y}{12m_W^2}$	$\frac{g'^2Y}{6m_W^2}$	$-\frac{g'^2Y}{6m_W^2}$	$-\frac{g'^2Y}{3m_W^2}$

Table A.2 – Explicit expressions for the new physics coefficients  $\mathcal{K}_{q\chi_q, l\chi_l}^0$  defined in eq. (A.3) for the  $\mathcal{O}'_{2W}$  and  $\mathcal{O}'_{2B}$  operators.

$(q_{\chi_q}, l_{\chi_l})$	$(u_L, e_L)$	$(d_L, e_L)$	$(q_L, e_R)$	$(u_R, e_L)$	$(d_R, e_L)$	$(u_R, e_R)$	$(d_R, e_R)$
$\beta_{n,W}$	$\frac{g'^2 - g^2}{12}$	$\frac{5(11g^2 - g'^2)}{12}$	$-\frac{1}{6}g'^2$	$-\frac{1}{3}g'^2$	$\frac{1}{6}g'^2$	0	0
$\beta_{n,Y}$	$\frac{51g^2 - 703g'^2}{324}$	$\frac{-51g^2 - 703g'^2}{324}$	$-\frac{883}{162}g'^2$	$-\frac{853}{81}g'^2$	$\frac{679}{162}g'^2$	$-\frac{1256}{81}g'^2$	$\frac{940}{81}g'^2$
$\beta_{c,W} = \frac{28g^2 - 3g'^2}{6}$	$\beta_{c,Y} = -\frac{17}{54}g^2$						

Table A.3 – The relevant  $\beta$ -functions.

The second term in eq. (1.20) is given by

$$\begin{aligned}
\Delta\rho_{\text{NLL},\Lambda}^{u\bar{u}\rightarrow l\bar{l}} &= 2\left(\rho_{\text{n},\Lambda}^{u_{\chi_u}\bar{u}_{\chi_u}\rightarrow l_{\chi_l}\bar{l}_{\chi_l}}\mathcal{F}_D + \frac{\delta\mathcal{C}_{\text{SM}}^0(u_{\chi_u}, l_{\chi_l})}{\mathcal{C}_{\text{SM}}^0(u_{\chi_u}, l_{\chi_l})}\sqrt{\rho_{\text{n},\Lambda}^{u_{\chi_u}\bar{u}_{\chi_u}\rightarrow l_{\chi_l}\bar{l}_{\chi_l}}} + \right. \\
&\quad \left. \delta_{\chi_u,L}\delta_{\chi_l,L}\sqrt{\rho_{\text{n},\Lambda}^{u_{\chi_u}\bar{u}_{\chi_u}\rightarrow l_{\chi_l}\bar{l}_{\chi_l}}}\rho_{c,\Lambda}\frac{g^2}{(4\pi)^2}L_u\Re\left[\frac{V_{\text{ud}'}\mathcal{C}_{\text{SM}}^+(s;\{u,d'\},l)}{\mathcal{C}_{\text{SM}}^0(u_{\chi_u}, l_{\chi_l})}\right]\right), \\
\Delta\rho_{\text{NLL},\Lambda}^{d\bar{d}\rightarrow l\bar{l}} &= 2\left(\rho_{\text{n},\Lambda}^{d_{\chi_d}\bar{d}_{\chi_d}\rightarrow l_{\chi_l}\bar{l}_{\chi_l}}\mathcal{F}_D + \frac{\delta\mathcal{C}_{\text{SM}}^0(d_{\chi_d}, l_{\chi_l})}{\mathcal{C}_{\text{SM}}^0(d_{\chi_d}, l_{\chi_l})}\sqrt{\rho_{\text{n},\Lambda}^{d_{\chi_d}\bar{d}_{\chi_d}\rightarrow l_{\chi_l}\bar{l}_{\chi_l}}} - \right. \\
&\quad \left. \delta_{\chi_d,L}\delta_{\chi_l,L}\sqrt{\rho_{\text{n},\Lambda}^{d_{\chi_d}\bar{d}_{\chi_d}\rightarrow l_{\chi_l}\bar{l}_{\chi_l}}}\rho_{c,\Lambda}\frac{g^2}{(4\pi)^2}L_t\Re\left[\frac{\mathcal{C}_{\text{SM}}^+(s;\{u',d\},l)V_{\text{u'd}}}{\mathcal{C}_{\text{SM}}^0(d_{\chi_d}, l_{\chi_l})}\right]\right), \\
\Delta\rho_{\text{NLL},\Lambda}^{u\bar{d}\rightarrow \nu l^+} &= 2\left(\rho_{c,\Lambda}\mathcal{F}_D + \frac{\delta\mathcal{C}_{\text{SM}}^+(s;\{u,d\},l)}{\mathcal{C}_{\text{SM}}^+(s;\{u,d\},l)}\sqrt{\rho_{c,\Lambda}(s,W)} \right. \\
&\quad + V_{\text{ud}}^*\frac{g^2}{(4\pi)^2}L_u\left(\sqrt{\rho_{c,\Lambda}\rho_{\text{n},\Lambda}^{u_{\chi_u}\bar{u}_{\chi_u}\rightarrow l_{\chi_l}\bar{l}_{\chi_l}}}\frac{\mathcal{C}_{\text{SM}}^0(u_{\chi_u}, l_{\chi_l})}{\mathcal{C}_{\text{SM}}^+(s;\{u,d\},l)}\right) \\
&\quad \left. - V_{\text{ud}}^*\frac{g^2}{(4\pi)^2}L_t\left(\sqrt{\rho_{c,\Lambda}\rho_{\text{n},\Lambda}^{d_{\chi_d}\bar{d}_{\chi_d}\rightarrow l_{\chi_l}\bar{l}_{\chi_l}}}\frac{\mathcal{C}_{\text{SM}}^0(d_{\chi_d}, l_{\chi_l})}{\mathcal{C}_{\text{SM}}^+(s;\{u,d\},l)}\right)\right),
\end{aligned}$$

where the factors  $\delta\mathcal{C}^{0(+)}$ , defined as

$$\begin{aligned}\delta\mathcal{C}_{\text{SM}}^0(q_{\chi_q}, l_{\chi_l}) &= \frac{\partial\mathcal{C}_{\text{SM}}^0(q_{\chi_q}, l_{\chi_l})}{\partial g^2}\delta g^2 + \frac{\partial\mathcal{C}_{\text{SM}}^0(q_{\chi_q}, l_{\chi_l})}{\partial g'^2}\delta g'^2, \\ \delta\mathcal{C}_{\text{SM}}^+(s; \{u, d\}, l) &= \frac{\partial\mathcal{C}_{\text{SM}}^+(s; \{u, d\}, l)}{\partial g^2}\delta g^2,\end{aligned}$$

take into account the RG running of the SM couplings  $g$  and  $g'$ .

The four coefficient functions  $P_{s,o}^q$  appearing in the fully-differential cross-section for the neutral DY process, eq. (1.34), can be expressed as

$$P_s^q = \hat{s}^2 \left( (\mathcal{C}_0(q_L, l_L))^2 + (\mathcal{C}_0(q_R, l_R))^2 \right), \quad P_o^q = \hat{s}^2 \left( (\mathcal{C}_0(q_L, l_R))^2 + (\mathcal{C}_0(q_R, l_L))^2 \right), \quad (\text{A.2})$$

where the  $\mathcal{C}_0$  functions can be split as

$$\mathcal{C}_0(q_{\chi_q}, l_{\chi_l}) = \mathcal{C}_{\text{SM}}^0(s; q_{\chi_q}, l_{\chi_l}) + \mathcal{K}_{q_{\chi_q}, l_{\chi_l}}^0, \quad (\text{A.3})$$

with a SM contribution

$$\mathcal{C}_{\text{SM}}^0(\hat{s}; q_{\chi_q}, l_{\chi_l}) = \frac{g^2 T^3(q_{\chi_q}) T^3(l_{\chi_l}) + g'^2 Y(q_{\chi_q}) Y(l_{\chi_l})}{\hat{s}} + \mathcal{O}\left(\frac{m_Z^2}{\hat{s}}\right), \quad (\text{A.4})$$

and new physics effects encoded in  $\mathcal{K}_{q_{\chi_q}, l_{\chi_l}}^0$ . The explicit expressions for the latter are reported in Table A.1 for the quark-lepton interaction in the Warsaw basis, and in Table A.2 for the  $W$  and  $Y$  parameters.

From the previous equations one can easily derive the expressions for the vectors  $\vec{V}_{s,o}^q$  defined in eq. (1.36) as

$$G_{s,o}^{u,d} \equiv \vec{V}_{s,o}^{u,d} \cdot \vec{G}, \quad (\text{A.5})$$

where  $\vec{G}$  are the Wilson coefficients in the Warsaw basis. Analogously we defined the  $\vec{V}_{s,o}^\perp$  vectors

$$G_{s,o}^\perp \equiv \vec{V}_{s,o}^\perp \cdot \vec{G}. \quad (\text{A.6})$$

We recall that the  $G_{s,o}^\perp$  coefficients are chosen to have components only along the operators contributing to the neutral DY process and to be orthogonal to the coefficient combinations  $G_{s,o}^{u,d}$ . Moreover  $\vec{V}_s^\perp$  and  $\vec{V}_o^\perp$  contribute to same-chirality and opposite-chirality subprocesses, respectively. We report the explicit values of the  $\vec{V}$  components in Table A.4.

The explicit expressions for the  $G_E^\pm$  and  $G_O^\pm$  coefficients can be derived by substituting the above expressions in the definitions in eqs. (1.47), (1.48) and (1.49).

Finally, we report the Wilson coefficients in the Warsaw basis (see the left column of

## Appendix A. Appendices for Chapter 1

	Generic quark-lepton operators							W and Y	
	$G_{lq}^{(3)}$	$G_{lq}^{(1)}$	$G_{qe}$	$G_{lu}$	$G_{ld}$	$G_{eu}$	$G_{ed}$	W	Y
$\vec{V}_s^u$	$\frac{3g^2+g'^2}{6}$	$\frac{-3g^2-g'^2}{6}$	0	0	0	$-\frac{4g'^2}{3}$	0	$-\frac{g^2(3g^2+g'^2)}{24m_W^2}$	$-\frac{g'^2(3g^2+65g'^2)}{72m_W^2}$
$\vec{V}_s^d$	$\frac{3g^2-g'^2}{6}$	$\frac{3g^2-g'^2}{6}$	0	0	0	0	$\frac{2g'^2}{3}$	$-\frac{g^2(3g^2-g'^2)}{24m_W^2}$	$\frac{g'^2(3g^2-17g'^2)}{72m_W^2}$
$\vec{V}_o^u$	0	0	$-\frac{g'^2}{3}$	$-\frac{2g'^2}{3}$	0	0	0	0	$-\frac{5g'^4}{18m_W^2}$
$\vec{V}_o^d$	0	0	$-\frac{g'^2}{3}$	0	$\frac{g'^2}{3}$	0	0	0	$-\frac{g'^4}{9m_W^2}$
$\vec{V}_s^\perp$	0	$\frac{2g'^2}{3}$	0	0	0	$\frac{-3g^2-g'^2}{12}$	$\frac{g'^2-3g^2}{6}$	0	$-\frac{g'^4}{18m_W^2}$
$\vec{V}_o^\perp$	0	0	$\frac{2g'^2}{3}$	$-\frac{g'^2}{3}$	$\frac{2g'^2}{3}$	0	0	0	$-\frac{g'^4}{9m_W^2}$

Table A.4 – Explicit expressions for the components of the  $\vec{V}_{s,o}^q$  and  $\vec{V}_{s,o}^\perp$  vectors. The first part of the table gives the components along the generic quark-lepton operators in the Warsaw basis, while the last two columns correspond to the components along the W and Y parameters.

Table 1.1) that are obtained by integrating out the minimal  $Z'$  model of Section 1.5

$$\begin{pmatrix} G_{lq}^{(3)} \\ G_{lq}^{(1)} \\ G_{qe} \\ G_{lu} \\ G_{ld} \\ G_{eu} \\ G_{ed} \end{pmatrix} = \frac{1}{M^2} \begin{pmatrix} 0 \\ \frac{g_{BL}^2}{3} + \frac{g_{BL}g_Y}{3} + \frac{g_Y^2}{12} \\ \frac{g_{BL}^2}{3} + \frac{g_{BL}g_Y}{2} + \frac{g_Y^2}{6} \\ \frac{g_{BL}^2}{3} + \frac{5g_{BL}g_Y}{6} + \frac{g_Y^2}{3} \\ \frac{g_{BL}^2}{3} - \frac{g_{BL}g_Y}{6} - \frac{g_Y^2}{6} \\ \frac{g_{BL}^2}{3} + g_{BL}g_Y + \frac{2g_Y^2}{3} \\ \frac{g_{BL}^2}{3} - \frac{g_Y^2}{3} \end{pmatrix}. \quad (\text{A.7})$$

## A.2 Kinematical variables

The charged leptons momenta we employ in our analyses are obtained by recombining photons (and lepton pairs from photon splitting) within a  $\Delta R^{\text{rec}} = 0.1$  recombination cone, with thresholds  $p_{T,\text{min}}^\gamma = 10$  GeV and  $|\eta|_{\text{max}}^\gamma = 3$ . Acceptance cuts  $p_{T,\text{min}}^\ell = 25$  GeV and  $|\eta|_{\text{max}}^\ell = 2.5$  are applied to the reconstructed lepton momenta. Events are selected to have 2 (same-flavor) or 1 reconstructed leptons for, respectively, the neutral and charged DY analyses.

The two variables employed in the charged analysis are the transverse momentum  $p_{T,\ell}$  and the rapidity  $\eta_\ell$  of the single observed lepton.

In the neutral case, the three variables are the invariant mass  $m_{\ell\ell}$  of the dilepton pair, the rapidity of the dilepton system relative to the beam axis in absolute value (called

$y$ ) and the cosine of the scattering angle  $c_* = \cos \theta_*$ . Two alternative definitions of  $\theta_*$  can be considered. The simplest option is to define it as the angle formed, in the rest frame of the dilepton pair, between the charge-minus lepton and the direction of motion of the dilepton rest frame relative to the lab frame. The second option is to define  $\theta_*$  as the angle between the momentum of the charge-minus lepton and the  $z$  axis in the Collins–Soper frame, along the lines of Ref. [259]. More precisely,  $c_*$  is defined by the formula

$$c_* = \frac{2p_{z,\ell\ell}}{m_{\ell\ell}|p_{z,\ell\ell}|} \frac{p_{z,\ell^-}E_{\ell^+} - p_{z,\ell^+}E_{\ell^-}}{(m_{\ell\ell}^2 + p_{\perp,\ell\ell}^2)^{1/2}}, \quad (\text{A.8})$$

where  $E_{\ell^\pm}$  and  $p_{z,\ell^\pm}$  denote the energy and longitudinal momentum of each lepton, while  $p_{z,\ell\ell}$  and  $p_{\perp,\ell\ell}$  are the longitudinal and transverse momentum of the lepton pair. The two definitions only coincide for the tree-level kinematics, where the dilepton pair has vanishing transverse momentum. However we have checked that the differential distributions obtained with the two definitions are almost identical, thus giving nearly equal results for the fits (the differences in the bounds being at most 2–3%). The results reported in ch 1 are obtained with the Collins–Soper definition of  $c_*$ .

We remark that the definition in eq. (A.8) contains the factor  $p_{z,\ell\ell}/|p_{z,\ell\ell}|$ , which takes into account the direction of the boost of the CoM system. Its presence is essential for the effectiveness of the fully-differential analysis as emphasized in Footnote 11. This factor is duly taken into account in existing experimental measurements (see e.g. Ref. [43]).

### A.3 Correlation matrices

In this appendix we report the correlation matrices for the fully-differential linearized fit on the 7 4-fermion Wilson coefficients presented in Section 1.4.4. The fit includes a 2% uncorrelated systematic uncertainty. The corresponding 95% CL bounds are given in Table 1.5 for the  $\tilde{G}_{lq}^{(3)}$ ,  $G_{E/O}^\pm$ ,  $G_{s/o}^\perp$  coefficients and in Table 1.6 for the Warsaw basis.

	$\tilde{G}_{lq}^{(3)}$	$G_E^+$	$G_E^-$	$G_O^+$	$G_O^-$	$G_s^\perp$	$G_o^\perp$
$\tilde{G}_{lq}^{(3)}$	1	-0.61	0.45	-0.056	-0.22	-0.21	-0.1
$G_E^+$	-0.61	1	-0.39	0.32	0.74	0.56	0.56
$G_E^-$	0.45	-0.39	1	0.28	-0.078	-0.36	0.1
$G_O^+$	-0.056	0.32	0.28	1	0.26	-0.43	0.47
$G_O^-$	-0.22	0.74	-0.078	0.26	1	0.64	0.56
$G_s^\perp$	-0.21	0.56	-0.36	-0.43	0.64	1	0.25
$G_o^\perp$	-0.1	0.56	0.1	0.47	0.56	0.25	1

	$G_{lq}^{(3)}$	$G_{lq}^{(1)}$	$G_{qe}$	$G_{lu}$	$G_{ld}$	$G_{eu}$	$G_{ed}$
$G_{lq}^{(3)}$	1	-0.09	0.23	0.2	-0.26	-0.097	-0.027
$G_{lq}^{(1)}$	-0.09	1	0.4	0.39	-0.39	0.94	-0.78
$G_{qe}$	0.23	0.4	1	0.99	-0.98	0.47	-0.55
$G_{lu}$	0.2	0.39	0.99	1	-0.95	0.44	-0.49
$G_{ld}$	-0.26	-0.39	-0.98	-0.95	1	-0.52	0.64
$G_{eu}$	-0.097	0.94	0.47	0.44	-0.52	1	-0.94
$G_{ed}$	-0.027	-0.78	-0.55	-0.49	0.64	-0.94	1

## A.4 LHC projections

In this appendix we report the projections for the LHC run 3, assuming an energy of 14 TeV and an integrated luminosity  $\mathcal{L} = 300 \text{ fb}^{-1}$ .

The 95% CL, single-parameter bounds for the Universal parameters W and Y are given by

$$\begin{aligned}
 W : \quad & [-6.8, 7.2] \times 10^{-5} \quad ([-8.2, 8.9] \times 10^{-5}), \\
 Y : \quad & [-17, 19] \times 10^{-5} \quad ([-18, 20] \times 10^{-5}),
 \end{aligned} \tag{A.9}$$

where the two sets of intervals correspond to the fully-differential and single-differential combined bounds (the latter in brackets). These bounds are obtained including only a 2% luminosity uncertainty, but no additional experimental systematic error. Comparing with the analogous HL-LHC bounds in eq. (1.46), we see that the all bounds are roughly a factor 2 weaker. The fully-differential analysis provides an improvement in the sensitivity, although significantly milder than in the HL-LHC case. This pattern is not unexpected, since the benefits of a fully-differential analysis tend to be larger when the number of expected events is large enough to allow the fits to be dominated by the linear interference terms. At the LHC with  $\mathcal{L} = 300 \text{ fb}^{-1}$  the importance of the quadratic terms in the fits is still high, thus explaining the much milder gain in sensitivity. As we will see in the following, a similar pattern is found for the fits on the seven 4-fermion operators and on the minimal  $Z'$  model.

In Tables A.5 and A.6 we report the LHC run 3 bounds for the single parameter and the profiled fits in the basis introduced in Section 1.4.3 and in the Warsaw basis, respectively. Also in this case the bounds are derived assuming no uncorrelated experimental systematic uncertainty. As for the HL-LHC, the main benefit of the fully-differential fit is in the determination of the  $G_O^+$  parameter, which improves by roughly 40% in the single-parameter fit. Mild improvements in the sensitivity to the other parameters (of order 10 – 20%) are also found.

Finally in Figure A.1 we report the projected LHC exclusion reach in the mass/coupling



#### A.4. LHC projections

95%CL [ $10^{-3} \text{ TeV}^{-2}$ ]	single parameter			profiled		
	fully diff.	fully diff. lin.	single diff.	fully diff.	fully diff. lin.	single diff.
$\tilde{G}_{lq}^{(3)}$	[-0.87, 0.87]	[-0.87, 0.87]	[-0.97, 0.97]	[-1.19, 1.06]	[-1.30, 1.30]	[-1.51, 1.27]
$G_E^+$	[-0.53, 0.47]	[-0.50, 0.50]	[-0.60, 0.53]	[-1.30, 0.74]	[-1.50, 1.50]	[-2.01, 0.85]
$G_E^-$	[-1.13, 1.20]	[-2.66, 2.66]	[-1.30, 1.51]	[-3.56, 2.80]	[-4.54, 4.54]	[-5.03, 3.29]
$G_O^+$	[-1.07, 0.87]	[-1.00, 1.00]	[-1.74, 1.94]	[-1.16, 1.45]	[-2.17, 2.17]	[-2.16, 3.41]
$G_O^-$	[-1.30, 1.16]	[-7.88, 7.88]	[-1.53, 1.35]	[-3.02, 3.70]	[-17.9, 17.9]	[-3.41, 4.90]
$G_s^\perp$	[-3.48, 2.75]	[-11.0, 11.0]	[-3.52, 2.81]	[-4.05, 3.79]	[-30.5, 30.5]	[-4.38, 3.92]
$G_o^\perp$	[-1.19, 1.17]	[-51.9, 51.9]	[-1.42, 1.40]	[-1.65, 1.47]	[-70.2, 70.2]	[-2.00, 2.00]

Table A.5 – 95% CL projected bounds (in  $10^{-3} \text{ TeV}^{-2}$  units) for the seven parameters  $\tilde{G}_{lq}^{(3)}$ ,  $G_{E,O}^\pm$  and  $G_{s,o}^\perp$  at the 14 TeV LHC with  $\mathcal{L} = 300 \text{ fb}^{-1}$ .

95%CL [ $10^{-3} \text{ TeV}^{-2}$ ]	single parameter			profiled		
	fully diff.	fully diff. lin.	single diff.	fully diff.	fully diff. lin.	single diff.
$G_{lq}^{(3)}$	[-1.09, 1.03]	[-1.06, 1.06]	[-1.35, 1.25]	[-1.19, 1.06]	[-1.30, 1.30]	[-1.51, 1.27]
$G_{lq}^{(1)}$	[-4.68, 7.51]	[-5.66, 5.66]	[-5.11, 10.64]	[-8.62, 10.56]	[-35.6, 35.6]	[-9.72, 13.5]
$G_{qe}$	[-4.71, 8.62]	[-6.57, 6.57]	[-6.11, 10.9]	[-7.23, 9.37]	[-375, 375]	[-10.9, 11.3]
$G_{lu}$	[-4.22, 6.42]	[-5.01, 5.01]	[-5.88, 10.6]	[-6.05, 10.3]	[-187, 187]	[-11.6, 13.7]
$G_{ld}$	[-16.3, 10.2]	[-18.0, 18.0]	[-19.2, 12.5]	[-16.9, 14.9]	[-419, 419]	[-20.2, 20.9]
$G_{eu}$	[-3.10, 3.54]	[-3.30, 3.30]	[-3.29, 3.83]	[-6.20, 10.3]	[-46.9, 46.9]	[-7.25, 11.7]
$G_{ed}$	[-13.5, 8.18]	[-10.3, 10.3]	[-15.5, 8.69]	[-16.9, 16.0]	[-121, 121]	[-17.9, 18.7]

Table A.6 – 95% CL projected bounds (in  $10^{-3} \text{ TeV}^{-2}$  units) for the four-fermion operator coefficients in the Warsaw basis at the 14 TeV LHC with  $\mathcal{L} = 300 \text{ fb}^{-1}$ .

plane for the three benchmark  $Z'$  models considered in Section 1.5. The mass exclusion reach is roughly 25% weaker than the projections for the HL-LHC (compare Figure 1.17). The improvement due to the fully-differential analysis is clearly visible. In particular it plays a significant role in the difficult-to-test benchmark with  $g_Y = -g_{BL}$ , allowing one to cover part of the parameter space not yet excluded by the EWPT, which is not accessible with the single-differential analysis.

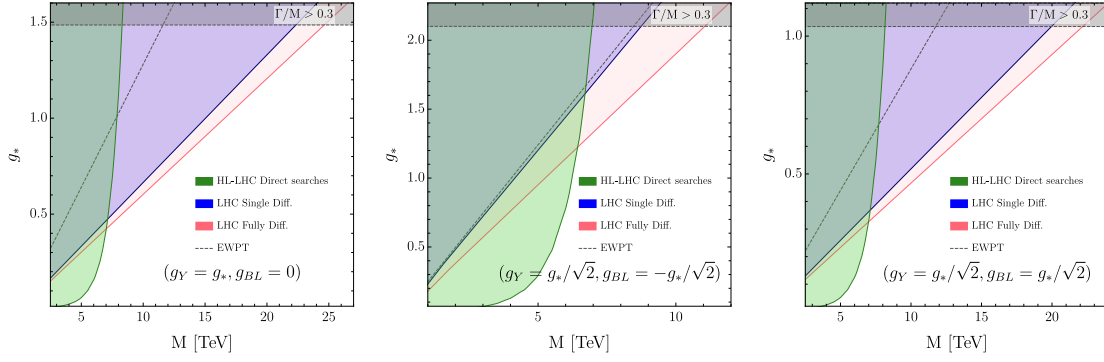


Figure A.1 – 95% CL (1 d.o.f) exclusion reach in the mass/coupling plane for three different  $Z'$  benchmark models at LHC with  $\mathcal{L} = 300 \text{ fb}^{-1}$ . The blue shaded region can be excluded through the fully-differential di-lepton DY analysis, while the orange one can be probed with the invariant-mass fit. The green shaded region corresponds to the exclusion from direct searches.

# B Appendices for Chapter 2

## B.1 Radiation integrals

The contribution of virtual radiation to the amplitude variation in eq. (2.43) is proportional to the integral

$$I \equiv \frac{-i}{(2\pi)^4} \int_{\delta\sigma} d^4q \frac{1}{q^2 - m_V^2 + i\epsilon} \frac{(k_i \cdot k_j)}{(q \cdot k_i)(q \cdot k_j)}, \quad (\text{B.1})$$

where we included a mass  $m_V \sim m_W$  for the virtual vector in order to verify explicitly that the integral is log-enhanced only in the  $\lambda \gg m_W^2$  regime, where the IR cutoff is much above the EW scale. We now proceed (following [260]) to the evaluation of  $I$  assuming, for simplicity, exactly massless hard 4-momenta  $k_i^2 = k_j^2 = 0$ . The integral is Lorentz-invariant, therefore it can only depend on the scalar product  $(k_i \cdot k_j)$ , that we set to

$$(k_i \cdot k_j) = \frac{1}{2}(k_i + k_j)^2 = \frac{1}{2}E^2, \quad (\text{B.2})$$

in what follows.

The calculation is conveniently performed in Sudakov coordinates [261]. Namely we parametrize the loop momentum  $q$  as

$$q = uk_i + vk_j + q_\perp^1 \zeta_1 + q_\perp^2 \zeta_2, \quad (\text{B.3})$$

where  $(\zeta_1)^2 = (\zeta_2)^2 = -1$ ,  $\zeta_{1,2} \cdot k_i = \zeta_{1,2} \cdot k_j = 0$  and  $\zeta_1 \cdot \zeta_1$ . In these coordinates

$$q^2 = uvE^2 - |q_\perp|^2, \quad (\text{B.4})$$

and the infinitesimal strip  $\delta\sigma$  (2.40) that defines the integration region is expressed as

$$|uv|E^2 \in [\lambda, \lambda + \delta\lambda]. \quad (\text{B.5})$$

## Appendix B. Appendices for Chapter 2

---

After the change of variables, the integral reads

$$I = \frac{i}{(2\pi)^4} \int_{\delta\sigma} \frac{dudv}{uv} \int \frac{d^2 q_\perp}{|q_\perp|^2 - uvE^2 + m_V^2 - i\epsilon}. \quad (\text{B.6})$$

The  $d^2 q_\perp$  integral must be performed up to an upper cutoff that justifies the usage of the Eikonal approximation formula in eq. (2.41) for the gauge boson vertices. In particular we notice that the actual denominators of the virtual legs in the diagram are not  $(k_{i,j} \cdot q)$  as in the Eikonal formula, but rather  $(k_{i,j} \cdot q) \pm q^2/2$ , with plus or minus for incoming and outgoing particles, respectively. Neglecting  $q^2/2$  is justified only if  $|q_\perp|^2/2$  is not as large as to compete with the minimum among  $|k_i \cdot q| = |u| E^2/2$  and  $|k_j \cdot q| = |v| E^2/2$ . Therefore the  $q_\perp$  integral should be cutoff at

$$|q_\perp|^2 < \Lambda^2, \quad \text{with} \quad \Lambda^2 = E^2 \min[|u|, |v|]. \quad (\text{B.7})$$

Similarly, the term proportional to  $uv$  in  $q^2$  should not be large compared to  $(k_{i,j} \cdot q)$ , therefore the  $u$  and  $v$  integrals are also bounded, in the region

$$|u| < 1, \quad |v| < 1, \quad (\text{B.8})$$

supplemented by eq. (B.5).

The integration boundaries of  $u$  and  $v$  are invariant under  $u \rightarrow -u$  and under  $v \rightarrow -v$  reflections. We can thus perform the integral (B.6) in the first quadrant of the  $(u, v)$  plane, provided we duly symmetrize the integrand. Furthermore we notice that first-quadrant integration region (restricted to  $u < 1$  and  $v < 1$ , owing to eq. (B.8)) is conveniently described by the coordinates  $\tau$  and  $y$ , defined by

$$u = \sqrt{\tau} e^y, \quad v = \sqrt{\tau} e^{-y}. \quad (\text{B.9})$$

Indeed in these coordinates the condition (B.5) merely sets the value of  $\tau$  to

$$\tau = \frac{\lambda}{E^2}, \quad \text{with} \quad \delta\tau = \frac{\delta\lambda}{E^2}, \quad (\text{B.10})$$

while the upper bound (B.7) on the  $|q_\perp|$  integral reads

$$\Lambda^2 = E^2 \sqrt{\tau} e^{-|y|} = E \sqrt{\lambda} e^{-|y|}. \quad (\text{B.11})$$

We can thus express the integral as

$$I = \frac{2i}{(2\pi)^3} \frac{\delta\lambda}{\lambda} \int_0^{y_M} dy \int_0^{E\sqrt{\lambda}e^{-y}} \frac{d^2 q_\perp}{|q_\perp|^2} \left[ \frac{1}{|q_\perp|^2 - \lambda + m_V^2 - i\epsilon} - \frac{1}{|q_\perp|^2 + \lambda + m_V^2 - i\epsilon} \right], \quad (\text{B.12})$$

where, since  $\Lambda^2$  is symmetric under  $y \rightarrow -y$ , we could take the  $y$  integral from 0 to

$$y_M = -\frac{1}{2} \log \tau = \log \frac{E}{\sqrt{\lambda}}, \quad (\text{B.13})$$

and multiply by a factor 2.

The  $d|q_\perp|^2$  integral in eq. (B.12) is readily performed. It is convenient to separate the terms that emerge from the upper  $|q_\perp|^2$  integration extreme from the one of the lower extreme  $|q_\perp|^2 = 0$ , obtaining two contributions to  $I$ ,  $I_U$  and  $I_L$ . We will readily see that the former contribution is suppressed, therefore

$$I \simeq I_L = \frac{1}{8\pi^2} \frac{\delta\lambda}{\lambda} \log \frac{E^2}{\lambda} \frac{i}{\pi} \log \left[ \frac{\lambda + m_V^2 - i\epsilon}{-\lambda + m_V^2 - i\epsilon} \right]. \quad (\text{B.14})$$

The logarithm gives quite different results in the two regimes  $\lambda \gg m_W^2 \sim m_V^2$  and  $\lambda \ll m_W^2 \sim m_V^2$ . In the second one, the argument of the logarithm has positive real part, almost equal to 1 up to  $m_V^2/\lambda$  power-corrections. In the first regime, the argument has negative real part and the log equals  $+i\pi$ , plus  $\lambda/m_V^2$  corrections. Namely

$$I \stackrel{\lambda \gg m_W^2}{=} -\frac{1}{8\pi^2} \frac{\delta\lambda}{\lambda} \log \frac{E^2}{\lambda} \left[ 1 + \mathcal{O}(m_V^2/\lambda) \right], \quad I \stackrel{\lambda \ll m_W^2}{=} -\frac{1}{8\pi^2} \frac{\delta\lambda}{\lambda} \log \frac{E^2}{\lambda} \cdot \mathcal{O}(\lambda/m_V^2), \quad (\text{B.15})$$

from which we recover eq. (2.44). More precisely, notice that the integral for each pair of external legs  $ij$  is controlled by the specific scale  $E^2 = 2(k_i \cdot k_j)$ . In eq. (2.44) we set all these scales equal up to corrections that are not log enhanced, but of order one. This in turn corresponds to order  $1/\log$  corrections to the evolution kernel and to single-logarithm corrections to the solutions of the IREE.

The contribution to  $I$  from the upper  $|q_\perp|^2$  integration extreme is suppressed. To see this it is convenient to employ the integration variable  $\rho = \exp(y - y_M)$ , obtaining

$$I_U = \frac{2i}{(2\pi)^3} \frac{\delta\lambda}{\lambda} \int_{\sqrt{\lambda}/E}^1 \frac{d\rho}{\rho} \frac{1}{\rho} \log \left[ \frac{1 - \rho(1 - m_V^2/\lambda)}{1 + \rho(1 + m_V^2/\lambda)} \right], \quad (\text{B.16})$$

where we could drop the  $-i\epsilon$  because the argument of the logarithm has positive real part in the entire range of integration. The  $\rho$  integral is finite for  $\sqrt{\lambda}/E \rightarrow 0$ , therefore it does not produce log-enhanced contributions. In particular the integral gives  $-\pi^2/4$  for  $\lambda \gg m_W^2 \sim m_V^2$  and it is power-suppressed in the opposite regime.

We now compute the contribution of real radiation to the density matrix variation, which we employ in eq. (2.51). The relevant integral that controls the contribution from a real

## Appendix B. Appendices for Chapter 2

---

radiation diagram like those in Figure 2.2, reads

$$I_R \equiv -\frac{1}{(2\pi)^3} \int_{\delta\sigma} \frac{d^3q}{2q^0} \frac{(k_i \cdot k_j)}{(k_i \cdot q)(k_j \cdot q)} = -\frac{1}{(2\pi)^3} \int_{\delta\sigma} d^4q \delta(q^2 - m_V^2) \theta(q^0) \frac{(k_i \cdot k_j)}{(k_i \cdot q)(k_j \cdot q)}, \quad (\text{B.17})$$

where we employed the eikonal formula in eq. (2.41), but ignored the “ $G$ ” factors that are included separately in eq. (2.51). Notice the presence of a minus sign, which is due to three factors of  $-1$ . The first minus is due to the fact that applying the eikonal formula to the conjugate amplitude gives the complex conjugate of the generator matrix “ $G_i$ ” of the corresponding leg, while eq. (2.51) is expressed in terms of the generators  $G_{ic} = -G_i^*$  of the conjugate representation. The second minus sign emerges from the sum over the polarizations of the real vector boson, which gives  $-\eta_{\mu\nu}$ . The third minus is because the contribution to the variation is minus the integral over the strip  $\delta\sigma$ , since the  $\lambda$  cutoff is a lower bound on the hardness.

In Sudakov coordinates (B.3), and setting  $(k_i \cdot k_j) = E^2/2$ , the integral becomes

$$I_R = -\frac{1}{(2\pi)^2} \int_{\delta\sigma} \frac{dudv}{uv} \theta(u+v) \int d|q_\perp|^2 \delta(uvE^2 - |q_\perp|^2 - m_V^2). \quad (\text{B.18})$$

The integration extremes of all the variables are like those of the virtual integral, including the condition (B.5) that defines the infinitesimal integration strip  $\delta\sigma$ . The delta function in eq. (B.18) has support only if  $uv > 0$ , and the theta function further restricts the integral to the first quadrant of the  $(u, v)$  plane. We can thus employ the  $\tau$  and  $y$  coordinates in eq. (B.9) and readily obtain

$$I_R = -\frac{1}{8\pi^2} \frac{\delta\lambda}{\lambda} \log \frac{E^2}{\lambda} \cdot \theta(\lambda - m_V^2). \quad (\text{B.19})$$

Evidently, the theta function condition is not satisfied for  $\lambda \ll m_W^2 \sim m_V^2$ , therefore the integral vanishes in this regime. In the other regime

$$I_R \stackrel{\lambda \gg m_W^2}{=} -\frac{1}{8\pi^2} \frac{\delta\lambda}{\lambda} \log \frac{E^2}{\lambda}, \quad (\text{B.20})$$

which is equal to the virtual radiation integral, as anticipated in the main text. Notice that the pre-factor of eq. (2.51) contains an additional  $1/2$ , due to the fact that the real radiation contribution is effectively counted twice in the equation by the two terms proportional to  $(G_i^A)(G_{jc}^A)$  and to  $(G_{ic}^A)(G_j^A)$ , which are equal after summing over  $i$  and  $j$ .

## B.2. High-energy EW multiplets

Bosons	$SU(2)_L$	$\mathcal{Y}$	Leptons	$SU(2)_L$	$\mathcal{Y}$
$W$	t	0	$(\nu_{\ell,-1/2}, \ell_{-1/2}^-)$	d	$-1/2$
$B$	s	0	$(\bar{\nu}_{\ell,+1/2}, \ell_{+1/2}^+)^t$	$\bar{d}$	$-1/2$
$H$	d	$+1/2$	$\ell_{+1/2}^-$	s	$-1$
$\bar{H}$	$\bar{d}$	$-1/2$	$\ell_{-1/2}^+$	s	$+1$

Quarks	$SU(2)_L$	$\mathcal{Y}$
$(u_{-1/2}, d_{-1/2})^t$	d	$+1/6$
$(\bar{u}_{+1/2}, \bar{d}_{+1/2})^t$	$\bar{d}$	$-1/6$
$u_{+1/2}$	s	$+2/3$
$\bar{u}_{-1/2}$	s	$-2/3$
$d_{+1/2}$	s	$-1/3$
$\bar{d}_{-1/2}$	s	$+1/3$

Table B.1 –  $SU(2)_L \times U(1)_Y$  quantum numbers of the SM particles in the high-energy regime.

## B.2 High-energy EW multiplets

The EW symmetry is effectively unbroken at energies much above the EW scale. Therefore in this regime it is convenient to describe the SM particles in terms of representations of the (linearly-realized) SM group  $SU(2)_L \times U(1)_Y$ , with generators

$$\mathcal{T}^A = \{\mathcal{T}^a, \mathcal{Y}\}, \quad a = 1, 2, 3. \quad (\text{B.21})$$

The generators act on the single particle states as

$$\mathcal{T}^A |p(k, \alpha)\rangle = |p(k, \beta)\rangle (T_r^A)^\beta_\alpha, \quad (\text{B.22})$$

with generator matrices  $T_r^A$  that define the representation “r” of the particle multiplet. The field  $\Phi_r^\alpha$  that interpolates the multiplet from the vacuum, namely

$$\langle 0 | \Phi_r^\alpha(0) | p(k, \beta) \rangle \propto \delta_\beta^\alpha, \quad (\text{B.23})$$

transforms with the same generator matrix, i.e.

$$[\Phi_r^\alpha(x), \mathcal{T}^A] = (T_r^A)^\alpha_\beta \Phi_r^\alpha(x). \quad (\text{B.24})$$

The  $SU(2)_L$  representations of the SM particles and the corresponding  $U(1)_Y$  charges are listed in Table B.1.

All the fermionic particles with helicity  $-1/2$  transforms as doublets (i.e.,  $r = d$ ), the

## Appendix B. Appendices for Chapter 2

---

anti-particles with helicity  $+1/2$  transform in the conjugate ( $r = \bar{d}$ ) of the doublet representation, while all the others are singlets. Obviously this is true only in the high energy limit where the fermions are effectively massless and the helicity corresponds the chirality of the corresponding interpolating fields. The doublet representation matrices are the standard

$$T_d^a = \left\{ \begin{pmatrix} 0 & +1/2 \\ +1/2 & 0 \end{pmatrix}, \begin{pmatrix} 0 & -i/2 \\ +i/2 & 0 \end{pmatrix}, \begin{pmatrix} +1/2 & 0 \\ 0 & -1/2 \end{pmatrix} \right\}, \quad T_d^a = -(T_d^a)^* = -(T_d^a)^t. \quad (\text{B.25})$$

The EW multiplets of bosonic particles are less well-known, but equally straightforward to work out employing the standard Goldstone Boson Equivalence Theorem, or better its stronger formulation in Ref.s [203, 262]. The point is that for massive  $W^\pm$  and  $Z$  vector bosons with 0 (longitudinal) helicity one can employ interpolating fields that are a specific combination of the regular gauge fields  $W_\mu^\pm$  and  $Z_\mu$  and of the Goldstone boson scalar fields  $\pi^\pm$  and  $\pi_Z$ . The longitudinal states are thus a linear combination of the quantum fluctuation modes associated to this two different type of fields, and the scattering amplitudes with external longitudinal states are a linear combination of Feynman diagrams where the external states are represented either as gauge fields or as Goldstone fields. This is a convenient formalism in the high energy limit because the polarization vector associated with gauge external lines vanishes as  $m_W/E$  (unlike the regular longitudinal polarization, that diverges as  $E/m_W$ ), and only the Goldstone diagrams survive. In essence this means that the Goldstones, and not the gauge, are the adequate interpolating fields for the longitudinal particles at high energy. Therefore the EW quantum numbers of the longitudinal particles are the ones of the Goldstones, and not of the gauge fields. The Goldstone bosons, together with the Higgs, form a doublet with  $+1/2$  hypercharge, and the corresponding conjugate doublet

$$H = \left( \pi^+, \frac{h + i\pi_Z}{\sqrt{2}} \right)^t, \quad \bar{H} = \left( \pi^-, \frac{h - i\pi_Z}{\sqrt{2}} \right)^t. \quad (\text{B.26})$$

Vector bosons with transverse helicity  $T = \pm 1$  are instead well-described by gauge fields even at high energy. Therefore they decompose into a triplet plus a singlet EW multiplet, which are readily obtained by undoing the Weinberg rotation

$$W^a = \left( \frac{W_T^+ + W_T^-}{\sqrt{2}}, i \frac{W_T^+ - W_T^-}{\sqrt{2}}, c_W Z_T + s_W \gamma_T \right)^t, \quad B = -s_W Z_T + c_W \gamma_T. \quad (\text{B.27})$$

Explicitly, the triplet generator matrices are

$$T_t^a = \left\{ \begin{pmatrix} 0 & 0 & 0 \\ 0 & 0 & -i \\ 0 & i & 0 \end{pmatrix}, \begin{pmatrix} 0 & 0 & i \\ 0 & 0 & 0 \\ -i & 0 & 0 \end{pmatrix}, \begin{pmatrix} 0 & -i & 0 \\ i & 0 & 0 \\ 0 & 0 & 0 \end{pmatrix} \right\}. \quad (\text{B.28})$$



We now proceed to the evaluation of the  $K_i$  exponentials in the explicit formula for the semi-inclusive density matrix (2.55), for external legs in the doublet (or anti-doublet) or in the triplet canonical representations defined by eq. (B.25) and (B.28). The  $K$  tensors in eq. (2.53) are

$$\left[K_d\right]_{\beta\bar{\beta}}^{\alpha\bar{\alpha}} = \left[K_{\bar{d}}\right]_{\beta\bar{\beta}}^{\alpha\bar{\alpha}} = c_d \delta_{\beta}^{\alpha} \delta_{\bar{\beta}}^{\bar{\alpha}} + \sum_a (T_d^a)^{\alpha}_{\beta} (T_{\bar{d}}^a)^{\bar{\alpha}}_{\bar{\beta}} = \delta_{\beta}^{\alpha} \delta_{\bar{\beta}}^{\bar{\alpha}} - \frac{1}{2} \delta^{\alpha\bar{\alpha}} \delta_{\beta\bar{\beta}}, \quad (\text{B.29})$$

$$\left[K_t\right]_{\beta\bar{\beta}}^{\alpha\bar{\alpha}} = c_t \delta_{\beta}^{\alpha} \delta_{\bar{\beta}}^{\bar{\alpha}} + \sum_a (T_t^a)^{\alpha}_{\beta} (T_{\bar{t}}^a)^{\bar{\alpha}}_{\bar{\beta}} = 2 \delta_{\beta}^{\alpha} \delta_{\bar{\beta}}^{\bar{\alpha}} + \delta_{\bar{\beta}}^{\alpha} \delta_{\beta}^{\bar{\alpha}} - \delta^{\alpha\bar{\alpha}} \delta_{\beta\bar{\beta}}. \quad (\text{B.30})$$

The exponential of eq. (B.29) is trivial and we readily obtain

$$\left[\exp\left(-\mathcal{L} K_d\right)\right]_{\beta\bar{\beta}}^{\alpha\bar{\alpha}} = e^{-\mathcal{L}} \delta_{\beta}^{\alpha} \delta_{\bar{\beta}}^{\bar{\alpha}} + e^{-\mathcal{L}/2} \sinh(\mathcal{L}/2) \delta^{\alpha\bar{\alpha}} \delta_{\beta\bar{\beta}}, \quad (\text{B.31})$$

where we defined

$$\mathcal{L} = \frac{g^2}{16\pi^2} \log^2(E^2/m_w^2). \quad (\text{B.32})$$

The exponential of eq. (B.30) is slightly more involved. First of all notice that the three tensor structures in the right-hand-side of eq. (B.30) commute so we can exponentiate all of them independently. In particular we get

$$\exp\left(-2\mathcal{L} \delta_{\beta}^{\alpha} \delta_{\bar{\beta}}^{\bar{\alpha}}\right) = e^{-2\mathcal{L}} \delta_{\beta}^{\alpha} \delta_{\bar{\beta}}^{\bar{\alpha}} \quad (\text{B.33})$$

$$\exp\left(-\mathcal{L} \delta_{\bar{\beta}}^{\alpha} \delta_{\beta}^{\bar{\alpha}}\right) = \cosh(\mathcal{L}) \delta_{\bar{\beta}}^{\alpha} \delta_{\beta}^{\bar{\alpha}} - \sinh(\mathcal{L}) \delta_{\beta}^{\alpha} \delta_{\bar{\beta}}^{\bar{\alpha}}, \quad (\text{B.34})$$

$$\exp\left(\mathcal{L} \delta^{\alpha\bar{\alpha}} \delta_{\beta\bar{\beta}}\right) = \delta_{\beta}^{\alpha} \delta_{\bar{\beta}}^{\bar{\alpha}} + \frac{1}{3} \left(e^{3\mathcal{L}} - 1\right) \delta^{\alpha\bar{\alpha}} \delta_{\beta\bar{\beta}}. \quad (\text{B.35})$$

Taking the product of the factors just found, we get

$$\left[\exp\left(-\mathcal{L} K_t\right)\right]_{\beta\bar{\beta}}^{\alpha\bar{\alpha}} = e^{-2\mathcal{L}} \left(\cosh(\mathcal{L}) \delta_{\bar{\beta}}^{\alpha} \delta_{\beta}^{\bar{\alpha}} - \sinh(\mathcal{L}) \delta_{\beta}^{\alpha} \delta_{\bar{\beta}}^{\bar{\alpha}}\right) + \frac{2}{3} e^{-\frac{3}{2}\mathcal{L}} \sinh(3\mathcal{L}/2) \delta^{\alpha\bar{\alpha}} \delta_{\beta\bar{\beta}}. \quad (\text{B.36})$$

## B.3 3<sup>rd</sup> family operators

The sensitivity to the 3<sup>rd</sup> family operators in Table 2.2 are summarized in this section. In Figure B.1 we report the two-dimensional contours in the  $(C_{tD}, C_{qD}^{(3)})$  and  $(C_{qD}^{(1)}, C_{qD}^{(3)})$  planes, with the third operator set to zero. We notice that the “with radiation” cross-section measurements (see the main text) is mostly effective to probe  $C_{qD}^{(3)}$  producing a significant sensitivity improvement on the combined bound in this direction. The effect is milder in the orthogonal directions. The likelihood is dominated by the linear term in the new physics parameters so all our result can be expressed in terms of the single operator reaches (at 95% CL) of and the correlations matrices in Table B.2. In the table we report

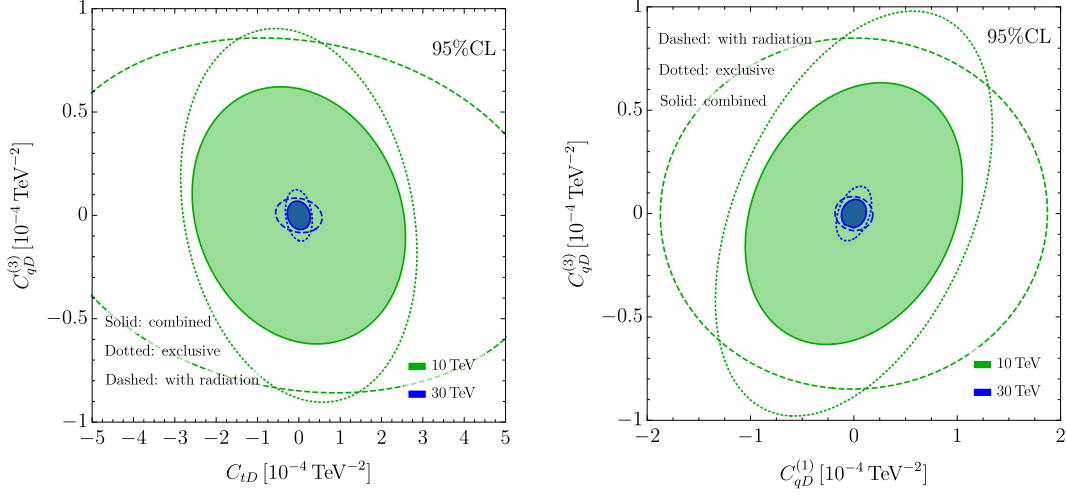


Figure B.1 – 95% CL contours in the  $(C_{tD}, C_{qD}^{(3)})$  (left) and  $(C_{qD}^{(1)}, C_{qD}^{(3)})$  (right) planes at the 10 and 30 TeV muon colliders.

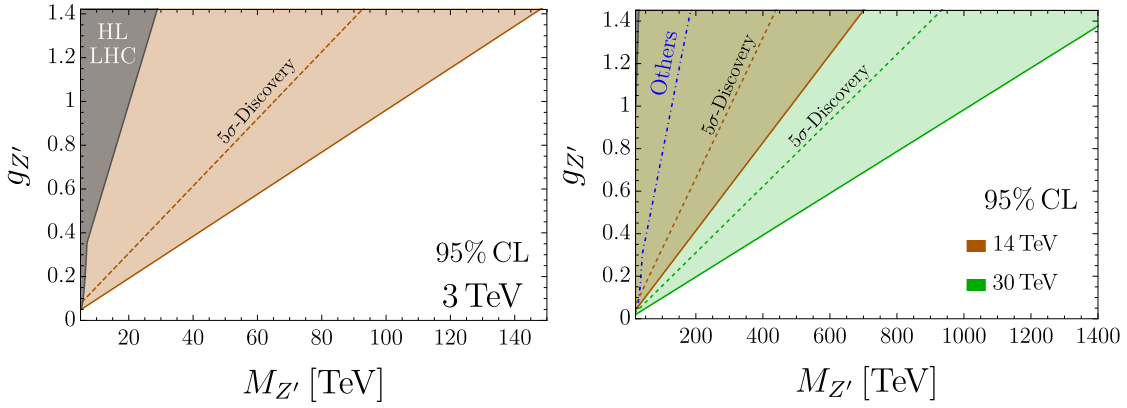


Figure B.2 – The same as the right panel of Figure 2.10 for various collider energies.

the sensitivity of exclusive cross-section measurements alone, and the combination of all the measurements.

## B.4 Summary plots

In this appendix we collect additional results skipped in the main text. In particular in Figure B.2 we report the sensitivity projections for the  $Y$ -universal  $Z'$  model, in the  $(g_{Z'}, M_{Z'})$  plane for the different collider energies. In Figure B.3 we collect the sensitivity projections for the composite Higgs model in the  $(m_*, g_*)$  plane for  $E_{\text{cm}} = 3, 14, 30$  TeV. Projections including composite top measurements can be found in Figure B.5. Finally, Figure B.4 shows the dependence of the bound on the value of the  $c_{tt}$  coefficients, as explained in the main text.

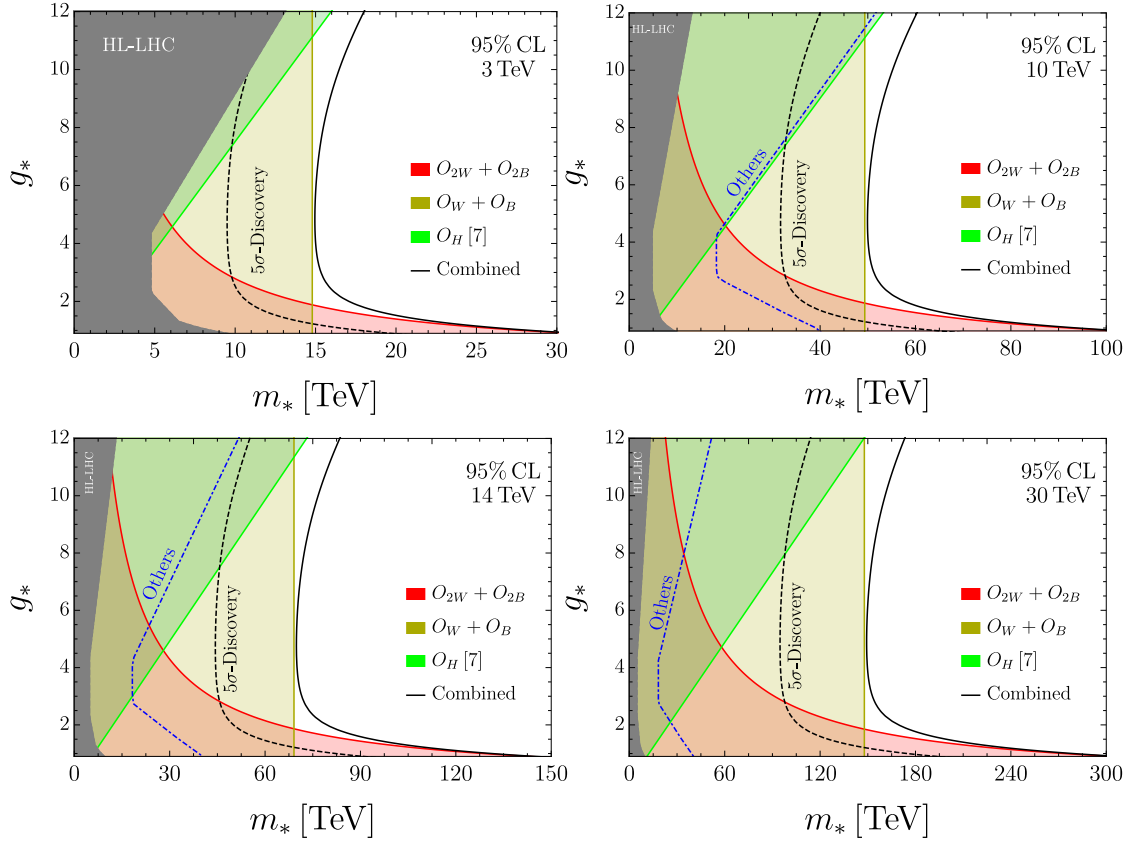


Figure B.3 – The same as the left panel of Figure 2.10 for various collider energies.

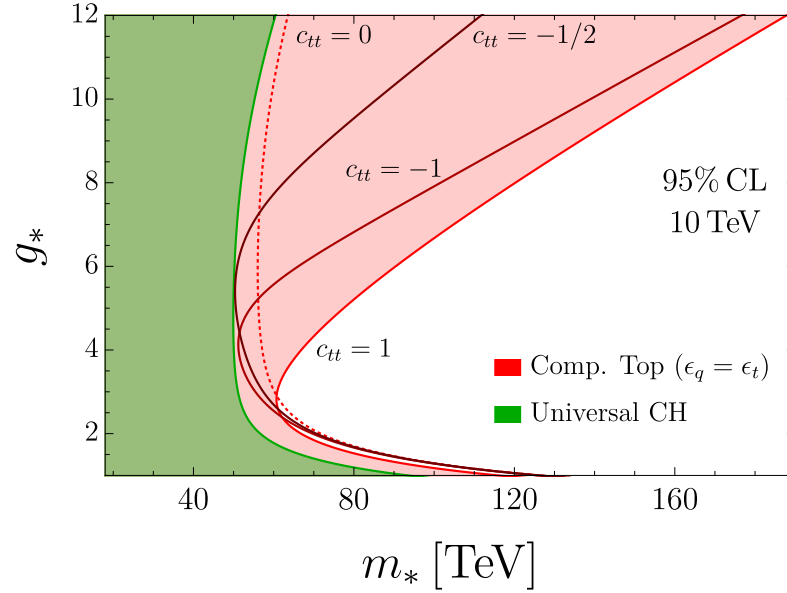


Figure B.4 – The same as the right panel of Figure 2.11 for different values of  $c_{tt}$  to show the model dependence of the result.

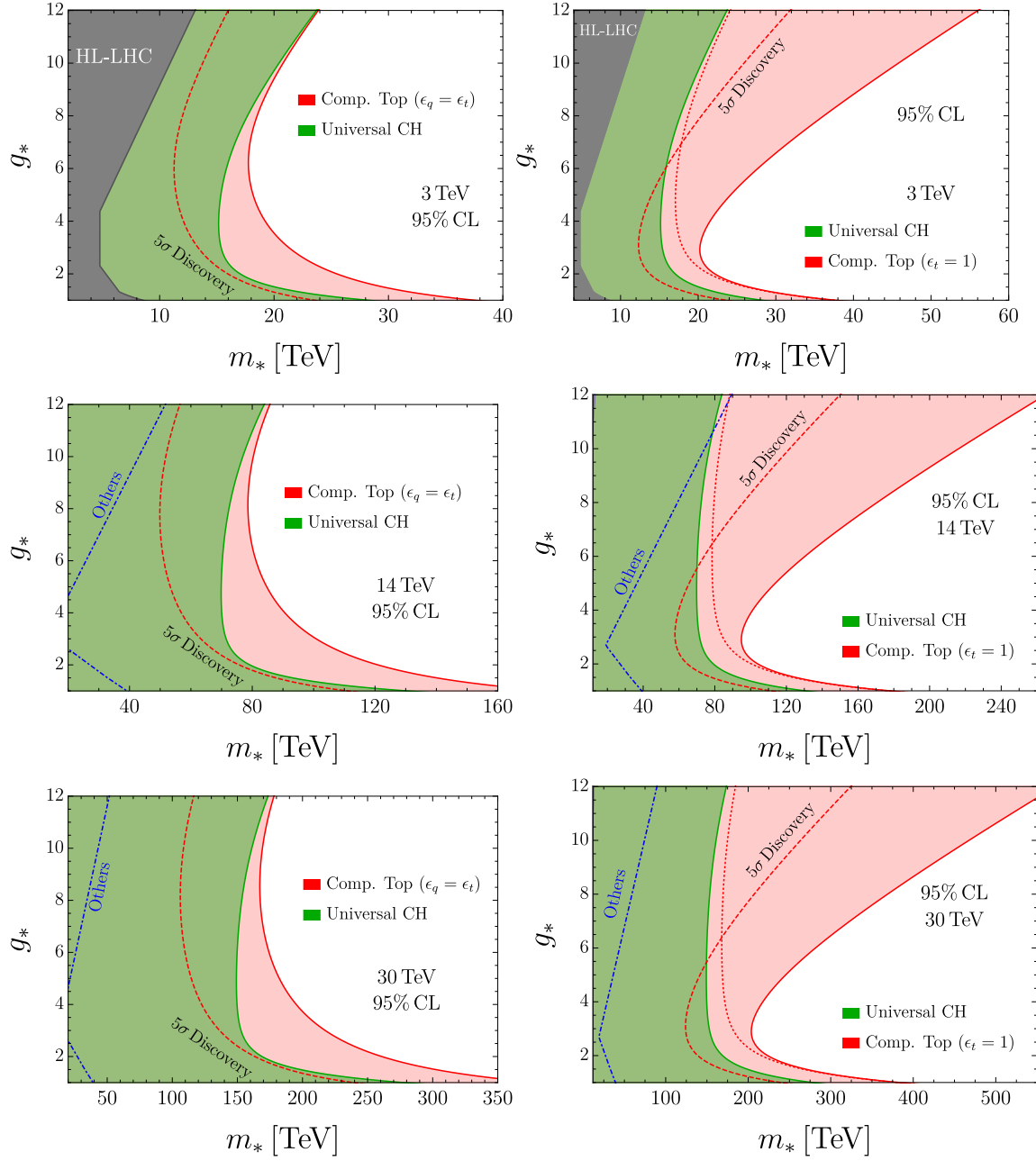
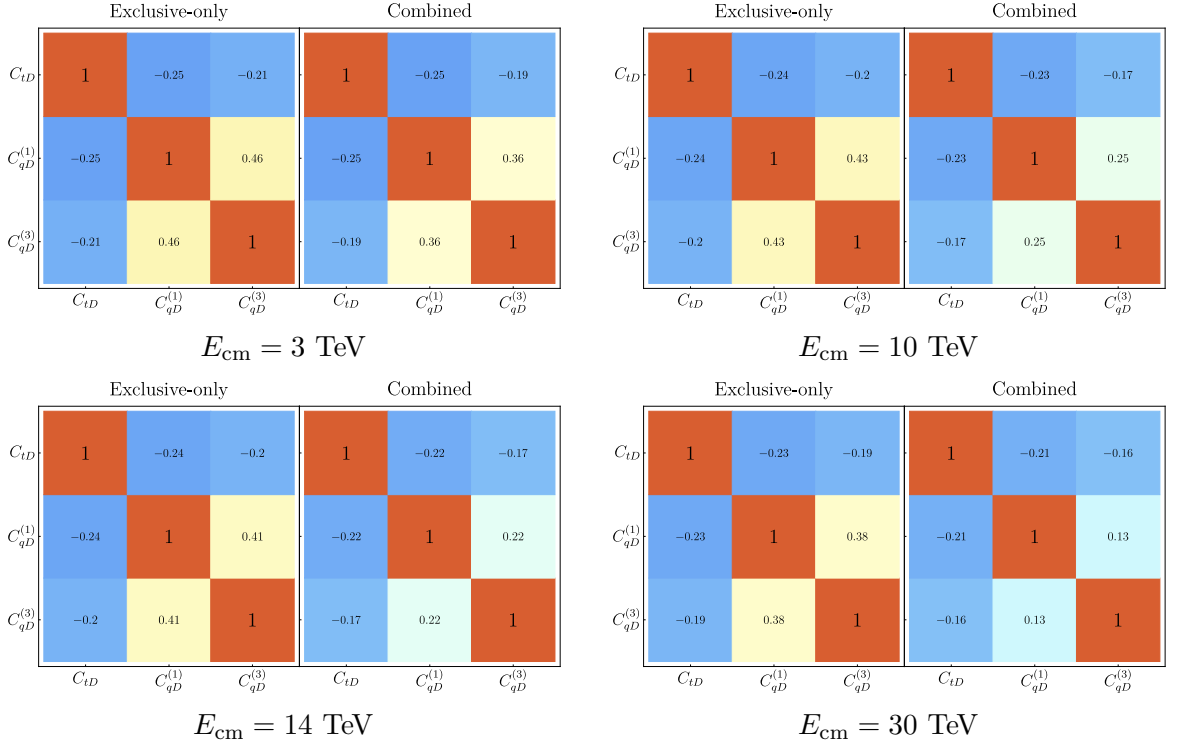


Figure B.5 – The same as Figure 2.11 for various collider energies. The blue line on the equally-composite (left panels) projections are taken from [206], while on the right-handed composite top scenario are taken from [210].

## B.4. Summary plots



	Exclusive-only [95% CL]			Combined [95% CL]		
	$C_{tD}$	$C_{qD}^{(1)}$	$C_{qD}^{(3)}$	$C_{tD}$	$C_{qD}^{(1)}$	$C_{qD}^{(3)}$
3 TeV	$[-24.4, 24.4]$	$[-9.47, 9.47]$	$[-6.68, 6.68]$	$[-23.1, 23.1]$	$[-8.59, 8.59]$	$[-5.45, 5.45]$
10 TeV	$[-2.24, 2.24]$	$[-0.97, 0.97]$	$[-0.71, 0.71]$	$[-2.04, 2.04]$	$[-0.81, 0.81]$	$[-0.49, 0.49]$
14 TeV	$[-1.15, 1.15]$	$[-0.52, 0.52]$	$[-0.38, 0.38]$	$[-1.03, 1.03]$	$[-0.42, 0.42]$	$[-0.25, 0.25]$
30 TeV	$[-0.26, 0.26]$	$[-0.13, 0.13]$	$[-0.10, 0.10]$	$[-0.22, 0.22]$	$[-0.10, 0.10]$	$[-0.05, 0.05]$

Table B.2 – Single-operator 95% CL reach and correlation matrices for the Wilson coefficient  $C_{qD}^{(3)}$ ,  $C_{qD}^{(1)}$  and  $C_{qD}^{(3)}$  of the operators of Table 2.2 at different collider energies. All results include exclusive cross-sections or combined measurements. The Wilson coefficient are expressed in  $10^{-4} \text{ TeV}^{-2}$ . Since the likelihood is dominated by the linear terms in the new physics parameters, the single parameter reach and the correlation characterize our results completely.



# C Appendices for Chapter 3

## C.1 Additional details on the models

In this appendix we go into more details in the construction of the three models presented in section 3.3. In particular for each model we report the quantum number of the spurions, the matrices that diagonalize the Yukawas and the tree-level flavor structures used to built the Wilson coefficients in sec. 3.4. The diagonalizing matrices are computed in the  $y_u \ll y_c \ll y_t$  and  $y_d \ll y_s \ll y_b$  limit and for each entry of the matrix we only report the leading term of this expansion. The tree-level flavor structures are the coefficients in the mass basis of all the possible fermion bilinears that can appear in the dim-6 effective operators as fixed by spurion analysis. Explicitly if an operator contains the bilinear  $\dots \bar{f}_\chi^i(\dots) g_\lambda^j \dots$  of quarks  $f, g = u, d$  with chirality  $\chi$  and  $\lambda$  and flavor  $i$  and  $j$ , by flavor symmetry it will must appear with a coefficient

$$[S^{f_\chi g_\lambda}]_{ij}.$$

By tree-level we mean that in building  $[S^{f_\chi g_\lambda}]_{ij}$  we only have two spurion insertions with the composite index contracted. In our conventions we take this structures to be normalized in such a way that they have the units of measure of a single coupling.

### C.1.1 $U(2) \times U(3)_{\text{RC}}$

This model is characterized by three diagonal right-handed mixings  $\varepsilon_u, \varepsilon_d$  and  $\varepsilon_t$ , and three left-handed off-diagonal mixings  $\lambda_{qu}, \lambda_{qd}$  and  $\lambda_{qt}$ . The mixing Lagrangian is reported in (3.46) These parameters break the flavor group that for this model is assumed to be

$$\mathcal{F} = U(3)_q \times U(3)_u \times U(3)_d \times U(2)_U \times U(3)_D \times U(1)_T.$$

The form that we assume for the  $\lambda$  mixing is reported in the main text in eq. (3.48), where we assume the numbers  $a$  and  $b$  to be  $O(1)$  complex numbers with arbitrary phases.

## Appendix C. Appendices for Chapter 3

The spurion non-abelian quantum numbers for these mixing parameters, with respect to the full flavor group are

	$U(3)_q$	$U(3)_u$	$U(3)_d$	$U(2)_U$	$U(3)_D$	$U(1)_T$
$\lambda_{q_u}$	3	1	1	2	1	0
$\lambda_{q_d}$	3	1	1	1	$\bar{3}$	0
$\lambda_{q_t}$	3	1	1	1	1	-1
$\varepsilon_u \delta_{Ai}$	1	$\bar{3}$	1	2	1	0
$\varepsilon_d \delta_{ai}$	1	1	$\bar{3}$	1	3	0
$\varepsilon_t \delta_{3i}$	1	$\bar{3}$	1	1	1	1

In this model, the Yukawa matrices are given by (3.47). The only non-trivial matrix that has to be diagonalized is  $Y_u$ . For  $Y_d$  the diagonalization matrix  $\tilde{U}_d$  can be rewritten in terms of the CKM matrix as in eq.(3.49). We define the  $U_u$  and  $V_u$  matrices by

$$Y_u = U_u \bar{Y}_u V_u^\dagger, \quad (\text{C.1})$$

where the bar indicates the diagonal and real matrix. The explicit form of  $U_u$  and  $V_u$  in the limit  $y_u \ll y_c \ll y_t$  is

$$U_u = \begin{pmatrix} 1 & -a^* b \frac{y_u y_c}{y_t^2} & a^* \frac{y_u y_c}{y_t^2} \\ ab^* \frac{y_u y_c}{y_t^2} & 1 & b^* \frac{y_c^2}{y_t^2} \\ -a \frac{y_u y_c}{y_t^2} & -b \frac{y_c^2}{y_t^2} & 1 \end{pmatrix}, \quad V_u = \begin{pmatrix} 1 & -a^* b \frac{y_c^2}{y_t^2} & a^* \frac{y_c}{y_t} \\ ab^* \frac{y_u^2}{y_t^2} & 1 & b^* \frac{y_c}{y_t} \\ -a \frac{y_c}{y_t} & -b \frac{y_c}{y_t} & 1 \end{pmatrix}. \quad (\text{C.2})$$

Finally we consider the tree-level flavor structures of this model in the mass basis.

$$S^{d_L d_R} = \bar{Y}_d \quad (\text{C.3})$$

$$S^{u_L d_R} = V_{\text{CKM}} S^{d_L d_R} \quad (\text{C.4})$$

$$S^{d_R d_R} = g_* \varepsilon_d^2 \quad (\text{C.5})$$

$$S^{u_L u_R} = \bar{Y}_u + (x-1) U_u^\dagger \tilde{Y}_t V_u \quad (\text{C.6})$$

$$S^{d_L u_R} = V_{\text{CKM}}^\dagger S^{u_L u_R} \quad (\text{C.7})$$

$$S^{u_R d_R} = 0 \quad (\text{C.8})$$

$$S^{u_R u_R} = g_* V_u^\dagger \text{diag}(\varepsilon_u^2, \varepsilon_u^2, x \varepsilon_t^2) V_u \quad (\text{C.9})$$

$$S^{u_L u_L} = \frac{1}{g_* \varepsilon_u^2} \left[ (\bar{Y}_u)^2 + \left( \frac{\varepsilon_u^2}{\varepsilon_t^2} x_1 - 1 \right) U_u^\dagger (\tilde{Y}_t)^2 U_u \right] + \frac{x_2}{g_* \varepsilon_d^2} V_{\text{CKM}} (\bar{Y}_d)^2 V_{\text{CKM}}^\dagger \quad (\text{C.10})$$

$$S^{u_L d_L} = S^{u_L u_L} V_{\text{CKM}} \quad (\text{C.11})$$

$$S^{d_L d_L} = V_{\text{CKM}}^\dagger S^{u_L u_L} V_{\text{CKM}} \quad (\text{C.12})$$



where we have defined the  $\tilde{Y}_t$  matrix as

$$\tilde{Y}_t = \begin{pmatrix} 0 & 0 & 0 \\ 0 & 0 & 0 \\ 0 & 0 & y_t \end{pmatrix}, \quad (\text{C.13})$$

and the  $x$  parameters are  $O(1)$  numbers that characterize the misalignment of these structure with respect to the Yukawas.

### C.1.2 $U(2)_{\text{RC}}^2$

This model is characterized by four diagonal right-handed mixings  $\varepsilon_u$ ,  $\varepsilon_d$ ,  $\varepsilon_t$  and  $\varepsilon_b$ , and four left-handed off-diagonal mixings  $\lambda_u$ ,  $\lambda_{qd}$ ,  $\lambda_{qt}$  and  $\lambda_{qb}$ . The mixing Lagrangian is written in (3.61) These parameters break the flavor group that for this model is assumed to be

$$\mathcal{F} = U(3)_q \times U(3)_u \times U(3)_d \times U(2)_U \times U(2)_D \times U(1)_T \times U(1)_B.$$

The form that we assume for the  $\lambda$  mixing is reported in the main text in eq. (3.63), where we assume the numbers  $a$ ,  $b$ ,  $a'$  and  $b'$  to be  $O(1)$  complex numbers with arbitrary phases. The spurion non-abelian quantum numbers for these mixing parameters, with respect to the full flavor group are

	$U(3)_q$	$U(3)_u$	$U(3)_d$	$U(2)_U$	$U(2)_D$	$U(1)_T$	$U(1)_B$
$\lambda_{qu}$	3	1	1	2	1	0	0
$\lambda_{qd}$	3	1	1	1	$\bar{3}$	0	0
$\lambda_{qt}$	3	1	1	1	1	-1	0
$\lambda_{qb}$	3	1	1	1	1	0	-1
$\varepsilon_u \delta_{Ai}$	1	$\bar{3}$	1	2	1	0	0
$\varepsilon_d \delta_{Bi}$	1	1	$\bar{3}$	1	2	0	0
$\varepsilon_t \delta_{3i}$	1	$\bar{3}$	1	1	1	1	0
$\varepsilon_b \delta_{3i}$	1	1	$\bar{3}$	1	1	0	1

In this model, the Yukawa matrices are given by (3.62). We define the diagonalizing matrices by

$$Y_u = U_u \bar{Y}_u V_u^\dagger, \quad \tilde{Y}_d^\dagger Y_d = U_d \bar{Y}_d V_d^\dagger, \quad (\text{C.14})$$

## Appendix C. Appendices for Chapter 3

where the bar indicates the diagonal and real matrices. The explicit form these matrices in the limit  $y_u \ll y_c \ll y_t$  and  $y_d \ll y_s \ll y_b$  is

$$\begin{aligned} U_u &= \begin{pmatrix} 1 & -a^* b \frac{y_u y_c}{y_t^2} & a^* \frac{y_u y_c}{y_t^2} \\ ab^* \frac{y_u y_c}{y_t^2} & 1 & b^* \frac{y_c}{y_t} \\ -a \frac{y_u y_c}{y_t^2} & -b \frac{y_c}{y_t} & 1 \end{pmatrix}, \quad V_u = \begin{pmatrix} 1 & -a^* b \frac{y_c^2}{y_t^2} & a^* \frac{y_c}{y_t} \\ ab^* \frac{y_u^2}{y_t^2} & 1 & b^* \frac{y_c}{y_t} \\ -a \frac{y_c}{y_t} & -b \frac{y_c}{y_t} & 1 \end{pmatrix}, \\ U_d &= \begin{pmatrix} 1 & -a'^* b' \frac{y_d y_s}{y_b^2} & a'^* \frac{y_d y_s}{y_b^2} \\ a' b'^* \frac{y_d y_s}{y_b^2} & 1 & b'^* \frac{y_s}{y_b} \\ -a' \frac{y_d y_s}{y_b^2} & -b' \frac{y_s}{y_b} & 1 \end{pmatrix}, \quad V_d = \begin{pmatrix} 1 & -a'^* b' \frac{y_s^2}{y_b^2} & a'^* \frac{y_s}{y_b} \\ a' b'^* \frac{y_d^2}{y_b^2} & 1 & b'^* \frac{y_s}{y_b} \\ -a' \frac{y_s}{y_b} & -b' \frac{y_s}{y_b} & 1 \end{pmatrix}. \end{aligned} \quad (\text{C.15})$$

Finally we consider the tree-level flavor structures of this model in the mass basis.

$$S^{d_L d_R} = \bar{Y}_d + (x - 1) U_d^\dagger \tilde{Y}_b V_d \quad (\text{C.16})$$

$$S^{u_L d_R} = V_{\text{CKM}} S^{d_L d_R} \quad (\text{C.17})$$

$$S^{d_R d_R} = g_* V_d^\dagger \text{diag}(\varepsilon_d^2, \varepsilon_d^2, x \varepsilon_b^2) V_d \quad (\text{C.18})$$

$$S^{u_L u_R} = \bar{Y}_u + (x - 1) U_u^\dagger \tilde{Y}_t V_u \quad (\text{C.19})$$

$$S^{d_L u_R} = V_{\text{CKM}}^\dagger S^{u_L u_R} \quad (\text{C.20})$$

$$S^{u_R d_R} = 0 \quad (\text{C.21})$$

$$S^{u_R u_R} = g_* V_u^\dagger \text{diag}(\varepsilon_u^2, \varepsilon_u^2, x \varepsilon_t^2) V_u \quad (\text{C.22})$$

$$S^{u_L u_L} = \frac{1}{g_* \varepsilon_u^2} \left[ (\bar{Y}_u)^2 + \left( \frac{\varepsilon_u^2}{\varepsilon_t^2} x_1 - 1 \right) U_u^\dagger (\tilde{Y}_t)^2 U_u \right] \quad (\text{C.23})$$

$$+ V_{\text{CKM}} \frac{1}{g_* \varepsilon_d^2} \left[ x_2 (\bar{Y}_d)^2 + \left( \frac{\varepsilon_d^2}{\varepsilon_b^2} x_3 - x_2 \right) U_d^\dagger (\tilde{Y}_b)^2 U_d \right] V_{\text{CKM}}^\dagger \quad (\text{C.24})$$

$$S^{u_L d_L} = S^{u_L u_L} V_{\text{CKM}} \quad (\text{C.25})$$

$$S^{d_L d_L} = V_{\text{CKM}}^\dagger S^{u_L u_L} V_{\text{CKM}} \quad (\text{C.26})$$

where we have defined the  $\tilde{Y}_t$  and  $\tilde{Y}_b$  matrices as

$$\tilde{Y}_{t/b} = \begin{pmatrix} 0 & 0 & 0 \\ 0 & 0 & 0 \\ 0 & 0 & y_{t/b} \end{pmatrix}, \quad (\text{C.27})$$

and the  $x$  parameters are  $O(1)$  numbers.

### C.1.3 $U(2)_{\text{LC}}$

This model is characterized by two diagonal left-handed mixings  $\varepsilon_q$  and  $\varepsilon_{q3}$ , and four right-handed off-diagonal mixings  $\lambda_u$ ,  $\lambda_d$ ,  $\lambda_t$  and  $\lambda_b$ . The mixing Lagrangian is written

### C.1. Additional details on the models

in (3.74) These parameters break the flavor group that for this model is assumed to be

$$\mathcal{F} = U(3)_q \times U(3)_u \times U(3)_d \times U(2)_{U+D} \times U(1)_{T+B}$$

The form that we assume for the  $\lambda$  mixing is reported in the main text in eq. (3.76), where we assume the numbers  $a$ ,  $b$  and  $b'$  to be  $O(1)$  complex numbers with arbitrary phases, while  $a'$  is  $O(0.1)$  with an arbitrary phase in order to reproduce the CKM. The spurion non-abelian quantum numbers for these mixing parameters, with respect to the full flavor group are

	$U(3)_q$	$U(3)_u$	$U(3)_d$	$U(2)_{U+D}$	$U(1)_{T+B}$
$\lambda_u$	1	$\bar{3}$	1	2	0
$\lambda_d$	1	1	$\bar{3}$	2	-1
$\lambda_t$	1	$\bar{3}$	1	1	-1
$\lambda_b$	1	1	$\bar{3}$	1	0
$\varepsilon_q \delta_{iA}$	3	1	1	$\bar{2}$	0
$\varepsilon_{q3} \delta_{i3}$	3	1	1	1	1

In this model, the Yukawa matrices are given by (3.75). We define the diagonalizing matrices by

$$Y_u = U_u \bar{Y}_u V_u^\dagger, \quad \tilde{U}_d^\dagger Y_d = U_d \bar{Y}_d V_d^\dagger, \quad (\text{C.28})$$

where the bar indicates the diagonal and real matrices. The explicit form these matrices in the limit  $y_u \ll y_c \ll y_t$  and  $y_d \ll y_s \ll y_b$  is

$$\begin{aligned}
 U_u &= \begin{pmatrix} 1 & -ab^* \frac{y_c^2}{y_t^2} & a \frac{y_c}{y_t} \\ a^* b \frac{y_u^2}{y_t^2} & 1 & b \frac{y_c}{y_t} \\ -a^* \frac{y_c}{y_t} & -b^* \frac{y_c}{y_t} & 1 \end{pmatrix}, \quad V_u = \begin{pmatrix} 1 & -ab^* \frac{y_u y_c}{y_t^2} & a \frac{y_u y_c}{y_t^2} \\ a^* b \frac{y_u y_c}{y_t^2} & 1 & b \frac{y_c}{y_t} \\ -a^* \frac{y_u y_c}{y_t^2} & -b^* \frac{y_c^2}{y_t^2} & 1 \end{pmatrix}, \\
 U_d &= \begin{pmatrix} 1 & -a'b'^* \frac{y_s^2}{y_b^2} & a' \frac{y_s}{y_b} \\ a'^* b' \frac{y_d^2}{y_b^2} & 1 & b' \frac{y_s}{y_b} \\ -a'^* \frac{y_s}{y_b} & -b'^* \frac{y_s}{y_b} & 1 \end{pmatrix}, \quad V_d = \begin{pmatrix} 1 & -a'b'^* \frac{y_d y_s}{y_b^2} & a' \frac{y_d y_s}{y_b^2} \\ a'^* b' \frac{y_d y_s}{y_b^2} & 1 & b' \frac{y_s}{y_b} \\ -a'^* \frac{y_d y_s}{y_b^2} & -b'^* \frac{y_s^2}{y_b^2} & 1 \end{pmatrix}.
 \end{aligned} \quad (\text{C.29})$$

## Appendix C. Appendices for Chapter 3

---

Finally we consider the tree-level flavor structures of this model in the mass basis.

$$S^{d_L d_R} = \bar{Y}_d + (x - 1) U_d^\dagger \tilde{Y}_b V_d \quad (\text{C.30})$$

$$S^{u_L d_R} = V_{\text{CKM}} S^{d_L d_R} \quad (\text{C.31})$$

$$S^{d_R d_R} = \frac{1}{g_* \varepsilon_q^2} \left[ (\bar{Y}_d)^2 + \left( \frac{\varepsilon_q^2}{\varepsilon_{q3}^2} x - 1 \right) V_d^\dagger (\tilde{Y}_b)^2 V_d \right] \quad (\text{C.32})$$

$$S^{u_L u_R} = \bar{Y}_u + (x - 1) U_u^\dagger \tilde{Y}_t V_u \quad (\text{C.33})$$

$$S^{d_L u_R} = V_{\text{CKM}}^\dagger S^{u_L u_R} \quad (\text{C.34})$$

$$S^{u_R d_R} = \frac{1}{g_* \varepsilon_q^2} \left[ \bar{Y}_u V_{\text{CKM}} \bar{Y}_d + \left( \frac{\varepsilon_q^2}{\varepsilon_{q3}^2} x - 1 \right) V_u^\dagger \tilde{Y}_t \tilde{Y}_b V_d \right] \quad (\text{C.35})$$

$$S^{u_R u_R} = \frac{1}{g_* \varepsilon_q^2} \left[ (\bar{Y}_u)^2 + \left( \frac{\varepsilon_q^2}{\varepsilon_{q3}^2} x - 1 \right) V_u^\dagger (\tilde{Y}_t)^2 V_u \right] \quad (\text{C.36})$$

$$S^{u_L u_L} = g_* U_u^\dagger \text{diag}(\varepsilon_q^2, \varepsilon_q^2, x \varepsilon_{q3}^2) U_u \quad (\text{C.37})$$

$$S^{u_L d_L} = S^{u_L u_L} V_{\text{CKM}} \quad (\text{C.38})$$

$$S^{d_L d_L} = V_{\text{CKM}}^\dagger S^{u_L u_L} V_{\text{CKM}} \quad (\text{C.39})$$

where we have defined the  $\tilde{Y}_t$  and  $\tilde{Y}_b$  matrices as

$$\tilde{Y}_{t/b} = \begin{pmatrix} 0 & 0 & 0 \\ 0 & 0 & 0 \\ 0 & 0 & y_{t/b} \end{pmatrix}, \quad (\text{C.40})$$

and the  $x$  parameters are  $O(1)$  numbers.

# Bibliography

- [1] L. Ricci, R. Torre, and A. Wulzer, *On the  $W\&Y$  interpretation of high-energy Drell-Yan measurements*, *JHEP* **02** (2021) 144 [[2008.12978](#)].
- [2] G. Panico, L. Ricci and A. Wulzer, *High-energy EFT probes with fully differential Drell-Yan measurements*, *JHEP* **07** (2021) 086 [[2103.10532](#)].
- [3] S. Chen, A. Glioti, R. Rattazzi, L. Ricci and A. Wulzer, *Learning from radiation at a very high energy lepton collider*, *JHEP* **05** (2022) 180 [[2202.10509](#)].
- [4] ATLAS collaboration, G. Aad et al., *Observation of a new particle in the search for the Standard Model Higgs boson with the ATLAS detector at the LHC*, *Phys. Lett. B* **716** (2012) 1 [[1207.7214](#)].
- [5] CMS collaboration, S. Chatrchyan et al., *Observation of a New Boson at a Mass of 125 GeV with the CMS Experiment at the LHC*, *Phys. Lett. B* **716** (2012) 30 [[1207.7235](#)].
- [6] H. Murayama, *Supersymmetry phenomenology*, in *ICTP Summer School in Particle Physics*, pp. 296–335, 2, 2000, [hep-ph/0002232](#).
- [7] S. Weinberg, *The Quantum Theory of Fields*, vol. 2. Cambridge University Press, 1996, [10.1017/CBO9781139644174](#).
- [8] S. Weinberg, *Baryon and Lepton Nonconserving Processes*, *Phys. Rev. Lett.* **43** (1979) 1566.
- [9] B. Grzadkowski, M. Iskrzynski, M. Misiak and J. Rosiek, *Dimension-six terms in the standard model lagrangian*, *JHEP* **10** (2010) 85 [[1008.4884](#)].
- [10] G. F. Giudice, C. Grojean, A. Pomarol and R. Rattazzi, *The Strongly-Interacting Light Higgs*, *JHEP* **06** (2007) 045 [[hep-ph/0703164](#)].
- [11] M. Farina, G. Panico, D. Pappadopulo, J. T. Ruderman, R. Torre and A. Wulzer, *Energy helps accuracy: electroweak precision tests at hadron colliders*, *Phys. Lett. B* **772** (2017) 210 [[1609.08157](#)].

- [12] K. Hagiwara, R. Peccei, D. Zeppenfeld and K. Hikasa, *Probing the weak boson sector in  $e^+ e^- \rightarrow w^+ w^-$* , *Nucl.Phys.B* **282** (1987) 253.
- [13] K. Hagiwara, J. Woodside and D. Zeppenfeld, *Measuring the  $wwz$  coupling at the tevatron*, *Phys.Rev.D* **41** (1990) 2113.
- [14] CMS collaboration, V. Khachatryan, A. M. Sirunyan, A. Tumasyan, W. Adam, E. Aşilar, T. Bergauer et al., *Measurement of the  $W^+W^-$  cross section in  $pp$  collisions at  $\sqrt{s} = 8$  tev and limits on anomalous gauge couplings*, *Eur.Phys.J.C* **76** (2016) 401 [[1507.03268](#)].
- [15] ATLAS collaboration, G. Aad, B. Abbott, J. Abdallah, O. Abdinov, B. Abeloos, R. Aben et al., *Measurements of  $w^\pm z$  production cross sections in  $pp$  collisions at  $\sqrt{s} = 8$  tev with the atlas detector and limits on anomalous gauge boson self-couplings*, *Phys.Rev.D* **93** (2016) [[1603.02151](#)].
- [16] A. Butter, O. J. P. Éboli, J. Gonzalez-Fraile, M. Gonzalez-Garcia, T. Plehn and M. Rauch, *The gauge-higgs legacy of the lhc run i*, *JHEP* **07** (2016) 152 [[1604.03105](#)].
- [17] Z. Zhang, *Time to go beyond triple-gauge-boson-coupling interpretation of  $w$  pair production*, *Phys.Rev.Lett.* **118** (2017) [[1610.01618](#)].
- [18] D. R. Green, P. Meade and M.-A. Pleier, *Multiboson interactions at the lhc*, *Rev.Mod.Phys.* **89** (2017) [[1610.07572](#)].
- [19] A. Biekötter, A. Knochel, M. Krämer, D. Liu and F. Riva, *Vices and virtues of higgs effective field theories at large energy*, *Phys.Rev.D* **91** (2015) [[1406.7320](#)].
- [20] A. Falkowski, M. Gonzalez-Alonso, A. Greljo and D. Marzocca, *Global constraints on anomalous triple gauge couplings in effective field theory approach*, *Phys.Rev.Lett.* **116** (2016) [[1508.00581](#)].
- [21] J. Baglio, S. Dawson and I. M. Lewis, *An nlo qcd effective field theory analysis of  $w^+w^-$  production at the lhc including fermionic operators*, *Phys.Rev.D* **96** (2017) [[1708.03332](#)].
- [22] R. Franceschini, G. Panico, A. Pomarol, F. Riva and A. Wulzer, *Electroweak Precision Tests in High-Energy Diboson Processes*, *JHEP* **02** (2018) 111 [[1712.01310](#)].
- [23] G. Panico, F. Riva and A. Wulzer, *Diboson interference resurrection*, *Phys.Lett.B* **776** (2018) 473 [[1708.07823](#)].
- [24] C. Grojean, M. Montull and M. Riemann, *Diboson at the lhc vs lep*, *JHEP* **03** (2019) 20 [[1810.05149](#)].

- 
- [25] S. Banerjee, C. Englert, R. S. Gupta and M. Spannowsky, *Probing electroweak precision physics via boosted higgs-strahlung at the lhc*, *Phys.Rev.D* **98** (2018) [1807.01796].
- [26] D. Liu and L.-T. Wang, *Prospects for precision measurement of diboson processes in the semileptonic decay channel in future LHC runs*, *Phys. Rev. D* **99** (2019) 055001 [1804.08688].
- [27] B. Henning, D. Lombardo, M. Riembau and F. Riva, *Measuring higgs couplings without higgs bosons*, *Phys.Rev.Lett.* **123** (2019) [1812.09299].
- [28] O. Domenech, A. Pomarol and J. Serra, *Probing the SM with Dijets at the LHC*, *Phys. Rev. D* **85** (2012) 074030 [1201.6510].
- [29] S. Alioli, M. Farina, D. Pappadopulo and J. T. Ruderman, *Precision Probes of QCD at High Energies*, *JHEP* **07** (2017) 097 [1706.03068].
- [30] S. Alioli, M. Farina, D. Pappadopulo and J. T. Ruderman, *Catching a new force by the tail*, *Phys.Rev.Lett.* **120** (2018) [1712.02347].
- [31] M. Farina, C. Mondino, D. Pappadopulo and J. T. Ruderman, *New physics from high energy tops*, *JHEP* **01** (2019) 231 [1811.04084].
- [32] R. K. Ellis, B. Heinemann, J. de Blas, M. Cepeda, C. Grojean, F. Maltoni et al., *Physics briefing book*, 1910.11775.
- [33] J. Fuentes-Martin, A. Greljo, J. Martin Camalich and J. D. Ruiz-Alvarez, *Charm physics confronts high- $p_t$  lepton tails*, 2003.12421.
- [34] J. D. Wells and Z. Zhang, *Effective theories of universal theories*, *JHEP* **01** (2016) 123 [1510.08462].
- [35] R. Barbieri, A. Pomarol, R. Rattazzi and A. Strumia, *Electroweak symmetry breaking after LEP-1 and LEP-2*, *Nucl. Phys. B* **703** (2004) 127 [hep-ph/0405040].
- [36] C. Englert, G. F. Giudice, A. Greljo and M. McCullough, *The  $\hat{H}$ -Parameter: An Oblique Higgs View*, *JHEP* **09** (2019) 041 [1903.07725].
- [37] CLICDP collaboration, H. Abramowicz et al., *Top-Quark Physics at the CLIC Electron-Positron Linear Collider*, *JHEP* **11** (2019) 003 [1807.02441].
- [38] J. A. Aguilar-Saavedra, C. Degrande, G. Durieux, F. Maltoni, E. Vryonidou, C. Zhang et al., *Interpreting top-quark lhc measurements in the standard-model effective field theory*, 1802.07237.

- [39] ATLAS collaboration, G. Aad, B. Abbott, J. Abdallah, O. Abdinov, B. Abeloos, R. Aben et al., *Measurement of the double-differential high-mass drell-yan cross section in pp collisions at  $\sqrt{s} = 8$  tev with the atlas detector*, *JHEP* **08** (2016) 9 [[1606.01736](#)].
- [40] CMS collaboration, *Measurements of the differential and double-differential drell-yan cross sections in proton-proton collisions at 8 tev*, .
- [41] CMS collaboration, *Measurement of the differential drell-yan cross section in proton-proton collisions at 13 tev*, tech. rep.
- [42] CMS collaboration, A. Tumasyan et al., *Search for new physics in the lepton plus missing transverse momentum final state in proton-proton collisions at  $\sqrt{s} = 13$  TeV*, [2202.06075](#).
- [43] ATLAS collaboration, M. Aaboud et al., *Measurement of the Drell-Yan triple-differential cross section in pp collisions at  $\sqrt{s} = 8$  TeV*, *JHEP* **12** (2017) 059 [[1710.05167](#)].
- [44] G. Altarelli, R. K. Ellis and G. Martinelli, *Large Perturbative Corrections to the Drell-Yan Process in QCD*, *Nucl. Phys. B* **157** (1979) 461.
- [45] J. Kubar-Andre and F. E. Paige, *Gluon corrections to the drell-yan model*, *Phys. Rev. D* **19** (1979) 221.
- [46] U. Baur, O. Brein, W. Hollik, C. Schappacher and D. Wackerroth, *Electroweak radiative corrections to neutral-current drell-yan processes at hadron colliders*, *Phys. Rev. D* **65** (2002) 033007.
- [47] S. Dittmaier and M. Krämer, *Electroweak radiative corrections to W boson production at hadron colliders*, *Phys. Rev. D* **65** (2002) 073007 [[hep-ph/0109062](#)].
- [48] R. Hamberg, W. L. van Neerven and T. Matsuura, *A complete calculation of the order  $\alpha - s^2$  correction to the Drell-Yan K factor*, *Nucl. Phys. B* **359** (1991) 343.
- [49] C. Anastasiou, L. Dixon, K. Melnikov and F. Petriello, *Dilepton rapidity distribution in the drell-yan process at next-to-next-to-leading order in qcd*, *Phys. Rev. Lett.* **91** (2003) 182002.
- [50] C. Anastasiou, L. J. Dixon, K. Melnikov and F. Petriello, *High precision QCD at hadron colliders: Electroweak gauge boson rapidity distributions at NNLO*, *Phys. Rev. D* **69** (2004) 094008 [[hep-ph/0312266](#)].
- [51] K. Melnikov and F. Petriello, *Electroweak gauge boson production at hadron colliders through  $\mathcal{O}(\alpha_s^2)$* , *Phys. Rev. D* **74** (2006) 114017.
- [52] C. Duhr, F. Dulat and B. Mistlberger, *Drell-Yan Cross Section to Third Order in the Strong Coupling Constant*, *Phys. Rev. Lett.* **125** (2020) 172001 [[2001.07717](#)].



- [53] C. Duhr, F. Dulat and B. Mistlberger, *Charged current Drell-Yan production at  $N^3LO$* , *JHEP* **11** (2020) 143 [[2007.13313](#)].
- [54] T. Becher and T. Neumann, *Fiducial  $q_T$  resummation of color-singlet processes at  $N^3LL+NNLO$* , *JHEP* **03** (2021) 199 [[2009.11437](#)].
- [55] E. Re, L. Rottoli and P. Torrielli, *Fiducial Higgs and Drell-Yan distributions at  $N^3LL'+NNLO$  with RadISH*, [2104.07509](#).
- [56] W. B. Kilgore and C. Sturm, *Two-Loop Virtual Corrections to Drell-Yan Production at order  $\alpha_s\alpha^3$* , *Phys. Rev. D* **85** (2012) 033005 [[1107.4798](#)].
- [57] F. Buccioni, F. Caola, M. Delto, M. Jaquier, K. Melnikov and R. Röntsch, *Mixed QCD-electroweak corrections to on-shell Z production at the LHC*, *Phys. Lett. B* **811** (2020) 135969 [[2005.10221](#)].
- [58] M. Delto, M. Jaquier, K. Melnikov and R. Röntsch, *Mixed QCD $\otimes$ QED corrections to on-shell Z boson production at the LHC*, *JHEP* **01** (2020) 043 [[1909.08428](#)].
- [59] R. Boughezal, Y. Li and F. Petriello, *Disentangling radiative corrections using the high-mass Drell-Yan process at the LHC*, *Phys. Rev. D* **89** (2014) 034030 [[1312.3972](#)].
- [60] L. Buonocore, M. Grazzini and F. Tramontano, *The  $q_T$  subtraction method: electroweak corrections and power suppressed contributions*, *Eur. Phys. J. C* **80** (2020) 254 [[1911.10166](#)].
- [61] S. Dittmaier, T. Schmidt and J. Schwarz, *Mixed NNLO QCD electroweak corrections of  $\mathcal{O}(N_f\alpha_s\alpha)$  to single-W/Z production at the LHC*, *JHEP* **12** (2020) 201 [[2009.02229](#)].
- [62] R. Bonciani, F. Buccioni, N. Rana and A. Vicini, *Next-to-Next-to-Leading Order Mixed QCD-Electroweak Corrections to on-Shell Z Production*, *Phys. Rev. Lett.* **125** (2020) 232004 [[2007.06518](#)].
- [63] Y. Li and F. Petriello, *Combining qcd and electroweak corrections to dilepton production in fewz*, *Phys.Rev.D* **86** (2012) [[1208.5967](#)].
- [64] S. Alioli, W. Dekens, M. Girard and E. Mereghetti, *Nlo qcd corrections to sm-eft dilepton and electroweak higgs boson production, matched to parton shower in powheg*, *JHEP* **08** (2018) 205 [[1804.07407](#)].
- [65] P. Artoisenet, V. Lemaitre, F. Maltoni and O. Mattelaer, *Automation of the matrix element reweighting method*, *JHEP* **12** (2010) 68 [[1007.3300](#)].
- [66] J. Alwall, R. Frederix, S. Frixione, V. Hirschi, F. Maltoni, O. Mattelaer et al., *The automated computation of tree-level and next-to-leading order differential cross sections, and their matching to parton shower simulations*, *JHEP* **07** (2014) 79 [[1405.0301](#)].

- [67] S. Dawson and P. P. Giardino, *New physics through Drell-Yan standard model EFT measurements at NLO*, *Phys. Rev. D* **104** (2021) 073004 [[2105.05852](#)].
- [68] C. Degrande, G. Durieux, F. Maltoni, K. Mimasu, E. Vryonidou and C. Zhang, *Automated one-loop computations in the SMEFT*, [2008.11743](#).
- [69] S. Alioli, P. Nason, C. Oleari and E. Re, *Nlo vector-boson production matched with shower in powheg*, *JHEP* **07** (2008) 60 [[0805.4802](#)].
- [70] T. Sjöstrand, S. Ask, J. R. Christiansen, R. Corke, N. Desai, P. Ilten et al., *An introduction to pythia 8.2*, *Comput.Phys.Commun.* **191** (2015) 159 [[1410.3012](#)].
- [71] S. Frixione, P. Nason and C. Oleari, *Matching nlo qcd computations with parton shower simulations: the powheg method*, *JHEP* **11** (2007) 70 [[0709.2092](#)].
- [72] S. Catani and M. Seymour, *A general algorithm for calculating jet cross-sections in nlo qcd*, *Nucl.Phys.B, Nucl.Phys.B* **485**, **510** (1997) 291 [[hep-ph/9605323](#)].
- [73] S. Frixione, Z. Kunszt and A. Signer, *Three jet cross-sections to next-to-leading order*, *Nucl. Phys. B* **467** (1996) 399 [[hep-ph/9512328](#)].
- [74] S. Frixione, *A General approach to jet cross-sections in QCD*, *Nucl. Phys. B* **507** (1997) 295 [[hep-ph/9706545](#)].
- [75] L. Barze, G. Montagna, P. Nason, O. Nicrosini and F. Piccinini, *Implementation of electroweak corrections in the powheg box: single w production*, *JHEP* **04** (2012) 37 [[1202.0465](#)].
- [76] L. Barze, G. Montagna, P. Nason, O. Nicrosini, F. Piccinini and A. Vicini, *Neutral current drell-yan with combined qcd and electroweak corrections in the powheg box*, *Eur.Phys.J.C* **73** (2013) 2474 [[1302.4606](#)].
- [77] A. Denner, B. Jantzen and S. Pozzorini, *Two-loop electroweak next-to-leading logarithmic corrections to massless fermionic processes*, *Nucl.Phys.B* **761** (2007) 1 [[hep-ph/0608326](#)].
- [78] S. Pozzorini, *Electroweak radiative corrections at high-energies*, Master's thesis, 2002.
- [79] J. H. Kuhn, A. Penin and V. A. Smirnov, *Summing up subleading sudakov logarithms*, *Eur.Phys.J.C* **17** (2000) 97 [[hep-ph/9912503](#)].
- [80] J. H. Kuhn, S. Moch, A. Penin and V. A. Smirnov, *Next-to-next-to-leading logarithms in four fermion electroweak processes at high-energy*, *Nucl.Phys.B, Nucl.Phys.B* **616**, **648** (2001) 286 [[hep-ph/0106298](#)].
- [81] B. Jantzen, J. H. Kuhn, A. A. Penin and V. A. Smirnov, *Two-loop electroweak logarithms in four-fermion processes at high energy*, *Nucl.Phys.B, Nucl.Phys.B* **731**, **752** (2005) 188 [[hep-ph/0509157](#)].

- 
- [82] E. Bothmann and D. Napoletano, *Automated evaluation of electroweak sudakov logarithms in sherpa*, [2006.14635](#).
  - [83] A. Celis, J. Fuentes-Martin, A. Vicente and J. Virto, *Dsixtools: The standard model effective field theory toolkit*, *Eur.Phys.J.C* **77** (2017) 405 [[1704.04504](#)].
  - [84] S. Brensing, S. Dittmaier, M. Krämer and A. Muck, *Radiative corrections to  $w^-$  boson hadroproduction: Higher-order electroweak and supersymmetric effects*, *Phys.Rev.D* **77** (2008) [[0710.3309](#)].
  - [85] S. Dittmaier and M. Huber, *Radiative corrections to the neutral-current drell-yan process in the standard model and its minimal supersymmetric extension*, *JHEP* **01** (2010) 60 [[0911.2329](#)].
  - [86] C. Carloni Calame, G. Montagna, O. Nicrosini and A. Vicini, *Precision electroweak calculation of the production of a high transverse-momentum lepton pair at hadron colliders*, *JHEP* **10** (2007) 109 [[0710.1722](#)].
  - [87] U. Baur, *Weak boson emission in hadron collider processes*, *Phys.Rev.D* **75** (2007) [[hep-ph/0611241](#)].
  - [88] A. Buckley, J. Ferrando, S. Lloyd, K. Nordström, B. Page, M. Rüfenacht et al., *Lhapdf6: parton density access in the lhc precision era*, *Eur.Phys.J.C* **75** (2015) 132 [[1412.7420](#)].
  - [89] J. Butterworth, S. Carrazza, A. Cooper-Sarkar, A. De Roeck, J. Feltesse, S. Forte et al., *Pdf4lhc recommendations for lhc run ii*, *J.Phys.G* **43** (2016) [[1510.03865](#)].
  - [90] S. Dulat, T.-J. Hou, J. Gao, M. Guzzi, J. Huston, P. Nadolsky et al., *New parton distribution functions from a global analysis of quantum chromodynamics*, *Phys.Rev.D* **93** (2016) [[1506.07443](#)].
  - [91] L. Harland-Lang, A. Martin, P. Motylinski and R. Thorne, *Parton distributions in the lhc era: Mmht 2014 pdfs*, *Eur.Phys.J.C* **75** (2015) 204 [[1412.3989](#)].
  - [92] S. Carrazza, J. I. Latorre, J. Rojo and G. Watt, *A compression algorithm for the combination of pdf sets*, *Eur.Phys.J.C* **75** (2015) 474 [[1504.06469](#)].
  - [93] S. Alioli, A. Arbuzov, D. Y. Bardin, L. Barze, C. Bernaciak, S. Bondarenko et al., *Precision studies of observables in  $pp \rightarrow w \rightarrow lv_l$  and  $pp \rightarrow \gamma, z \rightarrow l^+l^-$  processes at the lhc*, *Eur.Phys.J.C* **77** (2017) 280 [[1606.02330](#)].
  - [94] G. Cowan, K. Cranmer, E. Gross and O. Vitells, *Asymptotic formulae for likelihood-based tests of new physics*, *Eur.Phys.J.C*, *Eur.Phys.J.C* **71**, **73** (2011) 1554 [[1007.1727](#)].

- [95] D. S. M. Alves, J. Galloway, J. T. Ruderman and J. R. Walsh, *Running Electroweak Couplings as a Probe of New Physics*, *JHEP* **02** (2015) 007 [[1410.6810](#)].
- [96] G. Panico, L. Vecchi and A. Wulzer, *Resonant Diphoton Phenomenology Simplified*, *JHEP* **06** (2016) 184 [[1603.04248](#)].
- [97] D. B. Clark, E. Godat and F. I. Olness, *ManeParse : A Mathematica reader for Parton Distribution Functions*, *Comput. Phys. Commun.* **216** (2017) 126 [[1605.08012](#)].
- [98] E. Salvioni, G. Villadoro and F. Zwirner, *Minimal Z-prime models: Present bounds and early LHC reach*, *JHEP* **11** (2009) 068 [[0909.1320](#)].
- [99] T. Appelquist, B. A. Dobrescu and A. R. Hopper, *Nonexotic Neutral Gauge Bosons*, *Phys. Rev. D* **68** (2003) 035012 [[hep-ph/0212073](#)].
- [100] A. Ferrogli, A. Lorca and J. J. van der Bij, *The  $Z'$  reconsidered*, *Annalen Phys.* **16** (2007) 563 [[hep-ph/0611174](#)].
- [101] L. Basso, A. Belyaev, S. Moretti and C. H. Shepherd-Themistocleous, *Phenomenology of the minimal B-L extension of the Standard model:  $Z'$  and neutrinos*, *Phys. Rev. D* **80** (2009) 055030 [[0812.4313](#)].
- [102] E. Salvioni, A. Strumia, G. Villadoro and F. Zwirner, *Non-universal minimal  $Z'$  models: present bounds and early LHC reach*, *JHEP* **03** (2010) 010 [[0911.1450](#)].
- [103] L. Basso, A. Belyaev, S. Moretti and G. M. Pruna, *Tree Level Unitarity Bounds for the Minimal B-L Model*, *Phys. Rev. D* **81** (2010) 095018 [[1002.1939](#)].
- [104] L. Basso, A. Belyaev, S. Moretti, G. M. Pruna and C. H. Shepherd-Themistocleous,  *$Z'$  discovery potential at the LHC in the minimal  $B - L$  extension of the Standard Model*, *Eur. Phys. J. C* **71** (2011) 1613 [[1002.3586](#)].
- [105] L. Basso, S. Moretti and G. M. Pruna, *A Renormalisation Group Equation Study of the Scalar Sector of the Minimal B-L Extension of the Standard Model*, *Phys. Rev. D* **82** (2010) 055018 [[1004.3039](#)].
- [106] L. Basso, S. Moretti and G. M. Pruna, *Phenomenology of the minimal  $B - L$  extension of the Standard Model: the Higgs sector*, *Phys. Rev. D* **83** (2011) 055014 [[1011.2612](#)].
- [107] L. Basso, S. Moretti and G. M. Pruna, *Theoretical constraints on the couplings of non-exotic minimal  $Z'$  bosons*, *JHEP* **08** (2011) 122 [[1106.4762](#)].
- [108] A. Thamm, R. Torre and A. Wulzer, *Future tests of Higgs compositeness: direct vs indirect*, *JHEP* **07** (2015) 100 [[1502.01701](#)].

- 
- [109] X. Cid Vidal et al., *Report from Working Group 3: Beyond the Standard Model physics at the HL-LHC and HE-LHC*, *CERN Yellow Rep. Monogr.* **7** (2019) 585 [[1812.07831](#)].
- [110] J. P. Delahaye, M. Diemoz, K. Long, B. Mansoulié, N. Pastrone, L. Rivkin et al., *Muon Colliders*, [1901.06150](#).
- [111] “The international muon collider collaboration.” <https://muoncollider.web.cern.ch>.
- [112] C. Aime et al., *Muon Collider Physics Summary*, [2203.07256](#).
- [113] MUON COLLIDER collaboration, J. de Blas et al., *The physics case of a 3 TeV muon collider stage*, [2203.07261](#).
- [114] D. Buttazzo, D. Redigolo, F. Sala and A. Tesi, *Fusing Vectors into Scalars at High Energy Lepton Colliders*, *JHEP* **11** (2018) 144 [[1807.04743](#)].
- [115] R. Franceschini, *High(est) energy lepton colliders*, *Int. J. Mod. Phys. A* **36** (2021) 2142016.
- [116] R. Capdevilla, F. Meloni, R. Simoniello and J. Zurita, *Hunting wino and higgsino dark matter at the muon collider with disappearing tracks*, *JHEP* **06** (2021) 133 [[2102.11292](#)].
- [117] H. Al Ali et al., *The Muon Smasher’s Guide*, [2103.14043](#).
- [118] D. Buttazzo, R. Franceschini and A. Wulzer, *Two Paths Towards Precision at a Very High Energy Lepton Collider*, *JHEP* **05** (2021) 219 [[2012.11555](#)].
- [119] T. Han, D. Liu, I. Low and X. Wang, *Electroweak couplings of the Higgs boson at a multi-TeV muon collider*, *Phys. Rev. D* **103** (2021) 013002 [[2008.12204](#)].
- [120] N. Bartosik et al., *Preliminary Report on the Study of Beam-Induced Background Effects at a Muon Collider*, [1905.03725](#).
- [121] R. Capdevilla, D. Curtin, Y. Kahn and G. Krnjaic, *Discovering the physics of  $(g - 2)_\mu$  at future muon colliders*, *Phys. Rev. D* **103** (2021) 075028 [[2006.16277](#)].
- [122] M. Ruhdorfer, E. Salvioni and A. Weiler, *A Global View of the Off-Shell Higgs Portal*, *SciPost Phys.* **8** (2020) 027 [[1910.04170](#)].
- [123] M. Chiesa, F. Maltoni, L. Mantani, B. Mele, F. Piccinini and X. Zhao, *Measuring the quartic Higgs self-coupling at a multi-TeV muon collider*, *JHEP* **09** (2020) 098 [[2003.13628](#)].
- [124] A. Costantini, F. De Lillo, F. Maltoni, L. Mantani, O. Mattelaer, R. Ruiz et al., *Vector boson fusion at multi-TeV muon colliders*, *JHEP* **09** (2020) 080 [[2005.10289](#)].

- [125] R. Capdevilla, D. Curtin, Y. Kahn and G. Krnjaic, *A No-Lose Theorem for Discovering the New Physics of  $(g - 2)_\mu$  at Muon Colliders*, [2101.10334](#).
- [126] N. Bartosik et al., *Detector and Physics Performance at a Muon Collider*, *JINST* **15** (2020) P05001 [[2001.04431](#)].
- [127] W. Yin and M. Yamaguchi, *Muon  $g - 2$  at multi-TeV muon collider*, [2012.03928](#).
- [128] J. Kalinowski, T. Robens, D. Sokolowska and A. F. Zarnecki, *IDM Benchmarks for the LHC and Future Colliders*, *Symmetry* **13** (2021) 991 [[2012.14818](#)].
- [129] G.-y. Huang, F. S. Queiroz and W. Rodejohann, *Gauged  $L_\mu - L_\tau$  at a muon collider*, *Phys. Rev. D* **103** (2021) 095005 [[2101.04956](#)].
- [130] W. Liu and K.-P. Xie, *Probing electroweak phase transition with multi-TeV muon colliders and gravitational waves*, *JHEP* **04** (2021) 015 [[2101.10469](#)].
- [131] T. Han, S. Li, S. Su, W. Su and Y. Wu, *Heavy Higgs bosons in 2HDM at a muon collider*, *Phys. Rev. D* **104** (2021) 055029 [[2102.08386](#)].
- [132] S. Bottaro, A. Strumia and N. Vignaroli, *Minimal Dark Matter bound states at future colliders*, *JHEP* **06** (2021) 143 [[2103.12766](#)].
- [133] T. Li, M. A. Schmidt, C.-Y. Yao and M. Yuan, *Charged lepton flavor violation in light of the muon magnetic moment anomaly and colliders*, *Eur. Phys. J. C* **81** (2021) 811 [[2104.04494](#)].
- [134] P. Asadi, R. Capdevilla, C. Cesarotti and S. Homiller, *Searching for leptoquarks at future muon colliders*, *JHEP* **10** (2021) 182 [[2104.05720](#)].
- [135] M. Sahin and A. Caliskan, *Excited muon production at muon colliders via contact interaction*, [2105.01964](#).
- [136] J. Chen, C.-T. Lu and Y. Wu, *Measuring Higgs boson self-couplings with  $2 \rightarrow 3$  VBS processes*, *JHEP* **10** (2021) 099 [[2105.11500](#)].
- [137] G. Haghighat and M. Mohammadi Najafabadi, *Search for lepton-flavor-violating ALPs at a future muon collider and utilization of polarization-induced effects*, [2106.00505](#).
- [138] S. Bottaro, D. Buttazzo, M. Costa, R. Franceschini, P. Panci, D. Redigolo et al., *Closing the window on WIMP Dark Matter*, [2107.09688](#).
- [139] P. Bandyopadhyay, A. Karan and C. Sen, *Discerning Signatures of Seesaw Models and Complementarity of Leptonic Colliders*, [2011.04191](#).
- [140] C. Sen, P. Bandyopadhyay, S. Dutta and A. KT, *Displaced Higgs production in Type-III Seesaw at the LHC/FCC, MATHUSLA and Muon collider*, [2107.12442](#).

- 
- [141] T. Han, W. Kilian, N. Kreher, Y. Ma, J. Reuter, T. Striegl et al., *Precision Test of the Muon-Higgs Coupling at a High-energy Muon Collider*, [2108.05362](#).
  - [142] P. Bandyopadhyay, A. Karan and R. Mandal, *Distinguishing signatures of scalar leptoquarks at hadron and muon colliders*, [2108.06506](#).
  - [143] R. Dermisek, K. Hermanek and N. McGinnis, *Di-Higgs and tri-Higgs boson signals of muon  $g-2$  at a muon collider*, *Phys. Rev. D* **104** (2021) L091301 [[2108.10950](#)].
  - [144] S. Qian, C. Li, Q. Li, F. Meng, J. Xiao, T. Yang et al., *Searching for heavy leptoquarks at a muon collider*, [2109.01265](#).
  - [145] R. Ruiz, A. Costantini, F. Maltoni and O. Mattelaer, *The Effective Vector Boson Approximation in High-Energy Muon Collisions*, [2111.02442](#).
  - [146] M. Chiesa, B. Mele and F. Piccinini, *Multi Higgs production via photon fusion at future multi-TeV muon colliders*, [2109.10109](#).
  - [147] W. Liu, K.-P. Xie and Z. Yi, *Testing leptogenesis at the LHC and future muon colliders: a  $Z'$  scenario*, [2109.15087](#).
  - [148] D. Buttazzo and P. Paradisi, *Probing the muon  $g - 2$  anomaly with the Higgs boson at a muon collider*, *Phys. Rev. D* **104** (2021) 075021.
  - [149] L. Di Luzio, R. Gröber and G. Panico, *Probing new electroweak states via precision measurements at the LHC and future colliders*, *JHEP* **01** (2019) 011 [[1810.10993](#)].
  - [150] T. Han, Z. Liu, L.-T. Wang and X. Wang, *WIMPs at High Energy Muon Colliders*, *Phys. Rev. D* **103** (2021) 075004 [[2009.11287](#)].
  - [151] J. Chen, T. Li, C.-T. Lu, Y. Wu and C.-Y. Yao, *The measurement of Higgs self-couplings through  $2 \rightarrow 3$  VBS in future muon colliders*, [2112.12507](#).
  - [152] R. Capdevilla, D. Curtin, Y. Kahn and G. Krnjaic, *Systematically Testing Singlet Models for  $(g - 2)_\mu$* , [2112.08377](#).
  - [153] R. Franceschini and X. Zhao, “to appear.”
  - [154] M. Ciafaloni, P. Ciafaloni and D. Comelli, *Bloch-Nordsieck violating electroweak corrections to inclusive TeV scale hard processes*, *Phys. Rev. Lett.* **84** (2000) 4810 [[hep-ph/0001142](#)].
  - [155] M. Ciafaloni, P. Ciafaloni and D. Comelli, *Electroweak Bloch-Nordsieck violation at the TeV scale: ‘Strong’ weak interactions?*, *Nucl. Phys. B* **589** (2000) 359 [[hep-ph/0004071](#)].
  - [156] V. S. Fadin, L. N. Lipatov, A. D. Martin and M. Melles, *Resummation of double logarithms in electroweak high-energy processes*, *Phys. Rev. D* **61** (2000) 094002 [[hep-ph/9910338](#)].



## Bibliography

---

- [157] M. Melles, *Subleading Sudakov logarithms in electroweak high-energy processes to all orders*, *Phys. Rev. D* **63** (2001) 034003 [[hep-ph/0004056](#)].
- [158] J.-y. Chiu, F. Golf, R. Kelley and A. V. Manohar, *Electroweak Sudakov corrections using effective field theory*, *Phys. Rev. Lett.* **100** (2008) 021802 [[0709.2377](#)].
- [159] J.-y. Chiu, F. Golf, R. Kelley and A. V. Manohar, *Electroweak Corrections in High Energy Processes using Effective Field Theory*, *Phys. Rev. D* **77** (2008) 053004 [[0712.0396](#)].
- [160] J.-y. Chiu, A. Fuhrer, R. Kelley and A. V. Manohar, *Factorization Structure of Gauge Theory Amplitudes and Application to Hard Scattering Processes at the LHC*, *Phys. Rev. D* **80** (2009) 094013 [[0909.0012](#)].
- [161] J.-y. Chiu, A. Fuhrer, R. Kelley and A. V. Manohar, *Soft and Collinear Functions for the Standard Model*, *Phys. Rev. D* **81** (2010) 014023 [[0909.0947](#)].
- [162] A. Manohar, B. Shotwell, C. Bauer and S. Turczyk, *Non-cancellation of electroweak logarithms in high-energy scattering*, *Phys. Lett. B* **740** (2015) 179 [[1409.1918](#)].
- [163] A. V. Manohar and W. J. Waalewijn, *Electroweak Logarithms in Inclusive Cross Sections*, *JHEP* **08** (2018) 137 [[1802.08687](#)].
- [164] C. W. Bauer, N. Ferland and B. R. Webber, *Combining initial-state resummation with fixed-order calculations of electroweak corrections*, *JHEP* **04** (2018) 125 [[1712.07147](#)].
- [165] M. Ciafaloni, P. Ciafaloni and D. Comelli, *Towards collinear evolution equations in electroweak theory*, *Phys. Rev. Lett.* **88** (2002) 102001 [[hep-ph/0111109](#)].
- [166] P. Ciafaloni and D. Comelli, *Electroweak evolution equations*, *JHEP* **11** (2005) 022 [[hep-ph/0505047](#)].
- [167] B. Fornal, A. V. Manohar and W. J. Waalewijn, *Electroweak Gauge Boson Parton Distribution Functions*, *JHEP* **05** (2018) 106 [[1803.06347](#)].
- [168] C. W. Bauer, N. Ferland and B. R. Webber, *Standard Model Parton Distributions at Very High Energies*, *JHEP* **08** (2017) 036 [[1703.08562](#)].
- [169] C. W. Bauer, D. Provasoli and B. R. Webber, *Standard Model Fragmentation Functions at Very High Energies*, *JHEP* **11** (2018) 030 [[1806.10157](#)].
- [170] T. Han, Y. Ma and K. Xie, *High energy leptonic collisions and electroweak parton distribution functions*, *Phys. Rev. D* **103** (2021) L031301 [[2007.14300](#)].
- [171] J. Chen, T. Han and B. Tweedie, *Electroweak Splitting Functions and High Energy Showering*, *JHEP* **11** (2017) 093 [[1611.00788](#)].



- 
- [172] S. Dawson, *The Effective W Approximation*, *Nucl. Phys. B* **249** (1985) 42.
- [173] Z. Kunszt and D. E. Soper, *On the Validity of the Effective W Approximation*, *Nucl. Phys. B* **296** (1988) 253.
- [174] P. Borel, R. Franceschini, R. Rattazzi and A. Wulzer, *Probing the Scattering of Equivalent Electroweak Bosons*, *JHEP* **06** (2012) 122 [[1202.1904](#)].
- [175] T. Kinoshita, *Mass singularities of Feynman amplitudes*, *J. Math. Phys.* **3** (1962) 650.
- [176] T. D. Lee and M. Nauenberg, *Degenerate systems and mass singularities*, *Phys. Rev.* **133** (1964) B1549.
- [177] P. Ciafaloni and D. Comelli, *The Importance of weak bosons emission at LHC*, *JHEP* **09** (2006) 055 [[hep-ph/0604070](#)].
- [178] A. Denner and S. Pozzorini, *One loop leading logarithms in electroweak radiative corrections. 1. Results*, *Eur. Phys. J. C* **18** (2001) 461 [[hep-ph/0010201](#)].
- [179] P. P. Kulish and L. D. Faddeev, *Asymptotic conditions and infrared divergences in quantum electrodynamics*, *Theor. Math. Phys.* **4** (1970) 745.
- [180] R. Franceschini et al., *The CLIC Potential for New Physics*, [1812.02093](#).
- [181] ALEGRO collaboration, E. Adli et al., *Towards an Advanced Linear International Collider*, [1901.10370](#).
- [182] M. Ciafaloni, *The qcd coherent state from asymptotic dynamics*, *Physics Letters B* **150** (1985) 379.
- [183] S. Catani, F. Fiorani and G. Marchesini, *Qcd coherence in initial state radiation*, *Physics Letters B* **234** (1990) 339.
- [184] A. H. Müller, *Perturbative quantum chromodynamics*, Advanced series on directions in high energy physics. World Scientific, Singapore, 1989.
- [185] D. Amati, M. Ciafaloni and G. Veneziano, *Superstring collisions at planckian energies*, *Physics Letters B* **197** (1987) 81.
- [186] J. C. Collins, D. E. Soper and G. F. Sterman, *Factorization of Hard Processes in QCD*, *Adv. Ser. Direct. High Energy Phys.* **5** (1989) 1 [[hep-ph/0409313](#)].
- [187] J. Collins, *Foundations of Perturbative QCD*, Cambridge Monographs on Particle Physics, Nuclear Physics and Cosmology. Cambridge University Press, 2011, [10.1017/CBO9780511975592](#).
- [188] I. Feige and M. D. Schwartz, *Hard-Soft-Collinear Factorization to All Orders*, *Phys. Rev. D* **90** (2014) 105020 [[1403.6472](#)].

## Bibliography

---

- [189] N. Agarwal, L. Magnea, C. Signorile-Signorile and A. Tripathi, *The Infrared Structure of Perturbative Gauge Theories*, [2112.07099](#).
- [190] C. W. Bauer, S. Fleming and M. E. Luke, *Summing Sudakov logarithms in  $B \rightarrow X(s\gamma)$  in effective field theory*, *Phys. Rev. D* **63** (2000) 014006 [[hep-ph/0005275](#)].
- [191] C. W. Bauer, S. Fleming, D. Pirjol and I. W. Stewart, *An Effective field theory for collinear and soft gluons: Heavy to light decays*, *Phys. Rev. D* **63** (2001) 114020 [[hep-ph/0011336](#)].
- [192] C. W. Bauer and I. W. Stewart, *Invariant operators in collinear effective theory*, *Phys. Lett. B* **516** (2001) 134 [[hep-ph/0107001](#)].
- [193] C. W. Bauer, D. Pirjol and I. W. Stewart, *Soft-collinear factorization in effective field theory*, *Phys. Rev. D* **65** (2002) 054022.
- [194] M. Beneke, A. P. Chapovsky, M. Diehl and T. Feldmann, *Soft collinear effective theory and heavy to light currents beyond leading power*, *Nucl. Phys. B* **643** (2002) 431 [[hep-ph/0206152](#)].
- [195] M. Beneke and T. Feldmann, *Multipole expanded soft collinear effective theory with nonAbelian gauge symmetry*, *Phys. Lett. B* **553** (2003) 267 [[hep-ph/0211358](#)].
- [196] R. J. Hill and M. Neubert, *Spectator interactions in soft collinear effective theory*, *Nucl. Phys. B* **657** (2003) 229 [[hep-ph/0211018](#)].
- [197] T. Becher, A. Broggio and A. Ferroglia, *Introduction to Soft-Collinear Effective Theory*, vol. 896. Springer, 2015, [10.1007/978-3-319-14848-9](#), [[1410.1892](#)].
- [198] S. Weinberg, *Lectures on quantum mechanics; 1st ed.* Cambridge Univ. Press, Cambridge, 2013.
- [199] G. Giavarini and G. Marchesini, *IR Finite S Matrix in the QCD Coherent State Basis*, *Nucl. Phys. B* **296** (1988) 546.
- [200] S. Weinberg, *The Quantum theory of fields. Vol. 1: Foundations*. Cambridge University Press, 6, 2005.
- [201] M. Ciafaloni, P. Ciafaloni and D. Comelli, *Anomalous Sudakov Form Factors*, *JHEP* **03** (2010) 072 [[0909.1657](#)].
- [202] A. Denner and S. Pozzorini, *One loop leading logarithms in electroweak radiative corrections. 2. Factorization of collinear singularities*, *Eur. Phys. J. C* **21** (2001) 63 [[hep-ph/0104127](#)].
- [203] G. Cuomo, L. Vecchi and A. Wulzer, *Goldstone Equivalence and High Energy Electroweak Physics*, *SciPost Phys.* **8** (2020) 078 [[1911.12366](#)].

- 
- [204] G. Durieux and O. Matsedonskyi, *The top-quark window on compositeness at future lepton colliders*, *JHEP* **01** (2019) 072 [[1807.10273](#)].
- [205] J. de Blas et al., *Higgs Boson Studies at Future Particle Colliders*, *JHEP* **01** (2020) 139 [[1905.03764](#)].
- [206] R. K. Ellis et al., *Physics Briefing Book: Input for the European Strategy for Particle Physics Update 2020*, [1910.11775](#).
- [207] D. B. Kaplan and H. Georgi,  *$SU(2) \times U(1)$  Breaking by Vacuum Misalignment*, *Phys. Lett. B* **136** (1984) 183.
- [208] K. Agashe, R. Contino and A. Pomarol, *The Minimal composite Higgs model*, *Nucl. Phys. B* **719** (2005) 165 [[hep-ph/0412089](#)].
- [209] G. Panico and A. Wulzer, *The Composite Nambu-Goldstone Higgs*, vol. 913. Springer, 2016, [10.1007/978-3-319-22617-0](#), [[1506.01961](#)].
- [210] G. Banelli, E. Salvioni, J. Serra, T. Theil and A. Weiler, *The Present and Future of Four Top Operators*, *JHEP* **02** (2021) 043 [[2010.05915](#)].
- [211] D. B. Kaplan, *Flavor at SSC energies: A New mechanism for dynamically generated fermion masses*, *Nucl. Phys. B* **365** (1991) 259.
- [212] G. Durieux, M. Perelló, M. Vos and C. Zhang, *Global and optimal probes for the top-quark effective field theory at future lepton colliders*, *JHEP* **10** (2018) 168 [[1807.02121](#)].
- [213] R. Barbieri, *Flavour and Higgs compositeness: present and “near” future*, [1910.00371](#).
- [214] BELLE-II collaboration, W. Altmannshofer et al., *The Belle II Physics Book*, *PTEP* **2019** (2019) 123C01 [[1808.10567](#)].
- [215] A. Cerri et al., *Report from Working Group 4: Opportunities in Flavour Physics at the HL-LHC and HE-LHC*, *CERN Yellow Rep. Monogr.* **7** (2019) 867 [[1812.07638](#)].
- [216] B. Bellazzini, C. Csáki and J. Serra, *Composite Higgses*, *Eur. Phys. J. C* **74** (2014) 2766 [[1401.2457](#)].
- [217] R. Contino, *The Higgs as a Composite Nambu-Goldstone Boson*, in *Theoretical Advanced Study Institute in Elementary Particle Physics: Physics of the Large and the Small*, pp. 235–306, 2011, [1005.4269](#), DOI.
- [218] H. Georgi and D. B. Kaplan, *Composite higgs and custodial  $su(2)$* , *Physics Letters B* **145** (1984) 216.

## Bibliography

---

- [219] D. B. Kaplan, H. Georgi and S. Dimopoulos, *Composite Higgs Scalars*, *Phys. Lett. B* **136** (1984) 187.
- [220] H. Georgi, *Physics from vacuum alignment in a technicolor model*, *Nuclear Physics B* **416** (1994) 699.
- [221] L. Randall and R. Sundrum, *A Large mass hierarchy from a small extra dimension*, *Phys. Rev. Lett.* **83** (1999) 3370 [[hep-ph/9905221](#)].
- [222] A. Pomarol, *Gauge bosons in a five-dimensional theory with localized gravity*, *Phys. Lett. B* **486** (2000) 153 [[hep-ph/9911294](#)].
- [223] K. Agashe, A. Delgado, M. J. May and R. Sundrum, *RS1, custodial isospin and precision tests*, *JHEP* **08** (2003) 050 [[hep-ph/0308036](#)].
- [224] M. J. Dugan, H. Georgi and D. B. Kaplan, *Anatomy of a Composite Higgs Model*, *Nucl. Phys. B* **254** (1985) 299.
- [225] R. Contino, Y. Nomura and A. Pomarol, *Higgs as a holographic pseudoGoldstone boson*, *Nucl. Phys. B* **671** (2003) 148 [[hep-ph/0306259](#)].
- [226] R. Barbieri, B. Bellazzini, V. S. Rychkov and A. Varagnolo, *The Higgs boson from an extended symmetry*, *Phys. Rev. D* **76** (2007) 115008 [[0706.0432](#)].
- [227] A. Manohar and H. Georgi, *Chiral quarks and the non-relativistic quark model*, *Nuclear Physics B* **234** (1984) 189.
- [228] H. Georgi and L. Randall, *Flavor conserving cp violation in invisible axion models*, *Nuclear Physics B* **276** (1986) 241.
- [229] R. Rattazzi and A. Zaffaroni, *Comments on the holographic picture of the Randall-Sundrum model*, *JHEP* **04** (2001) 021 [[hep-th/0012248](#)].
- [230] R. Contino and A. Pomarol, *Holography for fermions*, *JHEP* **11** (2004) 058 [[hep-th/0406257](#)].
- [231] G. Cacciapaglia, C. Csaki, J. Galloway, G. Marandella, J. Terning and A. Weiler, *A GIM Mechanism from Extra Dimensions*, *JHEP* **04** (2008) 006 [[0709.1714](#)].
- [232] J. Santiago, *Minimal Flavor Protection: A New Flavor Paradigm in Warped Models*, *JHEP* **12** (2008) 046 [[0806.1230](#)].
- [233] R. Barbieri, D. Buttazzo, F. Sala, D. M. Straub and A. Tesi, *A 125 GeV composite Higgs boson versus flavour and electroweak precision tests*, *JHEP* **05** (2013) 069 [[1211.5085](#)].
- [234] C. Abel et al., *Measurement of the Permanent Electric Dipole Moment of the Neutron*, *Phys. Rev. Lett.* **124** (2020) 081803 [[2001.11966](#)].

- 
- [235] D. A. Demir, M. Pospelov and A. Ritz, *Hadronic EDMs, the Weinberg operator, and light gluinos*, *Phys. Rev. D* **67** (2003) 015007 [[hep-ph/0208257](#)].
- [236] J. de Vries, G. Falcioni, F. Herzog and B. Ruijl, *Two- and three-loop anomalous dimensions of Weinberg’s dimension-six CP-odd gluonic operator*, *Phys. Rev. D* **102** (2020) 016010 [[1907.04923](#)].
- [237] G. D’Ambrosio, G. F. Giudice, G. Isidori and A. Strumia, *Minimal flavor violation: An Effective field theory approach*, *Nucl. Phys. B* **645** (2002) 155 [[hep-ph/0207036](#)].
- [238] M. Redi and A. Weiler, *Flavor and CP Invariant Composite Higgs Models*, *JHEP* **11** (2011) 108 [[1106.6357](#)].
- [239] M. Redi, *Leptons in Composite MFV*, *JHEP* **09** (2013) 060 [[1306.1525](#)].
- [240] CMS collaboration, A. M. Sirunyan et al., *Search for new physics in dijet angular distributions using proton–proton collisions at  $\sqrt{s} = 13$  TeV and constraints on dark matter and other models*, *Eur. Phys. J. C* **78** (2018) 789 [[1803.08030](#)].
- [241] ATLAS collaboration, M. Aaboud et al., *Measurement of the  $t\bar{t}Z$  and  $t\bar{t}W$  cross sections in proton-proton collisions at  $\sqrt{s} = 13$  TeV with the ATLAS detector*, *Phys. Rev. D* **99** (2019) 072009 [[1901.03584](#)].
- [242] W. Altmannshofer and P. Stangl, *New physics in rare  $B$  decays after Moriond 2021*, *Eur. Phys. J. C* **81** (2021) 952 [[2103.13370](#)].
- [243] K. Agashe, R. Contino, L. Da Rold and A. Pomarol, *A Custodial symmetry for  $Zb\bar{b}$* , *Phys. Lett. B* **641** (2006) 62 [[hep-ph/0605341](#)].
- [244] PARTICLE DATA GROUP collaboration, R. L. Workman, *Review of Particle Physics*, *PTEP* **2022** (2022) 083C01.
- [245] M. Redi, *Composite MFV and Beyond*, *Eur. Phys. J. C* **72** (2012) 2030 [[1203.4220](#)].
- [246] A. Paul and D. M. Straub, *Constraints on new physics from radiative  $B$  decays*, *JHEP* **04** (2017) 027 [[1608.02556](#)].
- [247] L. Vecchi, *The Natural Composite Higgs*, [1304.4579](#).
- [248] R. Barbieri, D. Buttazzo, F. Sala and D. M. Straub, *Less Minimal Flavour Violation*, *JHEP* **10** (2012) 040 [[1206.1327](#)].
- [249] J. de Blas, M. Ciuchini, E. Franco, S. Mishima, M. Pierini, L. Reina et al., *The Global Electroweak and Higgs Fits in the LHC era*, *PoS EPS-HEP2017* (2017) 467 [[1710.05402](#)].

## Bibliography

---

- [250] J. Ellis, M. Madigan, K. Mimasu, V. Sanz and T. You, *Top, Higgs, Diboson and Electroweak Fit to the Standard Model Effective Field Theory*, *JHEP* **04** (2021) 279 [[2012.02779](#)].
- [251] R. Contino, M. Ghezzi, C. Grojean, M. Muhlleitner and M. Spira, *Effective Lagrangian for a light Higgs-like scalar*, *JHEP* **07** (2013) 035 [[1303.3876](#)].
- [252] G. Durieux, A. Irlles, V. Miralles, A. Peñuelas, R. Pöschl, M. Perelló et al., *The electro-weak couplings of the top and bottom quarks — Global fit and future prospects*, *JHEP* **12** (2019) 98 [[1907.10619](#)].
- [253] J. Mrazek, A. Pomarol, R. Rattazzi, M. Redi, J. Serra and A. Wulzer, *The Other Natural Two Higgs Doublet Model*, *Nucl. Phys. B* **853** (2011) 1 [[1105.5403](#)].
- [254] LHCb collaboration, R. Aaij et al., *Observation of CP Violation in Charm Decays*, *Phys. Rev. Lett.* **122** (2019) 211803 [[1903.08726](#)].
- [255] B. Keren-Zur, P. Lodone, M. Nardecchia, D. Pappadopulo, R. Rattazzi and L. Vecchi, *On Partial Compositeness and the CP asymmetry in charm decays*, *Nucl. Phys. B* **867** (2013) 394 [[1205.5803](#)].
- [256] M. Frigerio, M. Nardecchia, J. . Serra and L. Vecchi, *The Bearable Compositeness of Leptons*, *JHEP* **10** (2018) 017 [[1807.04279](#)].
- [257] MU2E collaboration, R. H. Bernstein, *The Mu2e Experiment*, *Front. in Phys.* **7** (2019) 1 [[1901.11099](#)].
- [258] MU3E collaboration, G. Hesketh, S. Hughes, A.-K. Perrevoort and N. Rompotis, *The Mu3e Experiment*, in *2022 Snowmass Summer Study*, 4, 2022, [2204.00001](#).
- [259] J. C. Collins and D. E. Soper, *Angular Distribution of Dileptons in High-Energy Hadron Collisions*, *Phys. Rev. D* **16** (1977) 2219.
- [260] L. D. Landau and E. M. Lifshitz, *Quantum Electrodynamics*, vol. 4 of *Course of Theoretical Physics*. Butterworth-Heinemann, 1982.
- [261] V. V. Sudakov, *Vertex parts at very high energies in quantum electrodynamics*, *Zh. Eksp. Teor. Fiz.* **30** (1956) 87.
- [262] A. Wulzer, *An Equivalent Gauge and the Equivalence Theorem*, *Nucl. Phys. B* **885** (2014) 97 [[1309.6055](#)].

# Curriculum Vitae

Lorenzo Ricci

CONTACT INFORMATION	BSP 725 (Cubotron UNIL) Rte de la Sorge CH-1015 Lausanne	Phone: +41 77 967 22 49 E-mail: lorenzo.ricci@epfl.ch
ACADEMIC EXPERIENCE	<b>École Polytechnique Fédérale de Lausanne</b> , Lausanne, Vaud, Switzerland Ph.D. student in Physics 1/10/2018 — <i>present</i> <ul style="list-style-type: none"> <li>Thesis: Electroweak Physics at Very High Energy</li> <li>Supervisor: Prof. Andrea Wulzer</li> </ul> Teaching assistant <ul style="list-style-type: none"> <li>Quantum Field Theory I (28hrs)– Prof. Riccardo Rattazzi 10/2021</li> <li>Quantum physics IV (28hrs)– Prof. João Penedones 2/2020</li> <li>Quantum physics I (28hrs)– Prof. Giuseppe Carleo 10/2019</li> <li>Quantum physics IV (28hrs)– Profs. João Penedones, Riccardo Rattazzi, Vincenzo Savona 2/2019</li> <li>Experimental physics I (28hrs)– Prof. Burmeister Guido 10/2018</li> </ul>	
PUBLICATIONS	[1] L. Ricci and M. Riembau, <i>Energy Correlators of Hadronically Decaying Electroweak Bosons</i> , 2207.03511. [2] S. Chen, A. Glioti, R. Rattazzi, L. Ricci and A. Wulzer, <i>Learning from radiation at a very high energy lepton collider</i> , <i>JHEP</i> <b>05</b> (2022) 180 [2202.10509]. [3] G. Panico, L. Ricci and A. Wulzer, <i>High-energy EFT probes with fully differential Drell-Yan measurements</i> , <i>JHEP</i> <b>07</b> (2021) 086 [2103.10532]. [4] L. Ricci, R. Torre and A. Wulzer, <i>On the W&amp;Y interpretation of high-energy Drell-Yan measurements</i> , <i>JHEP</i> <b>02</b> (2021) 144 [2008.12978].	
EDUCATION	<b>University of Padua</b> , Padua, Italy Master’s degree in Physics, 110/110 cum laude 10/2016 — 9/2018 <ul style="list-style-type: none"> <li>Thesis: Electroweak Physics at Very High Energy</li> <li>Supervisor: Prof. Andrea Wulzer</li> </ul> Bachelor’s degree in Physics, 110/110 cum laude 10/2013 — 9/2016 <ul style="list-style-type: none"> <li>Thesis: The generating functional for scalar field theories</li> </ul>	
TALKS	<i>Multi-Boson Interactions 2021</i> , Milan, Italy 8/2021 <i>Strong interactions from QCD to new strong dynamics at LHC and Future Colliders</i> , Trento, Italy 9/2022	
SCHOOLS	GGI-Florence, Doctoral School 1/2019	
PH.D. COURSES	Conformal Field theory and Gravity (Prof. João Penedones) Gauge Theories and the Standard Model (Prof. Riccardo Rattazzi) Advanced Quantum Field Theory (Prof. Alessandro Vichi) Before, Behind and Beyond the Standard Model (Prof. Andrea Wulzer) Supersymmetry (Prof. Luca Vecchi)	

LANGUAGES	Italian: Native language. English: Fluent (speaking, reading, writing). French: Intermediate (reading); basic (speaking, writing).
COMPUTER SKILLS	Advanced: Mathematica, L <sup>A</sup> T <sub>E</sub> X Basic: C++
NATIONALITY	Italian